Aachener Verfahrenstechnik Series
AVT.CVT – Chemical Process Engineering
Volume 45 (2024)

Matthias Heßelmann

Mathematical Process Modeling and Optimization of Electrochemical CO_2 Reduction from Micro- to Meter-Scale

Mathematical Process Modeling and Optimization of Electrochemical CO_2 Reduction from Micro- to Meter-Scale

Mathematische Modellierung und Optimierung der Elektrochemischen CO_2 Reduktion vom Mikro- zum Metermaßstab

Von der Fakultät für Maschinenwesen
der Rheinisch-Westfälischen Technischen Hochschule Aachen
zur Erlangung des akademischen Grades
eines Doktors der Ingenieurwissenschaften
genehmigte Dissertation

vorgelegt von

Matthias Heßelmann

Berichter:
Univ.-Prof. Dr.-Ing. Matthias Wessling
Assoc. Prof. Thomas Burdyny, PhD.

Tag der mündlichen Prüfung: 03.06.2024

Parts of this dissertation have been published. Reproduced with permission from:

Matthias Heßelmann, Berinike Clara Bräsel, Robert Gregor Keller, Matthias Wessling
Simulation-based guidance for improving CO_2 reduction on silver gas diffusion electrodes, Electrochemical Science Advances, 2022
DOI: 10.1002/elsa.202100160

Matthias Heßelmann, Hannah Minten, Tristan Geissler, Robert Gregor Keller, André Bardow, Matthias Wessling
Why Membranes Matter: Ion Exchange Membranes in Holistic Process Optimization of Electrochemical CO_2 Reduction, Advanced Sustainable Systems, 2023
DOI: 10.1002/adsu.202300077

Matthias Heßelmann, Daniel Felder, Wenzel Plischka, Sajad Nabi, John Linkhorst, Matthias Wessling, Robert Keller
Dynamics of the Boundary Layer in Pulsed CO_2 Electrolysis, Angewandte Chemie International Edition, 2024
DOI: 10.1002/anie.202406924

Titel: Mathematical Process Modeling and Optimization of Electrochemical CO_2 Reduction from Micro- to Meter-Scale

Autor: Matthias Heßelmann

Reihe: Aachener Verfahrenstechnik Series
AVT.CVT - Chemical Process Engineering
Volume: 45

Herausgeber: Aachener Verfahrenstechnik
Forckenbeckstraße 51
52074 Aachen
Tel.: +49 (0)241 8095470
Fax.: +49 (0)241 8092252
E-Mail: secretary.cvt@avt.rwth-aachen.de
http://www.avt.rwth-aachen.de/AVT

Volltext verfügbar: 10.18154/RWTH-2024-06303

Danksagung

Mit der Fertigstellung dieser Dissertation neigt sich für mich eine ganz besondere, intensive Zeit dem Ende. Dass ich an diesem Punkt angekommen bin, habe ich vielen Menschen zu verdanken, die auf unterschiedlichste Weise dazu beigetragen haben diese Arbeit erfolgreich abzuschließen und meine Promotionszeit zu bereichern. Daher im Folgenden ein paar Worte des Dankes.

Zunächst gilt mein Dank meinem Doktorvater Prof. Matthias Wessling. Matthias, vielen Dank für die langjährige Unterstützung und Betreuung während meiner Promotion. Mit deinen Ideen und Blicken für die großen Zusammenhänge in der Forschungswelt hast du mir stets kreativen Input für meine Arbeit gegeben. Die Möglichkeiten, die du mir zusätzlich gegeben hast, mich beruflich und persönlich weiterzuentwickeln, wie z.B. die Aufenthalte in Australien und den USA, sind für mich von unschätzbarem Wert.

Weiter gilt mein Dank meinem Zweitprüfer Prof. Tom Burdyny und dem Vorsitzenden der Prüfungskommission, Prof. Isaac Boxx.

Ich möchte mich darüber hinaus bei Dr.-Ing. Robert Keller bedanken. Auch bevor du Gruppenleiter der E-Chemie Gruppe geworden bist, hattest du mit deinem weitreichenden Wissen und Ideen bereits Vorbildcharakter und hast damit meine Promotion auch grundlegend geprägt. Vielen Dank Robert für deine gute Betreuung.

Besonderer Dank gilt auch meinen Kolleginnen und Kollegen der Chemischen Verfahrenstechnik (CVT), die mich durch die Höhen und Tiefen der Promotion begleitet haben. Ob durch fachliche Unterstützung, wertvolle Inputs in Diskussionen oder bei den vielen Freizeitaktivitäten neben der Arbeit, habt ihr wesentlich dazu beigetragen diese Dissertation mitzugestalten und meinen Spaß und die Begeisterung für die Themen und die Arbeit an der CVT jedes Mal aufs Neue zu entfachen. Hier möchte ich besonders meinen BürokollegInnen Jan Vehrenberg, Jonas Bäßler, Kristina Baitalow, Ann-Kathrin Mertens, Alexander Limper, Miriam Mineur und Tobias Harhues, sowie Florian Pradellok, Kerstin Brökelmann, Lea Greie, Stefan Herrmann, Daniel Felder, Wenzel Plischka und meinen engen ehemaligen Kollegen Morten Logemann, Patrick Bongartz, Johannes Lohaus und Georg Linz danken.

Darüber hinaus möchte ich mich bei all meinen Studierenden bedanken, die diese Arbeit ermöglicht haben. Hier möchte ich vor allem Berinike Bräsel, Yannik Kohlhaas, Tristan Geißler und Stefan Rattay hervorheben, die einen wesentlichen Anteil an den dargestellten Resultaten hatten.

Ganz besonderer Dank gilt meinen Freunden und meiner Familie (meinen Eltern, meinem Bruder und Mara, Maria und Hans-Peter, Jana und Johannes). Ihr habt mir nicht nur geholfen abseits der Arbeit auf andere

Gedanken zu kommen, sondern auch bei eigentlich allem, was anstand. Egal ob beim Umzug nach Aachen, Hamburg, Australien oder in die USA, ohne euch wäre der Weg bis hier hin und die Promotion nur sehr schwer zu bewältigen gewesen.

Zu guter Letzt möchte ich meiner Freundin Lena danken. Vielen Dank Lena, dass du trotz aller Umstände, die eine Promotion mit sich bringen kann, mich in allen Lagen unterstützt hast. Deine Geduld und Fürsorge besonders in den letzten Monaten vor dem Abschluss meiner Promotion sind nicht selbstverständlich und dafür bin ich dir sehr dankbar.

Aachen, July 2024

Matthias Heßelmann

Contents

Abstract

The defossilation and decarbonization of the chemical industry are imperative to achieve its future goal of becoming carbon neutral. Among the different attempts to tackle this goal, the low-temperature electrochemical CO_2 conversion poses a huge potential to create a closed-loop carbon cycle. The CO_2 electrolysis process uses electricity and water from renewable energy sources to convert CO_2 into sustainable building blocks, thus replacing fossil-based production chains. As most experimental characterization methods cannot completely resolve local mass transport and reaction phenomena in the electrode micro-environment, this thesis focuses on the mathematical modeling of CO_2 electrolysis to give profound insights and derive optimization potentials for steering productivity and selectivity. However, to fully exploit the potential of CO_2 electrolysis, research has to look beyond the electrolyzer and holistically assess the process integration with up- and downstream processing. Therefore, a multi-scale modeling approach is presented in this work that aims to decipher current bottlenecks of CO_2 electrolysis on multiple length scales using different modeling techniques. The micro-environment near a planar plate electrode for electrochemical CO_2 conversion to CO was rigorously modeled by accounting for the size of dissolved species in the electrolyte. The results from this study highlight the importance of enhancing hydrodynamics at the electrode and modulating the electrolyte concentration to improve reactant transport and reduce the cathodic overpotential. Due to mass transport limitations at planar plate electrodes, more advanced electrode geometries, i.e., gas diffusion electrodes, have been investigated within this work. The simulations of the multi-phase transport in gas diffusion electrodes reveal that increasing the electrolyte concentration and flow rate and the gas flow rate helps to overcome ionic conductivity and mass transport limitations. To assess the process on an industrially relevant length scale, a machine learning-based approach was introduced that links multiple surrogate models trained from simulation data of the gas diffusion electrode continuum model to simulate a pilot-scale two-dimensional electrolyzer. Finally, a holistic process optimization was carried out to assess the profitability of the process. The optimization highlights the need for reducing the energy demand and improving the selectivity of the electrochemical CO_2 reduction. Moreover, the often discussed CO_2 pumping effect in CO_2 electrolysis turns out to be a cost saver rather than a cost killer. The results from this thesis show that CO_2 electrolysis can become a viable option in the quest for sustainable production chains when controlling the investigated process parameters and optimizing the process from a holistic perspective.

Zusammenfassung

Die Defossilisierung und Dekarbonisierung der chemischen Industrie ist unabdingbar, um ihr zukünftiges Ziel der Kohlenstoffneutralität zu erreichen. Unter den verschiedenen Lösungen zur Verwirklichung dieses Ziels bietet die elektrochemische Umwandlung von CO_2 ein enormes Potenzial zur Realisierung eines geschlossenen Kohlenstoffkreislaufs. Da die meisten experimentellen Charakterisierungsmethoden nicht in der Lage sind, lokale Stofftransport- und Reaktionsphänomene in der nahen Elektrodenumgebung vollständig aufzulösen, konzentriert sich diese Arbeit auf die mathematische Modellierung der CO_2-Elektrolyse, um tiefere Einblicke zu ermöglichen und Optimierungspotenziale zur Steigerung von Produktivität und Selektivität abzuleiten. Um das Potenzial der CO_2-Elektrolyse voll auszuschöpfen, muss die Forschung jedoch auch die Peripherie des Elektrolyseurs betrachten und die Prozessintegration mit vor- und nachgelagerten Prozessen ganzheitlich bewerten. Daher wird in dieser Arbeit ein Multiskalen-Modellierungsansatz vorgestellt, der darauf abzielt, aktuelle Limitationen der CO_2-Elektrolyse auf mehreren Längenskalen mit Hilfe verschiedener Modellierungstechniken zu entschlüsseln. Die Mikroumgebung in der Nähe einer planaren Plattenelektrode für die elektrochemische CO_2-Umwandlung zu CO wurde unter Berücksichtigung der Größe der gelösten Spezies im Elektrolyten modelliert. Die Ergebnisse verdeutlichen die Bedeutung der Verbesserung der Strömungsbedingungen an der Elektrode und der Einstellung der Elektrolytkonzentration zur Verbesserung des Edukttransports und zur Verringerung der kathodischen Überspannung hervorhebt. Aufgrund des begrenzten Massentransports an planaren Plattenelektroden wurden im Rahmen dieser Arbeit industriell geeignetere Elektrodenkonzepte, sog. Gasdiffusionselektroden, untersucht. Die Simulationen des Mehrphasentransports in Gasdiffusionselektroden zeigen, dass eine Erhöhung der Elektrolytkonzentration und -durchflussmenge sowie der Gasdurchflussmenge dazu beiträgt, die Limitationen der ionischen Leitfähigkeit und des Massentransports zu überwinden. Um den Prozess auf einer industriell relevanten Längenskala zu bewerten, wurde ein auf maschinellem Lernen basierender Ansatz eingeführt. Dabei werden mehrere Surrogat-Modelle verknüpft, die aus Simulationsdaten des Gasdiffusionselektroden-Kontinuumsmodells trainiert wurden, um einen zweidimensionalen Elektrolyseur im Pilotmaßstab zu simulieren. Abschließend wurde eine ganzheitliche Prozessoptimierung durchgeführt, um die Rentabilität des Prozesses zu bewerten. Die Optimierung verdeutlicht die Notwendigkeit, den Energiebedarf zu senken und die Selektivität des Prozesses zu verbessern. Darüber hinaus zeigt die Kostenanalyse, dass der oft diskutierte CO_2-Pumpeffekt bei der CO_2-Elektrolyse als effiziente Regenerierungsmethode des Elektrolyten dienen kann und damit ein Einsparungspotenzial bietet. Die Ergebnisse dieser Arbeit zeigen, dass die CO_2-Elektrolyse eine vielversprechende Option auf der Suche nach nachhaltigen Produktionsketten sein kann, wenn die untersuchten Prozessparameter kontrolliert und der Prozess aus einer ganzheitlichen Perspektive optimiert wird.

1. Introduction

Carbon dioxide (CO_2) emissions into the atmosphere caused by humans have steadily increased since the Industrial Revolution in 1750; however, they have skyrocketed in the last decades from about 5 billion tons in the mid-20th century to more than 35 billion tons per year in 2021 [Frie2022; Gilf2021]. Carbon dioxide, among other gases (N_2O, CH_4, O_3) emitted by humankind, causes the anthropogenic greenhouse effect. The increased emission of such gases amplifies the natural greenhouse gas effect, resulting in a drastic temperature increase, referred to as global warming. To combat global warming and its consequences, e.g., extreme weather, the rise of sea level, and loss of biodiversity, 195 countries across the world signed the Paris Agreement in 2015. The agreement aims to reduce the worldwide CO_2 emissions to keep global temperature increase below 2 °C , preferably below 1.5 °C compared to the pre-industrial age [Shuk2019].

Defossillation and decarbonization of all sectors are imperative to achieve this goal [Hend2020]. However, some of the sectors cannot entirely be decarbonized, e.g., the chemical industry, the cement industry, and steel production, as they either rely on carbon sources or unavoidably emit CO_2 in the production processes. For these hard-to-abate sectors, CO_2 capture, utilization, and storage (CCUS) offers a huge technical, economic, and ecological potential to lower CO_2 emissions and provide sustainable substitutes to fossil-based feedstocks. Among the different applications for utilization of captured CO_2, the production of synthetic fuels, e.g., jet fuels, and the use of CO_2 in plastics and chemicals are of great interest with a technical potential of approx. 11 000 Mt/yr of captured CO_2 in 2030 [Bini2020].

1

The electrochemical conversion of CO_2 at ambient temperature is a promising technology that allows both defossillation and decarbonization of the industry. Moreover, by utilizing electricity from renewable energy sources and CO_2 to produce sustainable carbon building blocks, the carbon cycle can be closed. In this process, renewable electricity and water are used to electrochemically reduce CO_2 to a variety of different products, e.g., formic acid (HCOOH), carbon monoxide (CO), ethylene (C_2H_4), and ethanol (C_2H_5OH) as depicted in Figure 1.1. Techno-economic studies point out CO as an economically viable and atom-economic CO_2 reduction product [Verm2016a]. The mixture of CO and hydrogen (H_2), the so-called syngas, is an important feedstock for the chemical industry with applications ranging from methanol production to Fischer-Tropsch synthesis [Hern2017].

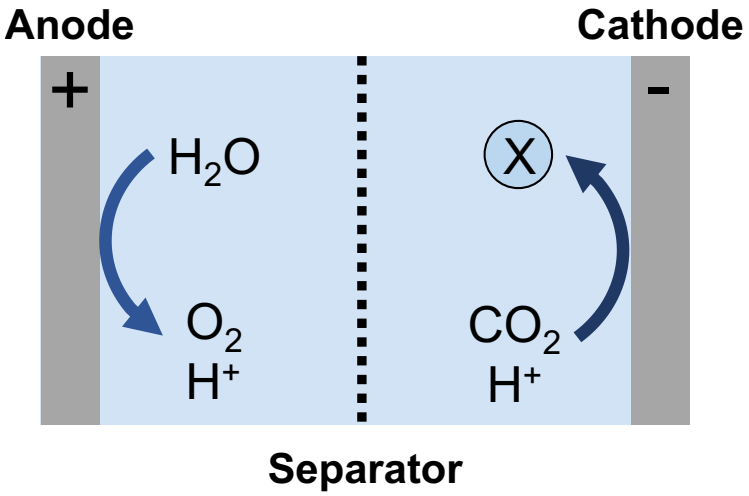

Figure 1.1.: Schematic of an electrolysis cell for CO_2 reduction to a target molecule X.

However, to fully exploit the potential of CCUS technologies such as electrochemical CO_2 reduction, they must operate at a commercial scale to be economically viable [Bini2020]. Currently, there are still several technical challenges to bring electrochemical CO_2 reduction from the laboratory to the industrial realization. The energy efficiency and the carbon efficiency of low-temperature CO_2 electrolysis are yet not competitive with conventional fossil-based technologies.

The scale-up and commercialization of CO_2 electrolysis require a profound understanding of the technology. Even though experimental research on CO_2 electrolysis has already given instructive insights into the process, current analytical and characterization methods limit the understanding of local mass transport and reaction phenomena in the process, which are essential to elucidate the transport of CO_2 to the electrocatalytically active sites. Furthermore, a holistic process analysis beyond electrolysis experiments is required to evaluate the technical and economic potential of this technology. This gap in research on electrochemical CO_2 reduction motivates the following main research question of this thesis:

Main research question:

What are the current bottlenecks of CO_2 electrolysis for industrial realization, and how to overcome them?

To address the main research question, this thesis presents mathematical modeling approaches on multiple length scales of the process to bridge research on fundamental mass transport and reaction mechanisms to holistic process analysis and optimization. Four sub-questions can be derived from the main research question to break down the problem. The sub-questions are discussed in four chapters, following the structure illustrated in Figure 1.2.

Sub-question no. 1:

How to modulate the local electrode environment to improve conditions for electrochemical CO_2 reduction?

The sufficient availability of dissolved CO_2 in the vicinity of the catalyst surface is essential to achieve high activity and selectivity for the CO_2 reduction reaction [Resa2017; Liu2016]. Interactions of the liquid species, the surrounding electrolyte properties, and flow conditions, as well as the electrode potential, affect the local catalyst environment, leading to a complex system for optimization. So far, experimental research lacks methods to resolve the near-electrode region. Therefore, Chapter 3 discusses a

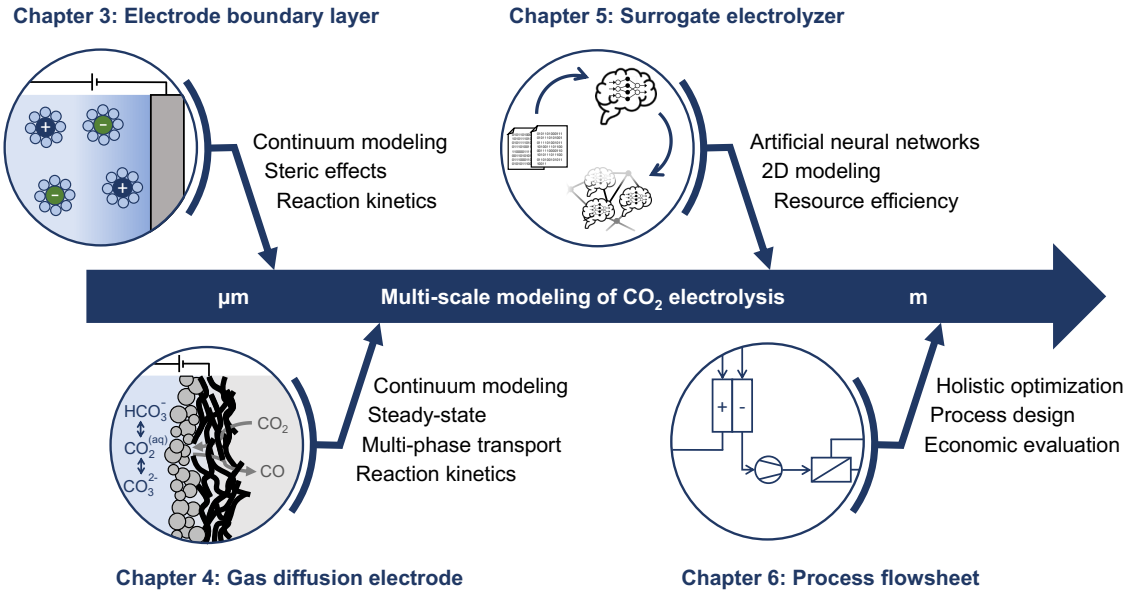

Figure 1.2.: Graphical illustration of the simulative approach for the holistic investigation of CO_2 electrolysis linked to the chapters elaborated in this thesis.

simulative approach to answer sub-question no.1. A one-dimensional transient model of the diffusive boundary layer is implemented in the in-house simulation tool E_nPe_n. The size-modified Poisson Nernst Planck equation is used to account for the solvated ion size as well as local electric field effects. Additionally, the Fraumkin-corrected Butler Volmer equation allows coupling the electrocatalytic reaction rate with the local CO_2 concentration. Thus, correlations between the aforementioned influencing factors, the immediate electrode environment, and the activity of the catalyst are identified and used to give insights on how to improve conditions for electrochemical CO_2 reduction.

Sub-question no. 2:

How to exploit the advantages of gas diffusion electrodes in CO_2 electrolysis?

Moving to industrially-relevant operating conditions (> 200 $mA\,cm^{-2}$ [Burd2019]), the use of gas diffusion electrodes (GDEs) is inevitable to overcome mass transport and solubility limitations in CO_2 electrolysis [Higg2018]. Yet, a comprehensive understanding of mass transport and

conversion phenomena within these complex structures is not well developed. To allow insights into GDEs, Chapter 4 presents a one-dimensional steady-state model of the GDE, which spatially resolves mass transport as well as homogeneous and electrochemical reactions within the electrode. The accurate description of gas and liquid transport in the GDE, considering dissociation reactions in the electrolyte and electrochemical reactions at the catalyst surface, allows to assess and understand the influence of global operating parameters on the local environment in the GDE. Thereby, the simulations show how operating conditions and the morphology of the GDE need to be tuned to increase the activity of the electrode.

Sub-question no. 3:

How to model industrial scale electrolyzers and optimize their operation?

Rigorous modeling of electrochemical CO_2 reduction is computationally costly. Therefore, the works in Chapter 3 and Chapter 4 as well as the literature, predominantly report one-dimensional models or two-dimensional models with only a size-limited representation of the actual electrolysis cell [Bohr2019; Kas2021]. The model-based investigation of mass transport and conversion phenomena in industrial-scale electrolyzers or even in laboratory-scale electrolysis cells is, therefore, nearly impossible. It becomes even more futile when using rigorous models for process optimization with standard optimization solvers. Chapter 5 introduces data-driven approaches to simulate the mass transport in CO_2 electrolysis at multiple scales and optimize the productivity of the process. In this approach, artificial neural networks (ANNs) are trained from simulative data of the model introduced in Chapter 4. Multi-scale modeling of the electrolysis cell is then achieved by linking multiple ANNs, each representing a section of the cell.

Sub-question no. 4:

What is the optimal process design and operating point of CO_2 electrolysis from a holistic perspective?

To complement the mechanistics on a micro- and macro-scale and demonstrate the competitiveness of CO_2 electrolysis, the technology must be viewed from a holistic perspective. Due to the limited CO_2 conversion and undesired side reactions, downstream processing of the product gases is inevitable to achieve the desired product specifications [Aler2021]. Hence, the process design and the economics of the overall process need to be elaborated to assess influencing factors and the distribution of costs. Chapter 6 compares different electrochemical cell types and product purification in CO_2-to-CO electrolysis and discusses the economics within a techno-economic study. Moreover, different designs of the overall process and operating points are possible. An elegant method to identify the optimal process configuration is holistic process optimization. The General Algebraic Modeling System (GAMS) software is used to optimize the specific production costs and investigate the sensitivity of the process to the most relevant economic and technical parameters.

Following the structured multi-scale simulation approach to address the aforementioned research questions, this thesis complements the literature on modeling and economically assessing electrochemical CO_2 reduction, as shown in Figure 1.3. First, Chapter 2 provides a basic background on electrolysis and separation technologies for purifying the product mixtures treated in this work. Moreover, state-of-the-art literature on the cell design, the operation, and the conceptualization of CO_2 electrolysis are described focusing on the eligibility for industrial realization. The following Chapters 3-5 present modeling approaches on different length scales of the process to address the main research objective of this thesis. Finally, Chapter 7 summarizes the work and points out future directions of modeling CO_2 electrolysis.

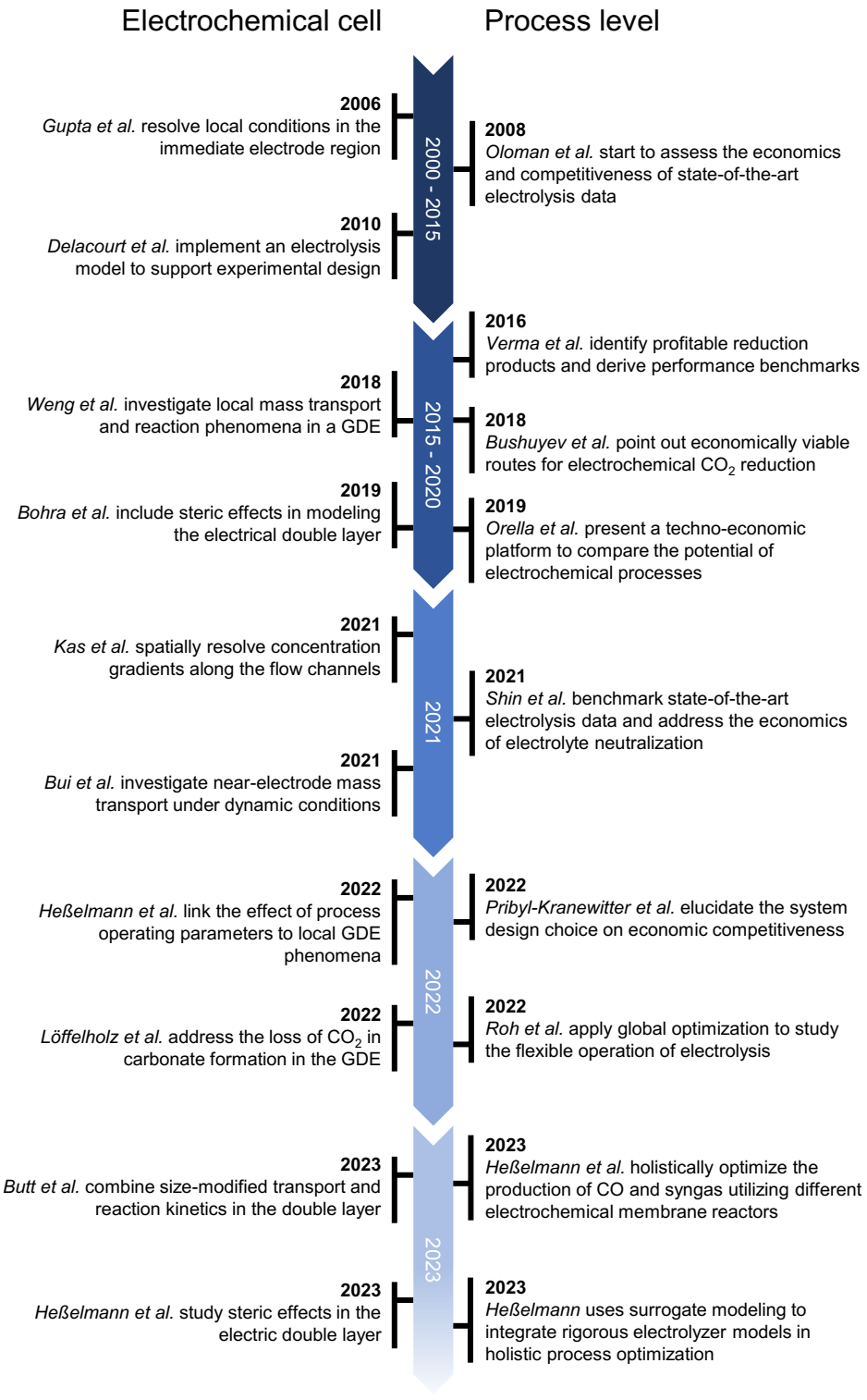

Figure 1.3.: Overview of selected literature related to this thesis. The literature sources are listed in the reference section.

Previous Publications in Student Theses

This thesiss content and results emanate from research conducted under the affiliation and position of the author as a research fellow and PhD candidate at RWTH Aachen University. The position is associated with the Chair of Chemical Process Engineering. The work comprises data based on the following student theses:

- Berinike Göbel, Master's thesis, 30.09.2019, *Modeling of CO_2 reduction to CO in an electrochemical membrane reactor*
- Tristan Geissler, Bachelor's thesis, 07.07.2020, *Techno economic assessment of the electrochemical CO2 conversion with holistic process optimization in GAMS*
- Sajad Nabi, Master's thesis, 24.08.2022, *Modeling the ion distribution in the near-electrode surface in electrochemical CO_2 reduction considering steric effects of ions*
- Maria Theotokatou, Master's thesis, 11.01.2023, *Optimization of CO_2 Electrolysis with Artificial Neural Networks*
- Stefan Rattay, Bachelor's thesis, 08.05.2023, *Implementation of a neural network based on a reactor model for CO_2 electrolysis*

2. Fundamentals

2.1. Electrolysis

This section describes the fundamentals of the electrolyzer, thermodynamics, kinetics, and mass transport in electrochemical conversion processes.

2.1.1. Electrochemical cell

Electrolysis is the subject of electrochemistry concerned with the chemical conversion of molecules by introducing electrical energy. Such processes are initiated in an electrochemical cell when applying an electric potential between two electrodes, as illustrated in Figure 2.1.

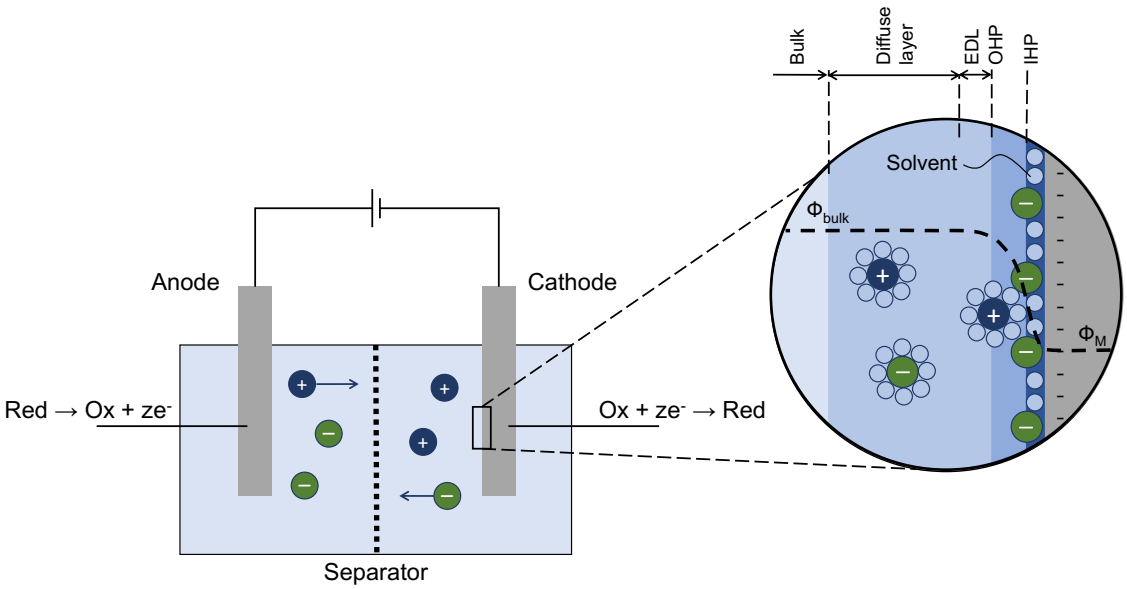

Figure 2.1.: Illustration of an electrolysis cell with a zoom-in on the cathode surface (Red: Reduced species, Ox: Oxidized species, z: number of electrons exchanged, e^-: electron, IHP: inner Helmholtz plane, OHP: outer Helmholtz plane, ϕ_{bulk}: bulk electrolyte potential, ϕ_M: potential of the metal electrode) [Schm2003; Bard2001].

Such cells are also referred to as electrolytic cells. In contrast, electrochemical cells that generate electricity are called galvanic cells. However, this thesis focuses solely on the first type of electrochemical cell. The positively charged electrode within the electrolytic cell is called anode, while the negatively charged electrode is called cathode. The two electrodes are separated by at least one electrolyte phase in which charge is carried by

the movement of ions. The electrolyte includes solutions of ionic species, i.e., salts dissolved in aqueous or organic solvents, as well as ionically conductive polymers and fused salts.
The applied cell potential required to drive charge transport and reactions within the electrochemical cell is the sum of potential differences between all conducting phases within the cell. The constituent potential differences are attributed to individual resistances caused by [Schm2003]:

- resistances at anode and cathode (electrochemical kinetics)
- resistances in the electrolyte (ionic conductivity)
- transport limitations
- contacts and additional parts
- resistances in the outer circuit

The transition in electric potential between two conducting phases, e.g., between electrode and electrolyte, happens almost entirely at the interface. This sharp change in potential implies the existence of a strong electric field at the interface, which significantly influences the behavior of charge carriers, i.e., electrons or ions, in the interfacial region. Hence, the potential difference at an interface predominately controls the charge direction and transfer rate [Bard2001]. The next section deals with reactions that occur due to the charge transfer at the electrode-electrolyte interface.

2.1.2. Electrochemical reactions and kinetics

The zoom-in in Figure 2.1 illustrates the interfacial region at the electrode-electrolyte junction, referred to as the electric double-layer (EDL), in which the electrochemical reactions occur. The boundary layer (BL) at an electrode surface comprises the diffuse layer, the EDL, and the compact layer (also called the Helmholtz or Stern layer). The compact layer of the BL contains solvent molecules and specifically absorbed molecules, which define the location of the inner Helmholtz plane (IHP) by the locus of their electrical centers. The diffuse layer extends from the bulk electrolyte to the outer

Helmholtz plane (OHP). The OHP is defined by the locus of centers of the nearest solvated ions at the immediate electrode surface. These ions are nonspecifically adsorbed and only interact with the electrode by long-range electrostatic forces [Bard2001].
The reactions occurring at the OHP are referred to as oxidation reactions and reduction reactions at the anode and cathode, respectively. The two reactions can be expressed as

$$Oxidation: \ Red \rightarrow Ox + ze^{-} \tag{2.1}$$

$$Reduction: \ Ox + ze^{-} \rightarrow Red \tag{2.2}$$

where *Red* is the reductant, *Ox* is the oxidant, and *z* is the number of electrons e^{-} transferred in the reaction [Schm2003]. Figure 2.2 depicts a detailed scheme of the different steps in the reduction reaction. The reactant species needs to be transported to the electrode surface (mass transport step), where electrons are transferred, and the reactant is electrochemically converted. This step is often accompanied by adsorption and desorption processes of the reacting species and reaction intermediates. After the charge transfer reaction, the formed product is transported through the BL back into the bulk. Moreover, chemical reactions, e.g., dissociation or catalytic decomposition, can occur along with the other aforementioned steps. Attributed to slow reaction or transport rates of one or more of these steps, the overall reaction might become rate-limited [Bard2001].

Each reaction and transport step represents a resistance to the overall electrochemical process, as described in Section 2.1.1. To overcome the individual resistances, a certain driving force is required, referred to as overpotential. The sum of the separate overpotentials η adds up to the cell voltage E_{cell} that is needed to operate the electrochemical cell

$$E_{cell} = E_c^N - E_a^N + \eta \tag{2.3}$$

where E_c^N and E_a^N are the cathodic and anodic half-cell Nernst potentials,

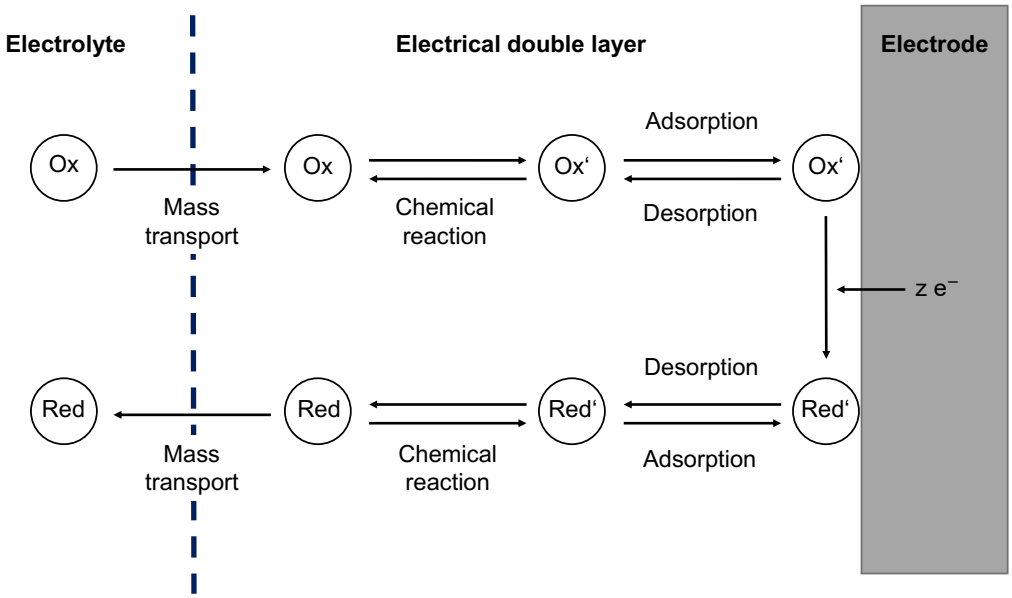

Figure 2.2.: Physical and chemical phenomena that can occur in the electric double-layer during different steps of electrochemical conversion, adopted from Schmidt [Schm2003].

describing the minimum voltage necessary to provide the required energy for a specific electrochemical conversion at specific conditions. The overpotential comprises (1) ohmic losses due to electrode and electrolyte conductivity, (2) activation energy needed for the electrochemical reaction, and (3) mass transport limitations [Bard2001; Schm2003]. The Nernst potential E^N is defined as

$$E^N = -\frac{\Delta G}{zF} \tag{2.4}$$

with ΔG as the change in Gibbs free energy, z as the charge number, and F as the Faraday constant [Mart2015]. For a specific reaction, typically standard electrode potentials E^0 are reported that are measured under standard conditions (25 °C, 1 atm, 1 M). The Nernst potential E^N for a specific reaction and specific operating conditions is then calculated using the Nernst equation

$$E^N = E^0 + \frac{RT}{zF} ln\frac{a_{Ox}}{a_{Red}} \tag{2.5}$$

in which R is the specific gas constant, T is the temperature, and a is the chemical activity of the oxidized and reduced species.

To describe the relationship between reaction rate and overpotential to drive the reaction, a kinetic equation is needed. The most well-known expression of heterogeneous electrode reaction kinetics is the Butler-Volmer equation [Butl1924a; Butl1924b; Butl1932]. The Butler-Volmer equation is an empirical equation derived from fundamental arguments from the transition state theory of electron transfer as described in more detail elsewhere [Dick2020]. The derived equation in the general form is defined as

$$j = j_0[exp(\frac{-\alpha zF}{RT}\eta) - exp(\frac{(1-\alpha)zF}{RT}\eta)] \tag{2.6}$$

where j is the current density, j_0 is the exchange current density, and α is the transfer coefficient. The current density is proportional to the reaction rate and describes the charge transfer rate normalized to the geometrical electrode area. The exchange current density is a measure of the exchange rates between oxidant and reductant species when the electrode and the electrolyte solution at the electrode surface are at equilibrium such that the cathodic and anodic current densities are equal and opposite. The transfer coefficient expresses the fraction of the electrostatic potential energy influencing the reduction (α) or oxidation ($1-\alpha$) reaction rate in equations 2.1-2.2 [Guid2014]. Both kinetic parameters j_0 and α need to be determined through experiments, which become more easily accessible when rewriting the Butler-Volmer equation by neglecting the second exponential term, which is valid for overpotentials » 25.6 mV [Schm2003]. The resulting equation is referred to as Tafel equation [Tafe1905a; Tafe1905b]

$$\eta = \frac{-\alpha z F}{RT} ln \frac{j}{j_0} \tag{2.7}$$

The exchange current density and transfer coefficient can then be extracted from chronoamperometry or chronopotentiometry measurements [Anan2021].

2.1.3. Mass transport

Mass transport in electrochemical cells is governed by one or more of the following driving forces: (1) a gradient in chemical potential (e.g., concentration), (2) a gradient in electrical potential, and (3) a gradient in density or gravity. The combination of these forces on a charged or uncharged body in the electrochemical cell is described by the Nernst-Planck equation

$$J_i(x) = -D_i \frac{\partial c_i(x)}{\partial x} - \frac{z_i F}{RT} D_i c_i(x) \frac{\partial \phi(x)}{\partial x} + c_i(x) v(x) \tag{2.8}$$

Here, $J_i(x)$ is the flux of species i along the x coordinate, D_i is the diffusion coefficient, $\frac{\partial c_i(x)}{\partial x}$ is the concentration gradient, $c_i(x)$ is the concentration of i at position x, $\frac{\partial \phi(x)}{\partial x}$ is the electrical potential gradient, and $v(x)$ is the volume flow velocity along the x coordinate [Bard2001]. It needs to be mentioned that species are assumed to be infinitesimally small in the derivation of equation (2.8). The limit of this assumption will be discussed in Chapter 3. The individual terms in equation (2.8) describe the three types of mass transport, namely diffusion, migration, and convection.
To solve the Nernst-Planck equation, an additional equation is needed to determine the electric potential gradient. The Poisson equation relates the electric field to the local ion concentrations by

$$\frac{\partial^2 \phi(x)}{\partial x^2} = -\frac{F}{\epsilon} \sum_i z_i c_i(x) \tag{2.9}$$

where ϵ is the dielectric permittivity of the solution [Bard2003].
The flux of the reacting species from the bulk solution to the electrode surface controls the reaction rate as well as the rate of product removal. As the concentration of the reactant approaches zero at the electrode, the limiting current density is reached, and the reaction rate and mass transport are in equilibrium. This state is then referred to as mass transport limited. To overcome mass transport limitations in electrochemistry, researchers presented several methods: the use of electrodes with increased specific surface area [Higg2018], the increase of fluid velocity or installation of mixing and turbulence promoters [Perc2018], and the optimization of cell design and operation, e.g., flow fields [Jung2021], ultrasound [Yang2021b], induction [Koda2022], and pulsed operation [Case2021].

2.2. Electrochemical CO_2 reduction

The main objective of the multi-scale modeling approach in this work is to identify the bottlenecks and optimization potentials for CO_2 electrolysis with regard to future industrial realization of the technology. The following section, therefore, presents a brief overview of the configuration and operation strategies of the CO_2 electrolyzer as the central element of this study. Moreover, the last subsection discusses process concepts and perspectives for commercializing electrochemical CO_2 reduction in the industry.

2.2.1. Electrolyzer configuration

From the basic representation of a CO_2 electrolysis flow cell as shown in Figure 2.1, several modifications to the cell design are possible in order to approach the following challenges for an industrially-relevant process: (1) low energy demand, (2) high product selectivity, (3) meaningful production rates, and (4) stable operation over long periods. Hence, the figures of merit to be optimized are the energy efficiency, the Faradaic efficiency, the current density, and the lifetime. Table 2.1 shows the industrial benchmark for each parameter. Here, only cell configurations using gas

diffusion electrodes and gaseous CO_2 as reactant are discussed due to the superior mass transport rates compared to plate electrodes [Higg2018].

Figure of merit	Desired range	Reference
Energy efficiency	> 75 %	[Step2022]
Faradaic efficiency	> 95 %	[Mase2021]
Current density	> 200 mA cm^{-2}	[Burd2019]
Lifetime	> 50 000 h	[Step2022]

Table 2.1.: Figures of merit for industrially-relevant CO_2 electrolysis to carbon monoxide.

The group of Kenis [Whip2010a] approached the aforementioned goals in cell design using a microfluidic cell with a 1.5 mm thin electrolyte gap separating the anode and cathode. Even though the original motivation of this cell design is to enable rapid catalyst and parameter screening, Bhargava et al. [Bhar2020] achieved remarkably high energy efficiencies of up to 80 % and current densities of approx. 800 mA cm^{-2} without compromising high Faradaic efficiencies for CO. The minimization of ohmic resistances and the compact design of microfluidic cells allow to reduce the cell voltage and overcome mass transport limitations due to short diffusion paths. However, in particular, microfluidic cells require precise control of the electrolyte flow to prevent product crossover [Jaya2010]. Thus, membrane-based flow cell designs are advantageous.

Generally, membranes in CO_2 electrolysis can be divided into dense and porous materials. Dense, ion-conductive membranes comprise anion exchange, cation exchange, and bipolar membranes. Compared to the microfluidic cell configuration, implementing an ion exchange membrane allows further design freedom. The zero gap design, as illustrated in Figure 2.3, is commonly used with an alkaline membrane directly mounted onto the cathode, referred to as membrane electrode assembly. Anion exchange membranes used in a zero gap cell demonstrate stable operation at Faradaic efficiencies > 90 % for CO, cell voltages < 3 V and industrially-relevant current densities > 200 mA cm^{-2} [Kutz2017]. Bipolar membranes

with the anion exchange membrane side facing the cathode, defined as forward bias orientation, have also been applied in the zero gap cell design [Prib2021]. In contrast, using a cation exchange membrane in a zero gap cell is not straightforward as the acidic nature of the cation exchange membrane favors the hydrogen evolution reaction [Dela2008; Yang2021a]. Besides the promising performance of zero gap electrolyzers, there are still several challenges to solve: High-resolution neutron imaging of the porous electrode in a zero gap cell revealed increased precipitation of hygroscopic salt crystals, accompanied by inhomogeneous water distribution. In turn, the local differences resulted in higher local reaction rates and thus local dry-out spots, which lead to electrode degradation and cell failure [Disc2022]. Furthermore, the alkalinity at the electrode surface enhances (bi)carbonate formation, imposing energy penalties and CO_2 loss due to (bi)carbonate crossover and subsequent protonation at the anode as well as stability issues with bipolar membranes arising from CO_2 evolution at the internal membrane junction [Mard2021; Rabi2020; Muro2020]. However, new materials, e.g., bipolar membranes with a 3D nanofiber junction [Shen2017], and alternative operating strategies such as pulsed operation [Xu2021] might help to diminish these issues.

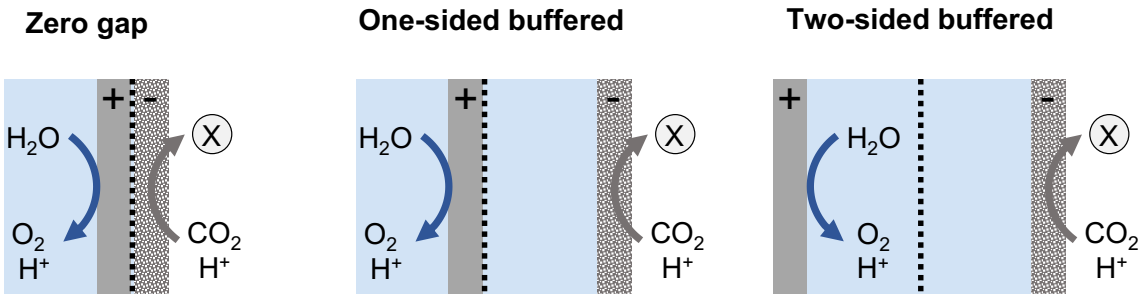

Figure 2.3.: Cell designs for low-temperature CO_2 electrolysis with oxygen evolution reaction on the anode, using a gas diffusion electrode and a separator.

The implementation of an electrolyte flow channel in membrane-based cells allows to specifically tailor the local electrode environments by choice of electrolyte [Chan2023]. The main effects of the electrolyte on the CO_2 reduction reaction are attributed to the pH, the conductivity, and the cation and anion identity of the electrolyte [Verm2016b]. The membrane-based flow cells comprise either one (anolyte or catholyte) or two (anolyte and

catholyte) electrolyte channels. However, Vennekötter et al. [Venn2019a] showed that in a configuration with two flow channels, high ohmic losses impose low energetic efficiency. Electrochemical cells with only one electrolyte channel, named one-sided buffered cells, are commonly used with bipolar membranes in reverse bias mode or cation exchange membranes. Whereas CO_2 electrolysis in the zero gap design with a cation exchange membrane shows only low selectivity, recent research in a one-sided buffered cell successfully demonstrated CO_2 reduction to multi-carbon products in acidic electrolyte [Xie2022c]. The CO_2 electrolysis in acidic media allows for high CO_2 conversion of up to 60 % due to the mitigation of (bi)carbonate formation. Moreover, the presence of certain electrolyte cations and anions at the electrode surface facilitates the CO_2 reduction reaction [Ma2022]. Similar effects also apply to bipolar membranes in the one-sided buffered cell design. Chen et al. [Chen2020] obtained up to 90 % Faradaic efficiency for converting CO_2 to formate at about 500 $mA\,cm^{-2}$. However, the high cell voltage in their cell design, which is mainly attributed to the energy penalty for water splitting in the bipolar membrane, resulted in a low energy efficiency of 15 %. One of the main downsides of using electrolytes in CO_2 electrolysis is the difficulty of controlling the gas-liquid interface in the gas diffusion electrode. When not controlled properly, liquid or gas breakthrough occurs, leading to unstable operation [Yang2020]. However, selecting suitable electrode materials, e.g., the diffusion medium [Baum2022], and electrode modifications, such as incorporating hydrophobic particles into the gas diffusion electrode [Wu2022], helps to mitigate electrode flooding. On the other hand, moderate electrolyte breakthrough might be advantageous as the liquid dissolves and removes salt precipitates, which block gas diffusion paths [Jean2018]. Besides the aforementioned dense ion-conductive membranes, Haas et al. [Haas2018] implemented a porous ZrO_2 diaphragm in a one-sided buffered cell for CO_2 to syngas conversion. They demonstrated stable operation for more than 1 200 hours at current densities of up to 300 $mA\,cm^{-2}$. Compared to polymeric ion exchange membranes, the ZrO_2 diaphragm offers high chemical, mechanical, and temperature stability, making it a

viable alternative for upscaling attempts [Verm1998; Xu2013].

Given the degree of freedom in electrochemical cell design and its implication on the figures of merit, a holistic assessment is required to evaluate economic viability. Therefore, Chapter 6 will discuss how common electrolyzer configurations affect the overall process layout end economics.

2.2.2. Electrolyzer operation

Besides the electrochemical cell design, systematically adjusting the operating parameters of the electrolyzer is important to maximize the figures of merit listed in Table 2.1. Figure 2.4 presents the adjustable operating parameters in CO_2 electrolysis. Bhargava et al. [Bhar2020] proposed several system design rules for optimizing CO_2 electrolysis to CO. They identified the following operating parameters as significant: electrolyte composition, electrolyte flow rate, and CO_2 flow rate.

The electrolyte helps in multiple ways to improve CO_2 reduction: Large cations lead to a more compact EDL, i.e., a lower OHP potential, as they adsorb more easily on the electrode surface due to weaker hydration shells compared to small cations [Mura1991]. Furthermore, certain cations, e.g., K^+, act as a co-catalyst for CO_2 reduction by stabilizing reaction intermediates [Verm2016b; Dogo1972]. Anions with high buffering capacity, e.g., OH^- and $HCO_3{}^-$ improve the selectivity for most CO_2 reduction products by modulating the surface pH, thus, decreasing the proton availability [Verm2016b]. Moreover, specific adsorption of weakly hydrated anions can suppress proton adsorption and enhance CO_2 reduction [Ogur2010; Mist2016]. In contrast, anions with low buffering capacity are more favorable for synthesizing multi-carbon products due to high local pH values [Hori1989; Resa2018]. High electrolyte concentration reduces the ohmic overpotential attributed to increased ionic conductivity [Verm2016b]. However, while high concentrations of certain electrolytes have a positive impact on the energy efficiency, Faradaic efficiency, and current density

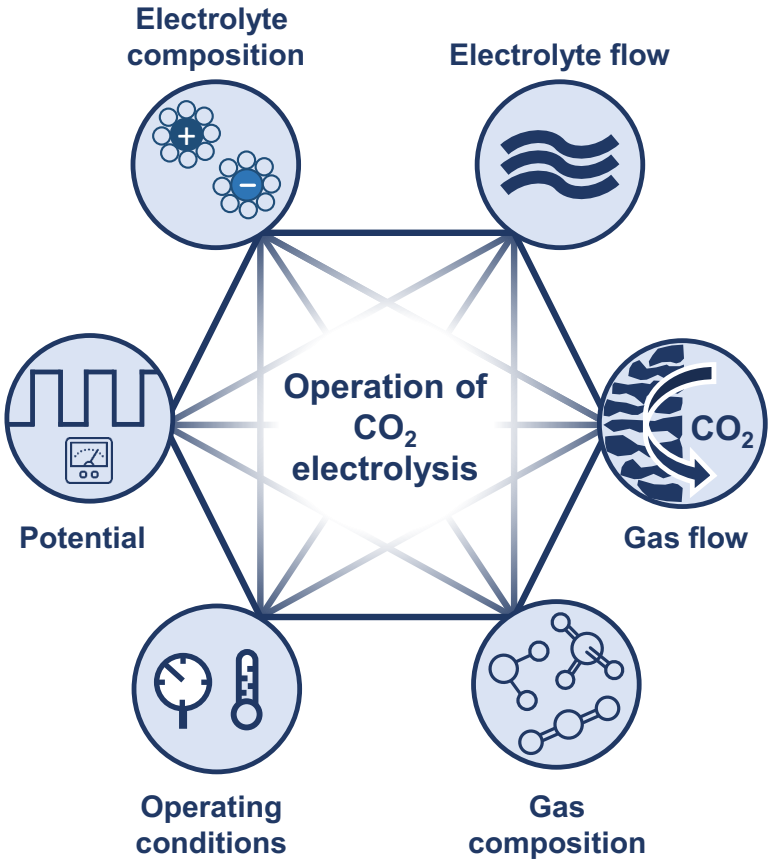

Figure 2.4.: Adjustable operating parameters in CO_2 electrolysis.

of the process, long-term stability might be affected due to corrosion of electrolyzer parts [Bhar2020]. The electrolyte flow rate should also be chosen high to increase the removal of OH^- ions from the catalyst surface and thus limit (bi)carbonate formation. Additionally, high shear forces can enhance the desorption of the reduction product [Bhar2020].

To overcome diffusion and/or solubility limitations of CO_2, the flow of gaseous CO_2 fed into the electrolyzer needs to be high, at least 3-4 times larger than the stoichiometrically required amount of CO_2 [Jean2018]. While high flow rates are desirable, Kim et al. [Kim2015], and Van Daele et al. [Van 2022] showed that even at low CO_2 feed fractions of down to 10 % still reasonably high Fradaic efficiencies of > 70 % for CO and formate can be reached. However, the obtained current densities in these works are fairly low compared to what is needed for an industrially-relevant process.

In addition, the controlled variation of the potential, referred to as pulsed electrolysis, has garnered increasing attention as an operation method to modulate the local microenvironment of the catalyst. The dynamic interplay of mass transport, reaction kinetics, and charge effects in pulsed electrolysis improves the following aspects of CO_2 electrolysis: Replenishment of CO_2 in the BL and relaxation of the surface pH during the off pulse [Bui2021], suppression of the hydrogen evolution reaction by enhancing the coverage of CO_2 reduction intermediates at the catalyst surface [Kim2020], and in the case of copper, induced oxide formation and catalyst morphology changes modulate the product selectivity [Lee2001; Jeon2021].

Revealing the influence of the aforementioned operating parameters on mass transport and reaction phenomena through experiments is difficult due to the limited resolution of common measurement technologies. Hence, Chapter 3 and Chapter 4 present modeling approaches to study CO_2 electrolysis to CO at the electrode vicinity and in the pore network of gas diffusion electrodes when changing relevant operating parameters.

2.2.3. Towards industrial realization

The future perspective of CO_2 electrolysis demands looking beyond experiments on a bench scale and under laboratory conditions. Moreover, a holistic assessment of process concepts, including up- and downstream, is necessary to evaluate the potential of electrochemical CO_2 valorization. First attempts on scaling up electrochemical cells for CO_2 reduction reach up to 100 cm^2 in geometrical surface area [Jean2018]. Also, stacks of three cells having a surface area of 61 cm^2 each have been reported [Endr2019]. Most recently, Sinton and co-workers [Edwa2023] even built a 10x800 cm^2 stack for CO_2-to-CO reduction. However, liquid breakthrough caused by pressure imbalance on a large scale and inadequate assembly and compression of cell stacks calls for optimization in pressure control,

electrode properties, and flow field design. Besides up-scaling, the durability of the electrolyzer of up to 50 000 operating hours is crucial for industrial realization [Step2022]. Yet, the longest continuous tests of CO_2 electrolyzers are only 1 200 - 4 380 hours [Haas2018; Kutz2017]. Whereas both works report stable operation in the tested period, degradation of electrolyzer compartments and operation instabilities might occur when getting closer to the desired operation time [Nwab2020]. Some of the failure modes in CO_2 electrolysis can be summarized as agglomeration and pulverization of catalyst particles [Roge2017; Wu2016], catalyst poisoning [Jeon2018], depolymerization and side-chain modification of the catalyst binder [Nwab2020], loss in hydrophobicity and dissolution of the gas diffusion layer [Dinh2018], salt precipitation [Nwab2020], bubble formation [Lee2001], expansion and deformation of the ion exchange membrane [Hori2003], and membrane polymer degradation [Fuji2012]. The different degradation mechanisms can lead to an increase in ohmic resistance, decrease in selectivity, reduction of the active surface area, change in wetting properties, and loss in ion exchange membrane performance and thus need to be mitigated. Pulsed electrolysis has already been introduced as a strategy to improve process stability, e.g., by influencing the catalyst morphology and avoiding salt precipitation [Jeon2021; Xu2021]. Moreover, tuning the composition of the electrode helps to maintain the desired hydrophobicity in the gas diffusion layer or improves its stability [Kim2016].

Apart from the electrolyzer, the up-and downstream processing need to be considered in holistic process development. As mentioned above, feeding pure CO_2 in excess enhances electrochemical CO_2 reduction. However, most CO_2 feedstocks contain impurities, and purification of those might be uneconomical. Thus, several studies have looked at direct CO_2 electrolysis from realistic CO_2 point sources [Choi2021; Zhai2009; Ko2020; Luc2019; Xu2020]. These studies found that CO_2 reduction selectivity decreases with certain flue gas impurities, i.e., nitrogen oxides and sulfur dioxide being present as these are favorably reduced. However, feeding pure CO_2 afterward restores catalyst activity [Ko2020]. Furthermore, the inter-

play of competitive adsorption on the catalyst surface and the incorporation of sulfur from flue gas can retain the CO_2 reduction selectivity on specific metals [Choi2021; Luc2019]. Moreover, coating the catalyst with ionomers hinders the mass transport of impurities to the active sites and suppresses parasitic side reactions [Xu2020]. Regarding process intensification, integrated concepts where CO_2 is captured in a solvent, which is then fed into the electrolyzer are also investigated [Chen2017; Li2019; Pang2022]. On the other hand, to the best of my knowledge, there is no experimental study on the downstream processing of electrolysis product streams. Yet, some groups demonstrate process concepts aiming for higher product purity beyond tuning the conventional process variables mentioned in the previous section. Using a solid-state electrolyte between two ion exchange membranes in a three-chamber cell configuration, Xia et al. [Xia2019] were able to produce highly concentrated formic acid without the need for further purification. However, the additional layer comes at the cost of an additional energy penalty, which calls for holistic optimization of the overall process from upstream processing, CO_2 electrolysis, to downstream processing [Lama2022].
Even though some challenges for the electrochemical CO_2 valorization are still to be solved, companies have already started to commercialize the process: CERT Systems [CERT2019], Dioxcycle [Diox2021], Dioxide Materials [Mate2009], RenewCO_2 [Rene2018], Twelve [twel2015].

2.3. Gas separation technologies

This thesis focuses on the electrochemical reduction of CO_2 to CO. Attributed to the limited conversion of CO_2 and the parallel occurring hydrogen evolution reaction, the target product CO needs to be separated from the other gases, i.e., CO_2 and H_2. Additionally, recycling of CO_2 back into the electrolyzer is desired to increase the reactant utilization rate. Membrane gas permeation, absorption, and adsorption processes are suitable technologies to separate the present gases. The different processes are described in the following sections.

2.3.1. Membrane gas permeation

Membrane gas permeation has become an industrially viable gas separation technology within the last decades [Bake2004]. Compared to conventional processes such as thermal purification processes, absorption, and adsorption, membrane gas permeation shows advantages in terms of flexibility, mobility, plant size, low energy demand, and low investment costs [Meli2007].

The separation of gases in gas permeation results from gas molecule-membrane material interactions. Process parameters, i.e., pressure and temperature, are used to influence the interactions. Figure 2.5 illustrates the gas permeation process for separating a binary gas mixture. In the schematic, the light blue molecules permeate faster through the membrane than the dark blue molecules, resulting in the enrichment of the dark blue molecules in the retentate, while the light blue molecules accumulate in the permeate.

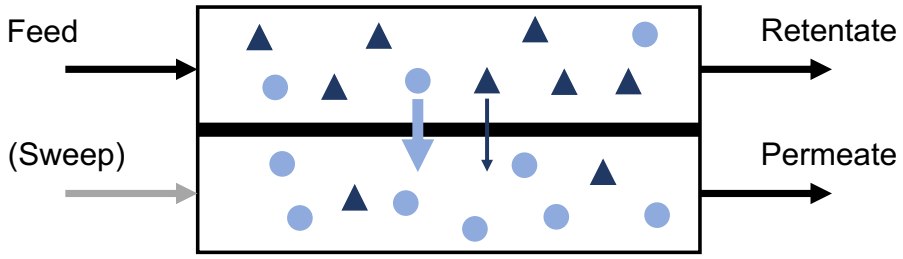

Figure 2.5.: Schematic of a gas permeation membrane module with two gas molecules. The membrane module is shown as a 4-end module with a feed, sweep, retentate, and permeate stream.

In almost all technical applications of gas permeation today, dense polymeric membranes are used [Meli2007]. The transport of gases in these membranes is described by the solution-diffusion model (SDM) [Wijm2006]. In the SDM, three steps govern the transport of a gas molecule through the membrane: (1) absorption of the gas molecule into the membrane at the feed side, (2) diffusion of the molecule through the membrane and (3) desorption of the molecule at the permeate side. Hence, the sorption and diffusion characteristics of the gas-membrane material system drive the gas permeation process and lead to the general expression of

the SDM for a binary gas mixture [Bake2004]

$$J_i = \frac{S_i D_i}{\delta}(x_i p_f - y_i p_p) \tag{2.10}$$

where J_i is the flux of component i through the membrane, S_i is the Henry's law sorption coefficient, D_i is the diffusion coefficient, δ is the thickness of the membrane, x_i and y_i are the mole fractions of component i in the feed and permeate, and p_f and p_p are the absolute pressures in the feed and permeate.

The first term of equation (2.10) is defined as the permeance Q_i, which is a gas - membrane specific value, while the product $S_i D_i$ is called permeability P_i and gives a gas - membrane material specific value. From these values, the selectivity α_{ij} is derived as

$$\alpha_{ij} = \frac{S_i}{S_j}\frac{D_i}{D_j} = \frac{Q_i}{Q_j} = \frac{P_i}{P_j} \tag{2.11}$$

The ratio D_i/D_j is referred to as mobility selectivity and reflects the different sizes of the two gas molecules. In general, the diffusivity decreases with increasing molecule size, and thus, the diffusion of small molecules through the membrane is faster. On the other hand, the solubility selectivity S_i/S_j reflects the relative condensability of two gases. While large molecules are more condensable than small molecules, large molecules more easily absorb into the membrane [Bake2004; Ghos1996].

Both diffusion and sorption depend on the gas-membrane interactions and the state of the membrane. Below the glass transition temperature of the polymer, the membrane is in a glassy state, and the mobility of the polymer chains is low. In this tough and rigid membrane state, the fixed polymer chains impair the diffusive transport of gas molecules along the concentration gradient. Above the glass transition temperature, the membrane is in the rubbery state, the polymer chains are highly flexible, and diffusion is magnitudes faster than in glassy polymers [Ghos1996]. In general, the dependence of the diffusion coefficient on the membrane state

is more pronounced than that of the solubility coefficient [Bake2004]. Thus, mobility selectivity mainly determines the permeation in glassy polymers, whereas rubbery polymers are sorption selective. Consequently, for selecting a suitable gas permeation membrane, the interactions between the membrane material and all gases must be well known.

Besides the membrane material, the process parameters influence the gas permeation process. The last term of the SDM in equation (2.10) describes the partial pressure difference, which is the driving force in gas permeation. Increasing the feed pressure or lowering the permeate pressure, e.g., by a vacuum pump, increases the flux of the permeating component. In the general definition of the SDM, the permeability, i.e., the sorption coefficient, is independent of the pressure, which is valid for small molecules, e.g., He, H_2, N_2, O_2, CH_4). For more condensable gases, e.g., CO_2, hydrocarbons, and vapors, the Henry law is not applicable, and different models need to be used to describe the real gas permeation behavior [Wijm2006].
In rubbery membranes, the permeability of condensable gases increases with increasing pressure, as described by the Flory-Huggins model [Petr2018]. In contrast, in glassy membranes, the degressive behavior of the permeability with increasing pressure is described by the dual-mode sorption model [Paul1979].

In addition to the effect of elevated pressures on the permeability, the presence of condensable gases influences the permeability and selectivity of membranes and leads to deviations from the expected ideal permeation behavior. This effect is called plasticization and is particularly prominent in glassy membranes in the presence of CO_2 and organic vapors in the gas mixture [Barb1988; Meli2007]. Increased absorption of these molecules in the polymer swells the membrane, and the rigid polymer matrix is loosened. In the swollen state, the diffusivity of the penetrating gas molecules increases and, in turn, decreases the mobility selectivity [Zhou1989]. Plasticization is an essential phenomenon in gas permeation

and requires particular consideration when separating gas mixtures containing condensable gases or vapors.

Apart from the pressure, the temperature is a process parameter that can be used to tune gas separation with membranes [Alde2019]. Both diffusion and sorption are dependent on the temperature, leading to the Arrhenius-van't Hoff equation for the permeance

$$Q_i(T) = Q_{i,0}[-\frac{E}{R}(\frac{1}{T} - \frac{1}{T_0})] \text{ with } E = E_D + \Delta H_S \tag{2.12}$$

where $Q_i(T)$ is the permeance at temperature T, $Q_{i,0}$ is the permeance at the reference temperature T_0, E is the activation energy comprising the activation energy for diffusion E_D and the enthalpy of sorption ΔH_S, and R is the ideal gas constant.
For small, non-condensable gas molecules, E_D is typically larger than $|\Delta H_S|$. As E_D is always positive, E also becomes positive in this case, meaning that the permeance increases as the temperature increases [Yamp2006]. In contrast, for condensable gases, ΔH_S is highly negative, and a reverse dependence of the permeance on the temperature is visible. Nonetheless, the membrane selectivity generally decreases with increasing temperature [Meli2007].

2.3.2. Absorption

Absorption refers to the separation process in which one or more components are transferred from one into another phase based on the physical or chemical interaction of the absorbate (absorbed component) and the absorbent (absorbing phase) [Rous1987].
The differentiation between physical and chemical absorption is based on the origin of the absorbate-absorbent interactions. While in physical absorption, the separation depends on the solubility of the gases and the partial pressure, in chemical absorption, reversible or irreversible reactions between the absorbate and the absorbent occur [Rous1987]. A typical

example of a chemical absorption process in the context of the gases considered in this work is amine scrubbing for the selective removal of CO_2 [Roch2009]. Figure 2.6 presents a simplified flowsheet of the process.

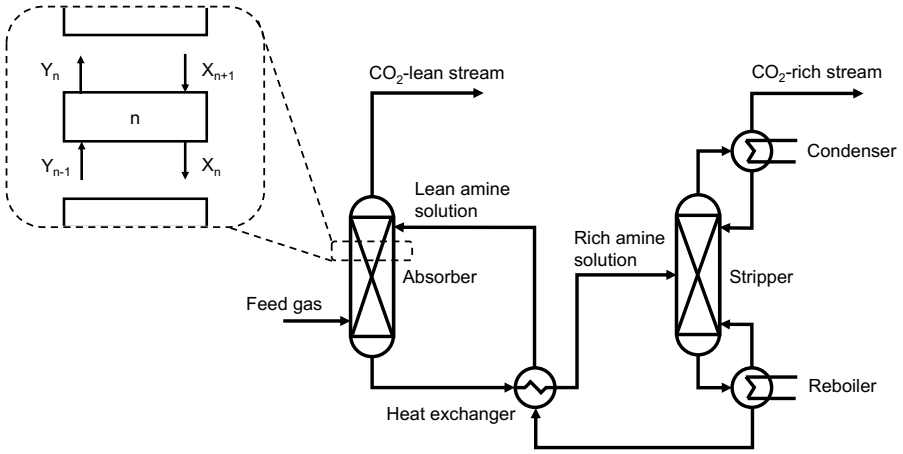

Figure 2.6.: Schematic flowsheet of an amine scrubbing process, adapted from Alie et al. [Alie2005].

The CO_2-containing feed gas enters the absorption column 'Absorber' where the gas stream is brought into contact with the lean amine solution. The counter-current absorption in an ideal tray, i.e., a stage where liquid and gas phases are in equilibrium, is illustrated in the zoom-in of the column. The gas and liquid streams enter the stage with a loading of Y_n and X_{n+1} and leave it with a loading of Y_{n-1} and X_n, respectively. The number of actual stages in the column depends on the efficiency of a tray which describes how close the separation in a stage approaches the ideal stage. The amine solution selectively takes up CO_2 and leaves the column at the bottom where the CO_2-lean gas stream leaves the process at the top with almost no CO_2 being present in the gas mixture. In the second column, 'Stripper', the CO_2-rich amine solution is thermally regenerated and desorbed, and CO_2 leaves the process at the top of the 'Stripper'. The lean amine solution is recycled back into the 'Absorber'.

Among the available amines, Monoethanolamine (MEA) has been comprehensively studied and successfully implemented into industrial CO_2 capture plants. The advantages of MEA over other alkanolamines are fast re-

action kinetics in the chemical binding of CO_2, low raw material costs, and a lower tendency to degradation [Kim2013].
The absorption of CO_2 in the aqueous MEA solution is of both physical and chemical nature. The liquid phase reactions for the CO_2-MEA-water system are the following [Zhan2011]

$$2\,H_2O \longleftrightarrow H_3O^+ + OH^- \tag{2.13}$$

$$MEAH^+ + H_2O \longleftrightarrow MEA + H_3O^+ \tag{2.14}$$

$$MEACOO^- + H_2O \longleftrightarrow MEA + HCO_3{}^- \tag{2.15}$$

$$CO_2 + 2\,H_2O \longleftrightarrow H_3O^+ + HCO_3{}^- \tag{2.16}$$

$$HCO_3{}^- + H_2O \longleftrightarrow H_3O^+ + CO_3{}^{2-} \tag{2.17}$$

Here, CO_2 is primarily captured by the formation of carbamate ($MEACOO^-$) and hydrogencarbonate $HCO_3{}^-$.

Amine scrubbing is mainly used for the removal of CO_2 from natural gas, flue gas, hydrogen, and other gases with low O_2 content to avoid oxidative degradation of the amine [Roch2009; Dutc2015]. Figure 2.7 illustrates qualitatively in which ranges in terms of gas flow rate and CO_2 concentration, amine scrubbing can be used efficiently and economically. According to this classification, amine scrubbing is applied for large gas streams and moderate CO_2 loadings in the gas stream of up to 20 - 30 mol-%. At high CO_2 concentrations in the gas mixture, the energy demand for regeneration of the Amine increases drastically, and other technologies or hybrid process concepts become more advantageous.
The application of absorptive separation processes, i.e., amine scrubbing, for emerging CO_2 utilization technologies such as electrolysis has only been described recently [Aler2021].

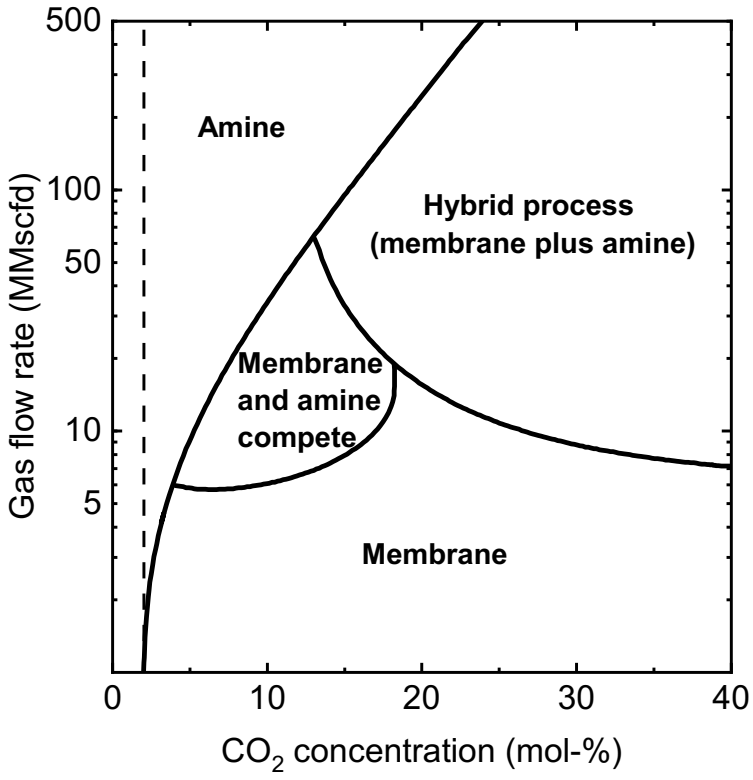

Figure 2.7.: Schematic classification of technologies for CO_2 separation dependent on mass flow and CO_2 inlet concentration. Adapted from Baker et al. [Bake2008].

2.3.3. Adsorption

Adsorption describes the physical or chemical fixation of the adsorbing component (adsorbate) onto a solid material (adsorbent). Like absorption, chemical and physical adsorption either describe the fixation due to chemical bonds between adsorbate and adsorbent (chemisorption) or weaker van der Waals forces between adsorbate and the solid surface (physisorption).

Adsorption processes are operated in a cyclic mode between adsorption and desorption. In the adsorption step, the adsorbate is selectively concentrated at the surface of the adsorbent. To regenerate the adsorbent, either the temperature is increased or the partial pressure of the adsorbate in the gas stream is reduced. The processes are then called Tempera-

ture Swing Adsorption (TSA) and Pressure Swing Adsorption (PSA). There are also other cyclic adsorption processes, i.e., the Inert-Purge Cycle and Displacement-Purge Cycle, as well as combinations of these. However, the most common cycle in adsorptive gas separation is the PSA [Rous1987]. Figure 2.8 illustrates the PSA process concept.

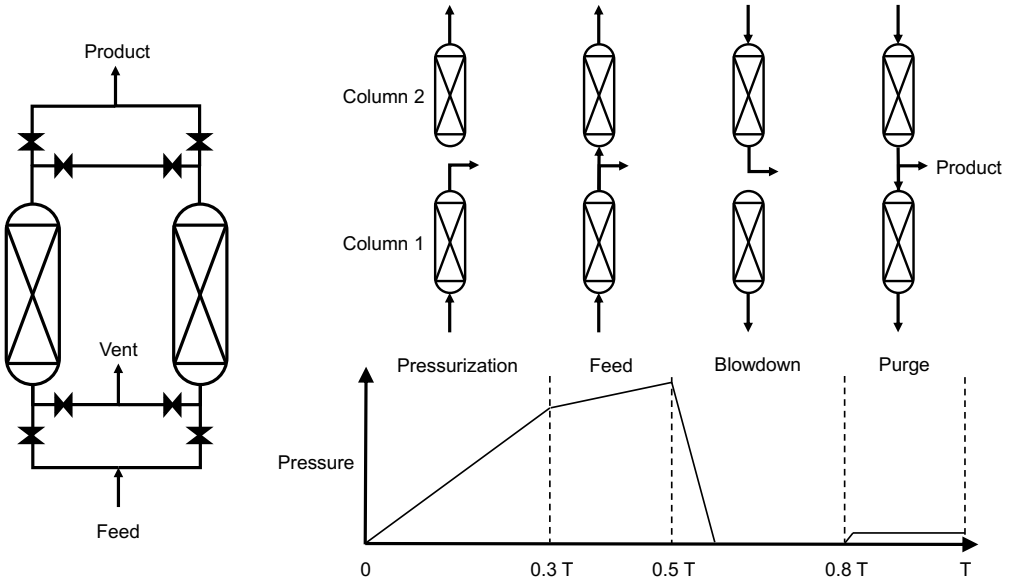

Figure 2.8.: Flowsheet of the basic two-bed PSA system according to Skarstrom [Skar1960] and schematic illustration of the pressure swing cycle adapted from Ruthven [Ruth1984].

The pressure swing cycle generally consists of four steps: (1) pressurization of the column, (2) adsorption of the adsorbate from the feed at high pressure, (3) depressurization of the column to atmospheric pressure, and (4) desorption of the adsorbate at atmospheric pressure. However, variations of the process are possible.

The separation performance of the process is defined by the selectivity, uptake capacity, and stability of the adsorbent. There are mainly four adsorbent materials commercially used in adsorption: molecular-sieve zeolites, activated alumina, silica gel, and activated carbon [Rous1987]. The adsorption selectivity of molecules onto the adsorbent depends on the difference in either adsorption kinetics or adsorption equilibrium. In the gas mixture discussed in this thesis (CO_2, CO, H_2), H_2 tends not to adsorb as

strongly as CO_2 and CO. Wilson et al. [Wils2020] identified commercially available high-density silicas and certain zeolites as efficient and selective absorbents for the bulk separation of CO_2 from CO and H_2. However, to obtain pure CO, multiple adsorption steps and adsorbent modifications by, e.g., impregnating activated alumina with copper or changing the structure of zeolites, are required [Yuba2008; Kasu1991; Wils2020].

For the separation of CO_2-CO-H_2 gas mixtures from CO_2 electrolysis, adsorption has been considered in several techno-economic assessments [Joun2018; Spur2018; Shin2021]. Despite the addressed complexity of adsorptive purification of CO, these studies use simplified calculation methods to account for the economics of the downstream process. Therefore, a more rigorous process flowsheeting is necessary to assess the applicability of adsorption technology for product separation in CO_2 electrolysis.

2

3. Investigation of the near-electrode region

Parts of this chapter have been published as:
Matthias Heßelmann, Daniel Felder, Wenzel Plischka, Sajad Nabi, John Linkhorst, Matthias Wessling, Robert Keller
Dynamics of the Boundary Layer in Pulsed CO_2 Electrolysis, Angewandte Chemie International Edition, 2024
DOI: 10.1002/anie.202406924

3.1. Introduction

The achievable activity and selectivity in electrochemical CO_2 reduction are significantly affected by the local mass transport and reaction phenomena in the immediate electrode environment [Resa2017; Ring2020; Ludw2020]. Hence, understanding and modulating the electrode micro-environment, i.e., the electric double-layer (EDL), would help steer activity and selectivity toward industrially relevant and commercially desirable directions. However, analytically resolving phenomena in the near-electrode region is challenging as the EDL is spatially concealed between the liquid electrolyte phase and the solid electrode phase, as shown in Figure 3.1 [Zaer2012; Shin2022]. Furthermore, complex species-species interactions and coupled electric field effects occur simultaneously, leading to highly convoluted measurement signals [Magn2019].

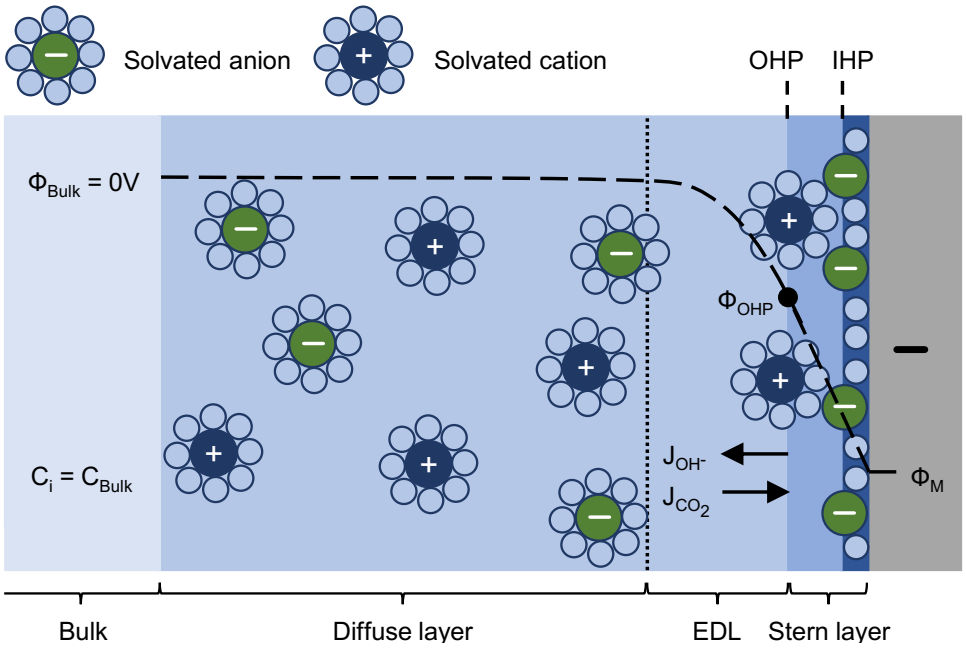

Figure 3.1.: Schematic illustration of the boundary layer (BL) modeled in this work. IHP and OHP stand for the inner and outer Helmholtz plane, respectively. In the following, the domain where electroneutrality is not maintained is referred to as EDL.

Therefore, researchers began to develop mathematical models of the BL to resolve the mass transport and reactions in the electrode vicinity. Bui et al. [Bui2021] reported a transient continuum model of the BL in

COMSOL Multiphysics to study local pH effects and reactant transport in pulsed electrolysis. The model uses the Nernst-Planck equation to simulate species transport and Tafel kinetics to describe the electrode reactions. They found that the enhancement in selective CO_2 reduction to multicarbons when applying a pulsed potential profile results from high local CO_2 concentrations and high pH values and overpotentials. Even though the model of Bui and co-workers allows comprehensive insights into the electrode-near micro-environment, it has several critical shortcomings when modeling the BL. First, their model neglects steric effects of ions, which become relevant in the considered potential regimes and significantly influence the local reaction conditions at the electrode [Bohr2019]. Bohra et al. [Bohr2019] and later Butt et al. [Butt2023] demonstrated that a size-modified expression of the Poisson-Nernst-Planck equation is necessary to correctly simulate the local mass transport in the immediate electrode environment. Several researchers have implemented the generalized modified Poisson-Nernst-Planck (GMPNP) or the size-modified Poisson-Nernst-Planck (SMPNP) to obtain a more realistic and complete representation of the BL in CO_2 electrolysis [Bohr2019; Bohr2020; Ring2020; Zhu2021; Butt2023; Yu2023].

Another shortcoming in most of the BL models presented in the literature is the definition of reaction kinetics. When resolving the double-layer, charge transfer reactions are assumed to occur at the reactant's plane of closest approach to the electrode, which is roughly the same as the outer Helmholtz plane [Gava2000]. Hence, the driving force for charge transfer reactions is the potential drop from the electrode to the outer Helmholtz plane and not the potential difference between the electrode and the bulk electrolyte, as assumed in the basic formulation of the Butler-Volmer or Tafel equation. The corrected formulation is the so-called Frumkin-corrected Butler-Volmer or Tafel equation [Frum1933]. Butt et al. [Butt2023] showed that the consideration of steric effects combined with the Frumkin-corrected equation in modeling the BL gives more valid results than simpler reaction-diffusion or Poisson Nernst-Planck modeling approaches.

The aforementioned models are numerically challenging and computationally demanding. Thus, either mass transport or kinetic expressions are simplified, or simulation times are limited to only a few seconds. However, to elucidate the underlying mass transport and reaction phenomena in CO_2 electrolysis, rigorous consideration of electrode reaction kinetics and species transport, as well as transient modeling, are indispensable.
Here, I present a time-dependent continuum model of the BL implemented in the computationally efficient in-house modeling framework E_nPE_n [Femm2017]. The model uses the SMPNP model to describe mass transport and the Frumkin-corrected Tafel kinetic expression to account for the electrochemical reactions. This allows me to study the electrochemical CO_2 reduction on different time scales to elaborate on species transport, activity, and selectivity when modulating relevant influencing factors, i.e., the applied potential, the electrolyte concentration, and the BL thickness.

3.2. Model description

Figure 3.1 sketches the BL at the cathode simulated in this work. As the concentration and potential gradients orthogonal to the electrode surface are of particular interest, a one-dimensional model was implemented. The domain of the model is confined by the two boundaries, i.e., the outer Helmholtz plane and the bulk solution. The electrochemical reactions only take place at the outer Helmholtz plane and comprise the CO_2 reduction reaction to CO and the alkaline hydrogen evolution reaction as silver is chosen as electrode material, see Reactions (3.1)-(3.2) [Hats2014].

$$CO_2 + H_2O + 2\,e^- \longrightarrow CO + 2\,OH^- \tag{3.1}$$

$$2\,H_2O + 2\,e^- \longrightarrow H_2 + 2\,OH^- \tag{3.2}$$

The electrolyte solution is composed of $KHCO_3$ dissolved in water, which is a commonly used buffer in CO_2 electrolysis. The model equations

are explained more thoroughly in the following and were implemented in the custom modeling framework E_nPE_n developed earlier by our group [Femm2017].

Governing equations

The mass transport of dissolved species i at the time t in the electrolyte solution is described by the general mass balance

$$\frac{\partial C_i}{\partial t} = -\nabla \cdot \vec{J}_i + S_i \tag{3.3}$$

where C_i is the concentration, ∇ is the Nabla operator, $\vec{J}_i$ is the flux, and S_i is the source or sink term. The SMPNP model is used to calculate the flux J_i of dissolved species by diffusion and migration within the BL. The SMPNP model was only reported recently for CO_2 electrolysis and demonstrated superior accuracy and numerical stability to the previously used GMPNP model [Butt2023]. For a more comprehensive comparison of the two models, readers are referred to the work of Butt et al. [Butt2023].

$$\vec{J}_i = -D_i \nabla C_i + \frac{D_i F C_i z_i}{RT} \nabla \Phi + D_i C_i \left(\frac{\beta_i N_A \sum_{j=1}^{n} a_j^3 \nabla C_j}{1 - \sum_{j=1}^{n} a_j^3 C_j} \right) \tag{3.4}$$

Here, D_i is the diffusion coefficient of component i, F is the Faraday constant, z_i is the charge number, R is the ideal gas constant, T is the temperature, Φ is the potential, and N_A is the Avogadro constant. The β_i factor accounts for the influence of the solvent molecule size on the chemical potential of each dissolved species and is calculated from the solvated ion size of ion i, a_i, and of the solvent a_0

$$\beta_i = \frac{a_i^3}{a_0^3} \tag{3.5}$$

The potential in Equation (3.4) is solved with the Poisson equation

$$\nabla \cdot (\epsilon_0 \epsilon_r \nabla \phi) = -F \sum_{i=1}^{n} z_i C_i \tag{3.6}$$

where ϵ_0 and ϵ_r are the vacuum and the relative permittivity of the electrolyte solution. Local variations in the concentration of cationic species are assumed to influence ϵ_r by

$$\varepsilon_r = \varepsilon_r^0 \left(\frac{M_{H_2O} - \sum_i^{n_{cat}} (w_i C_i)}{M_{H_2O}} \right) + \varepsilon_r^{min} \left(\frac{\sum_i^{n_{cat}} (w_i C_i)}{M_{H_2O}} \right) \tag{3.7}$$

with ϵ_r^0 and M_{H_2O} being the relative permittivity and molarity of water at room temperature, w_i being the number of water molecules in the hydration shell of ion i, and ε_r^{min} being the dielectric constant of water under the condition of dielectric saturation and is taken equal to Equation (3.6).

The source and sink terms in Equation (3.3) comprise production and consumption in the following homogeneous acid/base carbonate reactions occurring in the aqueous $KHCO_3$ solution

$$HCO_3^- + OH^- \underset{k_1{}^b}{\overset{k_1{}^f}{\rightleftharpoons}} CO_3^{2-} + H_2O \tag{3.8}$$

$$CO_2 + OH^- \underset{k_2{}^b}{\overset{k_2{}^f}{\rightleftharpoons}} HCO_3^- \tag{3.9}$$

$$H_2O \underset{k_3{}^b}{\overset{k_3{}^f}{\rightleftharpoons}} H^+ + OH^- \tag{3.10}$$

Here, k_k^f and k_k^b refer to the forward and backward kinetic constants of dissociation reactions (3.8)-(3.10). The contribution of S_i to the mass balance is calculated from

$$S_i = \sum_{k=1}^{m} (\mu_{i,k} + \nu_{i,k}) R_k \qquad \forall i = 1...n \tag{3.11}$$

$$R_k = k_k^f \prod_{l=1}^{n} C_l^{\mu_{l,k}} - k_k^b \prod_{l=1}^{n} C_l^{-\nu_{l,k}} \qquad \forall k = 1...m \tag{3.12}$$

where $\mu_{i,k} \geq 0$ is the stoichiometric coefficient of the consumed species i in reaction k and $\nu_{i,k} \leq 0$ is the stoichiometric coefficient of the produced species. The coefficients are zero if species i does not take part in the reaction. The reaction rate R_k includes the forward and backward reactions in the acid/base carbonate reactions (3.8)-(3.10).

Boundary conditions

The electrochemical reactions (3.1) and (3.2) are implemented as a flux boundary condition at the outer Helmholtz plane. The flux $J_{i,OHP}$ is determined using the Faraday law

$$J_{i,OHP} = \sum_{s} \frac{\nu_{i,s} j_s}{z_s F} \qquad \text{i} = CO_2, OH^- \tag{3.13}$$

Here, $\nu_{i,s}$ is the stoichiometric coefficient of species i in the electrochemical reaction s, and j_s is the current density calculated from the Frumkin-corrected Butler-Volmer equation for the CO_2 reduction reaction (CO_2RR) and the hydrogen evolution reaction (HER)

$$j_{CO_2RR} = -j_{0,CO_2RR} \frac{C_{CO_2,OHP}}{C_{CO_2,bulk}} exp\left[\frac{-\alpha_{CO_2RR} F}{R T}(E - E_{eq,CO_2RR} - \Phi_{OHP})\right] \tag{3.14}$$

In the Butler-Volmer equation, j_{0,CO_2RR} is the exchange current density, $C_{CO_2,OHP}$ is the CO_2 concentration at the OHP, $C_{CO_2,bulk}$ is the bulk electrolyte concentration of CO_2, α_{CO_2RR} is the cathodic transfer coefficient,

E is the applied electrode potential in V versus the point of zero charge (PZC), E_{eq,CO_2RR} is the equilibrium voltage and Φ_{OHP} is the potential at the outer Helmholtz plane. The Frumkin correction of the kinetic expression in Equation (3.14) considers that the effective electrode potential to drive the electrochemical reaction in the EDL is not the potential difference $E - \Phi_{Bulk}$ but $E - \Phi_{OHP}$ [Bard2001]. The same also applies to the HER.

$$j_{HER} = -j_{0,HER}\, exp\left[\frac{-\alpha_{HER}\, F}{R\, T}(E - E_{eq,HER} - \Phi_{OHP})\right] \tag{3.15}$$

The exchange current densities and the charge transfer coefficients in Equation (3.14) and (3.15) were fitted to literature data [Hats2014]. The point of zero charge was assumed to translate to a potential of approx. -0.6 V vs SHE, which is in a reasonable range for silver foil with a polycrystalline surface structure [Bohr2019; Kost1994; Hats2014; Lu2014]. The boundary condition for the potential was set to the potential at the outer Helmholtz plane, which is not constant but a function of the potential gradient at that position.

$$\Phi_{OHP} = E - L_{OHP}\frac{\partial \Phi}{\partial x} \tag{3.16}$$

The potential of the bulk solution, representing the left boundary condition, is set to zero, and the concentrations of the dissolved species are set to the bulk concentration of the respective electrolyte solution. Here, the bulk concentrations are calculated from Henry's law, the Sechenov equation, and the dissociation reactions (3.11). Henry's law is used to calculate the sorption equilibrium between gaseous CO_2, $C^0_{CO2,g}$ (high purity CO_2 gas at 1 bar), and dissolved CO_2 in water, $C^0_{CO2,aq}$

$$C^0_{CO2,aq} = K^0_H C^0_{CO2,g} \tag{3.17}$$

$$K^0_H = 93.4517\left(\frac{100}{T}\right) - 60.2409 + 23.3585\, ln\left(\frac{T}{100}\right) \tag{3.18}$$

where K_H^0 is the temperature-dependent Henry constant, calculated for 298.15 K in this work [Rieb2011]. From the concentration of dissolved CO_2 in water, the concentration of dissolved CO_2 in the electrolyte solution, $C_{CO2,aq}$, can be calculated as

$$log\left(\frac{C_{CO2,aq}^0}{C_{CO2,aq}}\right) = K_S C_S \tag{3.19}$$

Here, C_S is the electrolyte concentration, and K_S is the Sechenov's constant, defined as

$$K_S = \sum(h_{CO2} + h_{ion}) \tag{3.20}$$

$$h_{CO2} = h_{CO2}^0 + h_{CO2}^T(T - 298.15) \tag{3.21}$$

with h_i being the Sechenov parameters for all dissolved species [Weis1996]. Subsequently, the concentration of all dissolved species in the respective electrolyte solution can be calculated from the dissociation equilibrium, see Reactions (3.8)-(3.10). The simulation parameters are listed in Table A.1.

Numerical method

The model was implemented in C++ based on the custom in-house E_nPE_n modeling framework [Femm2017]. For solving the set of coupled equations described before, nonlinear solvers by PETSc [Bala1997] were used. The simulation time was set to 30 s with 214 950 temporal discretization steps, after which a steady state was assumed. A total number of 1 756 mesh elements was chosen for a BL thickness of 130 µm. The differential equations were solved in a backward Euler scheme.

3.3. Results and discussion

The following subsections present and discuss the validity of the model and the influence of electrolyte properties and double-layer characteristics on the activity and selectivity of electrochemical CO_2 reduction on a planar silver electrode.

3.3.1. Model validation

The model was validated with experiments from Hatsukade et al. [Hats2014] carried out in an electrochemical flow cell with an aqueous 0.1 M $KHCO_3$ electrolyte solution and silver foil as the cathode. For the validation, a BL thickness of 130 µm was assumed based on a similar value reported by Weng et al., who also used the data of Hatsukade et al. for validation. The polarization curve in Figure 3.2(a) shows a good fit of the simulated data with the experiments. Furthermore, the limiting current density for the electrochemical CO_2 reduction in the simulation is in good agreement with the experimental study, as shown in Figure 3.2(b). However, the model slightly overestimates the CO partial current density in the low and high potential regimes. Also, the simulated partial current density for the HER in Figure 3.2(c) is higher than the measured partial current densities between potentials of -1.35 V vs SHE and -1.75 V vs SHE. Besides the uncertainty in the model parameters taken from the literature, the potential of zero charge, the BL thickness, and the charge transfer reaction kinetics are not explicitly known for the experimental system of Hatsukade et al. For a more accurate fit, the potential of zero charge and the BL thickness must be determined experimentally. Nevertheless, the fitted parameters are in a reasonable range, and the model matches the order of magnitude of the experimental results and shows good agreement with the trends observed in the study by Hatsukade et al.

The in-house modeling framework E_nPE_n allows for highly efficient transient simulations of the BL and, therefore, outperforms recently reported studies on modeling the BL in electrochemical CO_2 reduction in terms of

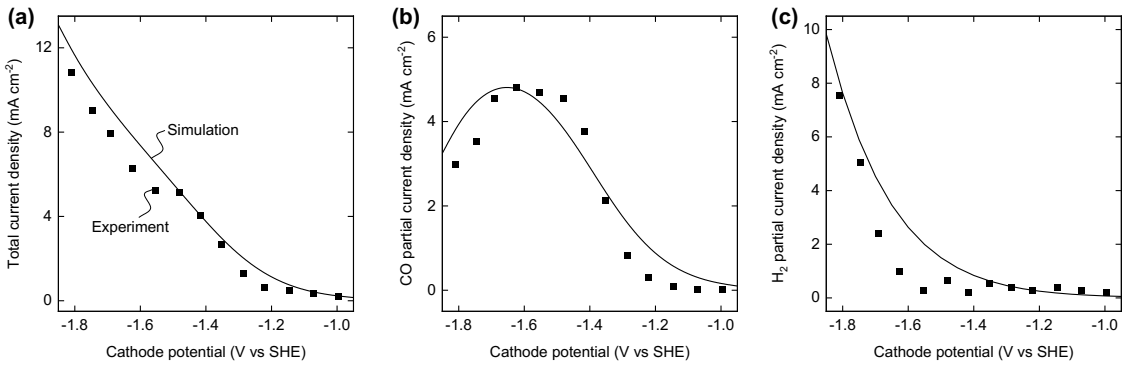

Figure 3.2.: Experimental (points) and simulated (curves) total (a) and partial current densities for the electrochemical CO_2 reduction to CO (b) and the HER (c) as a function of the applied cathode potential. The experimental data was taken from Hatsukade et al. [Hats2014].

simulation time [Bohr2019]. Figure 3.3 shows the current density in the range from 0 s to 15 s and the CO_2 concentration along the BL thickness at different simulation times. The current density peak within the first hundreds of µs in Figure 3.3(a) is attributed to the double-layer charging. The charging current is much larger than the faradaic current for the reduction reaction and can usually not be resolved experimentally as the double-layer charging is completed after a few µs to ms (400 µs in Figure 3.3(a)) [Bard2001; Kim2020; Ha1995]. Only when decreasing the data acquisition time of potentiostatic measurements as low as 0.2 ms Bui et al. [Bui2021] could show the double-layer charging experimentally. It must be mentioned that the charging current in the current model might be overestimated due to a simplification made for the Robin boundary condition at the cathode. The model assumes the same permittivity in the Stern layer as in the electrolyte. However, a recent work by Johnson et al. [John2023] shows that the capacitance of the Stern layer calculated under this assumption is higher than experimentally measured values. Future work should, therefore, use a more realistic surface charge boundary condition.

The CO_2 concentration profiles for the plotted time steps from 0.001 s to 1 s in Figure3.3(b) show that CO_2 is steadily depleted at the electrode as the concentration gradient along the BL increases, thus, leading to the decrease in current density in Figure3.3(a). Between the time step 1 s and 5 s, the slope of the CO_2 concentration profile changes, indicating emerg-

ing diffusion limitation as also shown by the plateauing CO_2 partial current density in Figure 3.2(b). From that time on, the current density and the CO_2 concentration profile only change slightly until after 11 s steady-state is reached, which is in good agreement with the work of Bohra et al. [Bohr2019] (steady-state after 10 s).

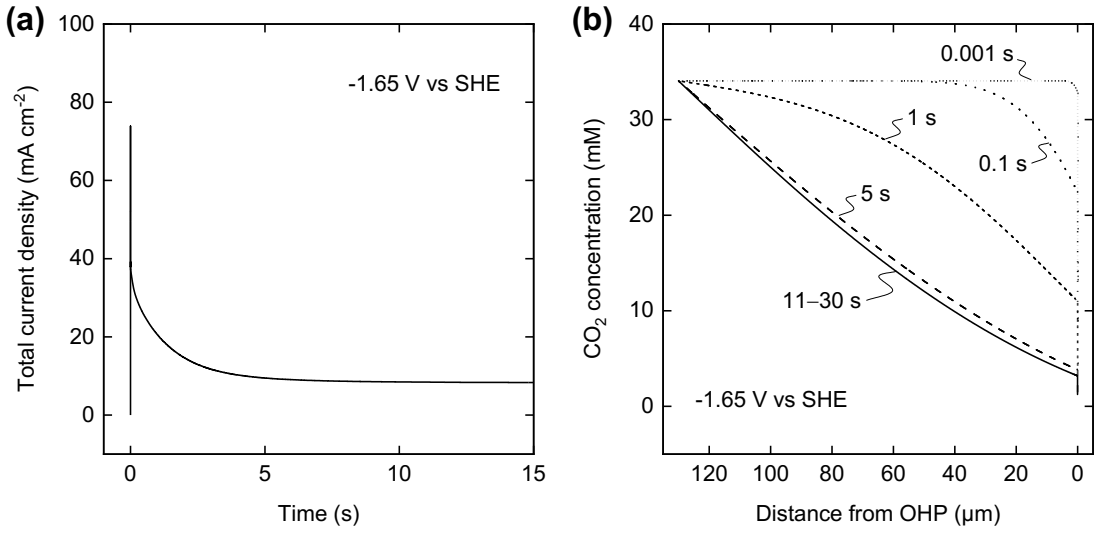

Figure 3.3.: Current density at -1.65 V vs SHE as a function of simulation time in the range from 0s to 15s (a); CO_2 concentration along the BL at -1.65 V vs SHE and different simulation times (b).

In the simulations carried out for the model validation, the CO_2 concentration in the BL significantly drops in steady-state when increasing the potential from -1.05 V vs SHE to -1.85 V vs SHE, as indicated in Figure 3.4(a). At -1.85 V vs SHE, CO_2 is almost completely depleted in the vicinity of the electrode (Figure 3.4(d)) resulting in the observed decrease in the CO_2 reduction rate in Figure 3.2(b). For an applied potential of -1.05 V vs SHE, the CO_2 concentration only changes slightly along the BL as the diffusion of CO_2 is faster than its consumption rate in the electrochemical reduction reaction. Only in the first 2 nm of the BL does the CO_2 concentration drop from 32.5 mM to 23.3 mM. At the same time, Figure 3.4(b) shows an increase in the pH in the BL from 6.8 in the bulk electrolyte to 8.7 and 11.6 at the near-electrode region for -1.05 V vs SHE and -1.85 V vs SHE, respectively. The trends observed for the pH in the BL are also in good agreement with CO_2 electrolysis experiments on Ag foam in a flow cell conducted by

Zhang et al. [Zhan2020] using operando Raman spectroscopy. However, in the simulations of this work, the pH at the immediate electrode surface strongly drops to 6.0 at -1.05 V vs SHE and 5.4 at -1.85 V vs SHE. The strong pH decrease is due to the electrostatic repulsion of OH^- ions at the negatively charged electrode and cannot be resolved with the techniques used by Zhang et al.

The significant changes in the local pH affect the dissociation reactions (3.8)-(3.10) as indicated by the plotted deviation from the equilibrium in Figure 3.4(c) and Figure 3.4(f). The deviation *dev* from the equilibrium for a general dissociation reaction

$$\alpha\mathrm{A} + \beta\mathrm{B} \underset{\mathrm{k}_i{}^b}{\overset{\mathrm{k}_i{}^f}{\rightleftharpoons}} \gamma\mathrm{C} + \delta\mathrm{D} \tag{3.22}$$

is calculated as

$$dev = 1 - \frac{k_i^b[C]^\gamma[D]^\delta}{k_i^f[A]^\alpha[B]^\beta} \tag{3.23}$$

where k_i^b is the backward reaction kinetic parameter, α-δ are the stoichiometric coefficients in Reaction (3.22), and k_i^f is the forward reaction kinetic parameter.

The dissociation reaction between $HCO_3{}^-$ and $CO_3{}^{2-}$ is in equilibrium for almost the entire domain. Only in the range from 3 nm to 0.9 nm and from 0.8 nm to 0 nm the equilibrium is strongly shifted to the left side of Reaction (3.8) and to the right side, respectively. The negative deviation from the equilibrium of Reaction (3.8) is most likely attributed to the drop in pH and, thus, the absence of OH^- ions at the electrode vicinity. However, at the immediate electrode surface, the equilibrium shifts to the right side as the $CO_3{}^{2-}$ concentration becomes almost zero due to enhanced electrostatic repulsion and steric exclusion. The deviation of the dissociation reaction of CO_2 to $HCO_3{}^-$ (Reaction (3.9)) is 1 for the entire domain, indicating that CO_2 is steadily consumed in the BL because of the

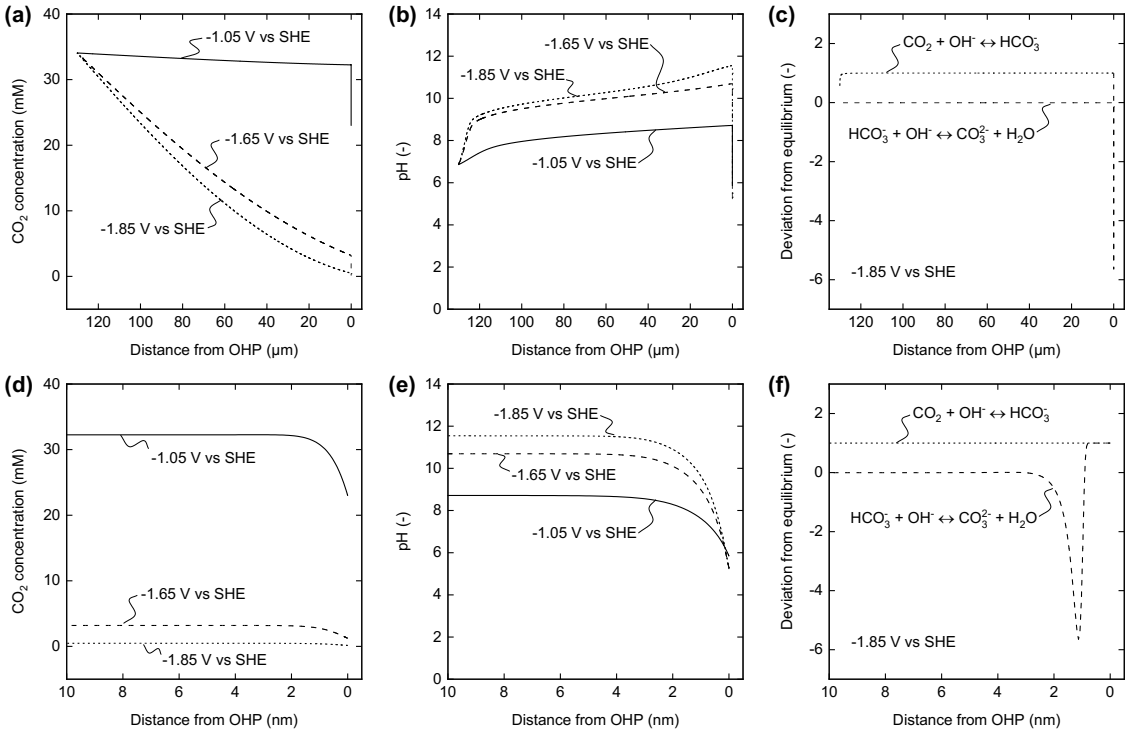

Figure 3.4.: CO_2 concentration in the BL (130 µm) at different potentials (a); pH in the BL (130 µm) at different potentials (b); Deviation from the equilibrium of reactions (3.8)-(3.9) in the BL at a potential of -1.85 V vs SHE (c); CO_2 concentration at the electrode vicinity for a BL thickness of 130 µm at different potentials (d); pH at the electrode vicinity for a BL thickness of 130 µm at different potentials (e); Deviation from the equilibrium of reactions (3.8)-(3.9) at the electrode vicinity for a BL thickness of 130 µm at a potential of -1.85 V vs SHE (f).

high alkalinity in the near-electrode region and sluggish reaction kinetics of the backward reaction.

The presented results highlight the importance of modulating the local electrode environment, i.e., reactant concentration and pH value, by tuning the flow conditions and the electrolyte solution properties. Therefore, the influence of the BL thickness and the electrolyte concentration are investigated more deeply in the following.

3.3.2. Boundary layer thickness

The BL thickness directly correlates with the hydrodynamic conditions at the electrode and with the applied current density or potential [Gupt2006;

Zhan2020]. Hence, modulating, e.g., the flow rate or implementing turbulence promoters, influences the BL thickness and thus affects mass transport in the near-electrode region. The beneficial effect of decreasing the BL thickness was, e.g., demonstrated experimentally by Clark and co-workers [Clar2018a] in an electrochemical flow cell using in-situ product characterization by differential electrochemical mass spectroscopy. When increasing the electrolyte flow rate by a factor of 8.5, they achieved six times higher CO partial current densities in a CO_2 saturated 0.1 M $CsHCO_3$ solution. Similar trends were also observed in another work by Clark et al. [Clar2018b] using 0.1 M $KHCO_3$ electrolyte solution.

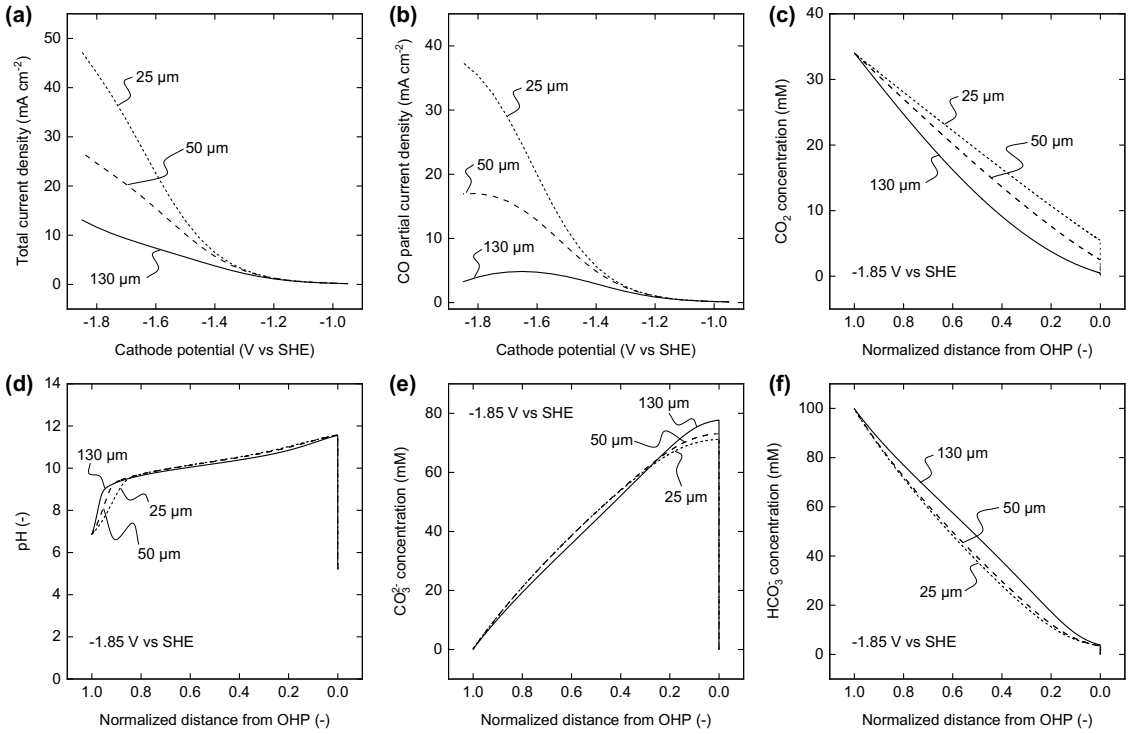

Figure 3.5.: Total current densities at BL thicknesses of 25 µm, 50 µm, and 130 µm as a function of the applied cathode potential (a); CO partial current density (b); CO_2 concentration in the BL as a function of the normalized distance from the OHP (c); pH in the BL (d); CO_3^{2-} concentration in the BL (e); HCO_3^- concentration in the BL (f).

Figure 3.5(a)-(b) shows the effect of decreasing the BL thickness on the simulated total current density and the CO partial current density. Changing the BL thickness by a factor of approx. 5 from 130 µm to 25 µ results in more than 11 times higher CO partial current density at -1.85 V vs SHE.

Furthermore, the potential at which mass transport limitation becomes apparent shifts to more negative potentials vs SHE attributed to the higher CO_2 availability at the electrode, as indicated by Figure 3.5(c). The shift of the mass transport-limited potential regime is also indicated by the change in the slope of the CO_2 concentration profiles, as discussed before.
Interestingly, the pH value in Figure 3.5(d) is not significantly impaired by the change in BL thickness. The pH is lower for smaller BLs in the distance from 100 % to 86 % to the OHP and follows an identical course in the remaining BL. The small difference in the pH profiles close to the electrode can be explained by the increasing production rate of OH^- in the charge transfer reactions when decreasing the BL thickness, as shown in Figure 3.5(a)-(b). Hence, even though diffusive mass transport is improved for lower BL thicknesses, the diffusive flux is balanced with the OH^- production rate. Also, the concentration profiles of ${CO_2}^{3-}$ and ${HCO_3}^-$ in Figure 3.5(e)-(f) follow a fairly similar trend for the different BL thicknesses. In the immediate electrode region, however, the ${CO_2}^{3-}$ concentration is lower for a decreasing BL thickness due to enhanced removal of ${CO_2}^{3-}$ ions.
Again, the general trend of pH gradients and ${HCO_3}^-$ and ${CO_2}^{3-}$ concentration profiles in the near-electrode region shows good agreement with the experimental work by Zhang et al. [Zhan2020]. Similar trends were also found in the study of Lu et al. [Lu2020].

In summary, these results highlight the importance of decreasing mass transport pathways, i.e., the BL thickness, in electrochemical flow cells. Besides enhancing the hydrodynamics at planar plate electrodes, the implementation of gas diffusion electrodes is a promising approach to improve the reactant transport to the reactive sites. More details on the mass transport and reaction phenomena in such electrodes are discussed in Chapter 4.

3.3.3. Electrolyte concentration

The electrolyte not only modulates the near-electrode reaction environment but also influences the polarization behavior, as shown in Figure 3.6(a).

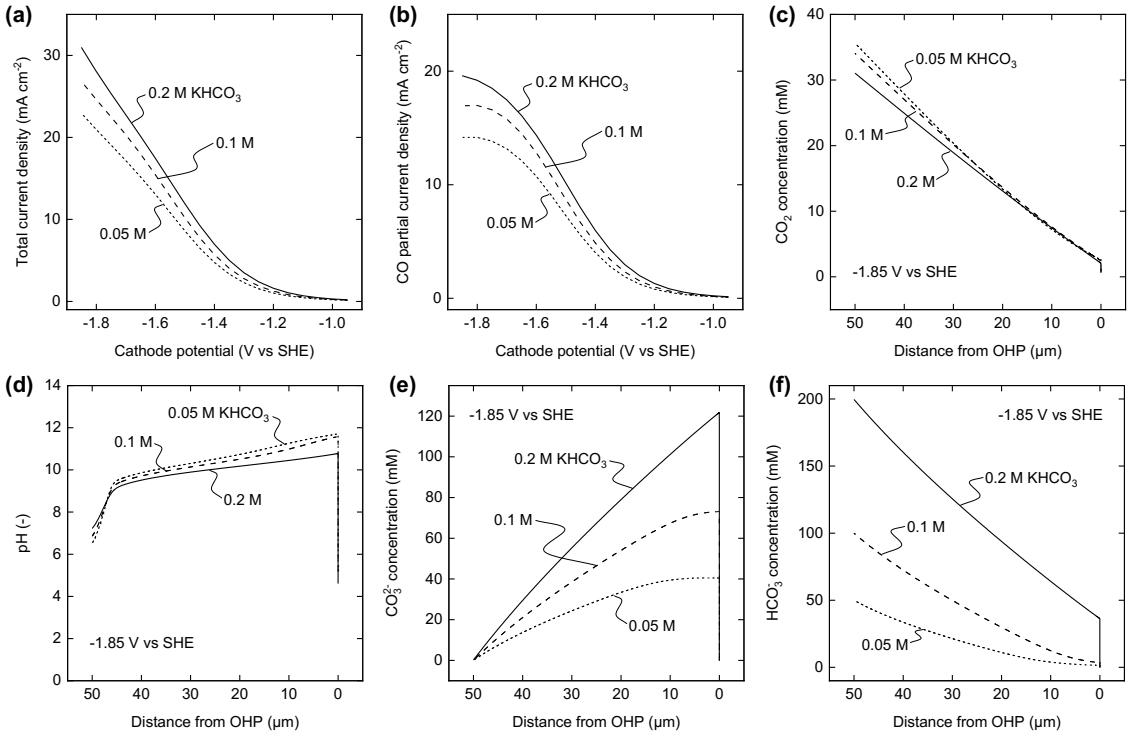

Figure 3.6.: Total current densities at $KHCO_3$ concentrations of 0.05 M, 0.1 M, and 0.2 M as a function of the applied cathode potential with a BL thickness of 50 µm (a); CO partial current density (b); CO_2 concentration in the BL as a function of the normalized distance from the OHP (c); pH in the BL (d); CO_3^{2-} concentration in the BL (e); HCO_3^- concentration in the BL (f).

When increasing the bulk electrolyte concentration from 0.05 M $KHCO_3$ to 0.1 M and 0.2 M, the polarization curve shifts to higher current densities, and the maximum total current density at -1.85 V vs SHE increases from 22.9 $mA\,cm^{-2}$ to 26.8 $mA\,cm^{-2}$ and 31.0 $mA\,cm^{-2}$, respectively. The increase in total current density when changing the bulk electrolyte concentration is mostly attributed to the increasing CO partial current density in Figure 3.6(b). A comparable trend for the current densities at the modeled planar plate electrode is also seen in gas diffusion electrodes as shown in the simulative works in Chapter 4 and in experimental works [Bhar2020]. However, the observed trend for the CO partial current density cannot solely be explained by the availability of more reactants

as the CO_2 concentration in the bulk electrolyte is less for higher $KHCO_3$ concentrations, as shown in Figure 3.6(c) [Zhon2017]. In the first part of the BL from 50 µm to 30 µm, the CO_2 concentration profiles differ due to the different initial bulk concentrations and are closer in the remaining BL, especially close to the OHP, which is in good agreement with the work of Zhu et al. [Zhu2021]. One reason for different current densities in Figure 3.6(b) is the cathodic overpotential required to drive the charge transfer reaction, which decreases with increasing electrolyte concentration, i.e., from -1.13 V vs SHE to -1.14 V vs SHE and -1.15 V vs SHE for the studied increase in the $KHCO_3$ concentration. Even though the absolute difference in the cathodic overpotential is small, the influence on the current density is more significant due to the exponential behavior of the Butler-Volmer kinetic in Equation (3.14)-(3.15).

A beneficial effect that is often ascribed to $KHCO_3$ is the co-catalytic function of K^+ in stabilizing the rate-limiting $CO_2^{\bullet -}$ reaction intermediate [Dogo1972]. Verma et al. [Verm2016b] hypothesized in their work that increasing the electrolyte concentration further improves the stabilizing effect of K^+. However, the results for the K^+ concentration in Figure 3.7 show that the K^+ concentration is almost identical when varying the $KHCO_3$ concentration between 0.05 M and 0.2 M. Hence, the improved reaction rates might be mainly due to the aforementioned higher cathodic overpotential. Again, it needs to be mentioned that the Stern layer capacitance is overestimated in the current model, which might lead to higher concentrations of K^+ in the electrode vicinity, as shown by Johnson et al. [John2023]. Therefore, the effect on the K^+ concentration when varying the electrolyte concentration might be blurred. Potentially, the enhanced stabilization of the $CO_2^{\bullet -}$ radical becomes more relevant at higher electrolyte concentrations and not in the concentration range studied here. Due to convergence issues, a further increase in the bulk electrolyte concentration beyond 0.2 M was not possible with the current model.
Furthermore, the higher $KHCO_3$ concentration of 0.2 M leads to an increased buffer capacity and thus lower pH values over almost the entire BL

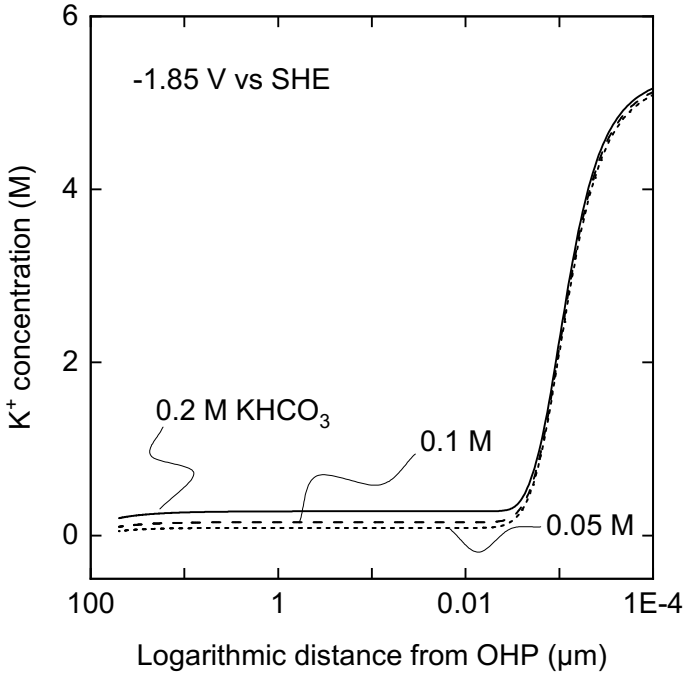

Figure 3.7.: K^+ concentration at -1.85 V vs SHE for 0.05 M, 0.1 M, and 0.2 M $KHCO_3$ over the logarithmic distance from the OHP.

compared to 0.05 M and 0.1 M, as shown in Figure 3.6(d). Nevertheless, the CO_2 concentration is higher for lower electrolyte concentrations, which is most likely due to the lower initial CO_2 concentration in the bulk and the higher consumption rate in the charge transfer reaction.

The downside of the enhanced buffer capacity of the 0.2 M $KHCO_3$ electrolyte solution is the increasing formation of ${CO_3}^{2-}$ and ${HCO_3}^{-}$ according to Reaction (3.8)-(3.9). Figure 3.6(e) shows that the ${CO_3}^{2-}$ concentration increases drastically from the bulk concentration of 0.33 mM to 121.3 mM at a distance of 6 nm from the electrode in case of the 0.2 M electrolyte solution. A common issue in electrolyte buffered CO_2 electrolysis, especially when using porous gas diffusion electrodes, is the precipitation of salts near the catalyst layer, leading to blockage of diffusion pathways and electrode flooding and thus losses in process activity and selectivity [Disc2022]. Even though this work deals with planar plate electrodes where the risk of salt formation is mitigated, the aforementioned

findings can be transferred to the operation of gas diffusion electrodes. In porous electrodes, the BL thickness in the catalyst layer pores would be in the range of the pore radius (~nm). As the CO_3^{2-} concentration does not change significantly when reducing the BL, as shown in Figure 3.5, the increased formation of CO_3^{2-} near the catalyst would lead to concentrations close to the solubility limit at electrolyte concentrations that are used in some experimental works [Bhar2020], which have higher bulk CO_3^{2-} concentrations (>~1.0 M). Therefore, these results highlight the importance of maintaining a balance between the buffer capacity of $KHCO_3$ and the risk of salt formation due to CO_3^{2-} formation.

The same conclusions also apply for HCO_3^-, even though the HCO_3^- profile shows a descending trend towards the electrode, as plotted in Figure 3.6(f). When increasing the $KHCO_3$ concentration from 0.05 M and 0.1 M to 0.2 M, the level of HCO_3^- concentration notably increases, especially in the region from 1 µm to 0.004 µm in front of the OHP. The higher HCO_3^- concentration close to the electrode might result not only from the higher bulk concentration but also from the increased local production of OH^- in the charge transfer reactions and the subsequent formation of HCO_3^- as in Reaction (3.9).

The simulation results on the variation of the electrolyte concentration reveal that high $KHCO_3$ concentrations are most favorable for electrochemical CO_2 reduction due to low cathodic overpotentials and enhanced buffer capacity. However, local increases in CO_3^{2-} and HCO_3^- concentration near the electrode surface limit the use of highly concentrated electrolyte solutions in CO_2 electrolysis in order to mitigate salt precipitation. It needs to be mentioned that in the conversion of the model results from V vs PZC to V vs SHE, the same voltage vs PZC (listed in Table A.1) was used even though the bulk pHs of the various electrolyte concentrations differ. However, the difference in the bulk pH, as shown in Figure 3.6(d), is minor, and therefore, the influence should be negligible.

3.4. Conclusion

This work reports a one-dimensional transient model of the BL at a planar plate electrode for the electrochemical conversion of CO_2 to CO. The model describes the transport and dissociation of dissolved species in the domain and accounts for their actual solvated size using the SMPNP model. Moreover, charge transfer reactions, i.e., the electrochemical CO_2 reduction and the hydrogen evolution reaction, are modeled with a Frumkin-corrected Butler-Volmer kinetic. The presented polarization curves and concentration profiles in the BL are in good agreement with experimental data from the literature, proving the good validity of the model. Interestingly, the pH drastically shifts in the near-electrode region from high alkaline pH values of approx. 12 to pH values of around 5-6 at the immediate electrode surface. These local changes are experimentally inaccessible and often not correctly resolved in most models. However, the results give essential insights on local increases in CO_3^{2-} and HCO_3^- concentration, which might lead to salt precipitation when, e.g., modulating the electrolyte concentration. Decreasing the BL thickness, i.e., improving the hydrodynamics at the electrode, leads to a significant increase in the CO partial current density attributed to enhanced CO_2 mass transport to the electrode. On the other hand, the pH, as well as the CO_3^{2-} and HCO_3^- concentrations, are not as strongly affected as the polarization behavior. Furthermore, the $KHCO_3$ concentration was varied to influence the activity and selectivity of CO_2 electrolysis. Besides the beneficial effects of increasing the electrolyte concentration on the cathodic overpotential and the buffering capacity, the aforementioned local increases in CO_3^{2-} and HCO_3^- concentration limit the use of highly concentrated electrolyte solutions. Surprisingly, the concentration of K^+ at the immediate electrode surface, which is thought to have a co-catalytic effect on the CO_2 reduction, is not significantly affected when increasing the $KHCO_3$ concentration in the studied regime.

While this work highlights the positive effects of changing the electrolyte solution characteristics and decreasing the BL thickness, i.e., improving the hydrodynamics at the planar plate electrode surface, the length of reactant

transport paths needs to be significantly reduced to enhance the activity and selectivity of the electrochemical CO_2 reduction. One promising approach is the use of porous electrodes, so-called gas diffusion electrodes, which will be discussed in the following chapter.

4. Elucidating mass transport and conversion phenomena in the GDE

Parts of this chapter have been published as:
Matthias Heßelmann, Berinike Clara Bräsel, Robert Gregor Keller, Matthias Wessling
Simulation-based guidance for improving CO_2 reduction on silver gas diffusion electrodes, Electrochemical Science Advances, 2022
DOI: 10.1002/elsa.202100160

4.1. Introduction

The research in electrically driven CO_2 valorization has emerged during the past 30 years [De L2019]. A remarkable development in the research field is the development of gas diffusion electrodes (GDEs), replacing the previously used full metal electrodes. GDEs, as illustrated in Figure 4.1, overcome the limited CO_2 solubility in aqueous electrolytes by enabling fast mass transport of diluted CO_2 towards the reactive sites of the catalyst due to short diffusion pathways [Cook1990; Weng2018; Dunw2018; Venn2019a; Higg2018; Shi2020]. As a result, significantly higher current densities and production rates of CO_2 reduction reaction products were achieved, moving the technology closer towards industrial application [De L2019].

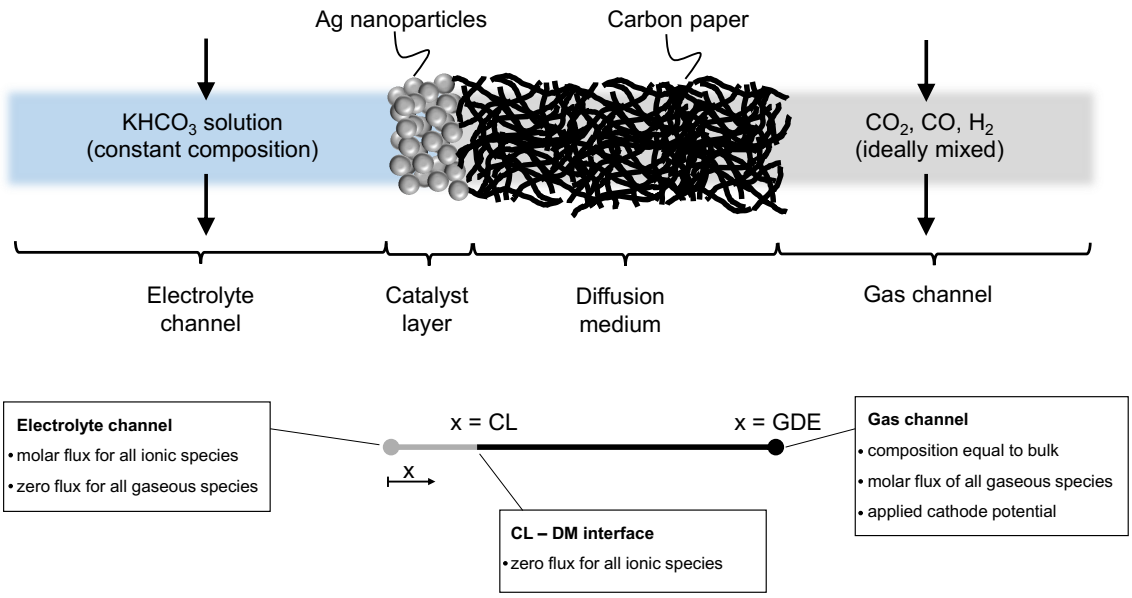

Figure 4.1.: Schematic of a GDE as considered in this work and model structure of the one-dimensional GDE model. CL and DM refer to the catalyst layer and diffusion medium, respectively

However, the experimental quantification of species transport within the GDE is difficult. At the moment, only modeling can help to obtain a comprehensive understanding of the influence of operating parameters and GDE properties on the CO_2 reduction. Only recently, a limited number of publications have been dedicated to this issue [Dela2010; Wu2014;

Weng2018; Weng2019; Brée2020; Tan2020; Kas2021].
Weng et al. [Weng2018] investigated how different states of wetting of the catalyst layer (CL) influence the mass transport towards the electrode and the CO_2 reduction rate. They showed that flooding of the CL negatively affects CO_2 mass transport, especially at high current densities. By either decreasing the catalyst loading or increasing the electrolyte flow rate and CL porosity, the CO_2 reduction reaction can be improved. Weng et al. assumed a constant gas composition in the gas channel. Hence, the model does not consider changes in the gas composition with varying fluid flow conditions. Thus, diffusion resistances in the gas phase cannot be represented. In particular, mass transport limitations at low gas flow rates as well as low CO_2 feed fractions might not be displayed correctly by the model. Recently, Bree et al. [Brée2020] modeled different reactor configurations with either a GDE or planar full metal electrode, based on an experimental study from Vennekötter et al. [Venn2019a] The model allows the computation of the ohmic and mass transport-related overpotentials in the different reactor configurations in order to assess the energy efficiency of the given reactors. The authors also considered three different configurations where GDEs were used as the cathode. However, in the study of Bree et al., the CO_2 gas was supplied in dead-end mode, where it is pressed through the GDE into the liquid layer. Furthermore, Bree et al. modeled gas transport in porous media using Fick's diffusion. However, Suwanwarangkul et al. [Suwa2003] depicted in a study on gas transport in solid oxide fuel cell anodes that the dusty gas model is the most appropriate to describe the transport of H_2, H_2O, CO, and CO_2 in porous media. Especially at high operating current density, the assumption of equimolar counter diffusion may not hold. Wu et al. [Wu2014] modeled a microfluidic cell for CO_2 reduction, including a GDE. The study investigates the influence of gas flow rate and composition, as well as channel dimensions and GDE porosity at current densities below 80 $mA\,cm^{-2}$. These current densities, however, are not relevant for industrial processes that operate above 200 $mA\,cm^{-2}$.[Burd2019] At high current densities, mass transport limitations become prominent, and therefore, the opti-

mal operation and design of the electrodes must be assessed at such relevant conditions. Tan et al. [Tan2020] presented a one-dimensional mass-transport model to predict the local CO_2 concentration and the local pH value within the GDE inside a flow cell at different current densities. Tan et al. simulated the influence of the CL thickness and CO_2 fraction at the three-phase boundary on the local CO_2 concentration within the CL. The consumption of CO_2 and the production of OH^- are calculated from Faraday's law at a given and fixed current density and constant Faradaic efficiency. The potential distribution within the GDE and electrochemical kinetics are not considered in the model. Therefore, the influence of changing conditions in the GDE on the electrochemical reactions cannot be displayed. Furthermore, mass transport within the diffusion medium (DM) is not implemented in the model, but a constant CO_2 fraction at the CL - DM junction is assumed. Thus, the investigation of mass transport limitations in the gas phase at different gas flow rates is not feasible. In a recent publication, Blake et al. [Blak2021] published both a numerical and an analytical model that approximates the cathodic CL environment. The models show good agreement with experimental data from Verma et al. [Verm2016b] and allow me to study the influence of geometrical changes of the CL and electrolyte flow on the energetics and the liquid species concentration within the CL. In their models, Blake et al. do not model gas diffusion within the GDE or the gas flow in the gas channel. However, the local gas transport in the GDE, as well as the composition of the bulk gas phase, have a significant impact on CO_2 reduction when operating a GDE in flow-by mode.[Jean2018; Bhar2020]

With the model described in this chapter, I study the electrochemical CO_2 reduction at industrially relevant current densities, considering varying compositions and flow rates in the bulk gas phase and the liquid electrolyte, diffusion resistances in the gas diffusion electrode, and non-equilibrium dissociation reactions. My work will, therefore, answer and discuss the following questions to guide research on GDEs:

- What is the local pH value at the catalyst layer when the bulk elec-

trolyte buffer strength is increased, and how does this affect CO_2 reduction?

- Can variation of the electrolyte flow rate influence the CO_2 reduction rate?
- Why is it beneficial to feed CO_2 in excess along the GDE?
- Can the GDE properties be tuned to increase the CO_2 reduction rate?

4.2. Methodology

This section describes a model of a GDE operating in flow-by mode. The overall model structure and the system of equations are described in the following. The gas channel is considered a well-mixed exchange reservoir with an inlet and outlet flow connected to the GDE via a mass balance. The electrolyte channel boundary is modeled as a flux boundary with a mass transport correlation and constant bulk composition. The description of mass transport in the GDE using the dusty gas model and Nernst-Planck equation in the gas and liquid phase allows for an accurate investigation of multi-component mass transport within the GDE. Table A.2 lists the simulation parameters.

4.2.1. Model structure

Figure 4.1 sketches the model structure considered in this work. In general, GDEs consist of a gas diffusion layer (GDL), a microporous layer (MPL), and a CL. The GDL and MPL form the DM. The developed model of the GDE is one-dimensional with respect to the direction orthogonal to the gas and liquid flow. Steady-state operation under ambient conditions is assumed. The temperature is taken to be constant, which is valid on a small scale [Whee2020]. The GDE consists of a CL and a DM. The bulk electrolyte concentration is assumed to be constant, while the gas channel is modeled as a zero-dimensional, well-mixed exchange volume. The cathode potential is taken as the input parameter for all simulations.

Silver nanoparticles are chosen as a catalyst. Thus, CO_2 reduction to CO and H_2 evolution are the only electrochemical reduction reactions considered [Hats2014]. In this study, an aqueous $KHCO_3$ solution is chosen as an electrolyte. Therefore, H_2O is the primary source for the hydrogen evolution reaction (HER) as the concentration of H^+ in a neutral electrolyte is at least eight orders of magnitude smaller than that of H_2O [Sing2017]. The gas phase consists of CO_2, water vapor, and the two gaseous products CO and H_2. Dissolved CO and H_2 in the liquid phase are neglected due to their low solubility [R L 2003].

The transport of species in the gas- and liquid phase must follow mass conservation, such that for species i

$$\frac{\partial \dot{n}_i}{\partial x} = R_{PT,i} + R_{CT,i} + R_{l,i} \tag{4.1}$$

where $\dot{n}_i$ is the molar flux of species i, $R_{PT,i}$, $R_{CT,i}$, and $R_{l,i}$ are the volumetric source terms due to phase transfer (PT), charge transfer reactions (CT) and homogeneous reactions occurring in the liquid phase (l). Mass conservation is written for all species except for H_2O. A source term for phase transfer is only considered in the CL for dissolved $CO_{2(aq)}$ and gaseous CO_2, respectively. $R_{CT,i}$ applies to species involved in the electrochemical reduction reactions, such as $CO_{2(aq)}$, OH^-, and gaseous CO and H_2. Homogeneous reactions in the liquid phase due to acid/base carbonate and water dissociation reactions occur in the electrolyte channel and the CL and apply to all dissolved species.

4.2.2. Gas phase

The dusty-gas model is used to model the multi-component gas flux of CO_2, CO, and H_2 within the porous GDE [Yuan2014]

$$\frac{p}{RT}\frac{\partial y_i}{\partial x} = \sum_{j=1 j\neq i}^{n} \frac{y_i \dot{n}_j - y_j \dot{n}_i}{D_{i,j}^{eff}} - \frac{\dot{n}_i}{D_{i,K}^{eff}} \tag{4.2}$$

where p is the local pressure in the gas phase, R is the specific gas constant, T is the temperature, and y_i and y_j are the fractions of gaseous species i and j. $D_{i,j}^{eff}$ is the effective binary diffusion coefficient of species i and j, and $D_{i,K}^{eff}$ is the effective Knudsen diffusion coefficient. Viscous flow is neglected because the gradient in pressure along the GDE is considered to be small.

The Bruggeman relationship describes effective diffusion coefficients for gas diffusion in porous media, considering the porosity ϵ_m and tortuosity τ_m of medium m [Yuan2014]

$$D^{eff} = \frac{\epsilon_m}{\tau_m} D = \epsilon^{\frac{3}{2}} D \tag{4.3}$$

Binary diffusion coefficients are calculated using an empirical correlation introduced by Fuller et al. [Full1966]

$$D_{i,j} = \frac{0.0101325 \cdot 10^{-3} T^{1.75} (M_i^{-\frac{1}{2}} + M_j^{-\frac{1}{2}})}{p_G (v_i^{\frac{1}{3}} + v_j^{\frac{1}{3}})} \tag{4.4}$$

where M_i and M_j are the molar mass of species i and j, p_G is the gas phase pressure, and v_i and v_j are the diffusion volumes for species i and j. In this model, changes in the binary diffusion coefficients due to changes in local pressure are neglected. All binary diffusion coefficients are calculated at ambient pressure (0.101325 MPa) and with diffusion volumes taken from Fuller et al. [Full1966]. The Knudsen diffusion coefficient $D_{i,K}$ for species i in a pore of medium m with diameter $d_{p,m}$ is defined as [Yuan2014]

$$D_{i,K} = \frac{2}{3} d_{p,m} \sqrt{\frac{8RT}{\pi M_i}} \tag{4.5}$$

The generalized Graham's law describes the molar diffusion flux of the n^{th} gaseous species H_2O. It considers the counter-current diffusion of the

gaseous species within the CL and DM and is defined as [Solc2001]

$$\sum_i \dot{n}_i \sqrt{M_i} = 0 \tag{4.6}$$

An additional equation is required to calculate the fraction of the nth gaseous species from the overall fractions

$$\sum_i y_i = 1 \tag{4.7}$$

The relationship of gaseous species fraction y_i and partial pressure p_i is given by

$$y_i = \frac{p_i}{p_G} \tag{4.8}$$

Since the gas phase is assumed to be saturated with gaseous H_2O at all times, the partial pressure of H_2O is set to its saturation pressure $p^{sat}_{H_2O}$ at ambient conditions and its fraction in the gas phase is given by

$$y_{H_2O} = \frac{p^{sat}_{H_2O}}{p_G} \tag{4.9}$$

Gaseous species that are produced by electrochemical reactions on the catalyst surface are assumed to be transported directly through the DM toward the gas channel. Gas bubbles and possible bubble dynamics within the liquid phase of the CL and the electrolyte channel are neglected. This is a valid assumption for small reactors with flowing electrolytes in a certain flow rate regime, as it has been shown that bubbles are effectively washed away by the flowing electrolyte without any impact on the reactor performance [Jaya2005].

4.2.3. Liquid phase

The Nernst-Planck equation is defined for all liquid phase species as [Schm2003]

$$\dot{n}_i = -D_i^{eff}\frac{\partial c_i}{\partial x} + u_i c_i \frac{\partial \phi_l}{\partial x} \tag{4.10}$$

where c_i is the molar concentration and u_i is the mobility of species i. ϕ_l denotes the electrolyte potential in the liquid phase. The liquid phase species comprise $CO_{2(aq)}$, K^+, H^+, $CO_3{}^{2-}$, $HCO_3{}^-$, OH^-. Liquid products formed in the reduction reaction are neglected, which is valid for silver electrocatalysts where CO and H_2 are the major reduction products [Hats2014]. The Nernst-Einstein relationship is used to determine the mobility u_i [Schm2003]

$$u_i = \frac{D_i^{eff} z_i F}{RT} \tag{4.11}$$

where z_i is the charge of species i and F is the Faraday constant. The effective diffusion coefficients are determined by applying the Bruggeman relationship, see Equation (4.3).

Next to the Nernst-Planck relationship, an additional equation is required in order to obtain a fully determined system. In this model, the electrolyte potential ϕ_l is determined by assuming an ohmic relationship of the local liquid potential ϕ_l and the local current density within the liquid phase i_l [Newm1962; Pinn2011]

$$i_l = -\sigma_l^{eff}\frac{\partial \phi_l}{\partial x} \tag{4.12}$$

The effective local conductivity σ_l^{eff} of the liquid phase within the GDE is calculated under consideration of the local concentration of ionic species [Newm2004]

$$\sigma_l^{eff} = F \sum_i |z_i|\, u_i c_i = \frac{F^2}{RT} \sum_i z_i^2 D_i^{eff} c_i \tag{4.13}$$

As aqueous $KHCO_3$ solution is used as a buffering electrolyte, the following four acid/base carbonate reactions occur in the liquid phase [Hash2018]

$$CO_2 + H_2O \underset{k_{-1}}{\overset{k_1}{\rightleftharpoons}} H^+ + HCO_3^- \tag{4.14}$$

$$HCO_3^- \underset{k_{-2}}{\overset{k_2}{\rightleftharpoons}} H^+ + CO_3^{2-} \tag{4.15}$$

$$CO_2 + OH^- \underset{k_{-3}}{\overset{k_3}{\rightleftharpoons}} HCO_3^- \tag{4.16}$$

$$HCO_3^- + OH^- \underset{k_{-4}}{\overset{k_4}{\rightleftharpoons}} H_2O + CO_3^{2-} \tag{4.17}$$

Here, H_2CO_3 species is ignored, as it is only relevant at pH values below 7.4 [Sull2012]. Equilibrium constants are taken from Schulz et al. [Schu2006]. In addition to the acid/base carbonate reactions, water dissociation takes place

$$H_2O \underset{k_{-W}}{\overset{k_W}{\rightleftharpoons}} H^+ + OH^- \tag{4.18}$$

In this model, reactions (4.14)-(4.18) are not assumed to be at equilibrium due to the continuous consumption and production of liquid phase species as the charge transfer reactions proceed. The resulting source term for liquid phase species i from *n* homogeneous liquid phase reactions is given by

$$R_{l,i} = \sum_n s_{i,k} \left(k_n \prod_{s_{n,j}<0} c_j - k_{-n} \prod_{s_{n,j}>0} c_j \right) \tag{4.19}$$

where k_n and k_{-n} are the forward and reverse reaction rates, $s_{i,k}$ is the stoichiometric coefficient of species i and j which are denoting the species

involved in reaction *n*.

Phase transfer between gas- and liquid phase is assumed to occur solely for CO_2 and H_2O. Dissolution of CO and H_2 in the liquid is neglected because their solubility in water is multiple orders lower than that of CO_2 [Torl2018]. The source term R_{PT,CO_2} regarding the phase transfer of CO_2 is written considering Henry's law

$$R_{PT,CO_2} = k_{PT,CO_2}\, a_V^S\, (H_{CO_2}\, p_G\, y_{CO_2} - c_{CO_{2(aq)}}) \tag{4.20}$$

The dissolution of CO_2 is modeled using a mass transfer coefficient k_{PT,CO_2} according to the film theory [Vija2005]

$$k_{PT,CO_2} = \frac{D_{CO_2}}{\delta} \tag{4.21}$$

where D_{CO_2} is the diffusion coefficient of $CO_{2(aq)}$ in the liquid phase. Furthermore, in Equation (4.20), H_{CO_2} is the Henry constant for CO_2 at ambient conditions and is set to $34{\cdot}10^{-5}\,\mathrm{mol\,m^{-3}\,Pa^{-1}}$.[Carr1991] The direction of CO_2 phase transfer is from gas phase to liquid phase because CO_2 in the liquid phase is consumed due to electrochemical reduction. Hence, the source term R_{PT,CO_2} in the mass conservation, Equation (4.1), is set negative for the gas phase and positive for the liquid phase.

4.2.4. Solid phase

Ohm's law is used to describe the electron transport within the solid phase s of the medium m, which is either the CL or the DM

$$i_{s,m} = -\sigma_{s,m}^{eff} \frac{\partial \phi_{s,m}}{\partial x} \tag{4.22}$$

where $i_{s,m}$ is the local current density in the solid phase, $\phi_{s,m}$ is the local

solid potential, and $\sigma_{s,m}^{eff}$ is the effective conductivity of the CL and DM, respectively. The electrical conductivity of the DM is corrected with the Bruggeman relationship, see Equation (4.3).

Charge conservation is assumed in the entire GDE, such that

$$\frac{\partial i_{s,CL}}{\partial x} = -\frac{\partial i_l}{\partial x} = -a_V^S \sum_k i_k \tag{4.23}$$

where i_k is the partial current density of reaction k, happening on the interfacial surface area a_V^S. The interfacial surface area a_V of the spherical catalyst nanoparticles in the CL is defined as surface area per volume

$$a_V = \frac{6\ (1 - \epsilon_{CL})}{d_{Ag}} \tag{4.24}$$

The distribution of liquid in the GDE is accounted for using the thin-film modeling approach. Thus, the walls of the pores are considered to be partly covered by a thin film of electrolyte, whereas the remaining volume of the pore is filled with gas. From that, the active surface area a_V^S follows as

$$a_V^S = a_V S \tag{4.25}$$

The thickness of the thin film δ is calculated as a function of saturation S based on the cross-sectional area A of a pore with a mean diameter d_p as follows

$$S = \frac{A_l}{A_p} = \frac{\frac{\pi}{4} d_p^2 - \frac{\pi}{4}(d_p - 2\delta)^2}{\frac{\pi}{4} d_p^2}, \tag{4.26}$$

$$\delta = \frac{d_p}{2}(1 - \sqrt{1 - S}) \tag{4.27}$$

The resulting fractions in the CL are $\epsilon_{CL}(1 - S)$ for the gas phase, $\epsilon_{CL} S$

for the liquid phase, and $1 - \epsilon_{CL}$ for the solid phase, where ϵ_{CL} is the porosity of the CL in the absents of a liquid phase. The thickness of the CL, L_{CL}, is determined using the catalyst loading of Ag nanoparticles m_{Ag} per geometrical electrode area A_E

$$L_{CL} = \frac{m_{Ag}}{A_E \, \rho_{Ag} \, (1 - \epsilon_{CL})} \tag{4.28}$$

where ρ_{Ag} is the density of silver.

4.2.5. Electrode kinetics

Two charge transfer reactions are considered at the catalyst surface in this model. These are the CO_2 conversion to CO and the HER from H_2O, see Equation (4.29) and Equation (4.30), respectively.

$$CO_{2(aq)} + H_2O + 2\,e^- \longrightarrow CO + 2\,OH^- \tag{4.29}$$

$$2\,H_2O + 2\,e^- \longrightarrow H_2 + 2\,OH^- \tag{4.30}$$

The source term relating $R_{CT,i}$ to the charge transfer reactions for liquid phase species i = $CO_{2(aq)}$, OH^- and gas phase species k = CO, H_2 is defined as

$$R_{CT,i} = \sum_k \frac{s_{i,k} \, a_v^S \, i_k}{N_{z,k} \, F} \tag{4.31}$$

where $s_{i,k}$ is the respective stoichiometric coefficient of species i in reaction k and $N_{z,k}$ is the number of electrons transferred in reaction k. The reaction kinetics of the charge transfer reactions are calculated from Tafel kinetics

$$i_{CO} = \frac{c_{CO_{2(aq)}}}{c^{sat}_{CO_2}} i_{0,CO} \, exp(\frac{-\alpha_{CO} F \eta_{CO}}{RT}) \tag{4.32}$$

$$i_{H_2} = i_{0,H_2} \, exp(\frac{-\alpha_{H_2} F \eta_{H_2}}{RT}) \tag{4.33}$$

where $i_{0,k}$ is the exchange current density, α_k is the charge transfer coefficient and η_k is the overpotential for reaction k. The exchange current density and the transfer coefficient are fitting parameters. In this work, these parameters are fitted to match experimental data for a 0.5 M $KHCO_3$ solution, determined in the work from Verma et al. [Verm2016b]. In the case of CO_2 reduction to CO, the limiting solubility of aqueous $CO_{2(aq)}$ is taken into account by the first term, where $c_{CO_{2(aq)}}$ is the local $CO_{2(aq)}$ concentration in the CL and $c^{sat}_{CO_2}$ is the saturation concentration of dissolved CO_2 at ambient conditions. H_2O is considered to be available in excess. The overpotential η_k includes ohmic losses due to electrical and ionic conductivity within the GDE accounted for by the local potentials of solid phase $\phi_{s,m}$ and liquid phase ϕ_l. The standard electrode potential E^0_k of reaction k is corrected for the operating conditions by the Nernst equation, where a pH value averaged over the CL is used to reduce numerical complexity. This leads to the overpotential of reaction k described by

$$\eta_k = \phi_{s,m} - \phi_l - (E^0_k - \frac{2.303 \, R \, T \, pH}{F}) - \frac{j_{total} w_{Ref}}{\sigma_{EC}} \tag{4.34}$$

The last term covers changes in the electrical conductivity of the electrolyte when varying the ion concentration. Thus, cathodic potentials in this work are not IR-corrected. Here j_{total} is the sum of both partial current densities, w_{Ref} is the distance of the GDE to the reference electrode and σ_{EC} is the ionic conductivity within the electrolyte channel determined analogously to Equation (4.13).

The partial current densities j_k are calculated by integrating the local cur-

rent densities i_k in the CL

$$j_k = \int_0^{CL} a_V^S \, i_k \, dx \tag{4.35}$$

4.2.6. Boundary conditions

The flow channels of electrolyte and gas are the boundary regions of the model. The composition in the electrolyte channel is taken constant, while the gas channel is modeled as an ideally mixed volume with an inlet and outlet.

Electrolyte channel

The diffusion layer between the GDE and the flowing electrolyte is modeled as a flux boundary condition with the molar flux described by

$$\dot{n}_{EC,i} = k_{EC,i} \, (c_{bulk,i} - c_{x=0,i}) \tag{4.36}$$

where $\dot{n}_{EC,i}$ is the molar flow leaving the electrolyte channel towards the GDE. Here, EC denotes the electrolyte channel at the GDE boundary $x = 0$. $c_{bulk,i}$ is the concentration of liquid phase species i and is assumed to be equal to the inlet composition. $c_{x=0,i}$ is the concentration in the GDE at position $x = 0$. The mass transfer coefficient $k_{EC,i}$ is calculated on the basis of the Sherwood- Reynold- Schmidt correlation for laminar flow ($Re < 3 \cdot 10^5$)

$$k_{EC,i} = 1.85 \frac{D_i}{L_E} \left(\frac{\rho v_{EC} L_E}{\mu}\right)^{\frac{1}{3}} \left(\frac{\mu}{\rho D_i}\right)^{\frac{1}{3}} \left(\frac{d_H}{L_E}\right)^{\frac{1}{3}} \tag{4.37}$$

where L_E and d_E are the length and depth of the electrode being equivalent to the length and depth of the flow channels and w_{EC} as the width of the electrolyte channel. ρ and μ are the density and viscosity of the liquid. The flow velocity v_{EC} is calculated from the electrolyte flow rate q_{EC} and the

channel dimensions w_{EC} and d_E. The hydraulic diameter d_h is given by

$$d_H = \frac{2 w_{EC} d_E}{w_{EC} + d_E} \tag{4.38}$$

At the electrolyte channel boundary $x = 0$, all gas phase molar fluxes are set to zero. As the DM is assumed to be dry, liquid phase molar fluxes and liquid phase properties (i_l, ϕ_l) are set to zero at $x = CL$.

Gas channel

A mass balance describes the inlet and outlet flows of the gas channel. Since dissolved CO and H_2 are neglected, the amount of CO and H_2 diffusing into the gas channel is governed by the rate of electrochemical reduction reactions. The molar flux density, $\dot{n}_{GC,i}$, is therefore calculated on the basis of the current density j_k of reaction k by Faraday's law

$$\dot{n}_{GC,i} = \frac{j_k}{N_{z,k} F} \tag{4.39}$$

The amount of gaseous CO_2 supplied by diffusion from the gas channel is assumed to be equal to the amount of CO_2 that is dissolved in the electrolyte. Therefore, Equation (4.20) is also used to calculate the molar flow $\dot{n}_{GC,CO_2}$ of CO_2 leaving the gas channel into the GDE.

The local gas phase fractions in the DM at the position of gas channel boundary $x = GDE$, $y_{x=GDE,i}$, are set equal to the gas phase fractions within the gas channel $y_{bulk,i}$.

4.2.7. Numerical method

The presented model equations are solved by gPROMS ModelBuilder. The overall model is divided into one composite model and three submodels that are solved in parallel during the simulation. Because of the opposite inlets of the electrolyte and gas channels, two different discretizing meth-

ods are used for the submodels. The electrolyte channel inlet model and liquid phase model are solved using a first-order back finite differential method. The gas phase model and the composite model are solved using a first-order forward finite differential method.

The differential-algebraic equations are solved using a fully implicit solver following the Runge-Kutta method. A non-uniform grid is used in the distribution domain, as large gradients are expected in the small CL compared to the ones occurring in the DM. A logarithmic grid transformation is applied to the distribution domain, leading to a high number of steps in the CL at the beginning of the domain and fewer steps in the DM. The number of step elements is set to 2 000.

4.3. Results and discussion

The following subsections present the simulation results and discuss the influence of electrode properties and operating parameters, such as the electrolyte concentration and flow rate, and the gas composition and flow rate.

4.3.1. Model validation

The kinetic parameters in the Tafel equation in Equation (4.32) and Equation (4.33) were fitted to match the experimental results for 0.5 M $KHCO_3$ in the work from Verma et al. [Verm2016b]. More detailed information on the reactor setup and the operating parameters used in the experiments is reported in the work from Whipple et al. [Whip2010b] and Verma et al. [Verm2016b]. Figure 4.2 shows simulation results from this work and experimental results from the work of Verma et al. The graphs present the partial current density of CO and H_2 as a function of the cathode potential at different $KHCO_3$ concentrations. When increasing the potential, also the CO and H_2 partial current densities increase. In the medium potential range from -1.2 V vs SHE to -1.6 V vs SHE, the partial current density of

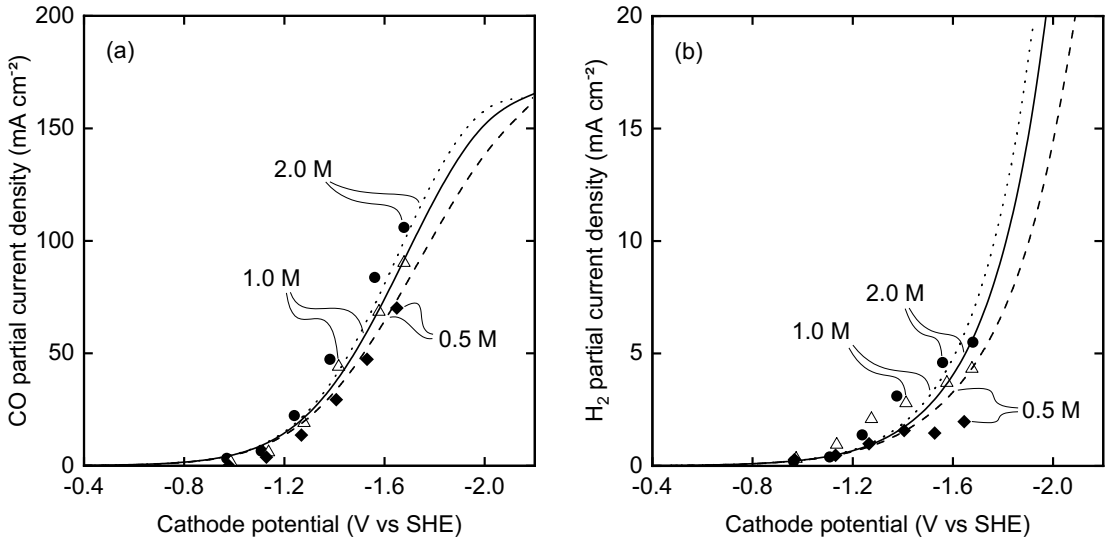

Figure 4.2.: Comparison of simulation (line) and experimental results (symbol) for (a) CO partial current densities and (b) H_2 partial current densities as a function of the cathode potential vs SHE for various $KHCO_3$ concentrations. The experimental data is taken from Verma et al. [Verm2016b].

CO differs stronger to the experimental results for higher concentrations of 2.0 M $KHCO_3$. Discrepancies at higher $KHCO_3$ concentrations above -1.2 V vs SHE may result from the beneficial effect of K^+ ions on the stabilization of the radical $CO_2^{\bullet -}$ intermediate in the electric double-layer, which is not accounted for in the model. For more detailed information on this, see: [Verm2016b; Bard2001; Resa2017; Dogo1972; Paul1988; Ring2019; Thor2012] The simulated H_2 partial current density differs strongly from the experimental results for all plotted $KHCO_3$ concentrations and for potentials higher than -1.4 V vs SHE. The deviation between simulation results and the experimental data might result from mass transport limitations of the reactants in the HER at elevated potentials.

4.3.2. Influence of the electrolyte buffer concentration

As shown in Figure 4.2, the partial current densities of both electrochemical reactions increase for each applied cathode potential when increasing the

concentration of $KHCO_3$ in the electrolyte. Figure 4.3 displays this effect for an extended range of $KHCO_3$ concentrations from 0.1 M to 3.5 M. The simulation results of the CO partial current density and the CO fraction at the gas channel outlet are shown for an applied cathode potential of -1.6 V vs SHE and -1.8 V vs SHE. At -1.6 V vs SHE, the increase in CO

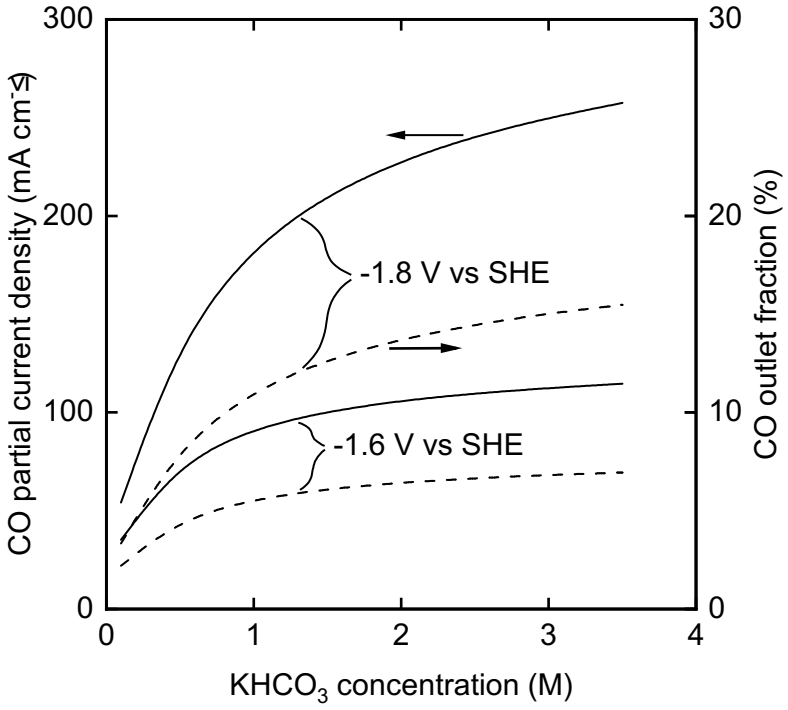

Figure 4.3.: CO partial current density (solid line) and CO fraction in the gas channel outlet (dashed line) at -1.6 V vs SHE and -1.8 V vs SHE as a function of electrolyte concentration.

partial current density is not as significant as for -1.8 V vs SHE. For the higher potential, a steep increase in CO partial current density occurs when increasing the $KHCO_3$ concentration from 0.1 M to 1.0 M. The positive effect of an increasing $KHCO_3$ concentration on the electrochemical CO_2 reduction becomes smaller at concentrations above 1.0 M as the curves of CO current density and CO outlet fraction start to flatten. Thus, the increase in CO partial current density in Figure 4.3 demonstrates that ionic conductivity has a beneficial effect on the energetics of the process. Furthermore, the $KHCO_3$ concentration has a more pronounced

effect on the electrochemical CO_2 reduction at high cathode potentials. At low cathode potentials, the electrochemical reactions are kinetically controlled as the resulting CO current density is limited by charge transfer. Thus, the electrolyte salt concentration weakly influences the attainable current density at low potentials, where the charge transfer resistance dominates. The influence becomes more pronounced at high potentials above -1.3 V vs SHE, as shown in Figure 4.2. However, Figure 4.3 also reveals that even though the ionic conductivity is further increased, the CO partial current density flattens. The electrical resistance of the electrolyte decreases when increasing the electrolyte concentration and becomes almost constant for $KHCO_3$ concentrations above 1.5 M. Thus, a limit is reached where the conductivity of the electrolyte cannot be increased any further. The correlation between the results shown in Figure 4.3 and the trend in the electrical conductivity of the electrolyte demonstrates that the flattening ohmic resistance is the reason for the stagnating CO partial current density when increasing the electrolyte concentration. These results highlight the need for an IR-drop compensation at every applied potential when investigating GDEs to exclude the influence of the ionic conductivity in the electrolyte channel.

Some studies also assign the increasing buffer capacity of $KHCO_3$ at increasing electrolyte concentration as a reason for the improved reduction rate in CO_2 electrolysis at elevated potentials [Hash2018]. To investigate the buffering effect, Figure 4.4 shows the pH value in the CL as a function of the cathode potential at different $KHCO_3$ concentrations. When increasing the cathode potential, the enhanced CO_2 reduction rate at high electrolyte concentrations results in an increased production of OH^- and, therefore, a higher pH, despite the higher buffering capacity. Because of this effect, the lines for 0.1, 1.0, and 3.0 M $KHCO_3$ intersect at about -1.3 V vs SHE to -1.6 V vs SHE. Consequently, the buffering effect of the electrolyte plays a more dominant role at lower potentials and becomes less significant at elevated potentials. The aforementioned results complement the findings of Chapter 3 in the low $KHCO_3$ concentration range at a planar plate

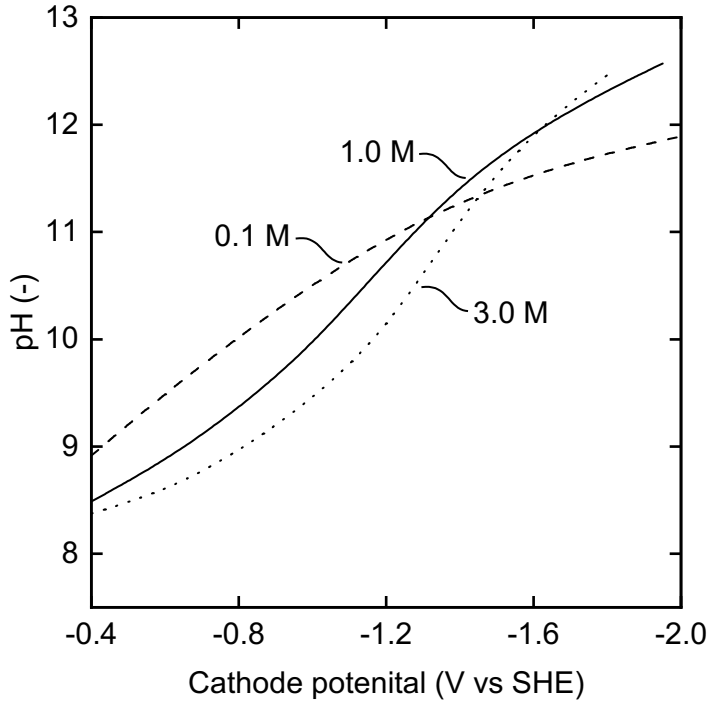

Figure 4.4.: Average pH in the CL as a function of applied cathode potential vs SHE for 0.1 M (dashed line), 1.0 M (solid line) and 3.0 M (dotted line) $KHCO_3$.

electrode.

Figure 4.5 shows the liquid phase concentrations of CO_2(aq), HCO_3^-, CO_3^{2-}, and OH^- in the CL as a function of cathode potential vs SHE and for 1.0 M and 2.0 M $KHCO_3$. As mentioned previously, liquid reduction products are neglected in this study due to the low selectivity of silver to other CO_2 reduction products other than CO. The shown concentrations are averaged values of the local liquid phase concentrations in the CL. The HCO_3^- concentration in the CL is higher in the case of 2.0 M $KHCO_3$ as more HCO_3^- is transported into the GDE from the bulk electrolyte. The concentration decreases strongly with increasing potential, which might be attributed to: (1) The depletion of HCO_3^- in Equation (4.17) due to the strong increase in OH^- production in the CO_2 reduction reaction. (2) CO_2 consumption in the reduction reaction is increased at higher

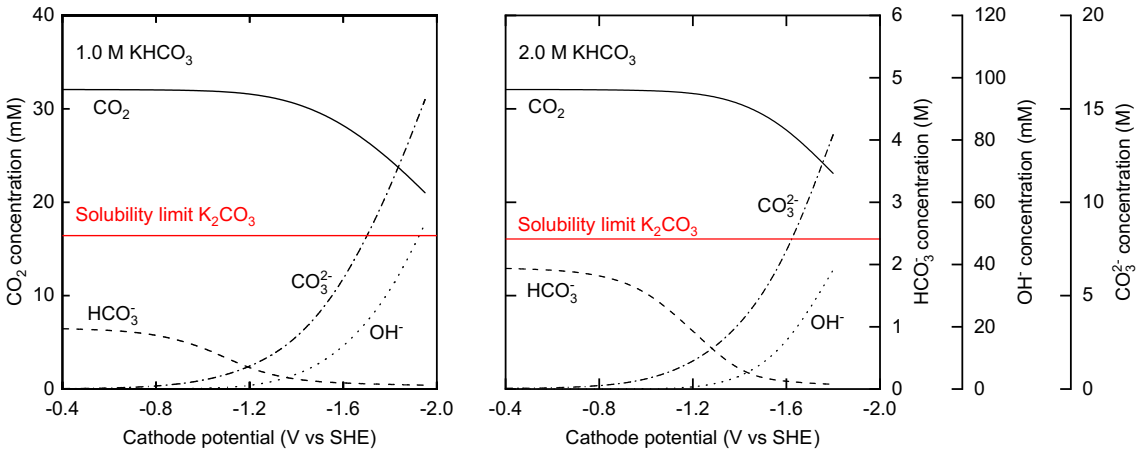

Figure 4.5.: Concentrations of liquid phase species CO_2(aq) (solid line), HCO_3^- (dashed line), CO_3^{2-} (dashed and dotted line) and OH^- (dotted line) in the CL as a function of cathode potential vs SHE for 1.0 M (left) and 2.0 M (right) $KHCO_3$. The concentrations are averaged over the thickness of the CL. The concentration at the solubility limit of K_2CO_3 is taken from Xu et al. [Xu2021].

potentials. Therefore, the reaction of CO_2 to HCO_3^- becomes slower, see Equation (4.16). The CO_2 concentration is close to its maximum solubility for both 1.0 M and 2.0 M $KHCO_3$ at low potentials because CO_2 is sufficiently supplied from the gas phase. With increasing potential, the CO_2 concentration decreases as it is consumed in the reduction reaction as well as reacted to CO_3^{2-}, due to the increasing OH^- concentration. The trend in CO_2 concentration differs only slightly for the 1.0 and 2.0 M $KHCO_3$ solutions despite the higher reduction rate for 2.0 M $KHCO_3$ as shown in Figure 4.2. The OH^- concentration in the CL is higher when using 2.0 M $KHCO_3$ compared to 1.0 M $KHCO_3$. As described before, this is attributed to the increased ionic concentration in the case of 2.0 M $KHCO_3$, which leads to a higher current density and, therefore, a higher OH^- production at the same potential. However, due to the enhanced buffering capacity of the 2.0 M $KHCO_3$ solution, the increase in OH^- gradient between CL and electrolyte channel leads to enhanced removal of OH^- in the CL. Murata et al. [Mura1991] also observed this phenomenon in an experimental study.

The CO_3^{2-} concentration increases with increasing OH^- concentration. At potentials above -1.6 V vs SHE, the concentration of CO_3^{2-} exceeds

the solubility limit of K_2CO_3 of 8.03 M and increases further with increasing potential. The precipitation of salt due to the high CO_3^{2-} concentration significantly impacts the operation of the GDE. Leonard et al. [Leon2020] showed that at galvanostatic operation, the cathode potential increases due to an increased kinetic potential attributed to higher local pH values. Additionally, due to the hygroscopic character of the precipitated salt crystals, water is "pumped" through the GDL via capillary action. This effect results in pore flooding of the DM and thus higher CO_2 mass transport resistance [Leon2020]. The neglect of salt precipitation is due to the model assumptions that the electrolyte salt is completely dissociated in water, and all ions are treated as point-like ions. However, the assumption of point-like ions does not hold for such high ion concentrations as observed for CO_3^{2-} [Bohi2017]. Furthermore, Landstorfer [Land2018] showed in a thermodynamic simulation study that the assumption of a completely dissolved electrolyte is questionable for concentrations beyond 0.5 M. He showed that the actual partial molar volume of the ionic species in the electrolyte is magnitudes larger than the solvent, indicating that the ions are strongly solvated. Therefore, the dissociation degree of strong electrolytes is decreased, thus leading to salt precipitation at relatively low concentrations.

Future modeling work of the aqueous electrolyte in electrochemical CO_2 reduction should account for the finite ion size in the near-electrode region to prevent unrealistically high ion concentrations at elevated potentials as presented in Chapter 3. On the other hand, there are a few studies where high electrolyte concentrations have been used successfully in the reduction of CO_2, e.g., a 7 M KOH solution was used in the work from De Arquer et al. [De A2020], and even 10 M KOH solution was applied as the electrolyte by Gabardo et al. [Gaba2018]. This demonstrates that there is a need for more research on the physics of electrolytes in electrochemical CO_2 reduction to obtain a better understanding of the influence of high ion concentrations in the CL.

In summary, the simulation results indicate that the positive effect of increasing $KHCO_3$ concentration on the electrochemical reduction of CO_2 results from (1) an increased electrical conductivity, (2) the buffering capacity of $KHCO_3$ at low potentials, and (3) HCO_3^- serving as an additional CO_2 source in the electrolyte channel. However, the latter is expected to play a subordinated role in the case of a GDE where CO_2 is sufficiently supplied by the feed gas. The results also reveal that the enhancement in CO partial current density is limited to a certain extent until the ohmic resistance in the bulk electrolyte cannot be reduced any further by increasing the electrolyte concentration. As mentioned before, the positive influence of the cationic species K^+ as co-catalyst for the CO_2 reduction reaction was not considered in the model. To my knowledge, no mathematical description of this phenomenon could be directly implemented in the system I am modeling. The deviation between simulation and experimental results in the validation in Figure 4.2, however, stresses the need for a mathematical description that accounts for the stabilizing effect of K^+ on the radical $CO_2^{\bullet -}$ intermediate in the electric double-layer.

4.3.3. Effect of electrolyte and gas flow rate

Electrolyte flow rate

Figure 4.6 illustrates the influence of the electrolyte flow rate, normalized to the geometrical area of the electrode, on the CO partial current density at an applied cathode potential of -1.8 V vs SHE for electrolyte concentrations of 1.0 M and 2.0 M $KHCO_3$. The CO partial current density is almost constant for 1.0 M $KHCO_3$, whereas a slight increase in the CO partial current density is visible at low flow rates and 2.0 M $KHCO_3$. Similar results were obtained in an experimental study from Bhargava et al. [Bhar2020]. At elevated potentials, the increase in CO partial current density in their experiments was even more pronounced, which they attributed to increasing removal of OH^- at higher flow rates as well as faster delivery of OH^- ions to the anode. Due to numerical instabilities, I was not able to simulate potentials above -2.0 V vs SHE with the given model.

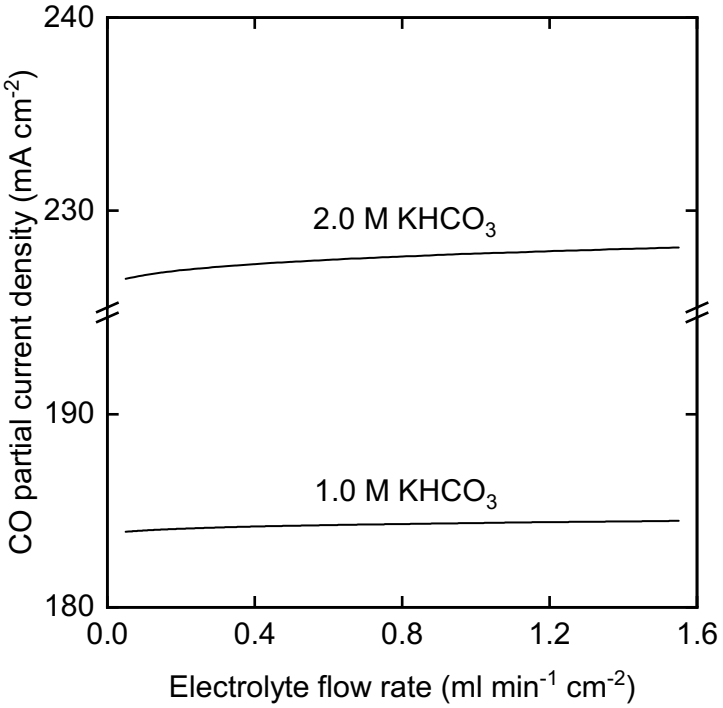

Figure 4.6.: CO partial current density as a function of normalized electrolyte flow rate at an applied cathode potential of -1.8 V vs SHE for 1.0 M and 2.0 M $KHCO_3$.

Figure 4.7 shows the liquid phase concentrations within the CL as a function of electrolyte flow rate at an applied cathode potential of -1.8 V vs SHE and for the case of 2.0 M $KHCO_3$. The HCO_3^- concentration in the CL is at a low level compared to the concentration in the electrolyte channel. Against intuition, the HCO_3^- concentration decreases with increasing flow rate even though the mass flow from bulk to CL increases with the flow rate. However, due to the increased carbonate removal from the CL at high flow rates and the constantly high production of OH^- due to Equation (4.29), bicarbonate is depleted in the CL because reaction Equation (4.17) outweighs the mass transfer from bulk to the CL. The CO_2 concentration in the CL remains constant with increasing flow rate because CO_2 is constantly transported into the electrolyte from the gas phase. Also, the concentration of OH^- does not change in the range of

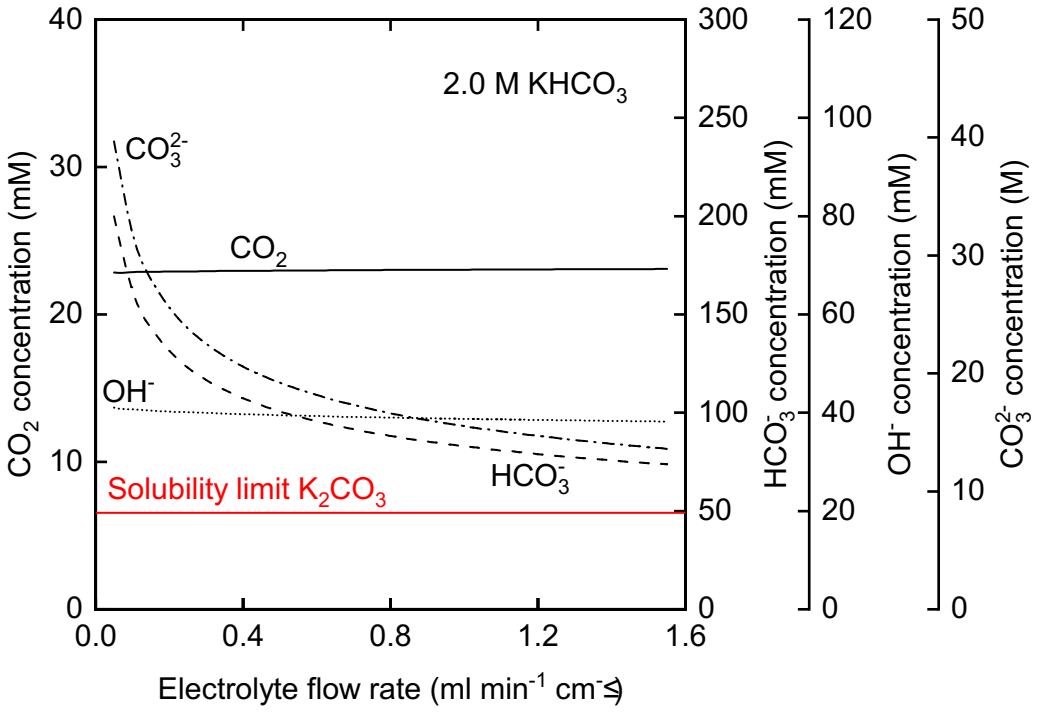

Figure 4.7.: Concentrations of liquid phase species CO_2(aq) (solid line), HCO_3^- (dashed line), CO_3^{2-} (dashed and dotted line) and OH^- (dotted line) in the CL as a function of normalized electrolyte flow rate at an applied cathode potential of -1.8 V vs SHE and 2.0 M $KHCO_3$. The concentrations are averaged over the thickness of the CL. The concentration at the solubility limit of K_2CO_3 is taken from Xu et al. [Xu2021].

the considered flow rates. As CO_2 is constantly available in the CL, the reduction reaction steadily produces CO and OH^-. The concentration of CO_3^{2-} decreases as the flow rate increases and starts to flatten out at higher flow rates > 0.4 ml min^{-1} cm^{-2}. The diffusion of CO_3^{2-} out of the CL is more pronounced with increasing flow rate. However, due to the high pH value of around 12.5 in the CL, CO_2 reacts to CO_3^{2-}, thus balancing the removal out of the CL. Comparing these results to the simulations of the different boundary layer thicknesses in Chapter 3 shows discrepancies in the effectiveness of removing CO_3^{2-} and HCO_3^- from the electrode by enhancing the hydrodynamics. For one, the differences might originate from the higher CO_3^{2-} concentration gradient between the GDE and the bulk electrolyte, thus increasing the driving force for diffusion. Moreover,

the simplified representation of the mass transport coefficient in the GDE model might overestimate the transport across the diffusive boundary layer.

In summary, high electrolyte flow rates improve the removal of ions from the GDE. Considering the aforementioned scaling issues in the GDE, high electrolyte flow rates should, therefore, be chosen to diminish the CO_3^{2-} concentration in the CL. It should be noted that the discussed simulations are made under the assumption of isothermal operating conditions. However, the temperature within the reactor rises at high current densities. In electrolyzers with an aqueous catholyte, elevated temperatures might lead to a mitigation of the CO_2 reduction reaction and an increase in HER due to lower solubility of CO_2 in the electrolyte. At the same time, reaction kinetics and diffusivity improve at elevated temperatures. Dufek et al. [Dufe2012] and Löwe et al. [Löwe2019] found that there is a trade-off between these two phenomena with a turning point at 60 °C and 50 °C, respectively. The electrolyte flow rate and additional cooling can then be used to set an optimal operation point for the electrolyzer. The consideration of non-isothermal conditions becomes particularly relevant for larger electrolyzers. Therefore, future modeling work should include energy balances and temperature dependence to help optimize the temperature control of the electrolyzer.

Gas flow rate

The graph of the CO partial current density in Figure 4.8 can be divided into two regions. In the first region, the CO partial current density increases rapidly as the amount of CO_2 fed into the reactor, and thus, the excess rate increases. In this region, the CO_2 fraction at the CL-DM interface is lower than the CO_2 feed fraction of 50% and 95%, respectively, as shown in Figure A.1. Thus, the reduction reaction to CO is limited by the mass transport of CO_2 from the gas channel towards the CL-DM interface in the GDE. When increasing the excess rate, more CO_2 is transported into the GDE, and the CO partial current density increases. In the second region,

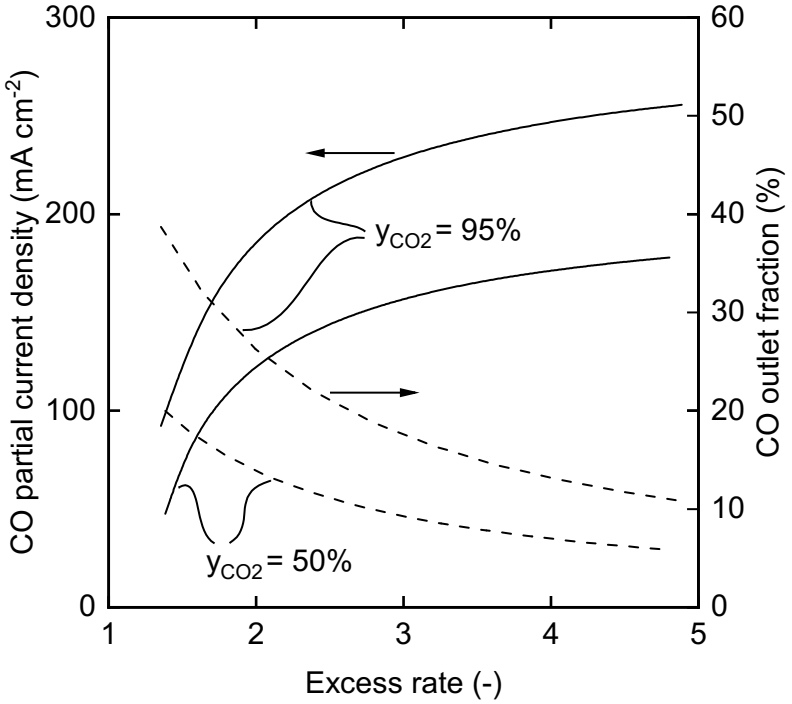

Figure 4.8.: CO partial current density (solid line) and CO outlet fraction (dashed line) as a function of the excess rate λ at an applied cathode potential of -1.9 V vs SHE and a $KHCO_3$ concentration of 1.0 M for a CO_2 inlet fraction of 50% and 95%. The inlet gas stream is composed of the respective CO_2 inlet fraction, a fraction of 0.1% CO and H_2 each, and the remaining fraction being gaseous H_2O.

at excess rates above 2.5, only a slight increase in the CO partial current density is apparent. This is attributed to the limited mass transport of gaseous CO_2 into the liquid electrolyte, as the aqueous CO_2 concentration in the CL stagnates. Therefore, the CO partial current density cannot increase further, even though more CO_2 is fed into the reactor. On the other hand, Figure 4.8 depicts that an increase in the excess rate results in a decline of the CO fraction in the outlet stream due to dilution with unreacted CO_2. A similar trend was also shown by Kim et al. [Kim2015]. When increasing the CO_2 feed fraction from 50% to 95%, diffusion into the GDE and phase transport into the liquid phase are enhanced due to higher partial pressure in the gas phase. These findings are in good agreement with experimental results from Jeanty et al. [Jean2018]. Their study shows

that the CO Faradaic efficiency increases with an increasing excess rate. However, above an excess rate of 3.0, the CO Faradaic efficiency cannot be increased any further.

Therefore, selecting the optimal feed flow rate is a trade-off between improved CO_2 reduction rate and dilution of the product stream. The inlet CO_2 fraction should be chosen as high as possible to enhance the dissolution of CO_2 into the electrolyte. Furthermore, pressure loss should be considered. Vennekötter et al. [Venn2019a] showed that the pressure loss over the GDE increases with increasing gas flow rate. Thus, liquid penetration in the GDE and, therefore, the CO_2 reduction reaction rate changes when varying the gas flow rate [Weng2018].

4.3.4. Tailoring the electrode properties

In the case of a low potential of -1.7 V vs SHE, the CO partial current density is only slightly affected by a change of DM porosity as shown in Figure 4.9. At higher potentials of -1.9 V vs SHE, an increase in DM porosity leads to a more pronounced decrease in CO partial current density. A highly porous DM is advantageous regarding gas phase mass transport, see Equation (4.3). Hence, a more significant amount of the inlet CO_2 at the gas channel can be transported into the CL and electrochemically reduced to CO. On the other hand, an increase in DM porosity follows a decrease in the solid phase. This impairs the electron transport from the current collector at the boundary of the DM and the gas channel through the DM to the CL. Attributed to the decrease in the solid phase, the electrical resistance of the DM increases, see Equation (4.22). At elevated cathode potentials, the current density is strongly affected by a reduced amount of solid phase in the DM. Consequently, the decreasing electrical conductivity outweighs the improvement of gas transport within the DM at high porosity and elevated potentials.

The influence of the CL porosity on the electrochemical CO_2 reduction

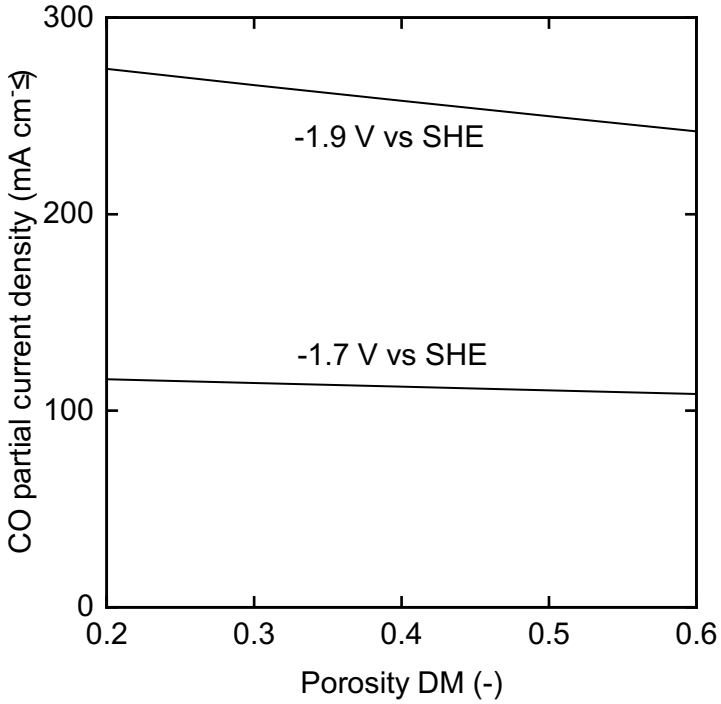

Figure 4.9.: CO partial current density as a function of DM porosity at an applied cathode potential of -1.7 V and -1.9 V vs SHE.

is studied from 0.2 to 0.6. The CL thickness is calculated based on the catalyst loading and the CL porosity from Equation (4.28). Thus, a change in CL porosity at a constant CL thickness will result in changes in the catalyst loading. Furthermore, a change in CL porosity leads to a change of the specific surface area a_v in Equation (4.24). Figure 4.10 shows the CO partial current density as a function of CL porosity at an applied cathode potential of -1.7 V and -1.9 V vs SHE for a constant CL thickness of 3 µm. In the simulated region, the mass loading reduces from 2.8 to 1.3 mg cm^{-2}. An increase in CL porosity leads to several aspects that influence the CO partial current density. For instance, mass transport is improved due to an increase in the effective diffusivity, see Equation (4.3). Furthermore, the average pore size within the CL increases. As the value for saturation is kept constant, this leads to an increase in film thickness that covers the catalyst surface, see Equation (4.26). However, an increase in film

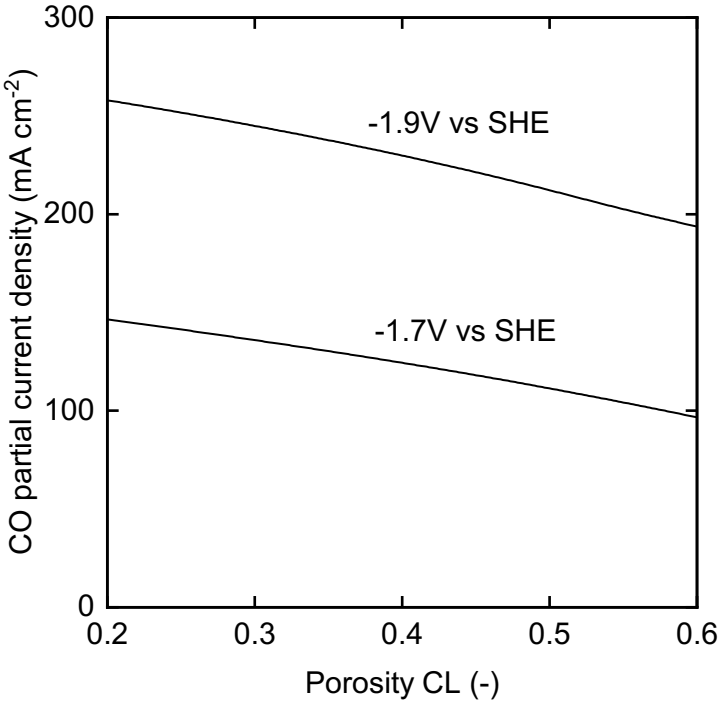

Figure 4.10.: CO partial current density as a function of CL porosity at an applied cathode potential of -1.7 V and -1.9 V vs SHE at a constant layer thickness.

thickness hinders the mass transport of dissolved CO_2 from the liquid-gas boundary to the catalyst surface. Hence, this has a mitigating effect on the CO partial current density. The volume-specific surface area decreases with increasing CL porosity, which can be taken from Equation (4.24). A decrease in the CO partial current density is apparent if the CL porosity is increased. The decrease in partial current density is attributed to the decrease in catalyst mass loading and, thus, the decrease in active sites being available for the CO_2 reduction. Consequently, the amount of available reaction sites for the reduction has a larger impact on the CO partial current density than the improved species transport.

In this work, the influence of the ionomer on mass transport and stability was neglected for simplification. In their experimental study, Verma et al. [Verm2016b] showed that this assumption is valid for the modeled

system as they did not see a significant change in CO partial current densities when preparing the GDE without adding Nafion. However, tailoring the ionomer content or post-treating the GDE with polymers, e.g., Nafion, has shown a beneficial effect on the CO_2R rate [Liu2018; Liu2019; De A2020; Ozde2020]. The increased Faradaic efficiency and energy efficiency reported in these studies is due to improved reactant transport in the polymeric layer, stabilization of the $CO_2^{\bullet-}$ intermediate near the catalyst surface, and protection against contaminants [Espo2018; Ponn2017]. Therefore, future modeling work should consider the effect of the ionomer on mass transport and kinetics.

4.4. Conclusion

A one-dimensional steady-state model was developed for the electrochemical reduction of CO_2 to CO in a continuous flow-through reactor. The model describes the cathode as a gas diffusion electrode, continuously provided with CO_2 coming from a gas channel on the one side and buffering $KHCO_3$ electrolyte on the other side. The model assumes an isoporous medium and accounts for different properties of CL and DM and the wetting of the CL. The model includes flow conditions of the gas phase, electron transport in the solid phase of the GDE, and multi-component mass transport from and to the electrolyte and gas channel. Furthermore, the model considers the electrochemical reduction of CO_2 to CO and the HER, phase transfer of liquid phase and gas phase species, and homogeneous equilibrium reactions within the electrolyte. This model formulation is the most comprehensive so far disclosed in the literature and allows me to explore the influence of relevant parameters such as electrolyte concentration, electrolyte and gas flow rate, gas composition, and properties of the CL and the DM at industrially relevant current densities.

The simulation results demonstrate that an increase of $KHCO_3$ improves the electrochemical reduction of CO_2 to CO. The predicted local pH and liquid phase concentrations indicate that its positive influence originates from an enhanced ionic conductivity in the electrolyte and improved buffer-

ing of OH^- ions in the CL. I found that high electrolyte flow rates enhance the removal of carbonate ions, thus lowering the risk of salt precipitation in the CL due to the local pH value conditions.

The simulations indicate that diffusion and solubility limitations of CO_2 in the GDE are influenced by the gas flow rate and the corresponding local CO_2 fraction along the gas channel. An increase in gas flow rate helps to overcome diffusion limitations in the GDL until CO_2 phase transfer into the electrolyte becomes limiting. However, at the same time, an increase in gas flow rate dilutes the produced CO in the product stream. Thus, the optimal flow rate is a trade-off between the desired CO production rate and the purity of the product. The gas phase transport in the GDE is mainly affected by the porosity and catalyst loading of the CL. Increasing porosity within the CL at constant thickness, meaning a decrease of catalyst loading, deteriorates the electrochemical reduction of CO_2. Also, an increase in the porosity of the DM shows a reducing effect on the production rate attributed to lower conductivity. Hence, both effects should be considered for an optimal design of the GDE.

The understanding of the influence of relevant operation parameters and electrode properties on the performance of GDEs gained in this study can be used to improve the operation and tailor the structure of GDEs. The modeling results help to keep the experimental effort low and thus accelerate the way to commercialization of CO_2 reduction processes. In future works, the model needs to be extended to a second dimension along the flow channels to account for changes in the gas and electrolyte composition as a function of the height of the electrolyzer. The concentration profile along the flow channel will influence the local mass transport that needs to be considered in large-scale electrolyzers.

5. Multi-dimensional modeling using data-driven surrogate models

5.1. Introduction

The continuum models presented in Chapter 3 and Chapter 4 allow local resolution and a deep understanding of species transport and reaction phenomena at the immediate electrode interface or in the porous structure of the gas diffusion electrode (GDE). On the downside, the high accuracy of these models makes them computationally demanding and, thus, difficult to extend to multiple dimensions or to use in holistic process assessment. However, assessing reactant concentration gradients in two dimensions, i.e., perpendicular to the electrode and along the flow channel, is particularly important when scaling up CO_2 electrolyzers to pilot-scale or industrial-scale. Kas et al. [Kas2021] modeled a 2D section of a GDE and showed CO_2 depletion in electrochemical reactions and carbonate formation in the electrolyte along the flow channel. Furthermore, they demonstrated that mass transport limitations become more significant at a certain conversion rate and height of the GDE. Hence, 2D simulations can help to optimize the modulation of the gas flow rate, the reactant composition, and the reaction rate when scaling up. In another work, Blake et al. [Blak2023] presented a 2D model of a CO_2 electrolyzer with 100 cm in height. At this scale, changes in catalyst layer pH and widening concentration boundary layers along the flow channel result in much greater reaction and local environment inhomogeneity compared to small-scale electrolyzers. However, the 2D continuum models of Blake et al. and Kas et al. are computationally demanding, and therefore, either simplifications of the model equations are necessary, or the size of the simulated domain needs to be reduced. Hence, computationally more efficient approaches are required to simulate CO_2 electrolysis on laboratory and industry length scales.

This chapter describes an approach in which surrogate models of the GDE continuum model from Chapter 4 are derived to mimic the behavior of an infinitesimally small section of the GDE. Several of these surrogate models are then connected via mass balances in the gas and liquid flow

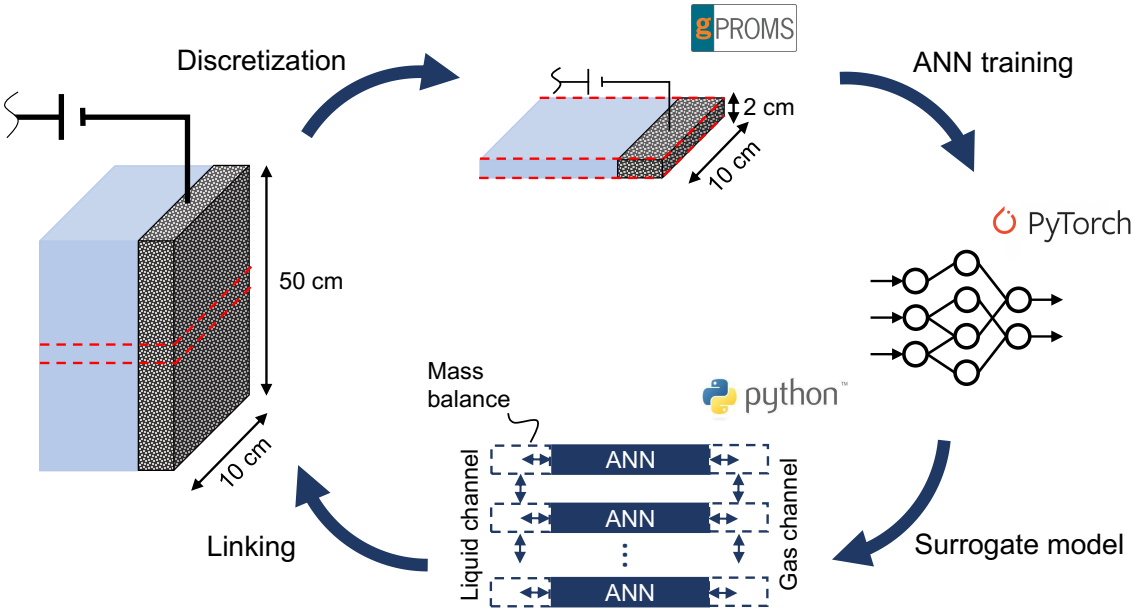

Figure 5.1.: Illustration of the multi-dimensional surrogate modeling approach for the simulation of a 500 cm^2 GDE.

channels along the flow direction to obtain a two-dimensional representation of the GDE. This approach is referred to as multi-dimensional surrogate modeling and is schematically shown in Figure 5.1.

The surrogate model of the GDE section is implemented as an artificial neural network (ANN). ANNs are biologically inspired computational networks related to the structure of the human brain. They comprise an input layer, one or more hidden layers, and an output layer. Each layer consists of one or more neurons, which have unique values and are fully interconnected with the neurons in the following layer, as illustrated in Figure 5.2.

The values of the previous neurons x_i determine the values of the neuron's net input $h(x_i)$ by simple multiplication with the respective weights w_i, and addition of the respective neuron's bias b, as stated in Equation 5.1 [Rasc2019].

$$h(x_i) = \sum_m w_i x_i + w_0 b \tag{5.1}$$

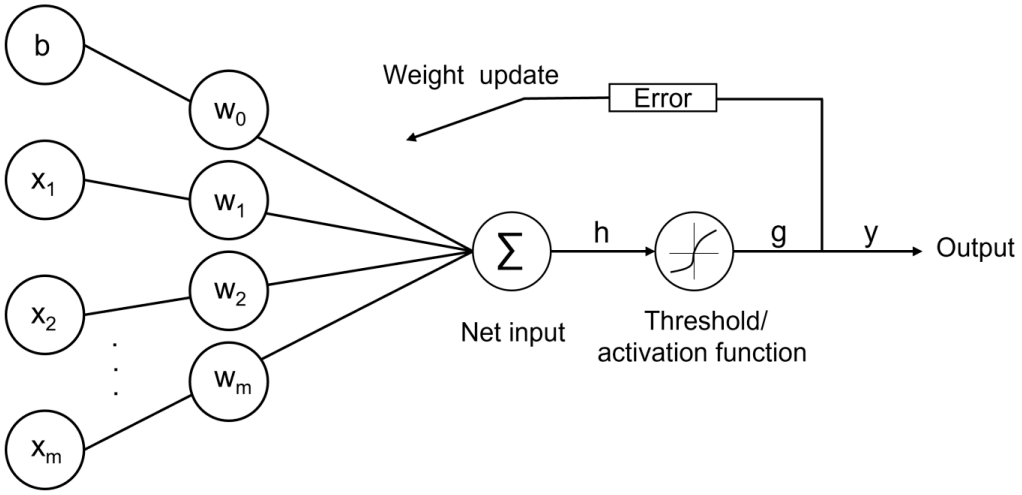

Figure 5.2.: Scheme of calculation of neuron values in an ANN during training adapted from Raschka et al. [Rasc2019].

After that, a well-chosen activation function is applied to the net input to calculate the resulting neuron value $g(h)$. This step is responsible for creating a non-linear relation. Next, the output error is evaluated, and if deemed necessary, the weights and biases are updated accordingly. This process is referred to as the backpropagation learning algorithm and comprises the computation of partial derivatives to update the weights and biases by means of gradient descent [Lópe2022]. The learning process is repeated a selected amount of times (epochs) with data from a training data set. Finally, the accuracy of the ANN is assessed with the help of evaluation metrics through the computation of data from a separate validation data set, whose target values are unknown to the trained ANN [Rasc2019]. The training data set in this work consists of simulation data of the GDE continuum model from Chapter 4. The methodology is described in more detail in the following section.

5.2. Methodology

The following subsections describe the procedures of generating training data with the GDE continuum model introduced in Chapter 4, identifying

the structure of the ANN, and training and validating the ANN. Finally, the method of connecting the surrogate models is elucidated.

5.2.1. Data generation

The multi-dimensional modeling approach in this thesis aims to simulate a GDE with a geometrical surface area of 500 cm^2 (50 cm x 10 cm, length x width). The 2D surrogate model of the GDE consists of 25 discrete elements, each represented by an ANN trained from data of the GDE continuum model. The training data set is generated in the gPROMS ModelBuilder using the Monte Carlo pseudo-random sampling method. The Monte Carlo method performs multiple simulations within set boundaries, including the lower and upper limits. For the simulation, the Monte Carlo sampling method manipulates the applied cathode potential, the feed gas composition, the electrolyte composition, and the saturation factor. The boundaries of each variable are listed in Table 5.1. The number of variables and sampling points results in a total number of 31 000 simulations.

Variable	Lower limit	Upper limit	Unit
Cathode potential	-1.8	-1.3	V vs SHE
CO_2 fraction	0.4	0.97	-
H_2 fraction	0.005	0.25	-
H_2O fraction	0.02	0.3	-
Gas flow rate	3 000	4 000	sccm
$CO_2^{(aq)}$	1	30	mM
Pore saturation	0.6	0.85	-

Table 5.1.: Variables manipulated within the Monte Carlo pseudo-random sampling method and boundary values.

The upper limits for the gas mole fractions are estimated based on the maximum conversion rate obtained with the GDE continuum model. The electrolyte composition is varied by changing the concentration of aqueous CO_2 in a 1 M $KHCO_3$ electrolyte. The concentration of each liquid species is then calculated using dissociation equilibrium constants, as described in Chapter 4.

5.2.2. Training and validation of ANNs

The ANNs are trained in the Python-based machine learning framework PyTorch [Pasz2017]. In this thesis, the architecture of the ANN, i.e., the number of hidden layers and neurons per layer, is determined using the hyperparameter optimization framework Optuna [Akib2019]. The tested hyperparameters, i.e., the parameters defining the ANN structure, include the learning rate, the batch size, the number of hidden layers, and the number of neurons per layer. The limits for each of the hyperparameters are listed in Table 5.2. Optuna works by sampling the defined hyperparameters within their boundaries and pruning unpromising trials at the early stages of the training.

Hyperparameter	Lower limit	Upper limit	Unit
Learning rate	1 E-04	1 E-03	-
Batch size	5 000	20 000	-
Number of hidden layers	1	4	-
Number of neurons per layer	1	750	-

Table 5.2.: Limits for hyperparameters in the ANN optimization in Optuna.

Subsequently, the optimal ANN architecture identified by Optuna was transferred to PyTorch for the training, validation, and testing of the ANN. First, the inputs and outputs of the training data set, which is 75% of the whole data set simulated in gProms, are transformed via normalization so that the values are in the range of [0,1]. Due to various outputs differing in many orders of magnitude, normalization levels these discrepancies and facilitates the training of the ANN. The data normalization of a value is performed as follows

$$Y_i = \frac{X_i - X_{min}}{X_{max} - X_{min}}, \tag{5.2}$$

where Y_i is the normalized value for a specific input/output data set, X_i is the current considered value, and X_{max} and X_{min} are the maximum and minimum value of the specific data set, respectively. The Adam training

algorithm is chosen to train the optimized ANN architecture given by Optuna. To evaluate the training progress, the mean squared error (MSE) as defined in Equation 5.3 is used.

$$MSE = \frac{1}{n}\sum_{i=1}^{n}(Y_i - \hat{Y}_i)^2 \tag{5.3}$$

Here, n refers to the sample size, Y_i is the value from the data set, and $\hat{Y}_i$ is the predicted value. The ReLU-function is chosen as the activation function for the neurons.
The validation of the ANN architecture was carried out using 25% of the whole data set. The inputs of the ANN comprise the cathode potential, the feed gas composition, the aqueous CO_2 concentration, and the pore saturation factor. The outputs are the gaseous and liquid species fluxes at the electrolyte and gas channel - GDE interface.
In addition to the commonly used method for training and validation of ANNs, as described above, the k-fold cross-validation method was implemented. The k-fold cross-validation method excludes $\frac{1}{k}$ data from the data set to use this subset of data as an unbiased test data set as illustrated in Figure 5.3. The data set is divided into a test data set and a validation data set. The difference in k-fold cross-validation compared to random validation during training is that with every iteration, a different fold is left out of the training so that every sample is used as a test sample once.

5.2.3. Model structure for multi-dimensional surrogate modeling

This work introduces multi-dimensional surrogate modeling to simulate the concentration gradients in the electrolyte and gas channel of a 500 cm^2 (50 cm x 10 cm) electrochemical cell in 2D. Following the approach introduced in Figure 5.1, the 500 cm^2 was discretized into 25 elements, each represented by an ANN trained from data of the gProms GDE model. Mass balances were formulated for the gas and electrolyte channels to calculate

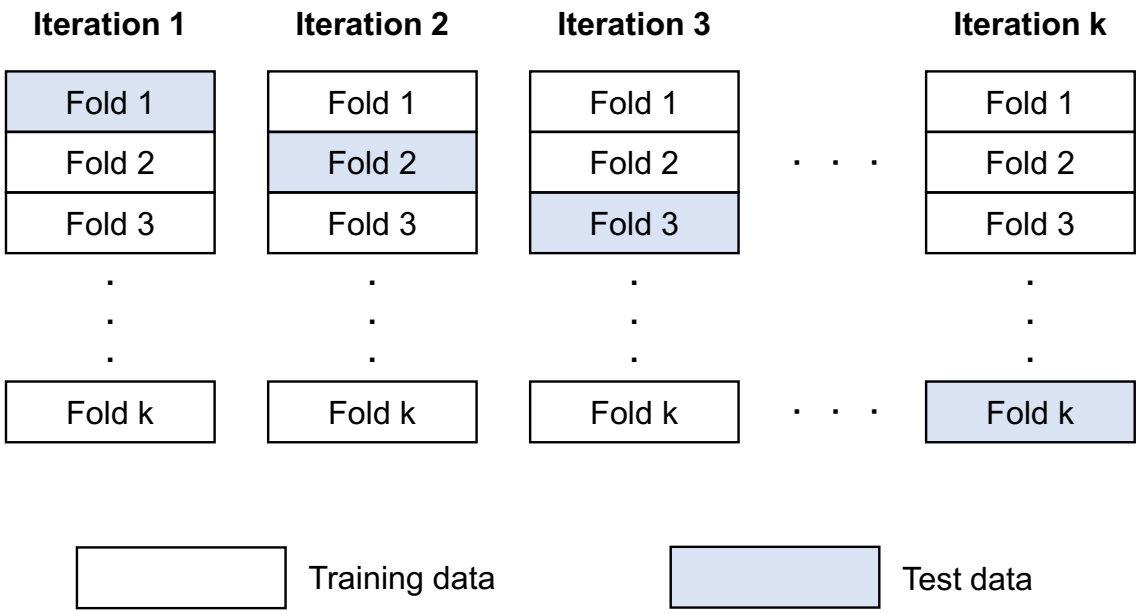

Figure 5.3.: Schematic illustration of the k-cross validation method adapted from Frochte [Froc2019].

the species mole fraction in each discrete element. It is assumed that each element is ideally mixed so that the mole fraction in the element equals the mole fraction in the outlet of each element. In the gas channel, the species mass balance is

$$0 = \dot{N}_{gas} y_{i,n-1} + J_{i,GDE,n} L_{GDE,n} w_{GDE} \epsilon_{GDL,0} - \dot{N}_{gas} y_{i,n} \tag{5.4}$$

where $\dot{N}_{gas}$ is the molar flow rate in the gas channel, $y_{i,n}$ is the molar fraction of component i = CO_2, CO, H_2 in element n, $y_{i,n-1}$ is the molar fraction of i in the previous element n-1, $J_{i,GDE,n}$ is the flux of i at the gas channel - GDE interface which is an output of the ANN, $L_{GDE,n}$ and w_{GDE} are the height and the width of the discrete element, and $\epsilon_{GDL,0}$ is the porosity of the gas diffusion layer. The molar fraction of H_2O was calculated from the closing condition for the k species

$$1 = \sum_{i=1}^{k} y_{i,n} \tag{5.5}$$

The electrolyte composition in each discrete element is calculated from the dissociation equilibrium of the acid/base carbonate Reactions 4.14-4.17 as in Chapter 4. Additionally, the electroneutrality constraint is implemented as

$$0 = \sum_{i=1}^{k} c_{i,n} q_i \tag{5.6}$$

where c_i is the concentration and q_i is the charge of liquid species i. However, as this only gives five equations to solve the concentration of the six liquid electrolyte species, another equation is needed. Here, the concentration of CO_2 $c_{CO_2,n}$ in element n is calculated from a mass balance

$$0 = \dot{V}_{elec} c_{CO_2,n-1} + J_{CO_2,GDE,n} L_{GDE,n} w_{GDE} - \dot{V}_{elec} c_{CO_2,n} \tag{5.7}$$

with $\dot{V}_{elec}$ being the volumetric flow rate of the electrolyte, $c_{CO_2,n-1}$ is the molar fraction of CO_2 in the previous element n-1, and $J_{CO_2,GDE,n}$ is the flux of CO_2 at the electrolyte channel - GDE interface which is an output of the ANN.

5.3. Results and discussion

The optimal ANN architecture identified by Optuna for the seven inputs and eight outputs comprises two hidden layers with 729 neurons in the first layer and 720 neurons in the second. Given the optimized ANN architecture, the MSE decreases after only a few epochs during training with the whole data set in PyTorch, as shown in the left plot in Figure 5.4. The final MSE after 100 epochs is $5.1 \cdot 10^{-5}$. A similar trend is also seen for the loss in MSE for the validation of the ANN with an MSE of $5.0 \cdot 10^{-5}$ after 100 epochs. The low magnitude of the MSE indicates a high accuracy of the ANN in predicting the behavior of the gProms GDE model. Furthermore, as validation and training loss are in a similar range, overfitting of the ANN can be excluded.

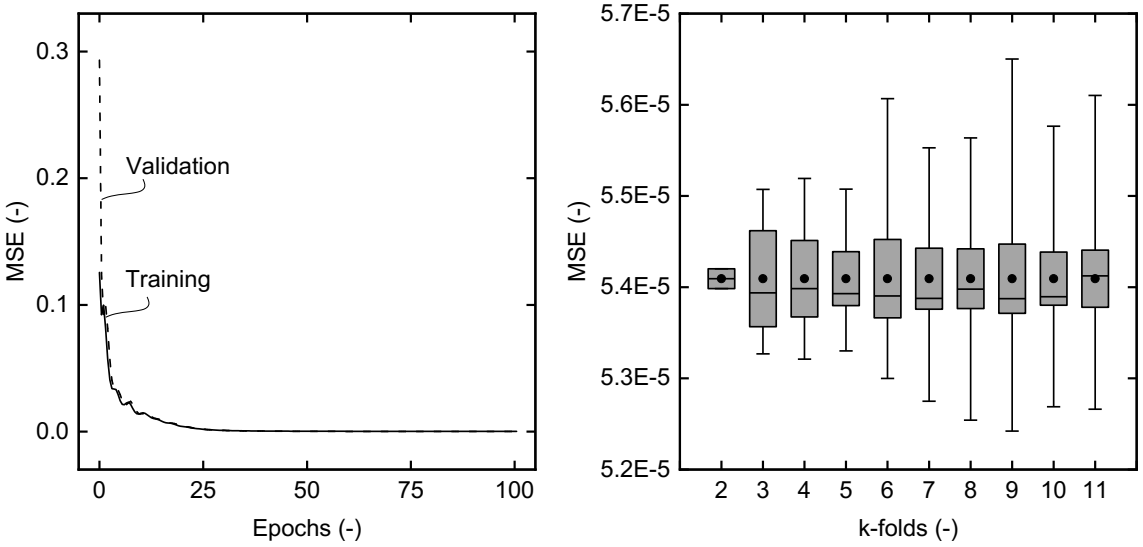

Figure 5.4.: Left graph: The progress of the loss function, i.e., the MSE, during training and validation of the ANN over the epochs using the whole data set (75% for training and 25% for validation). Right graph: MSE for different k-folds determined from k-cross-validation. The dot indicates the average MSE, the middle line in each boxplot represents the median, the upper and lower end of the boxes indicate 95% and 5% quartile, and the lower and upper antennae are the lower and upper Whisker of the boxplots.

5

To test the ANN architecture on predicting unseen data, k-cross validation with k >1 was performed. The average MSE in the right graph in Figure 5.4 for the different k-folds is almost constant at approx. $5.4 \cdot 10^{-5}$, demonstrating a suitable generalization of the ANN. Even with the 2-fold cross-validation, which only uses half of the data points than training with the whole data set, a similar MSE was achieved, indicating that the original data set is sufficiently large. For k >5, more pronounced deflections of the MSE can be seen. However, the relative change of the MSE is low. The ANN trained and validated with the whole data set was chosen in the following.

The parity plot in Figure 5.5 for the CO partial current density confirms the good accuracy of the trained ANN, as the predicted current densities are in good agreement with the simulated data points.

According to the multi-scale modeling approach presented in Figure 5.1,

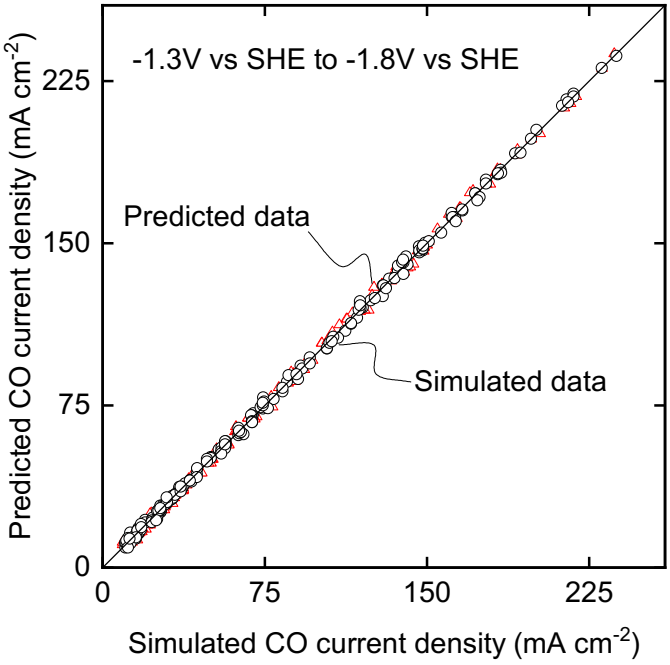

Figure 5.5.: Parity plot of the predicted partial CO current densities from the ANN and the simulated partial CO current densities from the gProms model.

a 2D surrogate model was built from the trained ANN. Figure 5.6 shows the CO_2 concentration in the electrolyte channel (left graph) and the CO_2 bulk gas fraction (right graph) along the electrolyte and gas flow channel, respectively. The 1 M KHCO3 solution enters the liquid flow channel with a concentration of dissolved CO_2 of 13.8 mM. At potentials as low as -1.3 V vs SHE, the CO_2 concentration increases linearly along the flow direction. Simultaneously, the CO_2 fraction in the gas channel stays nearly constant. Attributed to the low current density at -1.3 V vs SHE of about 20 $mA\,cm^{-2}$, as shown in Figure 5.7, most of the gaseous CO_2 bypasses the GDE while dissolved CO_2 diffuses into the electrolyte channel. Increasing the potential leads to a less pronounced increase in dissolved CO_2 in the electrolyte channel and more CO_2 being consumed from the gas channel, respectively. Interestingly, at -1.8 V vs SHE, the CO_2 concentration in the electrolyte channel starts stagnating towards the outlet of the flow channel. The CO_2 fraction in the gas channel further decreases due to increased consumption of CO_2 in the electrochemical reduction reaction, as shown in Figure 5.7. Consequently, the driving force for CO_2 dissolution into the liquid phase within the GDE decreases, and therefore also the diffusive CO_2 flux from the GDE to the electrolyte channel.

The decrease in CO_2 fraction due to increased consumption along the gas channel at elevated potentials also leads to a change in CO partial current density, as shown in Figure 5.7. However, the decrease in CO partial current density is neglectable for -1.3 V vs SHE and -1.6 V vs SHE and small for -1.8 V vs SHE, despite the strong decrease in the local CO_2 gas fraction at -1.8 V vs SHE. Comparing these results to the simulation study on the impacts of the CO_2 fraction on the electrochemical CO_2 reduction at different excess rates in Chapter 4, the decreasing trend of the CO partial current density with the CO_2 gas fraction is in the same range. The decrease in CO_2 fraction from 95% to 50% led to a decrease in the CO partial current density of approx. 30%. Here, the CO_2 fraction changes from 97% at the channel inlet to 75% at the outlet, resulting in a decrease of the CO partial current density of approximately 14%. However, when

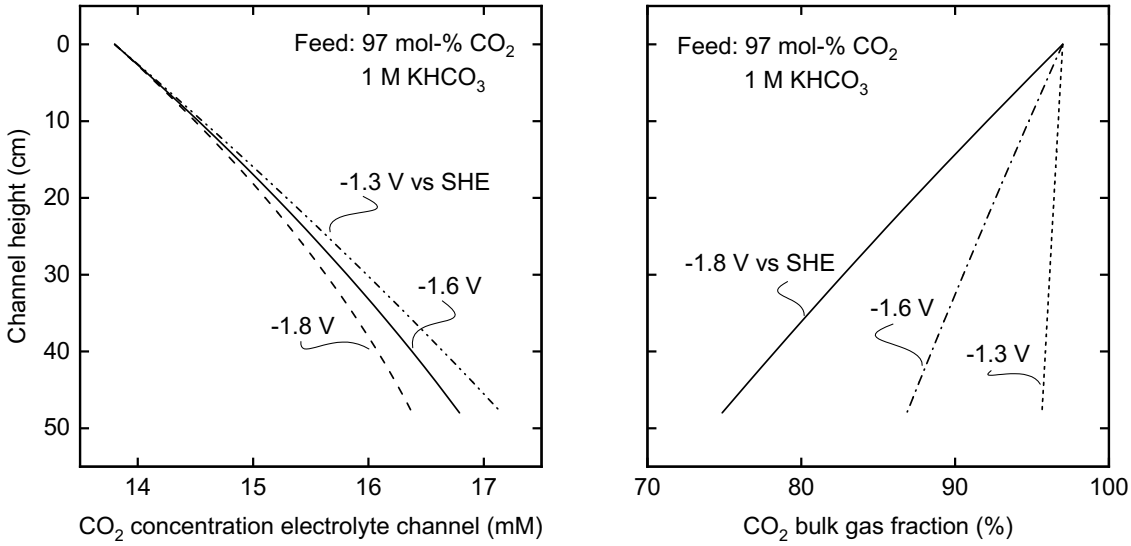

Figure 5.6.: Molar concentration and gas fraction of CO_2 in the electrolyte and gas channel along the height of the surrogate electrolyzer for different cathode potentials.

operating at an industrial scale, i.e., 1000 cm^2 to 1 m^2, the loss in CO partial current density is expected to be even higher than on the scale considered in this study [Bahn2022; Lehn2014].

One way to overcome the descending production rate of CO in large-scale electrolyzers is by increasing the gas flow rate. Figure 5.8 compares the CO_2 concentration in the bulk electrolyte channel and the CO_2 gas fraction in the gas channel for different gas flow rates. The CO_2 concentration in the electrolyte is not affected by an increase in the gas flow rate from 3 500 sccm to 4 000 sccm. When decreasing the flow rate to 3 000 sccm, the increase in the CO_2 concentration along the channel height is slightly lower compared to the higher flow rates. Hence, the amount of CO_2 dissolving into the electrolyte and diffusing into the bulk channel stays almost constant when changing the gas flow rate in the considered regime. However, a significant decrease in CO_2 concentration is apparent when applying a flow rate of 2 000 sccm as more CO_2 is converted in the CO_2 reduction reaction than transported into the bulk

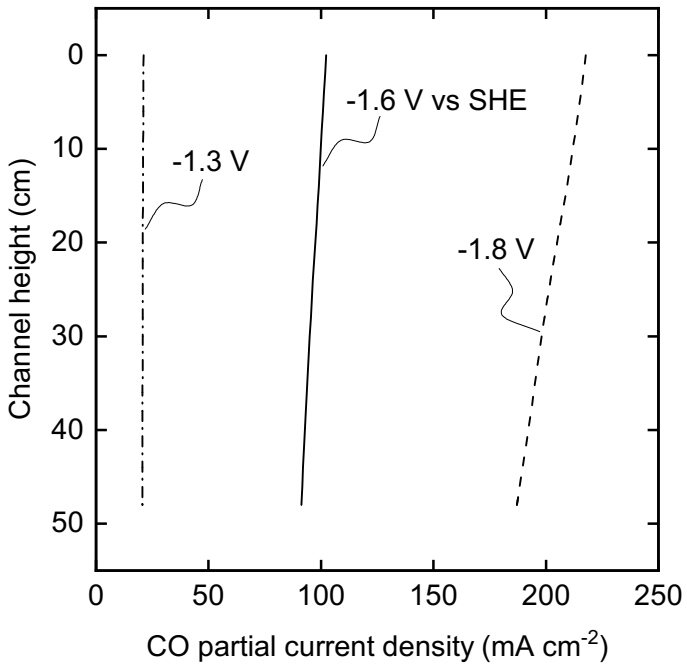

Figure 5.7.: CO partial current density along the height of the surrogate electrolyzer for different cathode potentials.

electrolyte channel. Moreover, the CO_2 concentration stagnates along the flow channel at this flow rate. Consequently, dissolved CO_2 diffuses from the bulk electrolyte into the GDE and also becomes a reactant for the reduction reaction. The difference in the CO_2 gas fraction as a function of the gas flow rate is more prominent compared to the CO_2 concentration in the electrolyte for the flow rates between 3 000 sccm and 4 000 sccm. Again, the CO_2 fraction decreases almost linearly for the considered flow rates. However, the drop is more significant for lower flow rates of 3 000 sccm and 2 000 sccm. Thus, an increased driving force for mass transport from the gas into the liquid phase along the entire channel length is achieved at higher flow rates. While increasing the flow rate might help to overcome mass transport issues in large-scale electrolyzers, the effort for CO_2 separation in the downstream process increases when the CO_2 conversion rate decreases. As shown in the economic sensitivity study in Chapter 6, a decrease in the per-pass conversion rate has a detrimental effect on process economics. Therefore, the mathematical optimization of large-scale electrolyzers regarding CO_2 mass transport and CO_2 utilization needs to be carried out using 2D models to resolve along the channel gradients.

It needs to be mentioned that a constant saturation of the GDE with liquid electrolyte was assumed. However, in systems on an industrial scale, pressure inhomogeneities and changing electrode wettability influence the liquid saturation of the GDE and significantly impact mass transport in the porous electrode and thus also the CO partial current density [Weng2018]. The saturation distribution along the GDE can be considered by considering the saturation factor introduced in Chapter 4 as an input of the ANN. However, this requires a model to relate the liquid saturation of the GDE and its wettability characteristics and the local partial pressure, e.g., from experiments or numerical simulations [Gost2009; Niu2018]. With a given saturation model, the saturation factor could be included as an output of the ANN to describe the local effects of electrode wettability.

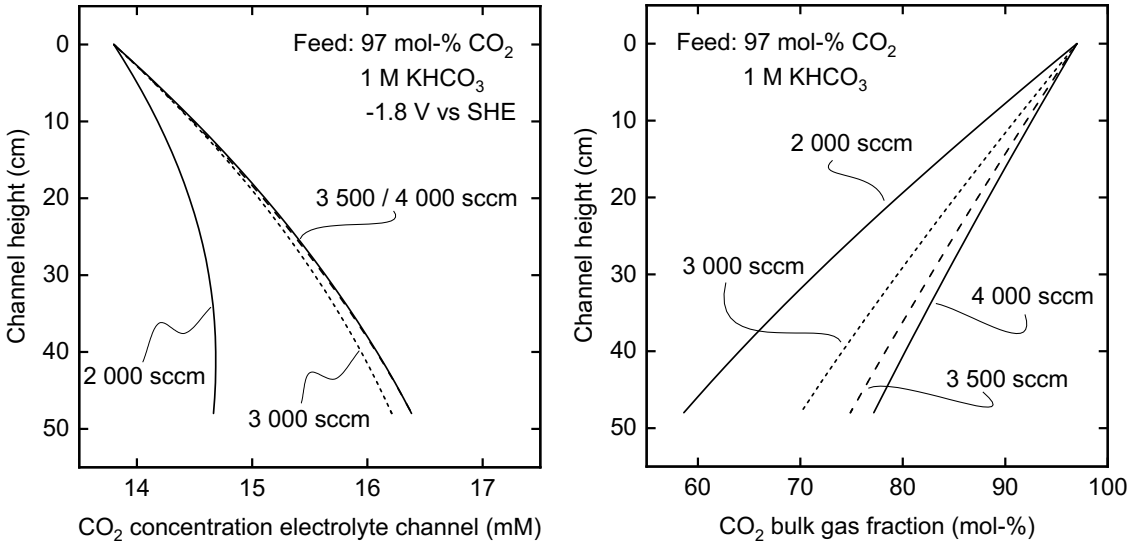

Figure 5.8.: Molar concentration and gas fraction of CO_2 in the electrolyte and gas channel along the height of the surrogate electrolyzer for different gas feed flow rates.

5

5.4. Conclusion

This proof of concept study has shown that ANNs can be used to efficiently model parts of electrolyzers for electrochemical CO_2 reduction at a relevant scale. Using the comprehensive continuum model from Chapter 4, data was generated to train an ANN that mimics the mechanistic GDE model. Scaling of the GDE to a 500 cm^2 geometrical electrode area was achieved by combining multiple surrogate models, each treated as a discrete element of the full-scale electrode.

The predicted output by the ANN and the given training data from the continuum model are in good agreement, proving the applicability of ANNs for mimicking the GDE model. Interestingly, the CO_2 concentration in the bulk electrolyte increases along the channel height but then stagnates due to a declining driving force for mass transport from the gas phase into the electrolyte. The partial pressure gradient along the gas channel is more pronounced for elevated potentials where the consumption rate of CO_2 is increased. Due to the descending transport of CO_2 into the liquid phase,

the CO partial current density drops at the inlet and the outlet position of the GDE, e.g., by 14% for 1.8 V vs SHE. The mass transport from the gas phase to the catalyst sites can be improved by increasing the gas flow rate. However, mass transport in large-scale electrolyzers must be optimized considering the separation effort in the downstream process to meet the holistic cost optimum.

In future work, the multi-scale modeling approach can be extended by combining continuum models on various length scales and parts of the electrolyzer. For example, a spatial resolution of the local mass transport in the near-electrode environment as in the model in Chapter 3 would allow a more comprehensive insight into the relation of changes in the bulk channels and the local reaction environment.

6. Techno-economic assessment using holistic process optimization

Parts of this chapter have been published as:
Matthias Heßelmann, Hannah Minten, Tristan Geissler, Robert Gregor Keller, André Bardow, Matthias Wessling
Why membranes matter: Ion exchange membranes in holistic process optimization of electrochemical CO_2 reduction, Advanced Sustainable Systems, 2023
DOI: 10.1002/adsu.202300077

6.1. Introduction

Current research on electrochemical CO_2 reduction focuses on decreasing the energy input and improving the CO_2 utilization even when operating at industrially relevant current densities [Liu2018; Haas2018; Larr2019; De A2020; Bhar2020; Nwab2021]. While many of these reports address important aspects of improving CO_2 electrolysis by the development of functional electrode materials, the design of efficient cell configurations, the control of process conditions and reactant transport, one essential question is not yet fully answered: Which ion exchange membrane is best suited for electrochemical CO_2 reduction in terms of economics?

The ion exchange membrane controls ion transport from one electrolyzer half-cell to the other and affects the reaction environment at the electrodes, the mass balance of the whole process, and, thus, the overall electrolyzer performance, i.e., Faradaic efficiency, cell voltage, and long-term operation stability. However, the question of which ion exchange membrane is best suited cannot be answered by focusing on the electrolyzer alone because downstream processing will significantly change depending on the membrane type. Figure 6.1 presents the three types of ion exchange membranes that are mainly used in CO_2 electrolysis: anion exchange membranes (AEMs), cation exchange membranes (CEMs), and bipolar membranes (BPMs). So far, studies on CO_2 electrolysis to CO using AEMs report among the best performance in terms of energy and Faradaic efficiency [Ma2017; Liu2018; Gaba2019; Zhen2019; Ma2020a]. However, a significant drawback often accounted to AEMs is the CO_2 pumping effect due to the crossover of HCO_3^- and CO_3^{2-} from the cathodic to the anodic half-cell and the subsequent protonation to CO_2, as illustrated in Figure 6.1 [Rabi2020]. Ma et al.[Ma2020a] found that 70% of the gaseous CO_2 at the cathode is captured in the catholyte and transported through the AEM to the anode, where it leaves the process in a mixture with, e.g., O_2 from oxygen evolution reaction (OER). Thus, substantial amounts of the reactant are either lost or have to be separated from other gases

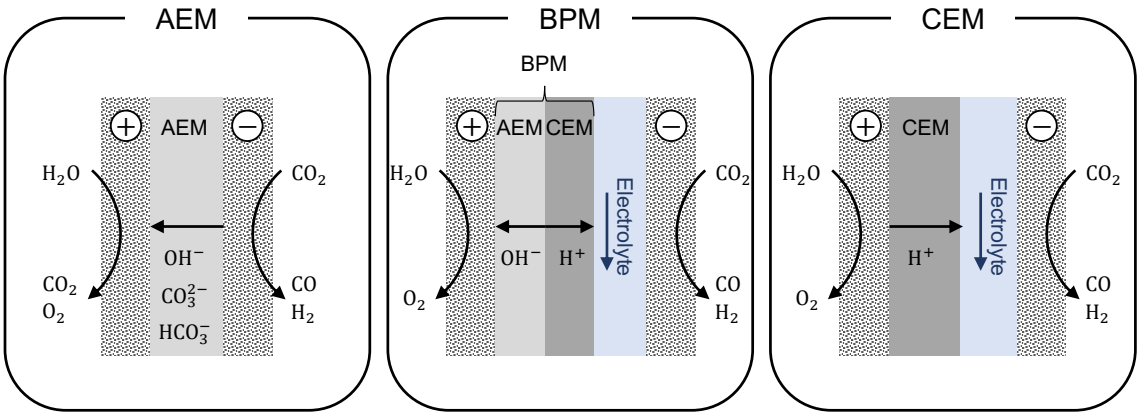

Figure 6.1.: Schematic illustration of the electrolyzer configurations with an anion exchange membrane (AEM) (left), bipolar membrane (BPM) (center), and a cation exchange membrane (CEM) (right). The electrolyzer design configurations are adapted from the experimental works underlying this study [Liu2018; Salv2017; Venn2019a].

evolving at the anode, resulting in additional costs. Moreover, stable anion exchange membranes have only been developed recently and need further improvement [Salv2021]. BPMs can be operated in two modes: the forward bias and the reverse bias mode. In the forward bias mode, the CEM faces the anode, and the AEM faces the cathode. This configuration has the great advantage of maintaining a basic pH value in the catholyte, which is beneficial for CO_2 reduction. The CEM prevents the crossover of HCO_3^- towards the anode to mitigate CO_2 losses at the anode. However, gaseous CO_2 may be released in the interface between the CEM and AEM, leading to delamination of the membrane [Patr2019]. The reverse bias mode, as shown in Figure 6.1, has a great advantage compared to the use of CEM and AEM alone: ion crossover can be mitigated, which enables the use of different electrolytes in the catholyte and anolyte compartment. This degree of freedom is especially advantageous for the electrochemical CO_2 reduction, as it enables the use of cost-effective, non-noble anode catalysts such as nickel [Venn2019b]. Patru et al.[Patr2019] show opportunities for reverse and forward bias for electrochemical CO_2 reduction. The third class of ion exchange membranes used in low-temperature CO_2 electrolysis are CEMs. CEMs such as Nafion® are widely used and well established in other electrochemical processes, e.g., in fuel cells and water

electrolysis, and are commercially available on a large scale. However, the major drawback of using CEMs in CO_2 electrolysis is due to the typically increased presence of H^+ ions at the membrane surface, which requires the implementation of a buffer layer between the membrane and the electrode [Ma2017; Venn2019a].

Several experimental studies discuss the advantages and disadvantages of each membrane type on electrochemical CO_2 reduction [Salv2017; Lin2019; Salv2019; Patr2019; Ma2020a; Ma2020b; Rabi2020; Blom2021; Xie2022a; Erik2022]. However, future research in the field would benefit from comparing the economic potential of the various electrolyzer configurations. Techno-economic analyses of CO_2 electrolysis discuss various products and evaluate influencing parameters [Verm2016a; Li2016; Spur2018; Joun2018; Ruma2019; Shin2021; Aler2021; Prib2022]. Only recently, researchers also began to systematically study the techno-economics of different ion exchange membrane reactors for CO_2 conversion [Shin2021; Prib2022]. Pribyl-Kranewitter et al. [Prib2022] simulated common electrolyzer designs for CO_2 electrolysis to carbon monoxide and formic acid and product separation in Microsoft Excel®and Aspen Plus®. However, they only considered fixed operating points without flowsheet optimization. Shin et al.[Shin2021] presented an economic evaluation of an AEM and BPM electrolyzer configuration for CO_2 electrolysis. Their results demonstrated that the production costs for CO are competitive with conventional processes. Furthermore, Shin et al. elucidate how the ion exchange membrane can address electrolyte regeneration in CO_2 electrolysis. However, even though the study highlights important aspects regarding the economic assessment and comparison between the AEM and BPM electrolyzer configuration, the simplified representation of the processes does not allow a profound evaluation of mass and energy balances and, thus, investment and operational costs. Therefore, the literature needs a holistic approach to identifying an optimal process configuration and operation point of electrolysis and downstream processing to minimize the overall production costs of electrochemical CO_2 reduction

products. Roh et al. [Roh2021] presented a globally optimized process for flexible operation of electrochemical CO_2 reduction and separation of the product stream. Yet, they only considered a one-side buffered CEM electrolyzer configuration, which might be less efficient and profitable than others. Furthermore, Roh et al. did not model the downstream processing on a detailed level. However, the separation process needs rigorous consideration to investigate the achievable purities of the desired products and assess recycle streams and losses in the overall process.

Here, I present a holistic approach to optimize and assess the economics of the electrochemical CO_2 conversion to CO or syngas by accounting for different electrochemical membrane reactor configurations. The mass and energy balances for each electrolyzer are based on state-of-the-art literature data. The downstream processing of the anodic and cathodic gas outlet streams is implemented using membrane gas permeation. Membranes offer unique advantages in terms of flexible operation, scalability, and costs, making them a viable option for downstream processing of the electrolysis off-gases [Bake2004; Scho2013b; Alsa2017]. The process flowsheet and operational parameters are optimized to minimize the specific production costs of the desired product. With this work, I can elucidate the following research questions on electrochemical membrane reactors and holistic process design:

- Which electrolyzer configuration is most economic for CO and syngas production?
- Which process parameters are key to increasing profit?
- Is it economic to operate CO_2 electrolysis to produce both carbon monoxide and hydrogen as syngas?
- Does the CO_2 pumping effect in AEMs negatively influence the overall process economics as often described, or could it offer advantages?

6.2. Methodology

This section describes the holistic optimization framework and the general assumptions made in this work. Furthermore, the underlying equations of each process unit and the cost model are introduced.

6.2.1. Process scheme

Holistic process optimization has been employed to determine the optimal process flowsheet and operating conditions of electrochemical CO_2 reduction to CO or syngas.

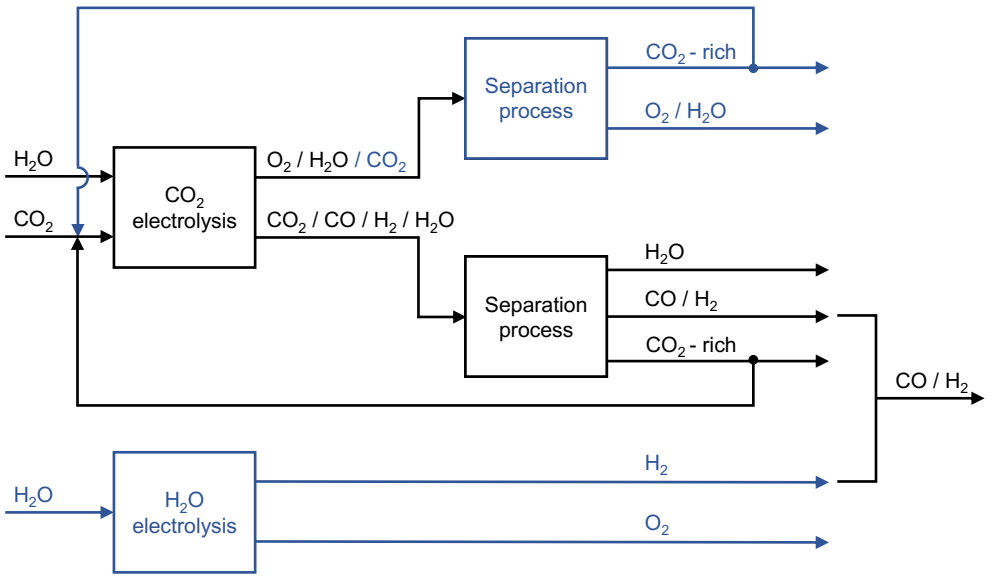

Figure 6.2.: Simplified block flow diagram of the process for electrochemical CO and H_2 production from CO_2 and H_2O. The grey blocks and streams are only considered for the AEM electrolyzer and the production of H_2 in water electrolysis, respectively.

Figure 6.2 sketches the process layout: CO_2 and H_2O are converted to CO and H_2 in an electrolyzer. Experimental data from state-of-the-art CO_2 electrolysis literature is used to fit regression models that account for energetics and mass conversion [Liu2018; Salv2017; Venn2019a]. Here, the most prominent electrolyzer configurations in low-temperature CO_2 electrolysis using AEMs, BPMs, and CEMs are compared. The

cathodic product stream is purified in the separation process to meet the desired specifications. In this work, the downstream processing of the gaseous products is achieved by adsorptive drying and membrane gas permeation. For the AEM electrolyzer configuration, CO_2 crossover is considered, and the amount of CO_2 in the anodic off-gas being purified and recycled or emitted to the atmosphere is an optimization task. For syngas production, additional H_2 is purchased from H_2O electrolysis. The ratio of H_2 produced in CO_2 electrolysis and H_2 purchased is a degree of freedom in the optimization. The desired products in this study are CO with a purity of $\geq$ 98% as, e.g., used in phosgene production, and syngas with H_2:CO ratios of 1:1 and 2:1 used, e.g., in oxo-synthesis and Fischer-Tropsch synthesis, respectively [Heus2005; Webe1970; Lu2007]. For scaling the syngas processes, the product streams are set to the same heating value for scaling the syngas processes as the CO product gas stream. The objective of the holistic optimization is to minimize the specific production costs (€/$t_{product}$) of the overall process by adapting the process configuration, i.e., the process flowsheet, the ratio of recycle and purge streams, and the selection of the gas permeation membrane materials, as well as relevant process parameters, i.e., the current density of the electrolyzer, the electrode area, the compression ratio, and the gas permeation membrane area. Based on the process optimization, the economics are investigated.

The process model, including models of the different unit operations, is implemented in the General Algebraic Modeling System (GAMS). To optimize the present nonlinear problem, the Branch-And-Reduce Optimization Navigator (BARON) solver is chosen to find initial values, and the CONOPT solver is applied to identify the optimum. The model structure is adapted from the work of Scholz et al. [Scho2015].

6.2.2. Process units

Electrolysis process

For the techno-economic assessment of the electrolysis process, five parameters are required to estimate the economics of the process: (1) the current density (j), (2) the cell voltage (V), (3) the Faradaic efficiency (FE_i) for i = CO, H_2, (4) the CO_2 conversion rate, and (5) the geometrical electrode surface area (A_{geom}). This data is usually determined in experiments or calculated using rigorous mathematical models that account for mass transport and electrochemical reaction kinetics. The parameters describing the electrolysis performance in this study are taken from representative experimental studies [Liu2018; Salv2017; Venn2019a]. The current density is chosen as the optimization variable. The cell voltage and the Faradaic efficiencies are calculated for the given current density based on regression curves that are fitted to experimental data so that each performance indicator is described by

$$y = f(x, \beta),\ y^T = (V, FE_i)\ and\ x^T = (j) \tag{6.1}$$

where y is the performance indicator, which is either the cell voltage or the Faradaic efficiency, x is the current density that is to be optimized, and β are the fitting parameters β_0, β_1, ..., β_n that are adapted so that the regression curve matches the experimental data. The regression analysis is conducted in Microsoft Excel®. The experimental data taken from the literature, the regression curves, and the coefficients of determination are listed in Equations (A.1)-(A.6).

The amount of gas produced, $\dot{N}_i$, in the electrochemical reactions is calculated from Faraday's law

$$\dot{N}_i = \frac{j \cdot FE_i \cdot A_{geom}}{z \cdot F} \tag{6.2}$$

Here, z is the number of electrons transferred in the electrochemical reaction, and F is the Faraday constant. The conversion rate of CO_2 in the electrolysis is assumed to be constant but is varied within a sensitivity study. The energy consumption of the electrolyzer is calculated from the current density and the cell voltage.

$$P_{elec} = j \cdot A_{geom} \cdot V \tag{6.3}$$

Adsorptive dehumidification

Adsorptive drying of the electrolysis off-gases is considered to minimize the risk of water condensation in the compressors and swelling of the gas separation membrane. The investment and operation costs are approximated using a shortcut equation derived from data from Scholz et al. [Scho2013a].

Compressor

The compressors are modeled as multi-stage isentropic compression with interstage cooling. The compression ratio and the number of compression stages are optimization variables in this work. The isentropic outlet temperature T_{out} of each compression stage is calculated from

$$T_{out} = T_{in} \cdot \left(\frac{p_{out}}{p_{in}} \right)^{(\kappa-1)/\kappa} \tag{6.4}$$

where T_{in} is the inlet temperature, p_{in} and p_{out} are the inlet and outlet pressure, and κ is the isentropic exponent. The power consumption of the compressors P_c to compress a molar flow $\dot{N}$ is determined by

$$P_c = \dot{N} \cdot \frac{\kappa}{\kappa - 1} \cdot R \cdot (T_{out} - T_{in}) \tag{6.5}$$

Gas permeation membrane

Membrane processes are known to be flexible in operation, e.g., for fast start-up/shutdown, easily scalable by numbering up, and cost-effective when using polymeric membranes [Bake2004]. Furthermore, gas permeation technology is already implemented on a larger scale, e.g., air separation, natural gas processing, and biogas upgrading [Bake2002; Chen2015]. In this study, different membrane materials for separating the electrolysis off-gases have been evaluated [Alqa2017; Mura2010; Davi2011; Aitk1992]. The membrane materials have been selected according to reasonable selectivity values and the availability of permeance data for the respective gases. Even though some of these membranes are not yet commercially available, they are based on polymers that are produced on an industrial scale.
The membrane model is discretized along the length using a constant step size. The species flux J_i through the membrane is modeled using the Solution-Diffusion Model (SDM)

$$J_i = Q_i \cdot \delta \cdot (y_{r,i} \cdot p_r - y_{p,i} \cdot p_p) \tag{6.6}$$

where Q_i is the permeance of species i in the membrane, δ is the thickness of the selective layer of the membrane, which is assumed to be 0.5 µm for all membrane materials due to missing information in the respective references. $y_{r,i}$ and $y_{p,i}$ are the molar fractions of i in the retentate and the permeate, respectively. p_r and p_p are the absolute pressures on the feed and permeate side. Temperature gradients due to heat dissipation, the Joule-Thomson effect, and pressure losses are neglected. Furthermore, constant permeances and ideal gas behavior are assumed. The membrane module configuration, the membrane material selection, the membrane area, and the stage-cut are optimized in this study.

The gas permeation process for separating the anodic outlet gas stream is modeled using a surrogate model in the overall process flowsheet to

reduce complexity and computational costs. The surrogate model is derived from separate simulations in which the aforementioned membrane processes are optimized for different CO_2:O_2 ratios and flow rates. The optimization results are fed into a regression model to fit the anodic gas separation performance.

6.2.3. Economic evaluation

For the optimization of the process, the specific production costs *PC* (€/$t_{product}$) of either CO or syngas are chosen as the objective function. Thus, the optimization problem is to minimize *PC*.

$$PC = \frac{1}{m_{product}} \cdot (CC_{total} \cdot d_{year} + OC_{total}) \tag{6.7}$$

Here, $m_{product}$ is the mass of product per year, CC_{total} are the capital costs of the plant, d_{year} is the depreciation factor calculated from the lifetime of the plant and the interest rate, and OC_{total} are the yearly operational costs. The production capacity of the plant is set to 80 000 $t\,a^{-1}$, which is the amount required for producing, e.g., toluene diisocyanates in a typical world-scale plant, assuming stoichiometric conversion [Cove]. For comparison of the CO and the syngas production processes, the higher heating value HHV_i of the final product stream is taken constant. The heating value defines the amount of energy in the fuel (here, either CO or syngas). The heating value for a product stream of 80 000 $t_{CO}\,a^{-1}$ calculates to 808 900 $MJ\,a^{-1}$. From this value, the amount of syngas to be produced is calculated as 45 200 $t\,a^{-1}$ (1:1) and 32 900 $t\,a^{-1}$ (2:1). The HHV_i for CO and H_2 is tabulated in Table A.5.

Capital costs

The capital costs are the sum of the capital costs of each process unit. The capital costs of the electrolyzer $CC_{electrolyzer}$ are calculated based on an investment cost analysis for a hydrogen fuel cell [Inst2013]. The bare module

costs $BC_{electrolyzer}$ of the electrolyzer are calculated per geometric electrode area and comprise cost for the electrodes, the ion exchange membrane, and surroundings, including aluminum end plates, bipolar graphite plates, and busbars for electricity supply. All parameters for calculating $BC_{electrolyzer}$ for each electrolyzer type are given in the Appendix.

$$CC_{electrolyzer} = BC_{electrolyzer} \cdot A_{geom} \tag{6.8}$$

Capital costs for the compressor $CC_{compressor}$ are estimated with Guthrie's method [Bieg1997; Guth1969]. This method allows the calculation of the bare module costs of the compressor $BC_{compressor}$ based on reference costs C_0 for the equipment with a reference compression duty S_0.

$$BC_{compressor} = C_0 \cdot \left(\frac{S}{S_0}\right)^{\alpha} \tag{6.9}$$

In this equation, S is the required compression duty determined in the optimization, and α is the scaling factor, which considers the economy of scale and is, therefore, lower than 1. The reference values and the scaling factor are taken from Biegler et al. [Bieg1997] and are tabulated in Table A.3. The capital costs of the compressor are then calculated to

$$CC_{compressor} = BC_{compressor} \cdot UF \cdot (MPF + MF - 1) \tag{6.10}$$

where UF is the update factor, MPF is the material and pressure factor, and MF is the module factor. UF takes into account the change in price level between 1969 and now. MPF and MF account for the material and size of the compressor.

The capital costs of the membrane module $CC_{membrane}$ are calculated based on the required membrane surface area A_{mem} and area-specific membrane module costs for polymeric membranes $BC_{membrane}$, listed in

Table A.3 [Zhao2009].

$$CC_{membrane} = BC_{membrane} \cdot A_{mem} \tag{6.11}$$

Capital costs for drying the electrolysis off-gas before compression are calculated using data for adsorptive drying from Scholz et al. [Scho2013a].

Operation costs

Operation costs include expenditure on utilities $OC_{utilities}$, i.e., energy and reactants, CO_2 emissions $OC_{emissions}$, replacement of electrolyzer and gas permeation membrane components $OC_{replacement}$, as well as maintenance costs $OC_{maintenance}$.

$$OC_{total} = OC_{utilities} + OC_{emissions} + OC_{replacement} + OC_{maintenance} \tag{6.12}$$

Energy is consumed in the electrolyzer and the compressor units. The utility costs for electrical energy $UC_{electricity}$ in the base case scenario are taken to 0.09 €/kWh. The utility costs for reactants UC_i comprise carbon dioxide and hydrogen from water electrolysis. Expenses for water are neglected. For the base case, a CO_2 price of 25 $/t is assumed, which is calculated for carbon capture from flue gas [Schn2011]. For the AEM electrolyzer, the ratio of recycling CO_2 from the anodic off-gas is a degree of freedom in the optimization. In the case of recycling, the expenses for purifying CO_2 from the anode are calculated in a surrogate model, which has been fitted to simulation results from optimization runs for different CO_2:O_2 ratios and flow rates. Costs for hydrogen are considered for the production of syngas. Hydrogen is produced in water electrolysis and implemented as a shortcut equation described in more detail in [Hess2023]. The ratio of purchased hydrogen from water electrolysis is optimized in this study. The operation costs for utilities are calculated to

$$OC_{utilities} = t_{year} \cdot (UC_{electricity} \cdot (P_c + P_{elec}) + UC_{CO_2} \cdot \dot{m}_{feed,CO_2} \tag{6.13}$$

$$+ UC_{H_2} \cdot \dot{m}_{water\ electrolysis,H_2}) \tag{6.14}$$

In this equation, t_{year} is the annual operation time of the plant, and $\dot{m}_{feed,CO_2}$ and $\dot{m}_{water\ electrolysis,H_2}$ are the required mass streams of CO_2 in the feed of the CO_2 electrolyzer and H_2 from water electrolysis, both calculated in the optimization.

As CO_2 is separated from the desired product but not fully recycled, additional costs for the emission of purged CO_2, $\dot{m}_{purge,CO_2}$, need to be considered. Emission costs are also considered for the processes with an AEM electrolyzer, where CO_2 is not recovered from the anodic off-gas. Emitters of CO_2 need to buy certificates from the European Union to release carbon dioxide to the environment. The CO_2 certificate price EC_{CO2} assumed in this study is 25 €/t.

$$OC_{emissions} = EC_{CO2} \cdot \dot{m}_{purge,CO_2} \cdot t_{year} \tag{6.15}$$

The operation costs also consider the replacement of the electrodes, the ion exchange membrane, and the gas permeation membrane. The lifetime, $t_{lifetime}$, of the electrodes and ion exchange membrane, is taken to 2.5 years [T Sm2011]. After this operation period, the parts have to be exchanged. For the gas permeation membranes, a lifetime of 5 years is assumed [Zhao2009]. The replacement costs are summed up over the plant lifetime, t_{plant}, of 20 years and then depreciated per year.

$$OC_{replacement} = d_{year} \cdot t_{plant} \cdot \left(\frac{1}{t_{lifetime,electrolyzer}} \cdot (BC_{IEM} + BC_{catalyst}) + \frac{1}{t_{lifetime,membrane}} \cdot BC_{membrane}\right) \tag{6.16}$$

Maintenance of the components of the CO_2 electrolyzer and the gas per-

meation membrane process is assumed to be 2.5% of the total capital costs depreciated per year.

6.3. Results and discussion

The following section first presents operation costs for electrochemical CO and syngas production using the AEM, BPM, and CEM electrolyzer configurations. Then, the sensitivity of economics of electrochemical CO_2 conversion to CO is examined. Lastly, the CO_2 pumping effect in AEM electrolyzers is assessed.

6.3.1. Electrochemical membrane reactor configuration for CO and syngas production

The specific production costs for CO using the AEM electrolyzer, as shown in Figure 6.3, are 796 €/t_{CO} and lower than those using the BPM and CEM reactor with 837 €/t_{CO} and 1 071 €/t_{CO}, respectively. The CO prices from conventional state-of-the-art production processes reported in the literature range from 522 €/t_{CO} to 1 070 €/t_{CO} [Joun2018; Verm2016a]. Thus, the CO_2 electrolysis processes considered in this study already achieve competitive CO production costs. The electrolyzer is the main cost driver in CO production and constitutes 75% - 84% of the total production costs. Similar values are reported in the literature [Shin2021]. The costs for electrolysis are mainly responsible for the cost difference between the three electrolyzer configurations and are the lowest for the AEM electrolyzer.

Table 6.1.: Key operational parameters of the electrolyzer in the base case scenario.

Parameter	AEM	BPM	CEM	Unit
Current density	230	70	58	$mA\,cm^{-2}$
Cell voltage	3.0	2.8	3.0	V
CO Faradaic efficiency	95	89	82	%
Per-pass conversion	20	20	20	%
Anodic CO_2:O_2 ratio	2:1	-	-	-

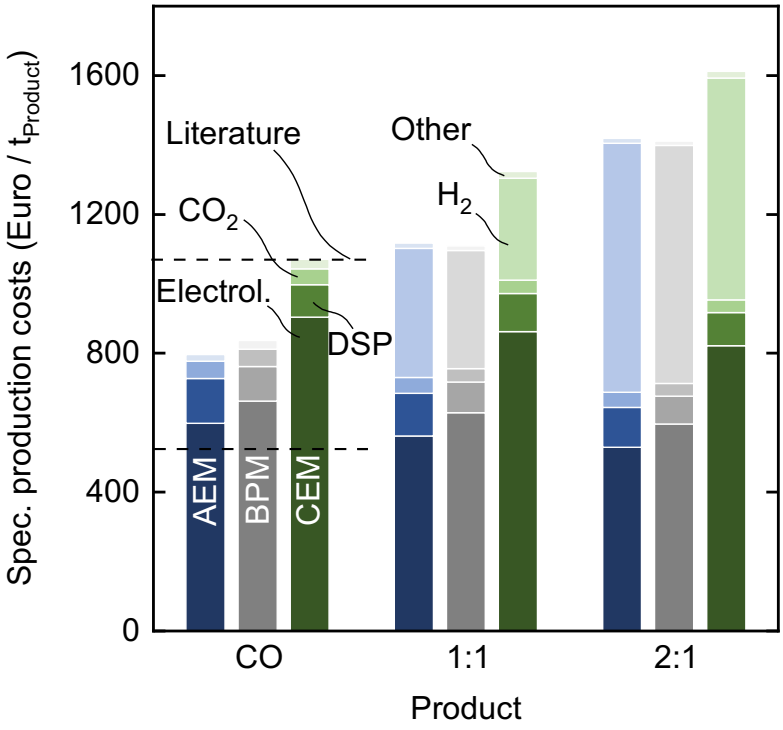

Figure 6.3.: Specific production costs for the different reactor configurations and products CO and syngas (1:1, 2:1), respectively. The costs are divided into expenditure for the electrolysis process (Electrol.), the downstream processing (DSP), the reactants CO_2 and H_2, as well as other process-related expenditures like CO_2 emission costs and costs for deionized water. The electrolysis and the downstream processing expenses comprise investment, operational, replacement, and maintenance costs. The dashed lines represent CO prices from the literature [Joun2018; Verm2016a].

The expenditures for separating the product gases are slightly higher for the AEM reactor, making up 16% of the total production costs. The higher downstream processing costs are attributed to the additional separation of the anodic off-gas due to the crossover of CO_2, which is about 8% of the total production costs. The optimized flowsheet presented in Figure 6.3 assumes a CO_2:O_2 ratio of 2:1 in the anodic gas outlet stream of the AEM electrolyzer, which means that the crossover of CO_3^{2-} dominates. In the base case scenario, the optimization results that it is more economical to recycle CO_2 with a purity of $\geq$ 98% than emitting it as shown in the process flowsheet of the CO production process using the AEM electrolyzer in Fig-

ure 6.4. A similar share of anodic downstream processing costs of approx. 6% was also reported by Shin et al. [Shin2021].
The flowsheets for the BPM and CEM electrolysis processes for CO production are presented in Figure A.2 and Figure A.3. At the operation point of the BPM and CEM electrolyzers, listed in Table 6.1, the Faradaic efficiency of CO is about 89% and 82%, respectively. Thus, substantial amounts of H_2 are co-produced but not purified and are not considered an additional valuable product when pure CO is the target product. In future work, implementing a second objective function - the minimization of H_2 production costs - could improve the economics of the BPM and CEM electrolysis processes and make them more competitive.

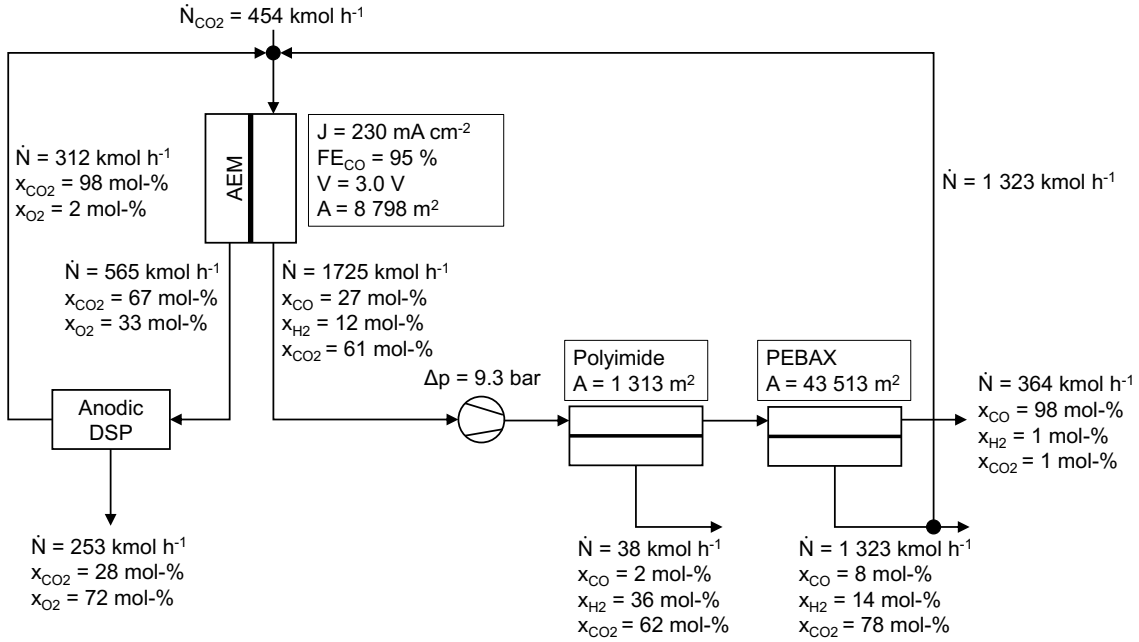

Figure 6.4.: Flowsheet of electrochemical CO production using an AEM electrolyzer for the base case scenario. The water removal unit is not shown in the flowsheet, as only the water removal costs are considered. The anodic downstream processing is only shown as a block because it is not modeled rigorously in the overall process flowsheet but is considered as a surrogate model. The gas permeation membrane materials used in the process are Polyimide and PEBAX.

In the optimized flowsheets, the permeate stream of the second membrane step is mainly recycled into the gaseous feed of the electrolyzer. The mole fraction of CO_2 in the feed thereby decreases to about 70 mol-%, e.g., for producing pure CO using a BPM electrolyzer. In this work, it is

assumed that the decreased CO_2 feed fraction does not have an impact on the electrochemical CO_2 reduction, which is valid for CO_2 fractions between 60 mol-% and 100 mol-% as shown by Kim et al. [Kim2015] At higher potentials, as considered in the work of Kim et al., a further decrease in the CO_2 feed fraction, however, would lower the production rate of CO due to mass transport limitations [Hess2022]. In future work, more rigorous models of the electrolysis process need to be implemented in the optimization model to consider the detrimental effect of decreasing CO_2 feed fractions at high current densities.

For the production of syngas with ratios of 1:1 and 2:1, the process using the BPM electrolyzer shows the lowest specific production costs with 1 111 €/t_{syngas} and 1 411 €/t_{syngas}, respectively. The respective flowsheets of the two processes are given in Figure 6.5 and Figure 6.6. Low downstream processing expenditures and costs for additional H_2 result in lower production costs compared to the AEM and CEM electrolyzer when using the BPM electrolyzer. However, the AEM electrolysis process costs are in a similar range. For both syngas products, the costs for electrolysis with the CEM configuration strongly dominate due to a high cell voltage and large electrode areas needed, even though more H_2 is produced in the CEM electrolyzer than in the other two. The specific production costs and the flowsheets of the BPM electrolysis processes show that most of the H_2 contained in the syngas is purchased from water electrolysis: For syngas with a ratio of 1:1, approx. 87% of H_2 in the final product is produced from water electrolysis. The amount of purchased H_2 is even higher for the 2:1 ratio (93%). The same applies to the other electrolyzer configurations shown in Figure A.4 - Figure A.7. In turn, the CO_2 electrolyzer is operated at a point where mostly CO is produced in syngas production. These findings emphasize that CO_2 electrolysis should be used and optimized for CO production only and not for the co-production of CO and H_2. For syngas production, a combination with water electrolysis is economically more promising.

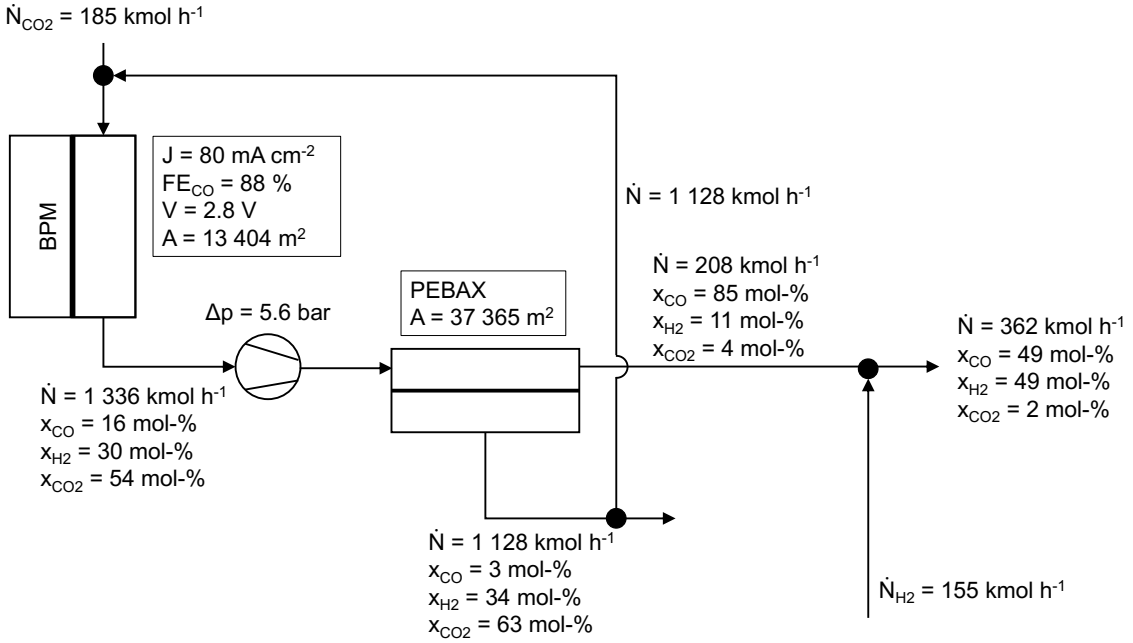

Figure 6.5.: Flowsheet of electrochemical syngas (ratio 1:1) production using a BPM electrolyzer for the base case scenario. The water removal unit is not considered in the flowsheet, as only the costs for water removal are taken into account. The gas permeation membrane material used in the process is PEBAX.

The electrolyzer constitutes 39% - 69% of the overall capital expenditures (CAPEX) for the AEM and CEM electrolyzer in CO production, as shown in the left graph in Figure 6.7. The wide range is mainly attributed to the different operating current densities of 230 mA cm^{-2} and 58 mA cm^{-2} as identified in the holistic optimization as a trade-off between CAPEX and operational expenditures (OPEX). The lower current density leads to a significantly larger electrolyzer area for the CEM configuration to achieve the required production rate. Compared to CO production, the decrease in the expenses for the production of syngas is attributed to the lower production capacity and purity of CO from CO_2 electrolysis and the lower effort for downstream processing as the total product flow rate decreases when keeping the heating value of the product stream constant. The distribution of investment costs between the electrolysis and downstream processing are similar for the different products.

The right graph in Figure 6.7 shows that the OPEX for the electrolysis

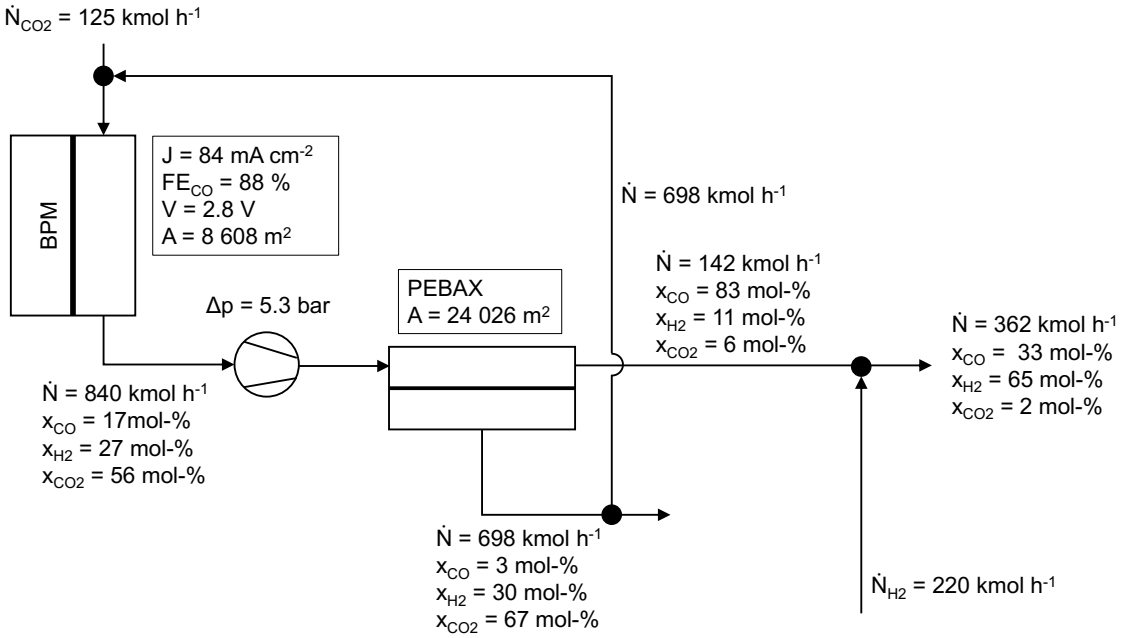

Figure 6.6.: Flowsheet of electrochemical syngas (ratio 2:1) production using a BPM electrolyzer for the base case scenario. The water removal unit is not considered in the flowsheet, as only the costs for water removal are taken into account. The gas permeation membrane material used in the process is PEBAX.

dominates. The OPEX of the AEM and BPM processes are similar. The main cost driver of electrolysis is the electricity demand. The electricity costs account for 92% and 75% of the electrolysis-related OPEX for the AEM and CEM electrolyzer, respectively. The share of electricity costs is lower for the CEM electrolyzer even though the electricity demand is more significant (60 MW for AEM and 70.4 MW for CEM). The increased electricity demand is attributed to the worse energetics of the CEM compared to the AEM and BPM electrolyzer. The underlying experimental data for the AEM (Liu et al. [Liu2018]) and BPM (Salvatore et al. [Salv2017]) electrolyzer were generated in a zero-gap cell assembly, whereas a one-sided buffered cell design was chosen for the CEM electrolyzer (Vennekötter et al. [Venn2019a]). As the acidic environment of the CEM promotes hydrogen evolution reaction (HER) at the cathode, the buffer layer is typically necessary between the cathode and the membrane [Ma2017; Venn2019a]. The buffer layer causes additional ohmic losses, which lead to increased electricity demand. Even though some studies show that CO_2 reduction may work in an acidic or zero-gap assembly with CEM, the performance is not

yet on the level of AEM characteristics in terms of faradaic efficiency and cell voltage [Mont2021; Huan2021; Xie2022c; Hua2022; Pan2022]. The remaining electrolysis-related OPEX are attributed to replacement costs, which have an increased influence on the economics of the CEM electrolysis process. IrOx needs to be used as an anode catalyst in the AEM and CEM configuration because of the neutral to acidic pH in the anolyte [Vass2022]. The use of the noble catalyst material results in increased electrolyzer replacement costs, which are even more pronounced for the CEM electrolyzer due to the large electrode areas that need to be replaced. Thus, these costs show a more significant contribution (8%) to the electrolysis-related OPEX compared to the BPM electrolysis process (1.6%).

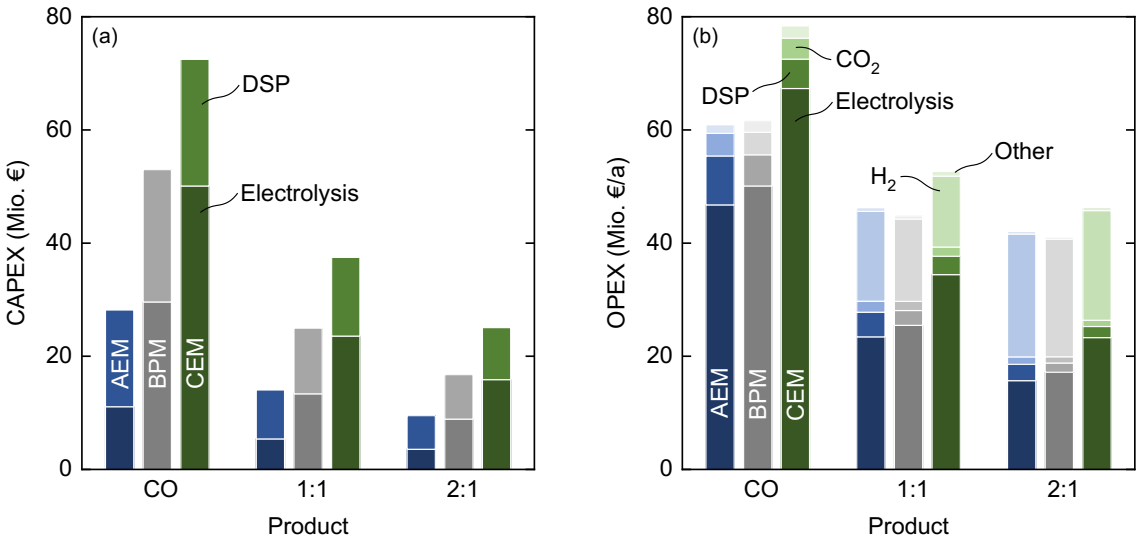

Figure 6.7.: (a) CAPEX and (b) OPEX for the different reactor configurations and production of CO and syngas (1:1, 2:1), respectively. The heating value is kept constant for the three products. The CAPEX comprises investment costs for CO_2 electrolysis and costs for downstream processing. In this study, H_2 from water electrolysis is purchased and only considered in the OPEX. The OPEX comprises expenses related to the electrolysis, the downstream processing, the reactants CO_2 and H_2, and other operation-related expenditures. The electrolysis and downstream processing OPEX include electricity costs and component replacement. Minor expenditures, i.e., costs for deionized water and maintenance, are summed up to other process-related costs. A more detailed overview of the different cost contributors is specified in the methodology section.

6.3.2. Sensitivity analysis in holistic process optimization

The previous results highlight that electrochemical CO_2 reduction should be applied and optimized for the selective electroreduction of CO_2 to CO and not for the co-electrolysis to syngas. Therefore, the following results and discussion focus on the production of pure CO only. Attributed to the low maturity level of electrochemical CO_2 reduction technology and the associated uncertainty of technical end economic parameters, the sensitivity of the production costs towards changes in the most relevant influencing factors is assessed. The process flowsheet and operation point are optimized for each scenario in Table 6.2.

Table 6.2.: Economic and technical parameters considered in the sensitivity study.

Parameter	Worst case	Base case	Best case	Unit
Electricity price	0.135	0.09	0.045	€/kWh
Bare electrolyzer costs	+30	0	-30	%
CO_2 feedstock price	45	22	0	€/t_{CO2}
CO_2 certificate price	50	25	0	€/t
Cell voltage	+40	0	-40	%
Faradaic efficiency CO	-20	0	+20	%
Per-pass conversion	10	20	30	%

The most significant influence on the specific production costs in Figure 6.8 is seen for a change in electricity price: The electricity price of the basic scenario is assumed to be 0.09 €/kWH according to the German industry electricity price from 2017 [BMVi]. The price variation by + 50% covers the expected German industry electricity price of 2030, assuming the phase-out of coal-fired power generation [Gier]. The lower limit of -50% is, e.g., reached by Norway, whose electricity production is mainly based on hydropower [IEA]. The change in electricity costs affects both the CO_2 electrolysis and the downstream processing. However, due to the minor contribution of the downstream processing costs to the overall production costs, as presented in Figure 6.3, the significant sensitivity towards the electricity price is mainly attributed to the electrolysis process. The electricity costs for the AEM, BPM, and CEM electrolysis processes account for 67.5%, 63.8%, and 59.1% of the specific production costs. The

impact of the electricity price on the AEM electrolysis process is slightly more pronounced compared to the BPM and CEM process configurations due to the higher share of electricity costs for the AEM electrolyzer, as mentioned before. However, despite the significant contribution of electricity costs to the production costs of the AEM electrolysis process, the absolute production costs are still comparatively low due to the superior energetics of the electrolyzer.

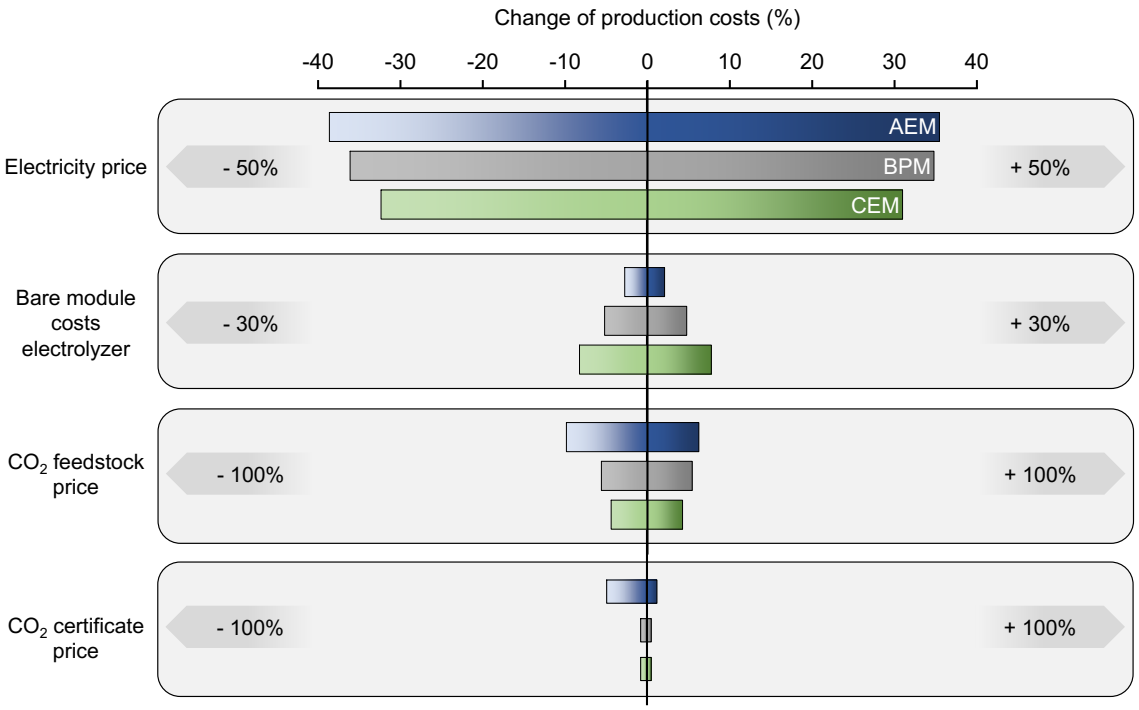

Figure 6.8.: Sensitivity of the different reactor configurations for CO production towards a change in economic parameters.

The bare module costs of the electrolyzers have been calculated based on material costs for the main components, i.e., the electrode catalysts, the ion exchange membrane, the housing, and the periphery. In the basic scenario, the costs are calculated to 1 050 €/m^2 for the AEM, 780 €/m^2 for the BPM, and 1 030 €/m^2 for the CEM electrolyzer configuration. These costs are in a comparable range to those reported in the literature [Verm2016a; Li2016; Joun2018]. When varying the bare module costs between -30% and +30%, the specific production costs respond nearly

linearly to the change, as shown in Figure 6.8. The CEM electrolyzer process configuration shows the highest sensitivity toward electrolyzer investment costs. Intuitively, an increase in electrolysis capital costs would be compensated by decreasing the electrode area. That, in turn, increases the current density of the electrolyzer to maintain the desired production capacity of the plant. Such a relationship can be seen for the AEM electrolyzer in Figure A.8, where the change in the bare module costs is compensated by the change in electricity costs due to the variation of the operation point, i.e., the current density. Consequently, the specific production costs show negligible sensitivity to the capital costs of the electrolyzer. However, due to the poor energetics of the CEM electrolyzer, the electrode area and the current density are only varied slightly by the optimizer for a change in bare module costs. Therefore, the capital expenditures for the electrolysis are only partially balanced, leading to higher and lower production costs when increasing and decreasing the bare module costs, respectively.

The sensitivity of specific production costs towards the CO_2 price and the CO_2 emission costs behave similarly. Production costs using the BPM and CEM electrolyzer exhibit a nearly linear change. The impact of the CO_2 price is more pronounced than the one of CO_2 emission costs because of the larger contribution to the overall production costs, as shown in Figure 6.3. The optimizer does not vary the operation point of the electrolyzer for the different scenarios in both sensitivity parameters. However, an increase in the CO_2 price or the CO_2 emission costs increases the overall CO_2 utilization rate, meaning less loss of CO_2 in the downstream processing. The CO_2 utilization rate is the share of CO_2 in the feed gas that is converted to the final product CO. Between the worst case scenario and the best case scenario of the CO_2 price, the CO_2 utilization rate varies between 90% - 85% for the BPM and 87% - 81% for the CEM electrolyzer (same values for the CO_2 emission costs). The change in utilization rate is mainly attributed to the amount of CO_2 that is lead out in the permeate stream of the first gas permeation membrane step. When increasing the

CO_2 price or the CO_2 emission costs, the membrane is scaled down by the optimizer, and so is the CO_2 flux through the membrane. The non-linear trend in the AEM electrolysis process toward the CO_2 price and the CO_2 emission costs is attributed to a change in the process flowsheet: At a certain point for decreasing CO_2 prices and CO_2 emission costs, the anodic off-gas is not separated anymore but emitted to the environment. The change in treating the off-gas leads to a more pronounced decrease in the CO production costs because additional costs for the anodic downstream processing are omitted.

The electrolysis process contributes most to the overall process cost and reacts most sensitively to changes in economic parameters. Hence, further optimization of the electrolyzers is required. Figure 6.9 therefore shows how the change of relevant technical electrolysis parameters influences process economics.

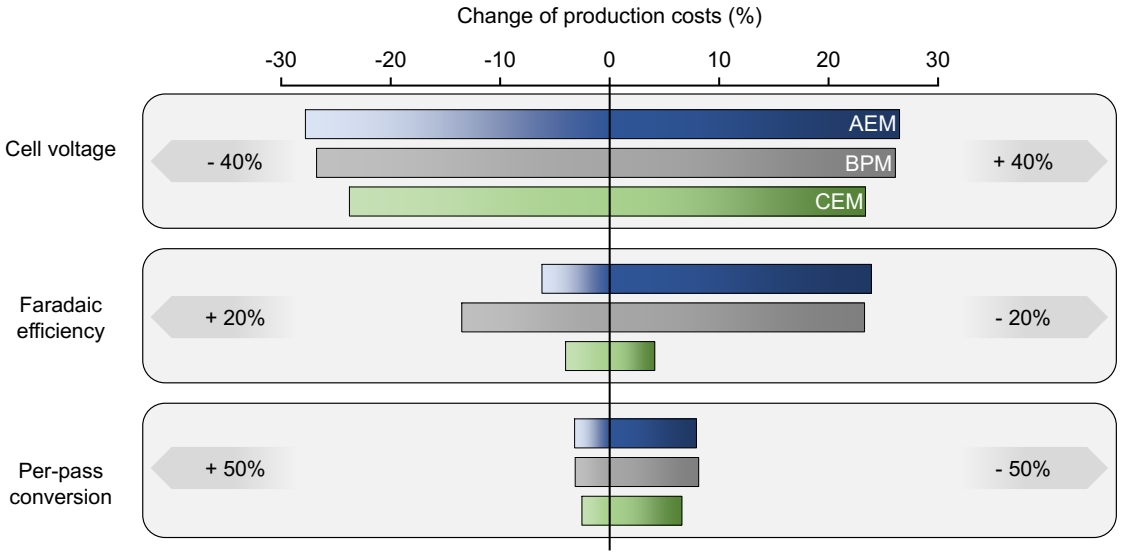

Figure 6.9.: Sensitivity of the different reactor configurations for CO production towards a change in technical parameters of the electrolyzer.

In the sensitivity study of the cell voltage, the output data of the regression models, i.e., the polarization plots, are shifted by +/- 40% from the base case scenario plots. The cell voltage significantly influences

the CO production costs. The expenditures for electricity consumption of the electrolyzer are the main contributor to the specific production costs. Furthermore, cell voltage variations solely affect the operation of the electrolyzer but not the downstream processing when keeping the product requirements constant. Therefore, the sensitivity trend in the tornado chart towards the cell voltage is fairly linear. Moreover, due to the high share of electricity costs for electrolysis in the production costs with the AEM electrolyzer process, the change in cell voltage shows a more pronounced influence. The operation point of the AEM electrolyzer changes from 230 $mA\,cm^{-2}$ (3 V) to 405 $mA\,cm^{-2}$ (1.9 V) and 158 $mA\,cm^{-2}$ (4 V) in the best and worst case scenarios, respectively. Thereby, the electricity demand increases from the best to the worst case scenario from 38 MW to 80 MW, and the electrode size increases from 5 000 m^2 to 12 800 m^2.

The CEM electrolyzer process shows the lowest sensitivity towards a change in Faradaic efficiency for CO. Even though in the best-case scenario, the CEM electrolyzer is allowed to operate at a point with Faradaic efficiencies for CO of up to 89% at current densities below 40 $mA\,cm^{-2}$, the operation point of the electrolyzer is not varied significantly from the basic scenario (58 $mA\,cm^{-2}$ and 82% Faradaic efficiency for CO). In the worst and best case scenarios, the current density of the electrolyzer is optimized to 55 $mA\,cm^{-2}$ (79% Faradaic efficiency for CO) and 61 $mA\,cm^{-2}$ (85% Faradaic efficiency for CO), respectively. Thus, mostly energetics but also capital costs of the electrolyzer determine the operation point even when the Faradaic efficiency is improved.

In contrast, the AEM and BPM electrolysis processes are more susceptible to variations in the Faradaic efficiency. It must be noted that for the AEM and BPM electrolyzer, an increase of the Faradaic efficiency by approx. 5% and 12% already lead to an efficiency of 100%, resulting in a nonlinear trend in the tornado charts. For the BPM electrolyzer, e.g., the operation point is optimized to 70 $mA\,cm^{-2}$ (71% Faradaic efficiency for CO) and 111 $mA\,cm^{-2}$ (100% Faradaic efficiency for CO) in the worst and best case scenario, respectively. In the worst case scenario, the

current density is not changed significantly compared to the base case scenario (68 $mA\,cm^{-2}$ and 89% Faradaic efficiency) as higher current densities would lead to even lower Faradaic efficiencies and also higher cell voltages. However, larger electrode areas are needed at the lower current density to achieve the required production capacity. Hence, the energy demand of the electrolyzer increases from 60 MW in the base case to 75 MW in the worst case. The expenses for the downstream processing also increase between the base and worst scenarios by 44%. At large, the increase in electrolysis and separation costs leads to the strong influence of Faradaic efficiency on production costs. Consequently, improvements in mass transport of CO_2 to the catalyst sites and suppression of the HER in BPM electrolyzers, by, e.g., modification of the gas diffusion electrode using functional ionomers as presented by De Arquer et al. [De A2020], could improve the process economics. Most AEM electrolyzers reported in the literature already reach high Faradaic efficiencies for CO production because of the alkaline environment at the cathode and the resulting absence of H^+ ions [Liu2018; Yin2019; Larr2019; Xu2021]. The strong sensitivity when decreasing the Faradaic efficiency, however, underlines the importance of investigating and optimizing long-term stability in AEM electrolyzers to maintain a constant operating point. Xu et al. [Xu2021], e.g., presented a self-cleaning strategy by periodic operation of the electrolyzer and were able to operate at constant Faradaic efficiency for more than 157 h. Furthermore, Petrov et al. [Petr2022] showed that casting membranes with internal micro channels significantly improves water management and potassium crossover, increasing energy efficiency and long-term stability of CO_2 electrolyzers.

The per-pass conversion of CO_2 to CO is 20% in the base case scenario and is varied between 30% (+ 50%) and 10% (- 50%). The variation of the per-pass conversion causes a non-linear change in specific production costs with a more pronounced sensitivity to a decrease in the per-pass conversion than an increase. The lower per-pass conversion leads to a dilution of the cathodic gas stream and, when keeping the desired produc-

tion capacity constant, also to a larger gas flow rate in the downstream processing. The electrolyzer is not scaled, and the optimizer does not change the operating point when varying the per-pass conversion. Thus, the elevated specific production costs are mainly attributed to increased energy consumption in the compression and larger gas permeation membrane areas to separate CO_2. For the AEM electrolyzer, e.g., the share of costs for downstream processing in the overall production costs increases from 16% to 22% when changing the CO_2 per-pass conversion from 20% to 10%. Additionally, the CO_2 utilization rate decreases for the lowest per-pass conversion, e.g., from 85% to 73% for the CEM electrolyzer. Thus, larger expenditures for CO_2 emissions and replenishment need to be considered for lower CO_2 per-pass conversions.

Interestingly, an increase in the per-pass conversion to state-of-the-art values of around 20-30% reported by different groups [Jean2018; Bhar2020; Jeng2020] does not significantly improve the specific production costs. This is because when increasing the per-pass conversion, less unconverted CO_2 is in the downstream flow of the electrolyzer, thus lowering the CO_2 mole fraction and the total flow rate of the cathodic gas outlet stream. The lower flow rate reduces the downstream processing unit sizes, whereas the lower partial pressure of CO_2 in the downstream needs to be compensated by an increase in compression ratio to maintain a sufficient driving force for gas permeation. As the compressor is the main cost driver in the downstream processing, the trade-off between unit size and compression ratio mainly causes the non-linear behavior in Figure 6.9 when changing the per-pass conversion. To overcome this trend, alternative technologies for gas purification could be considered, e.g., absorption and adsorption.

The sensitivity toward the per-pass conversion is similar for all three electrolyzer configurations but with a slightly lower amplitude for the CEM electrolyzer due to a lower share of downstream processing costs in the production costs. It must be mentioned that a change in per-pass conversion is assumed not to affect the electrolysis process. However, in real systems, the per-pass conversion results from many influencing

factors, e.g., the CO_2 feed flow rate and composition, the electrolyte, the structure and composition of the gas diffusion electrode, and the temperature and pressure. Thus, changes in these parameters would also affect the operation of the electrolyzer and, therefore, expenditures for electrolysis. Furthermore, Jeng et al. [Jeng2020] showed that increasing the per-pass conversion by decreasing the CO_2 feed flow rate also increases the fraction of CO_2 being converted to carbonates. Thus, increased costs for the anodic downstream processing are expected.

In summary, the sensitivity study highlights three major influencing factors on the economics of the CO_2-to-CO electrolysis process: the electricity price, the cell voltage, and the Faradaic efficiency. Therefore, the future development in CO_2 electrolysis process needs to focus on decreasing the electricity demand of the electrolyzer as well as improving the reactant mass transport. The AEM electrolyzer configuration already shows promising results due to the energetically efficient zero-gap cell design and the favorable conditions at the electrode. However, a major obstacle often associated with the application of AEMs in CO_2 electrolysis is the HCO_3^- and CO_3^{2-} crossover, which leads to the evolution of CO_2 at the anode side [Rabi2020; Blom2021]. Therefore, the following section deals with this subject in more detail.

6.3.3. CO_2 crossover in AEM electrolyzers

The specific production costs in Figure 6.10 are the lowest for a CO_2:O_2 ratio of 0:1, at which no CO_2 evolves at the anode and no purification of the anodic off-gas or expenditure for CO_2 emission costs is required. The costs increase by approx. 8.5% when CO_3^{2-} becomes the dominant permeating species, indicating that the expenditures for the anodic downstream processing do not contribute significantly to the overall process costs, as mentioned before. When the CO_2:O_2 ratio changes from 2:1 to 4:1 for HCO_3^- crossover, the specific production costs do not increase significantly. In the anodic downstream processing, CO_2 is concentrated

in the permeate of the two-step membrane gas permeation process. As gas permeation is a partial pressure-driven process, increasing the concentration of the faster-permeating component in the feed results in a higher driving force for separation. Hence, the expenditures for purification of the anodic off-gas only increase slightly because of the higher flow rate of CO_2, which evolves at the anode. Simultaneously, the CO_2 utilization of the overall process decreases from 92% to 79% and 75% when CO_3^{2-} and HCO_3^- become the dominant permeating species in the AEM. Therefore, the lower CO_2 utilization for the case of CO_2 evolution at the anode is attributed to the higher loss of CO_2 in the anodic downstream processing. In summary, CO_2 pumping does not significantly impair the economics of the AEM-based process. Also, the loss of CO_2 in the anodic off-gas is beneficial even for the highest CO_2:O_2 ratio. Moreover, the recovery of gaseous CO_2 from CO_3^{2-} and HCO_3^- crossed over the AEM implies an additional advantage over the BPM and CEM electrolyzers.

Rabinowitz et al. [Rabi2020] discuss the problem of CO_2 loss via carbonate formation in low-temperature CO_2 electrolysis. The energy needed to regenerate CO_2 from CO_3^{2-} in the liquid electrolyte is ideally 56 $kJ\,mol_{CO2}^{-1}$ ($|\Delta G^0|$), but realistically >230 $kJ\,mol_{CO2}^{-1}$ [Rabi2020; Keit2018]. For the BPM and CEM electrolyzer, where CO_3^{2-} is transported out of the electrolyzer in the catholyte outlet, the additional energy penalty for regeneration of CO_2 from CO_3^{2-} needs to be considered. In the AEM electrolyzer, CO_3^{2-} is assumed to be the dominant ion transferring across the ion exchange membrane in the considered current density range and for long operation times [Larr2019; Ma2020a]. CO_3^{2-} is protonated to CO_2 at the anode and leaves the electrolyzer. As more than 80% of the CO_2 evolving at the anode is recycled to the cathode, CO_3^{2-} is thereby indirectly regenerated. However, an additional energy penalty needs to be considered for the protonation of CO_3^{2-} at the anode side, which leads to a shift in pH and, thus, an increase in the OER overpotential [Parr2014]. The increased overpotential is already included in the experimental data, which is used to fit the regression model of the electrolyzer. The energy required to sepa-

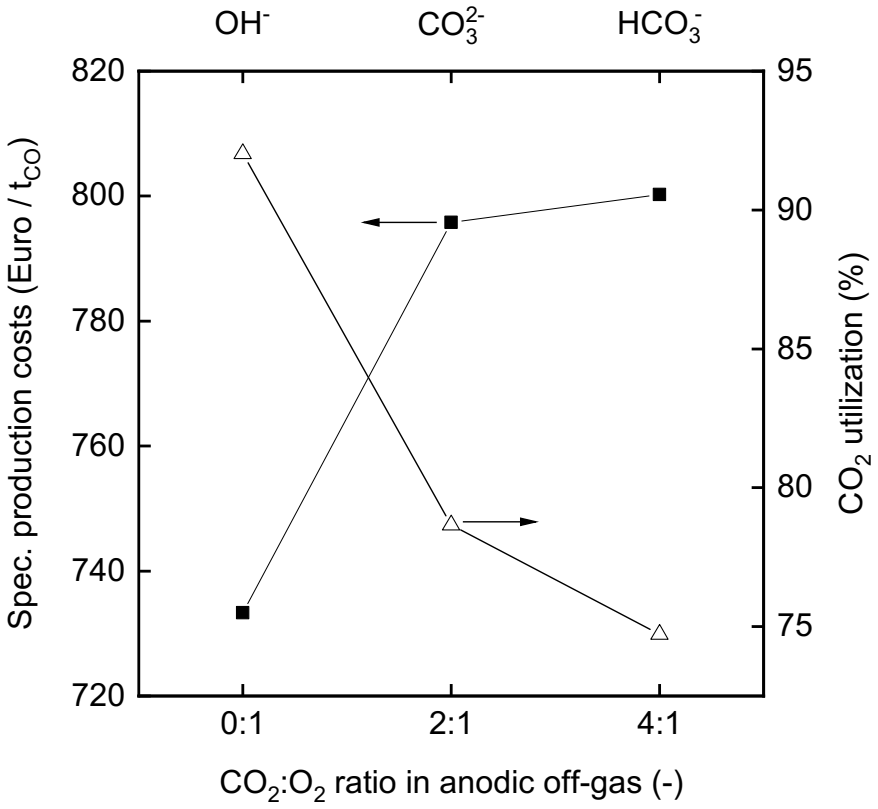

Figure 6.10.: Specific production costs and CO_2 utilization rate for an AEM electrolyzer and the production of CO at different CO_2:O_2 ratios in the anodic off-gas. The different CO_2:O_2 ratios result from the crossover of either OH^-, CO_3^{2-}, or HCO_3^-.

rate CO_2 from O_2 in the anodic off-gas using membrane gas permeation is calculated to be 22 $kJ\,mol_{CO2}^{-1}$. Table 6.3 compares the specific energy demand for the separation of CO_2 and O_2 to the literature. The thermodynamically required energy for separating the gas mixture is 2.3 $kJ\,mol_{CO2}^{-1}$. Alerte et al. [Aler2021] report a value of 2 501 $kJ\,mol_{CO2}^{-1}$ for the anode gas separation using amine absorption. The enormous energy demand results from the high heating duty in the amine regeneration. Therefore, amine scrubbing might not be a suitable technology for the anodic off-gas separation because (1) it is usually not applied for CO_2 fractions >25% and (2) certain amines tend to degrade when brought in contact with O_2 [Roch2009; Lepa2011]. Shin et al. [Shin2021] employed pressure swing adsorption for the separation of a 1:1 mixture of CO_2 and O_2. Their shortcut

calculation results in an energy demand of 1.3 $kJ\,mol_{CO2}{}^{-1}$ which is less than the absolute standard Gibbs free mixing energy of 3.4 $kJ\,mol_{CO2}{}^{-1}$, calculated from Aspen Plus V11. The contradiction highlights the importance of more rigorous consideration of the separation process.

Table 6.3.: Comparison of the specific energy demand for separating the anodic off-gas compared to literature and the ideally required Gibbs free energy of mixing.

	Ideal	Our work	Alerte et al. [Aler2021]	Shin et al. [Shin2021]
Separation technology	-	Gas permeation	Amine absorption	Pressure swing adsorption
CO_2:O_2 ratio	2:1	2:1	2:1	1:1
Energy demand ($kJ\,mol_{CO2}{}^{-1}$)	2.3	22.2	2 501	1.3
Comment	Calculation in Appendix	Base case	Without heat integration	Based on shortcut calculation method

In summary, the indirect regeneration of CO_2 from the electrolyte by the ionic crossover of carbonate and subsequent separation of the anodic off-gas using membrane gas permeation is energetically more favorable than regenerating CO_2 directly from the electrolyte by, e.g., a calcination cycle [Keit2018]. Thereby, the CO_2 pumping effect is a cost saver than a cost killer, as often described. Moreover, even higher energy efficiency and better economics could be achieved when using a liquid-to-liquid anode reaction without oxygen evolution, as demonstrated by Xie et al. [Xie2022b].

6.4. Conclusion

A process model was developed to optimize the electrochemical production of CO and syngas, including downstream processing of the respective

product gases by membrane gas permeation. This study compares the three ion exchange membranes used in low-temperature CO_2 electrolysis: anion exchange membrane, bipolar exchange membrane, and cation exchange membrane. The results indicate that the AEM-based electrolyzer is best suited for CO production due to low electricity costs and capital costs for the electrolyzer. The calculated CO production costs of around 796 €/t_{CO} are already competitive with reported market prices for CO. Most surprisingly and against the often ascribed detriment, this work showed that the CO_2 pumping effect in the AEM electrolyzer does not significantly impair the economics of the process. Quite the contrary, the release of CO_2 at the anode and the subsequent separation and recycling using gas permeation offers an efficient indirect regeneration of HCO_3^- and CO_3^{2-}. Future work, therefore, needs to focus on elucidating the energetics and long-term stability of this operation mode. The BPM electrolyzer configuration shows the lowest production costs for syngas with H_2:CO ratios of 1:1 and 2:1, mainly attributed to the lower costs for additional H_2 production from water electrolysis. The holistic optimization reveals that the process for syngas production is economically more promising when H_2 is purchased from water electrolysis and not co-produced with CO in the CO_2 electrolyzer. Thus, electrochemical membrane reactors for CO_2 reduction to CO need to be optimized for the selective synthesis of CO and not for the co-electrolysis to syngas. This finding is also supported by the strong sensitivity of production costs to changes in Faradaic efficiency, as demonstrated in the sensitivity study. Moreover, the results highlight membrane-based gas separation as a suitable technology for downstream processing in electrochemical CO_2-to-CO conversion. The low costs of polymeric membrane modules, the variety of selective membrane materials, and the flexibility in flowsheet design offer advantages compared to other conventional separation technologies.

7. Conclusion and Outlook

Electrochemical CO_2 reduction plays a crucial role in mitigating climate change by converting carbon dioxide into valuable products, offering a sustainable approach to reducing greenhouse gas emissions. This technology holds the potential to create a closed-loop carbon cycle, enabling the production of clean fuels and chemicals while simultaneously reducing the reliance on fossil fuels.
Within this work, mathematical modeling of electrochemical CO_2 reduction has been applied on different length scales of the process to identify its current bottlenecks for industrial realization and derive pathways to overcome these hurdles. Referring to the sub-questions derived in Chapter 1, the following answers can be concluded from this thesis:

Sub-question no. 1:

How to control the local electrode environment to improve conditions for electrochemical CO_2 reduction?

Sub-question no. 1 was approached by implementing a one-dimensional transient model of the boundary layer at a planar plate electrode accounting for species size-dependent transport in the domain. Two important control knobs were investigated to steer activity and selectivity of the electrochemical CO_2 reduction to CO, i.e., the boundary layer thickness and the electrolyte concentration. Decreasing the boundary layer thickness by improving the hydrodynamics at the electrode significantly improves the reduction rate of CO_2 due to enhanced reactant mass transport. Interestingly, the effect on removing of CO_3^{2-} and HCO_3^- with improved hydrodynamics is less pronounced. The simulation results also highlight the importance of modulating the electrolyte concentration. On the one hand, high $KHCO_3$ concentrations reduce the cathodic overpotential and help to buffer the pH in the boundary layer, thus improving the electrochemical CO_2 conversion. However, high electrolyte concentrations also pose a risk for salt precipitation due to CO_3^{2-} and HCO_3^- at the electrode vicinity. The concentration of K^+ at the electrode surface, which has a beneficial effect on the CO_2 reduction reaction, was found to be independent of the $KHCO_3$ concentration

within the studied regime. The reported model allows for an accurate representation and investigation of mass transport and reaction phenomena happening in the near-electrode environment but also raises the need for more advanced electrode structures.

Sub-question no. 2:

How to exploit the advantages of gas diffusion electrodes in CO_2 electrolysis?

To tackle this question, a one-dimensional steady-state gas diffusion electrode (GDE) model was developed to analyze the electrochemical reduction of CO_2 to CO in a continuous flow-through reactor. The model considers various aspects such as gas diffusion, electrolyte properties, electrode wetting, flow conditions, mass transport, and electrochemical reactions. The simulations reveal that increasing the concentration of $KHCO_3$ electrolyte improves the CO_2 reduction process by enhancing ionic conductivity and buffering of OH^- ions. High electrolyte flow rates facilitate carbonate ion removal, reducing the risk of salt precipitation. The gas flow rate affects diffusion and helps to overcome solubility limitations of CO_2, with a trade-off between CO production rate and product purity. The porosity and catalyst loading of the cathode influence gas-phase transport and CO_2 reduction, emphasizing the importance of optimal design. The insights gained from this study can contribute to the advancement and commercialization of CO_2 reduction processes by guiding operation improvements and electrode structure tailoring.

Sub-question no. 3:

How to model industrial scale electrolyzers and optimize their operation?

To address sub-question no. 3, a multi-scale modeling approach was developed. This proof of concept study demonstrates the use of artificial neural networks (ANNs) to efficiently model electrolyzer components for electrochemical CO_2 reduction at a relevant scale. By training an ANN

with data generated from a comprehensive continuum GDE model, the ANN successfully mimics the behavior of the GDE. Notably, the concentration of CO_2 in the bulk electrolyte increases along the channel height but reaches a stagnation point due to a declining driving force for gas-to-electrolyte mass transport. The partial pressure gradient along the gas channel is more prominent at elevated potentials with increased CO_2 consumption rates. Enhancing the gas flow rate can improve mass transport from the gas phase to the catalyst sites. However, optimizing mass transport in large-scale electrolyzers should consider downstream separation efforts for cost optimization.

Sub-question no. 4:

What is the optimal process design and operating point of CO_2 electrolysis from a holistic perspective?

A process model was developed to optimize the electrochemical production of CO and syngas, with downstream processing using membrane gas permeation. The study compares three ion exchange membranes (anion exchange (AEM), bipolar (BPM), and cation exchange membrane (CEM)) for low-temperature CO_2 electrolysis. The results indicate that AEM-based electrolyzers are best suited for CO production due to low electricity and capital costs, with competitive CO production costs. The pumping effect of CO_2 in the AEM electrolyzer does not significantly affect the process economics; instead, it offers efficient regeneration of HCO_3^- and CO_3^{2-}. Further research should, therefore, focus on the energetics and long-term stability of this operation mode. The BPM electrolyzer configuration shows the lowest production costs for syngas production, primarily due to lower costs for additional H_2 production from water electrolysis. The optimization reveals that purchasing H_2 from water electrolysis, rather than co-producing it with CO in the CO_2 electrolyzer, is more economically promising. Hence, electrochemical membrane reactors for CO_2 reduction should be optimized for selective CO synthesis rather than co-electrolysis to syngas. Membrane-based gas separation is highlighted as a suitable technology for downstream processing, offering advantages in terms of

cost, variety of materials, and flexibility in design compared to conventional separation technologies.

This thesis highlights the importance of investigating and optimizing CO_2 electrolysis from a multi-scale and holistic point of view. With local reaction phenomena and charge transport processes at the electrode surface affecting mass transport within the electrode and the spatial reactant and product distribution in the electrolyzer and vice versa, interrelated multi-scale modeling approaches are necessary to get a comprehensive understanding of electrochemical CO_2 reduction. Furthermore, the profitability of the process not only depends on the electrolysis process but also its interplay with up- and downstream processing. Hence, process design and operation need to be assessed holistically. Therefore, future work needs to combine the presented models in this thesis to integrate the different length scales and parts of the electrochemical conversion process. Data-driven approaches, as introduced in Chapter 5, offer an efficient way to develop more comprehensive models for CO_2 electrolysis and should be pursued.

A. Appendix

Modeling and simulation parameters

Table A.1.: Modeling and simulation parameters used in modeling the electric double layer in Chapter 3.

Symbol	Value	Unit	Ref.
Global conditions			
T	298.15	K	-
$p_{CO_2,gas}$	1	bar	-
c_{KHCO_3}	0.1	M	-
Charge transfer reactions			
$i_{0,CO}$	$4.5 \cdot 10^{-3}$	A m^{-2}	-
i_{0,H_2}	$3.0 \cdot 10^{-3}$	A m^{-2}	-
α_{CO}	0.68	–	-
α_{H_2}	0.41	–	-
E^0_{CO}	-0.51	VvsSHE	[Newm2004]
$E^0_{H_2}$	-0.4	VvsSHE	[Newm2004]
E^{PZC}	-0.6	VvsSHE	
Electrolyte reactions			
$k_1 f$	$6.0 \cdot 10^6$	$mol^{-1}m^3s^{-1}$	[Burd2017]
$k_2 f$	2.23	$mol^{-1}m^3s^{-1}$	[Burd2017]
$k_3 f$	$2.4 \cdot 10^{-2}$	$molm^{-3}$ s^{-1}	[Sing2017; Sing2015; Atki2014]
$k_1 b$	$1.07 \cdot 10^6$	s^{-1}	[Burd2017]
$k_2 b$	$5.23 \cdot 10^{-5}$	s^{-1}	[Burd2017]

$k_3 b$	$2.4 \cdot 10^6$	$mol^{-1} m^3 s^{-1}$ [Sing2017; Sing2015; Atki2014]	
Diffusion coefficients			
D_{CO_2}	$1.91 \cdot 10^{-9}$	$m^2 s^{-1}$	[Newm2004]
D_{K^+}	$1.957 \cdot 10^{-9}$	$m^2 s^{-1}$	[Newm2004]
D_{H^+}	$9.311 \cdot 10^{-9}$	$m^2 s^{-1}$	[Newm2004]
D_{OH^-}	$5.273 \cdot 10^{-9}$	$m^2 s^{-1}$	[Newm2004]
$D_{HCO_3^-}$	$1.185 \cdot 10^{-9}$	$m^2 s^{-1}$	[Newm2004]
$D_{CO_3^{2-}}$	$0.923 \cdot 10^{-9}$	$m^2 s^{-1}$	[Newm2004]
Solvation sizes			
a_{CO_2}	$0.23 \cdot 10^{-9}$	m	[Bohr2019]
a_{K^+}	$0.662 \cdot 10^{-9}$	m	[Nigh1959]
a_{H^+}	$0.56 \cdot 10^{-9}$	m	[Nigh1959]
a_{OH^-}	$0.6 \cdot 10^{-9}$	m	[Nigh1959]
$a_{HCO_3^-}$	$0.8 \cdot 10^{-9}$	m	[Bohr2019]
$a_{CO_3^{2-}}$	$0.788 \cdot 10^{-9}$	m	[Nigh1959]
a_{H_2O}	$0.3 \cdot 10^{-9}$	m	[Nigh1959]
Hydration numbers			
w_{K^+}	4	–	[Bock1972; Bock1998]
w_{H^+}	10	–	[Bock1972; Bock1998]
Sechenov's constants			
$h^0_{CO_2}$	-0.0172	$m^3 kmol^{-1}$	[Weis1996]
$h^T_{CO_2}$	-0.000338	$m^3 kmol^{-1}$	[Weis1996]
h_{K^+}	0.0922	$m^3 kmol^{-1}$	[Weis1996]
h_{OH^-}	0.0839	$m^3 kmol^{-1}$	[Weis1996]
$h_{HCO_3^-}$	0.0967	$m^3 kmol^{-1}$	[Weis1996]
$h_{CO_3^{2-}}$	0.1423	$m^3 kmol^{-1}$	[Weis1996]

Table A.2.: Modeling and simulation parameters used in modeling a GDE in Chapter 4.

Symbol	Value	Unit	Ref.
Operating conditions			
T	298.15	K	-
p_{GC}	1	atm	-
q_{EC}	15.5	ml min^{-1}	-
q_{GC}	70	sccm	-
y_{in,CO_2}	0.95	–	-
Reactor geometry			
L_E	0.05	m	[Verm2016b]
d_E	0.02	m	[Verm2016b]
w_{EC}	$1.5 \cdot 10^{-4}$	m	[Verm2016b; Whip2010a]
w_{Ref}	$0.75 \cdot 10^{-4}$	m	[Verm2016b; Whip2010a]
w_{GC}	$3 \cdot 10^{-4}$	m	-
GDE properties			
L_{DM}	325	μm	[El-K2014]
L_{CL}	3	μm	Eqn. 4.28
$m_{loading}$	2	mg cm^{-2}	[Verm2016b]
d_{Ag}	100	nm	[Verm2016b]
ρ_{Ag}	10490	kg m^{-3}	[R L 2003]
$d_{p,CL}$	35	nm	-
$d_{p,DM}$	1467	nm	[El-K2014]
ϵ_{CL}	0.32	–	-
ϵ_{DM}	0.6	–	[Jhon2012]
$\sigma^{eff}_{s,CL}$	176	S m^{-1}	-
$\sigma_{s,DM}$	272.5	S m^{-1}	[El-K2014]
S	0.64	–	[Zeny2016]
Charge transfer reactions			
E^0_{CO}	-0.11	VvsSHE	[Newm2004]
$E^0_{H_2}$	0	VvsSHE	[Newm2004]
$i_{0,CO}$	$2.48 \cdot 10^{-3}$	A m^{-2}	-
i_{0,H_2}	$1.8 \cdot 10^{-4}$	A m^{-2}	-

α_{CO}	0.16	–	-
α_{H_2}	0.13	–	-
Electrolyte reactions			
K_1	$10^{-6.37}$	M	[Schu2006]
K_2	$10^{-10.25}$	M	[Schu2006]
K_3	$4.3 \cdot 10^7$	M^{-1}	[Schu2006]
K_4	$5.6 \cdot 10^3$	M^{-1}	[Schu2006]
K_W	10^{-14}	M^2	[Schu2006]
k_1	$3.71 \cdot 10^{-2}$	s^{-1}	[Schu2006]
k_2	59.44	s^{-1}	[Schu2006]
k_3	$4.18 \cdot 10^3$	$M^{-1}\ s^{-1}$	[Schu2006]
k_4	$6 \cdot 10^9$	$M^{-1}\ s^{-1}$	[Schu2006]
k_W	$1.4 \cdot 10^{-3}$	$M\ s^{-1}$	[Schu2006]
Diffusion coefficients			
D_{CO_2}	$1.91 \cdot 10^{-9}$	$m^2\ s^{-1}$	[Newm2004]
D_{K^+}	$1.957 \cdot 10^{-9}$	$m^2\ s^{-1}$	[Newm2004]
D_{H^+}	$9.311 \cdot 10^{-9}$	$m^2\ s^{-1}$	[Newm2004]
D_{OH^-}	$5.273 \cdot 10^{-9}$	$m^2\ s^{-1}$	[Newm2004]
$D_{HCO_3^-}$	$1.185 \cdot 10^{-9}$	$m^2\ s^{-1}$	[Newm2004]
$D_{CO_3^{2-}}$	$0.923 \cdot 10^{-9}$	$m^2\ s^{-1}$	[Newm2004]
D_{CO_2-CO}	$1.67 \cdot 10^{-5}$	$m^2\ s^{-1}$	-
$D_{CO_2-H_2}$	$6.83 \cdot 10^{-5}$	$m^2\ s^{-1}$	-
$D_{CO_2-H_2O}$	$2.18 \cdot 10^{-5}$	$m^2\ s^{-1}$	-
D_{CO-H_2}	$7.96 \cdot 10^{-5}$	$m^2\ s^{-1}$	-
D_{CO-H_2O}	$2.67 \cdot 10^{-5}$	$m^2\ s^{-1}$	-
$D_{H_2-H_2O}$	$9.43 \cdot 10^{-5}$	$m^2\ s^{-1}$	-

A

Table A.3.: Modeling and simulation parameters for the holistic process optimization in the base case scenario in Chapter 6.

Parameter	Value	Unit	Reference
Molar heat capacity		$kJ\,kmol^{-1}\,K^{-1}$	[Dean1999]
Hydrogen	28.84		
Carbon monoxide	29.14		

Carbon dioxide	37.13		
Oxygen	29.38		
Molar mass		$g\,mol^{-1}$	
Hydrogen	2.016		
Carbon monoxide	28.01		
Carbon dioxide	44.01		
Oxygen	31.998		
Membranes			
Polyimide permeability		barrer	[Alqa2017]
Hydrogen	50		
Carbon monoxide	1		
Carbon dioxide	13		
Pebax permeability		barrer	[Mura2010]
Hydrogen	32.11		
Carbon monoxide	1.39		
Carbon dioxide	55.85		
Oxygen	4.69		
Matrimid permeability		barrer	[Davi2011]
Hydrogen	13.53		
Carbon monoxide	3.46		
Carbon dioxide	0.25		
PRISM permeability		barrer	[Aitk1992]
Hydrogen	14		
Carbon monoxide	5.6		
Carbon dioxide	0.25		
Membrane			
Membrane cost	50	$€\,m^{-2}$	[Zhao2009]
Membrane thickness	0.5	µm	
Membrane lifetime	5	a	[Zhao2009; He2009]
Compressor			
Polytrophic exponent	1.4		
Efficiency	95	%	[Camp2000]

Scaling of compressor			[Bieg1997]
Reference cost	23000	$	
Reference power	100	Hp	
Scaling exponent	0.77		
Material and pressure factor	2.9		
Module factor	3.11		
Electrolyzer			
Conversion ratio	20	%	
Stack cost	454	€ m^{-2}	[Inst2013]
Anion exchange membrane (AEM)			
Faraday efficiency CO	95	%	[Liu2018]
Max. current density	520	$mA\,cm^{-2}$	[Liu2018]
Cathode Ag loading	20	$g\,m^{-2}$	[Liu2018]
Anode IrO_2 loading	20	$g\,m^{-2}$	[Liu2018]
Cation exchange membrane (CEM)			[Venn2019a]
Max current density	160	$mA\,cm^{-2}$	
Cathode Ag loading	50	$g\,m^{-2}$	
Anode IrO_2 loading	20	$g\,m^{-2}$	
Bipolar membrane			[Salv2017]
Max. current density	200	$mA\,cm^{-2}$	
Cathode Ag loading	15	$g\,m^{-2}$	
Anode Ni-Foam loading	346	$g\,m^{-2}$	
Catalytic membrane lifetime	2.5	a	[Spör2017]
Catalyst cost		€ g^{-1}	
Silver (Ag)	0.685		[Boera]
Iridium dioxide (IrO_2)	7.726		[Molb]
Nickel (Ni)	0.01294		[Boerb]
Capacity method with degression exponent			

Fumapem F14100	246	$	[Fuelb]
Fumapem F14100	0.06	m^2	[Fuelb]
Battelle 25 kW	2656340	$	[Inst2013]
Battelle 25 kW	4240	m^2	[Inst2013]
Sustainion X37-50	221	$	[Diox]
Sustainion X37-50	0.0644	m^2	[Diox]
Fumatech FBM	190	$	[Fuela]
Fumatech FBM	0.06	m^2	[Fuela]
Degression exponent	0.83175		
Cost updating factor			
1969	119		[Vata2002]
2019	607.5		[Scot2020]
Cost update factor	5.105		
Price of utility j			
Electricity	0.09	€ kWh^{-1}	[BMVi]
Carbon dioxide (Flue gas)	25	$\$\ t^{-1}$	[Zimm2017]
Carbon dioxide (Air capture)	50	$\$\ t^{-1}$	[Zimm2017]
Hydrogen	1250.6	$\$\ t^{-1}$	[El-E2019]
Carbon dioxide emission cost		€ t^{-1}	[Die 2019]
2020	25		
2025	55		
Miscellaneous			
USD to € conversion ration	0.8971	€ $\$^{-1}$	
Annual operating hour	8000	h	
Annualized depreciation factor	0.102		
Project lifetime	20	a	
Interest rate	8	%	
Factor for total investment cost	1.2		

Factor for fixed operating cost	0.025	a^{-1}

Regression models of electrolysis processes

AEM electrolyzer [Liu2018]

$$FE_{CO}[\%] = 95 \tag{A.1}$$

$$V[V] = 0.31 ln(j[mA\ cm^{-2}]) + 1.27 \tag{A.2}$$

BPM electrolyzer [Salv2017]

$$FE_{CO}[\%] = 2.36 \cdot 10^{-6}(j[mA\ cm^{-2}])^3 - 2.39 \cdot 10^{-3}(j[mA\ cm^{-2}])^2 + 2.19 \cdot 10^{-1}(j[mA\ cm^{-2}]) + 84.78 \tag{A.3}$$

$$V[V] = 1.60(j[mA\ cm^{-2}])^{0.13} \tag{A.4}$$

CEM electrolyzer [Venn2019a]

$$FE_{H_2}[\%] = 4.50 \cdot 10^{-3}(j[mA\ cm^{-2}])^2 - 2.65 \cdot 10^{-1}(j[mA\ cm^{-2}]) + 18.06 \tag{A.5}$$

$$V[V] = 1.85(j[mA\ cm^{-2}])^{0.12} \tag{A.6}$$

Calculation of standard Gibbs free energy of mixing

The absolute Gibbs free energy of mixing is calculated from Aspen Plus V11, using the Peng-Robinson property method.

$$\Delta G^0_{mix} = \Delta H^0_{mix} - T^0 \Delta S^0_{mix} \tag{A.7}$$

$$\Delta H^0_{mix} = H^0_{mix} - \sum x_i H^0_i \tag{A.8}$$

$$\Delta S^0_{mix} = S^0_{mix} - \sum x_i S^0_i \tag{A.9}$$

Table A.4.: Values for the calculation of the absolute Gibbs free energy for the 2:1 and 1:1 (CO_2:O_2) mixture taken from Aspen Plus V11.

Parameter	Value	Unit
$H^0_{1:1}$	-186.80	kJ mol^{-1}
$H^0_{2:1}$	-253.14	kJ mol^{-1}
$H^0_{CO_2}$	-381.92	kJ mol^{-1}
$H^0_{O_2}$	8.31	kJ mol^{-1}
$S^0_{1:1}$	0.031	kJ mol^{-1} K^{-1}
$S^0_{2:1}$	0.032	kJ mol^{-1} K^{-1}
$S^0_{CO_2}$	0.030	kJ mol^{-1} K^{-1}
$S^0_{O_2}$	0.0058	kJ mol^{-1} K^{-1}

Component	HHV_i [MJ kg^{-1}]	Reference
Carbon monoxide	10.11	[Lins2005]
Hydrogen	141.7	[Lins2005]

Table A.5.: Higher heating values of the product gases.

Supporting results

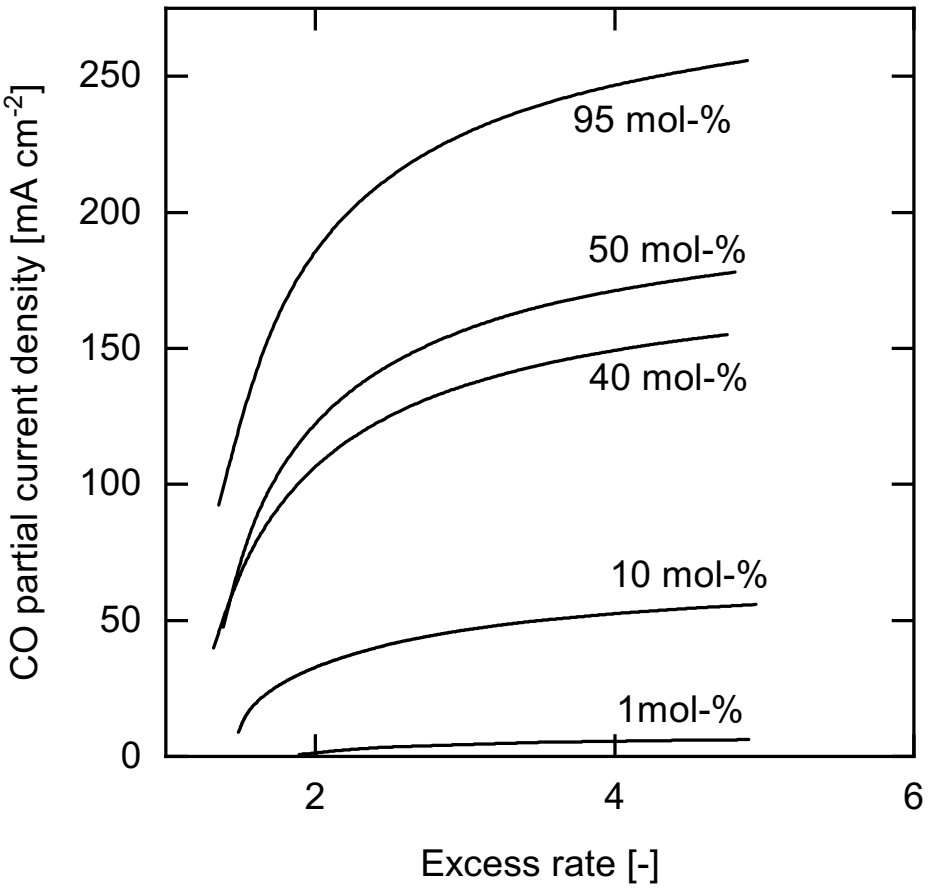

Figure A.1.: Averaged concentration of dissolved CO_2 in the CL on the left axis and averaged CO_2 fraction at the CL-GDL interface as a function of the excess rate at an applied cathode potential of -1.8 V vs SHE and 1.0 M $KHCO_3$ solution for the case of a CO_2 inlet fraction of 50 % and 95 %.

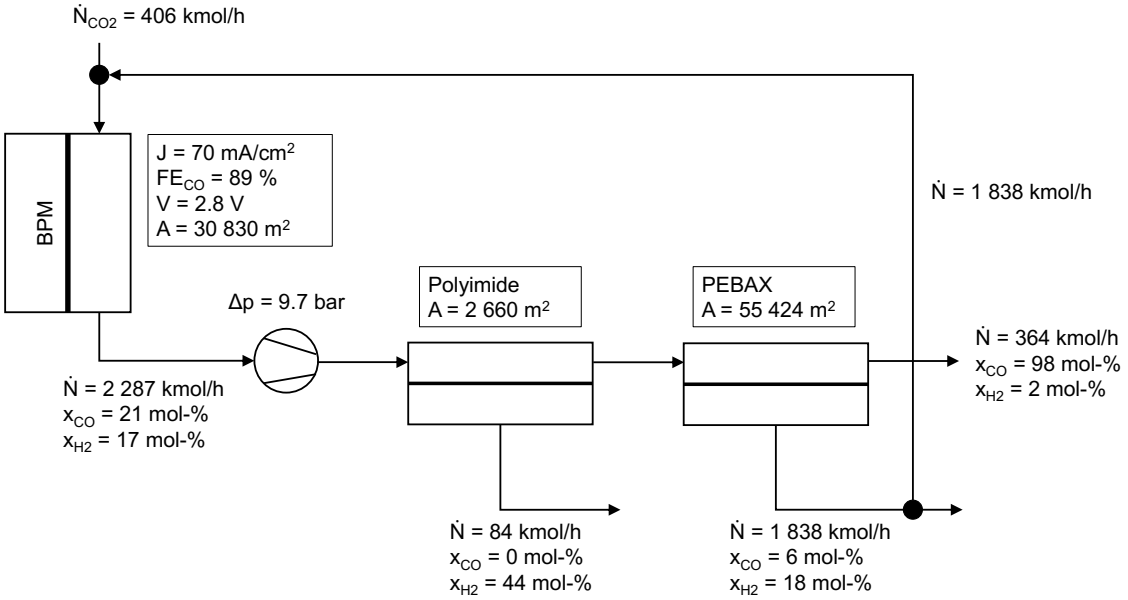

Figure A.2.: Flowsheet of electrochemical CO production using a BPM electrolyzer for the base case scenario. The water removal unit is not considered in the flowsheet as only the costs for water removal were taken into account.

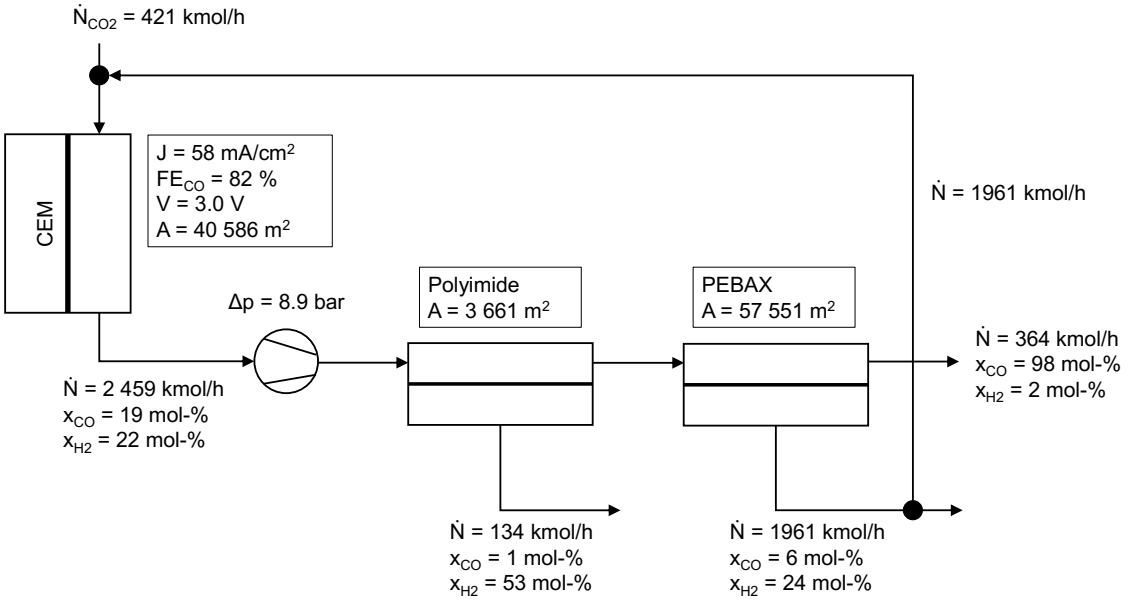

Figure A.3.: Flowsheet of electrochemical CO production using a CEM electrolyzer for the base case scenario. The water removal unit is not considered in the flowsheet as only the costs for water removal were taken into account.

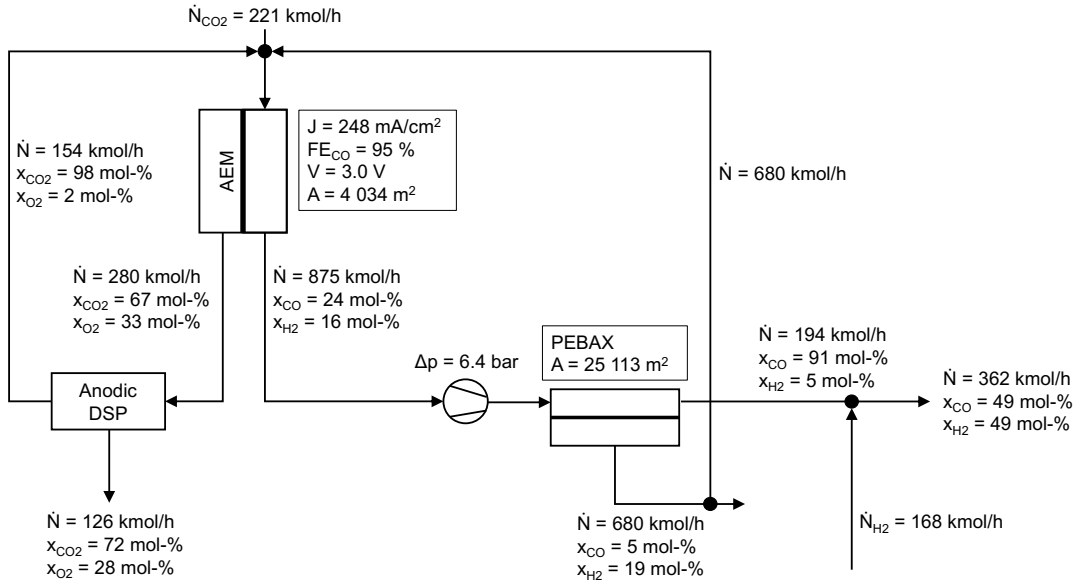

Figure A.4.: Flowsheet of electrochemical syngas (ratio 1:1) production using a AEM electrolyzer for the base case scenario. The water removal unit is not considered in the flowsheet as only the costs for water removal were taken into account. The anodic DSP is only shown as a block because it is not modeled rigorously in the overall process flowsheet but considered as a surrogate model.

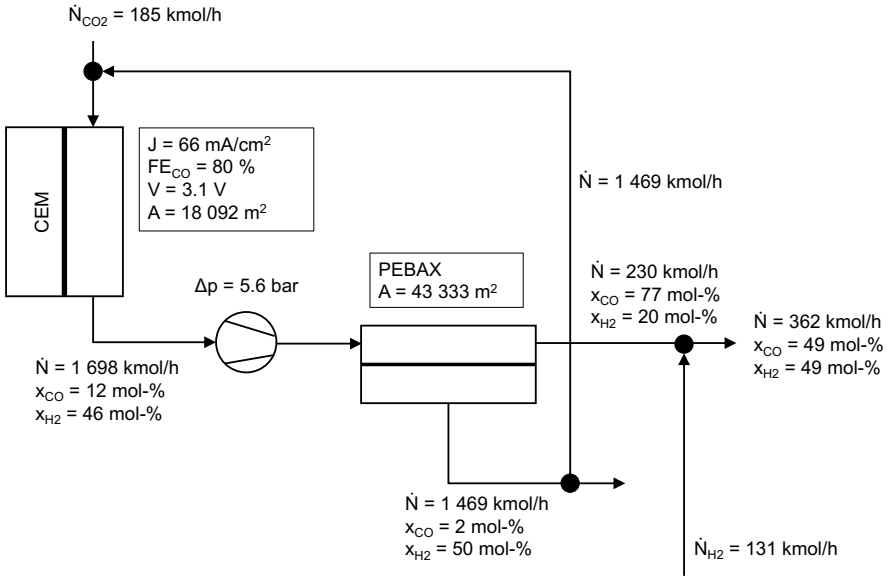

Figure A.5.: Flowsheet of electrochemical syngas (ratio 1:1) production using a CEM electrolyzer for the base case scenario. The water removal unit is not considered in the flowsheet as only the costs for water removal were taken into account.

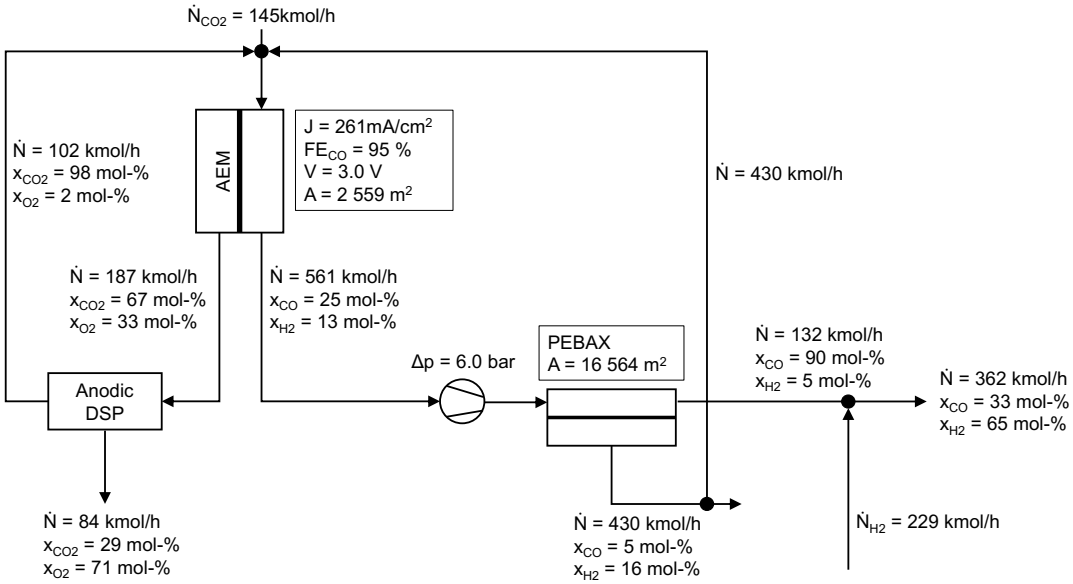

Figure A.6.: Flowsheet of electrochemical syngas (ratio 2:1) production using a AEM electrolyzer for the base case scenario. The water removal unit is not considered in the flowsheet as only the costs for water removal were taken into account. The anodic DSP is only shown as a block because it is not modeled rigorously in the overall process flowsheet but considered as a surrogate model.

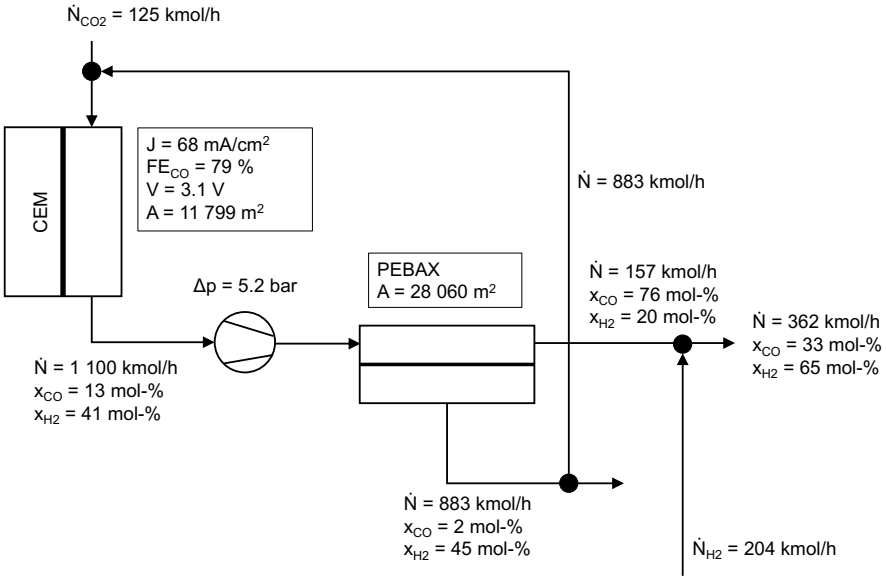

Figure A.7.: Flowsheet of electrochemical syngas (ratio 2:1) production using a CEM electrolyzer for the base case scenario. The water removal unit is not considered in the flowsheet as only the costs for water removal were taken into account.

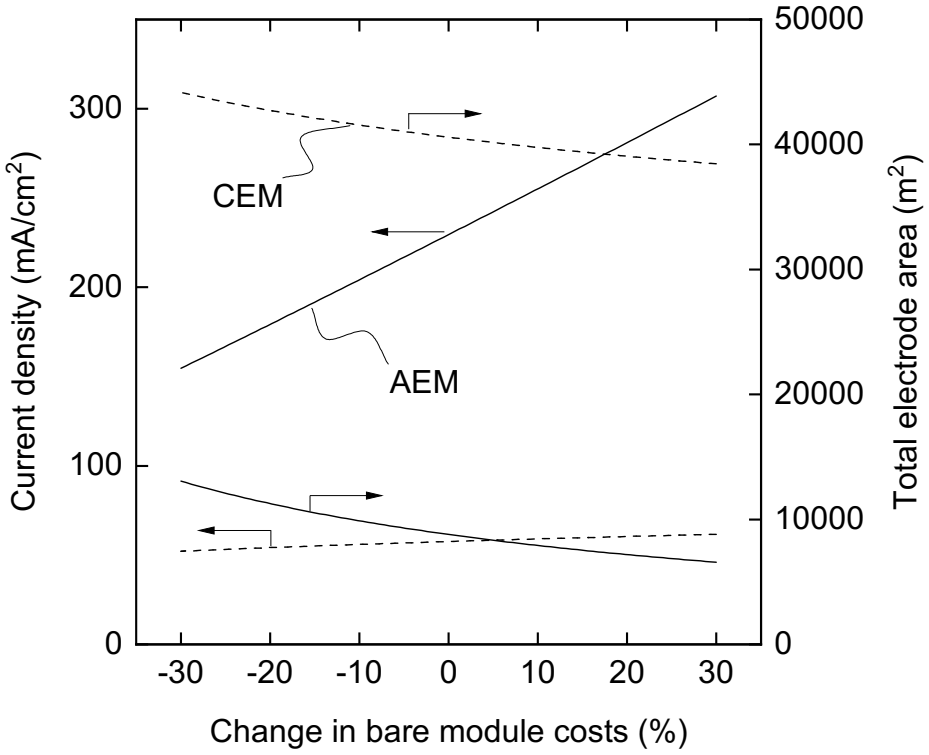

Figure A.8.: Sensitivity of the current density and total electrode area to a change in the bare module costs of the AEM and CEM electrolyzer.

Bibliography

[Aitk1992] C. Aitken, W. Koros, and D. Paul. “Effect of structural symmetry on gas transport properties of polysulfones”. *Macromolecules* 25.13 (1992). DOI: 10.1021/ma00039a018 (cit. on pp. 118, 153).

[Akib2019] T. Akiba, S. Sano, T. Yanase, T. Ohta, and M. Koyama. “Optuna: A Next-generation Hyperparameter Optimization Framework”. In*Proceedings of the 25rd ACM SIGKDD International Conference on Knowledge Discovery and Data Mining*. 2019 (cit. on p. 96).

[Alde2019] M. Alders, C. von Bargen, A. König, and M. Wessling. “Chilled MembranesEfficient gas permeation at sub-ambient temperatures”. *Journal of Membrane Science* 576 (2019). DOI: 10.1016/j.memsci.2019.01.037 (cit. on p. 28).

[Aler2021] T. Alerte, J. P. Edwards, C. M. Gabardo, C. P. O’Brien, A. Gaona, J. Wicks, A. Obradovi, A. Sarkar, S. A. Jaffer, H. L. MacLean, et al. “Downstream of the CO_2 Electrolyzer: Assessing the Energy Intensity of Product Separation”. *ACS Energy Letters* 6.12 (2021). DOI: 10.1021/acsenergylett.1c02263 (cit. on pp. 6, 30, 112, 139, 140).

[Alie2005] C. Alie, L. Backham, E. Croiset, and P. L. Douglas. “Simulation of CO_2 capture using MEA scrubbing: a flowsheet decomposition method”. *Energy conversion and management* 46.3 (2005). DOI: 10.1016/j.enconman.2004.03.003 (cit. on p. 29).

[Alqa2017] Y. Alqaheem, A. Alomair, M. Vinoba, and A. Pérez. “Polymeric Gas-Separation Membranes for Petroleum Refining”. *International Journal of Polymer Science* 2017.117 (2017). DOI: 10.1155/2017/4250927 (cit. on pp. 118, 153).

[Alsa2017] S. Alsayegh, J. Johnson, X. Wei, B. Ohs, J. Lohaus, and M. Wessling. "CO_2 aided H_2 recovery from water splitting processes". *International Journal of Hydrogen Energy* 42.34 (2017). DOI: 10.1016/j.ijhydene.2017.07.023 (cit. on p. 113).

[Anan2021] S. Anantharaj, S. Noda, M. Driess, and P. W. Menezes. "The pitfalls of using potentiodynamic polarization curves for Tafel analysis in electrocatalytic water splitting". *ACS Energy Letters* 6.4 (2021). DOI: 10.1021/acsenergylett.1c00608 (cit. on p. 15).

[Atki2014] P. W. Atkins and J. De Paula. *Atkins' physical chemistry*. Oxford university press, 2014 (cit. on pp. 149, 150).

[Bahn2022] F. K. Bahnamiri, M. Khalili, P. Pakzad, and M. Mehrpooya. "Techno-economic assessment of a novel power-to-liquid system for synthesis of formic acid and ammonia, based on CO_2 electroreduction and alkaline water electrolysis cells". *Renewable Energy* 187 (2022). DOI: 10.1016/j.renene.2022.01.085 (cit. on p. 103).

[Bake2002] R. W. Baker. "Future directions of membrane gas separation technology". *Industrial & engineering chemistry research* 41.6 (2002). DOI: 10.1021/ie0108088 (cit. on p. 118).

[Bake2004] R. W. Baker. *Membrane technology and applications*. John Wiley & Sons, 2004 (cit. on pp. 25–27, 113, 118).

[Bake2008] R. W. Baker and K. Lokhandwala. "Natural gas processing with membranes: an overview". *Industrial & Engineering Chemistry Research* 47.7 (2008). DOI: 10.1021/ie071083w (cit. on p. 31).

[Bala1997] S. Balay, W. D. Gropp, L. C. McInnes, and B. F. Smith. "Efficient management of parallelism in object-oriented numerical software libraries". In*Modern software tools for scientific computing*. Springer, 1997. Pp. 163–202. (Cit. on p. 43).

[Barb1988] T. Barbari, W. Koros, and D. Paul. "Gas transport in polymers based on bisphenol-A". *Journal of Polymer Science Part B: Polymer Physics* 26.4 (1988). DOI: 10.1002/polb.1988.090260401 (cit. on p. 27).

[Bard2001] A. J. Bard, L. R. Faulkner, J. Leddy, and C. G. Zoski. *Electrochemical methods: fundamentals and applications*. Vol. 2nd ed. Wiley New York, 2001 (cit. on pp. 10–13, 15, 42, 45, 74).

[Bard2003] A. J. Bard, M. Stratmann, and E. Calvo. *Encyclopedia of electrochemistry. Vol. 2. Interfacial kinetics and mass transport*. 2003 (cit. on p. 16).

[Baum2022] L. M. Baumgartner, C. I. Koopman, A. Forner-Cuenca, and D. A. Vermaas. "When Flooding Is Not Catastrophic Woven Gas Diffusion Electrodes Enable Stable CO_2 Electrolysis". *ACS Applied Energy Materials* (2022). DOI: 10.1021/acsaem.2c02783 (cit. on p. 19).

[Bhar2020] S. S. Bhargava, F. Proietto, D. Azmoodeh, E. R. Cofell, D. A. Henckel, S. Verma, C. J. Brooks, A. A. Gewirth, and P. J. Kenis. "System design rules for intensifying the electrochemical reduction of CO_2 to CO on Ag nanoparticles". *ChemElectroChem* 7.9 (2020). DOI: 10.1002/celc.202000089 (cit. on pp. 17, 20, 21, 51, 54, 60, 80, 110, 136).

[Bieg1997] L. T. Biegler, I. E. Grossmann, and A. W. Westerberg. *Systematic methods of chemical process design*. Prentice-Hall international series in the physical and chemical engineering sciences. Upper Saddle River, NJ: Prentice-Hall, 1997 (cit. on pp. 120, 154).

[Bini2020] K. Biniek, K. Henderson, M. Rogers, and G. Santoni. "Driving CO_2 emissions to zero (and beyond) with carbon capture, use, and storage". *McKinsey Quarterly* (2020). (Cit. on pp. 1, 2).

[Blak2021] J. Blake, J. Padding, and J. Haverkort. "Analytical modelling of CO_2 reduction in gas-diffusion electrode catalyst layers". *Electrochim. Acta* (2021). DOI: 10.1016/j.electacta.2021.138987 (cit. on p. 60).

[Blak2023] J. W. Blake, V. Konderla, L. M. Baumgartner, D. A. Vermaas, J. T. Padding, and J. Haverkort. "Inhomogeneities in the Catholyte Channel Limit the Upscaling of CO_2 Flow Electrolysers". *ACS Sustainable Chemistry & Engineering* 11.7 (2023). DOI: 10.1021/acssuschemeng.2c06129 (cit. on p. 92).

[Blom2021] M. A. Blommaert, S. Subramanian, K. Yang, W. A. Smith, and D. A. Vermaas. "High Indirect Energy Consumption in AEM-Based CO_2 Electrolyzers Demonstrates the Potential of Bipolar Membranes". *ACS Applied Materials & Interfaces* 14.1 (2021). DOI: 10.1021/acsami.1c16513 (cit. on pp. 112, 137).

[BMVi] BMVi. *Strompreise für Industriekunden in Ländern Europas 2018*. URL: https://de.statista.com/ (visited on 10/28/2020) (cit. on pp. 130, 155).

[Bock1972] J. O. Bockris and P. Saluja. “Ionic solvation numbers from compressibilities and ionic vibration potentials measurements”. *The Journal of Physical Chemistry* 76.15 (1972). (Cit. on p. 150).

[Bock1998] J. O. Bockris and A. K. Reddy. “Ion-solvent interactions”. *Modern Electrochemistry 1: Ionics* (1998). (Cit. on p. 150).

[Boera] Boerse. *Weltmarktpreis Nickel*. URL: https://www.boerse.de/rohstoffe/Nickel/XC0005705543 (visited on 10/20/2020) (cit. on p. 154).

[Boerb] Boerse. *Weltmarktpreis Silber*. URL: https://www.boerse.de/rohstoffe/Silber/XC0009653103 (visited on 10/20/2020) (cit. on p. 154).

[Bohi2017] K. Bohinc, G. V. Bossa, and S. May. “Incorporation of ion and solvent structure into mean-field modeling of the electric double layer”. *Adv. Colloid Interface Sci.* 249 (2017). DOI: 10.1016/j.cis.2017.05.001 (cit. on p. 79).

[Bohr2019] D. Bohra, J. H. Chaudhry, T. Burdyny, E. A. Pidko, and W. A. Smith. “Modeling the electrical double layer to understand the reaction environment in a CO_2 electrocatalytic system”. *Energy & Environmental Science* 12.11 (2019). DOI: 10.1039/C9EE02485A (cit. on pp. 5, 37, 42, 45, 46, 150).

[Bohr2020] D. Bohra, J. Chaudhry, T. Burdyny, E. Pidko, and W. Smith. “Mass transport in catalytic pores of GDE-based CO_2 electroreduction systems”. *ChemRxiv. Cambridge: Cambridge Open Engage* (2020). DOI: 10.26434/chemrxiv.13073348.v1 (cit. on p. 37).

[Brée2020] L. C. Brée, M. Wessling, and A. Mitsos. “Modular modeling of Electrochemical Reactors: Comparison of CO_2-Electolyzers”. *Comput. Chem. Eng.* (2020). DOI: 10.1016/j.compchemeng.2020.106890 (cit. on p. 59).

[Bui2021] J. C. Bui, C. Kim, A. Z. Weber, and A. T. Bell. “Dynamic boundary layer simulation of pulsed CO_2 electrolysis on a copper catalyst”. *ACS Energy Letters* 6.4 (2021). DOI: 10.1021/acsenergylett.1c00364 (cit. on pp. 22, 36, 45).

[Burd2017] T. Burdyny, P. J. Graham, Y. Pang, C.-T. Dinh, M. Liu, E. H. Sargent, and D. Sinton. “Nanomorphology-enhanced gas-evolution intensifies CO_2 reduction electrochemistry”. *ACS Sustainable Chemistry & Engineering* 5.5 (2017). DOI: 10.1021/acssuschemeng.7b00023 (cit. on p. 149).

[Burd2019] T. Burdyny and W. A. Smith. “CO_2 reduction on gas-diffusion electrodes and why catalytic performance must be assessed at commercially-relevant conditions”. *Energy & Environmental Science* 12.5 (2019). DOI: 10.1039/C8EE03134G (cit. on pp. 4, 17, 59).

[Butl1924a] J. A. V. Butler. “Studies in heterogeneous equilibria. Part II.The kinetic interpretation of the nernst theory of electromotive force”. *Transactions of the Faraday Society* 19.March (1924). (Cit. on p. 14).

[Butl1924b] J. Butler. “Studies in heterogeneous equilibria. Part III. A kinetic theory of reversible oxidation potentials at inert electrodes”. *Transactions of the Faraday Society* 19.March (1924). (Cit. on p. 14).

[Butl1932] J. A. V. Butler. “The mechanism of overvoltage and its relation to the combination of hydrogen atoms at metal electrodes”. *Transactions of the Faraday Society* 28 (1932). (Cit. on p. 14).

[Butt2023] E. N. Butt, J. T. Padding, and R. Hartkamp. “Size-modified Poisson–Nernst–Planck approach for modeling a local electrode environment in CO_2 electrolysis”. *Sustainable Energy & Fuels* 7.1 (2023). DOI: 10.1039/D2SE01262F (cit. on pp. 37, 39).

[Camp2000] J. M. Campbell, L. L. Lilly, and R. A. Hubbard. *Gas conditioning and processing*. 8. ed. Norman, Okla.: Campbell Petroleum Series, 2000 (cit. on p. 153).

[Carr1991] J. J. Carroll, J. D. Slupsky, and A. E. Mather. “The Solubility of Carbon Dioxide in Water at Low Pressure”. *Journal of Physical and Chemical Reference Data* 20.6 (1991). DOI: 10.1063/1.555900 (cit. on p. 67).

[Case2021] R. Casebolt, K. Levine, J. Suntivich, and T. Hanrath. “Pulse check: Potential opportunities in pulsed electrochemical CO_2 reduction”. *Joule* 5.8 (2021). DOI: 10.1016/j.joule.2021.05.014 (cit. on p. 16).

[CERT2019] CERT Systems Inc. *CERT Systems Inc*. 2019. URL: https://co2cert.com/ (visited on 01/20/2023) (cit. on p. 24).

[Chan2023] H.-M. Chang and I. V. Zenyuk. “Membrane electrode assembly design to prevent CO_2 crossover in CO_2 reduction reaction electrolysis”. *Communications Chemistry* 6.1 (2023). DOI: 10.1038/s42004-022-00806-0 (cit. on p. 18).

[Chen2015] X. Y. Chen, H. Vinh-Thang, A. A. Ramirez, D. Rodrigue, and S. Kaliaguine. “Membrane gas separation technologies for biogas upgrading”. *Rsc Advances* 5.31 (2015). DOI: 10.1039/C5RA00666J (cit. on p. 118).

[Chen2017] L. Chen, F. Li, Y. Zhang, C. L. Bentley, M. Horne, A. M. Bond, and J. Zhang. “Electrochemical reduction of carbon dioxide in a monoethanolamine capture medium”. *ChemSusChem* 10.20 (2017). DOI: 10.1002/cssc.201701075 (cit. on p. 24).

[Chen2020] Y. Chen, A. Vise, W. E. Klein, F. C. Cetinbas, D. J. Myers, W. A. Smith, T. G. Deutsch, and K. C. Neyerlin. “A robust, scalable platform for the electrochemical conversion of CO_2 to formate: identifying pathways to higher energy efficiencies”. *ACS Energy Letters* 5.6 (2020). DOI: 10.1021/acsenergylett.0c00860 (cit. on p. 19).

[Choi2021] B.-U. Choi, Y. C. Tan, H. Song, K. B. Lee, and J. Oh. “System design considerations for enhancing electroproduction of formate from simulated flue gas”. *ACS Sustainable Chemistry & Engineering* 9.5 (2021). DOI: 10.1021/acssuschemeng.0c08632 (cit. on pp. 23, 24).

[Clar2018a] E. L. Clark and A. T. Bell. “Direct observation of the local reaction environment during the electrochemical reduction of CO_2”. *Journal of the American Chemical Society* 140.22 (2018). DOI: 10.1021/jacs.8b04058 (cit. on p. 49).

[Clar2018b] E. L. Clark, J. Resasco, A. Landers, J. Lin, L.-T. Chung, A. Walton, C. Hahn, T. F. Jaramillo, and A. T. Bell. “Standards and protocols for data acquisition and reporting for studies of the electrochemical reduction of carbon dioxide”. *Acs Catalysis* 8.7 (2018). DOI: 10.1021/acscatal.8b01340 (cit. on p. 49).

[Cook1990] R. L. Cook, R. C. MacDuff, and A. F. Sammells. “High rate gas phase CO_2 reduction to ethylene and methane using gas diffusion electrodes”. *J. Electrochem. Soc.* 137.2 (1990). DOI: 10.1149/1.2086515 (cit. on p. 58).

[Cove] Covestro AG. *Gas phase technology: 60% less energy consumption*. URL: https://www.covestro.com/ (visited on 04/09/2021) (cit. on p. 119).

[Davi2011] O. C. David, D. Gorri, A. Urtiaga, and I. Ortiz. “Mixed gas separation study for the hydrogen recovery from H_2/CO/N_2/CO_2 post combustion mixtures using a Matrimid membrane”. *Journal of Membrane Science* 378.1-2 (2011). DOI: 10.1016/j.memsci.2011.05.029 (cit. on pp. 118, 153).

[De A2020] F. P. G. De Arquer, C.-T. Dinh, A. Ozden, J. Wicks, C. McCallum, A. R. Kirmani, D.-H. Nam, C. Gabardo, A. Seifitokaldani, X. Wang, et al. “CO_2 electrolysis to multicarbon products at activities greater than 1 A cm- 2”. *Science* 367.6478 (2020). DOI: 10.1126/science.aay4217 (cit. on pp. 79, 88, 110, 135).

[De L2019] P. De Luna, C. Hahn, D. Higgins, S. A. Jaffer, T. F. Jaramillo, and E. H. Sargent. “What would it take for renewably powered electrosynthesis to displace petrochemical processes?” *Science* 364.6438 (2019). DOI: 10.1126/science.aav3506 (cit. on p. 58).

[Dean1999] J. A. Dean and N. A. Lange. *Lange’s handbook of chemistry*. 15. ed. McGraw-Hill handbooks. New York, NY: McGraw-Hill, 1999 (cit. on p. 152).

[Dela2008] C. Delacourt, P. L. Ridgway, J. B. Kerr, and J. Newman. “Design of an electrochemical cell making syngas (CO+ H_2) from CO_2 and H_2O reduction at room temperature”. *J. Electrochem. Soc.* 155.1 (2008). DOI: 10.1149/1.2801871 (cit. on p. 18).

[Dela2010] C. Delacourt and J. Newman. “Mathematical Modeling of CO_2 Reduction to CO in Aqueous Electrolytes II. Study of an Electrolysis Cell Making Syngas (CO+ H_2) from CO_2 and H_2O Reduction at Room Temperature”. *J. Electrochem. Soc.* 157.12 (2010). DOI: 10.1149/1.3502533 (cit. on p. 58).

[Dick2020] E. J. Dickinson and A. J. Wain. “The Butler-Volmer equation in electrochemical theory: Origins, value, and practical application”. *Journal of Electroanalytical Chemistry* 872 (2020). DOI: 10.1016/j.jelechem.2020.114145 (cit. on p. 14).

[Die 2019] Die Bundesregierung. *Grundlage für CO_2-Preis steht*. 2019. URL: https://www.bundesregierung.de/breg-de/themen/klimaschutz/nationaler-emissionshandel-1684508 (visited on 10/28/2020) (cit. on p. 155).

[Dinh2018] C.-T. Dinh, T. Burdyny, M. G. Kibria, A. Seifitokaldani, C. M. Gabardo, F. P. Garca de Arquer, A. Kiani, J. P. Edwards, P. De Luna, O. S. Bushuyev, et al. “CO_2 electroreduction to ethylene via hydroxide-mediated copper catalysis at an abrupt interface”. *Science* 360.6390 (2018). DOI: 10.1126/science.aas9100 (cit. on p. 23).

[Diox] Dioxide Materials. *Sustainion X37-50*. URL: https://dioxidematerials.com/product/sustainion-anion-exchange-membrane/ (visited on 10/22/2020) (cit. on p. 155).

[Diox2021] Dioxycle. 2021. URL: https://dioxycle.com/ (visited on 01/20/2023) (cit. on p. 24).

[Disc2022] J. Disch, L. Bohn, S. Koch, M. Schulz, Y. Han, A. Tengattini, L. Helfen, M. Breitwieser, and S. Vierrath. “High-resolution neutron imaging of salt precipitation and water transport in zero-gap CO_2 electrolysis”. *Nature Communications* 13.1 (2022). DOI: 10.1038/s41467-022-33694-y (cit. on pp. 18, 53).

[Dogo1972] R. Dogonadze, J. Ulstrup, and Y. I. Kharkats. “A theory of electrode reactions through bridge transition states; bridges with a discrete electronic spectrum”. *J. Electroanal. Chem. Interfacial Electrochem.* 39.1 (1972). DOI: 10.1016/S0022-0728(72)80475-3 (cit. on pp. 20, 52, 74).

[Dufe2012] E. J. Dufek, T. E. Lister, S. G. Stone, and M. E. McIlwain. “Operation of a pressurized system for continuous reduction of CO_2”. *J. Electrochem. Soc.* 159.9 (2012). DOI: 10.1149/2.011209jes (cit. on p. 83).

[Dunw2018] M. Dunwell, X. Yang, B. P. Setzler, J. Anibal, Y. Yan, and B. Xu. “Examination of near-electrode concentration gradients and kinetic impacts on the electrochemical reduction of CO_2 using surface-enhanced infrared spectroscopy”. *ACS Catalysis* 8.5 (2018). DOI: 10.1021/acscatal.8b01032 (cit. on p. 58).

[Dutc2015] B. Dutcher, M. Fan, and A. G. Russell. “Amine-based CO_2 capture technology development from the beginning of 2013 A Review”. *ACS applied materials & interfaces* 7.4 (2015). DOI: 10.1021/am507465f (cit. on p. 30).

[Edwa2023] J. P. Edwards, T. Alerte, C. P. OBrien, C. M. Gabardo, S. Liu, J. Wicks, A. Gaona, J. Abed, Y. C. Xiao, D. Young, et al. “Pilot-Scale CO_2 Electrolysis Enables a Semi-empirical Electrolyzer Model”. *ACS Energy Letters* 8 (2023). DOI: 10.1021/acsenergylett.3c00620 (cit. on p. 22).

[El-E2019] R. S. El-Emam and H. Özcan. “Comprehensive review on the techno-economics of sustainable large-scale clean hydrogen production”. *Journal of Cleaner Production* 220 (2019). DOI: 10.1016/j.jclepro.2019.01.309 (cit. on p. 155).

[El-K2014] A. El-Kharouf. “Understanding GDL properties and performance in polymer electrolyte fuel cells”. Dissertation. Birmingham, UK: University of Birmingham, 2014 (cit. on p. 151).

[Endr2019] B. Endrodi, E. Kecsenovity, A. Samu, F. Darvas, R. Jones, V. Török, A. Danyi, and C. Janáky. “Multilayer electrolyzer stack converts carbon dioxide to gas products at high pressure with high efficiency”. *ACS energy letters* 4.7 (2019). DOI: 10.1021/acsenergylett.9b01142 (cit. on p. 22).

[Erik2022] B. Eriksson, T. Asset, F. Spanu, F. Lecoeur, M. Dupont, F. Garces-Pineda, J. R. G. Mascaros, S. Cavaliere, J. Rozière, and F. Jaouen. “Mitigation of Carbon Crossover in CO_2 Electrolysis by Use of Bipolar Membranes”. *Journal of The Electrochemical Society* (2022). DOI: 10.1149/1945-7111/ac580e (cit. on p. 112).

[Espo2018] D. V. Esposito. “Membrane-Coated Electrocatalysts - An Alternative Approach To Achieving Stable and Tunable Electrocatalysis”. *ACS Catalysis* 8 (2018). DOI: 10.1021/acscatal.7b03374 (cit. on p. 88).

[Femm2017] R. Femmer and S. V. V. Nikonenko. “Ion transport in electrolyte and polyelectrolyte systems”. PhD thesis. Rheinisch-Westfälische Technische Hochschule Aachen, 2017 (cit. on pp. 38, 39, 43).

[Frie2022] P. Friedlingstein, M. W. Jones, M. O’Sullivan, R. M. Andrew, D. C. Bakker, J. Hauck, C. Le Quéré, G. P. Peters, W. Peters, J. Pongratz, et al. “Global carbon budget 2021”. *Earth System Science Data* 14.4 (2022). DOI: 10.5194/essd-14-1917-2022 (cit. on p. 1).

[Froc2019] J. Frochte. *Maschinelles Lernen: Grundlagen und Algorithmen in Python*. Carl Hanser Verlag GmbH Co KG, 2019 (cit. on p. 98).

[Frum1933] A. Frumkin. “Wasserstoffüberspannung und Struktur der Doppelschicht”. *Zeitschrift für physikalische Chemie* 164.1 (1933). DOI: 10.1515/zpch-1933-16411 (cit. on p. 37).

[Fuela] FuelCellStore. *FuelCellStore*. URL: https://www.fuelcellstore.com/fuel-cell-components/membranes/fumatech-membranes/fumatech-other/fumasep-fbm (visited on 10/28/2021) (cit. on p. 155).

[Fuelb] FuelCellStore. *Fumapem F-14100*. URL: https://www.fuelcellstore.com/fumapem-f-14100 (visited on 10/22/2020) (cit. on p. 155).

[Fuji2012] C. Fujimoto, D.-S. Kim, M. Hibbs, D. Wrobleski, and Y. S. Kim. “Backbone stability of quaternized polyaromatics for alkaline membrane fuel cells”. *Journal of Membrane Science* 423 (2012). DOI: 10.1016/j.memsci.2012.08.045 (cit. on p. 23).

[Full1966] E. N. Fuller, P. D. Schettler, and J. C. Giddings. “New method for prediction of binary gas-phase diffusion coefficients”. *Industrial & Engineering Chemistry* 58.5 (1966). DOI: 10.1021/ie50677a007 (cit. on p. 63).

[Gaba2018] C. M. Gabardo, A. Seifitokaldani, J. P. Edwards, C.-T. Dinh, T. Burdyny, M. G. Kibria, C. P. OBrien, E. H. Sargent, and D. Sinton. “Combined high alkalinity and pressurization enable efficient CO_2 electroreduction to CO”. *Energy Environ. Sci.* 11.9 (2018). DOI: 10.1039/c8ee01684d (cit. on p. 79).

[Gaba2019] C. M. Gabardo, C. P. O’Brien, J. P. Edwards, C. McCallum, Y. Xu, C.-T. Dinh, J. Li, E. H. Sargent, and D. Sinton. “Continuous carbon dioxide electroreduction to concentrated multi-carbon products using a membrane electrode assembly”. *Joule* 3.11 (2019). DOI: 10.1016/j.joule.2019.07.021 (cit. on p. 110).

[Gava2000] D. J. Gavaghan and S. W. Feldberg. “Extended electron transfer and the Frumkin correction”. *Journal of Electroanalytical Chemistry* 491.1-2 (2000). DOI: 10.1016/S0022-0728(00)00210-2 (cit. on p. 37).

[Ghos1996] K. Ghosal, R. Chern, B. Freeman, W. Daly, and I. Negulescu. “Effect of basic substituents on gas sorption and permeation in polysulfone”. *Macromolecules* 29.12 (1996). DOI: 10.1021/ma951310i (cit. on p. 26).

[Gier] M. Gierkink, D. Lencz, and F. Arnold. *Auswirkungen einer Beendigung der Kohleverstromung bis 2038 auf den Strommarkt, CO_2-Emissionen und ausgewählte Industrien: Eine Analyse des Abschlussberichts der WSB-Kommission*. Köln. (Visited on 08/01/2019) (cit. on p. 130).

[Gilf2021] D. Gilfillan and G. Marland. “CDIAC-FF: global and national CO_2 emissions from fossil fuel combustion and cement manufacture: 1751–2017”. *Earth System Science Data* 13.4 (2021). DOI: 10.5194/essd-13-1667-2021 (cit. on p. 1).

[Gost2009] J. T. Gostick, M. A. Ioannidis, M. W. Fowler, and M. D. Pritzker. “Wettability and capillary behavior of fibrous gas diffusion media for polymer electrolyte membrane fuel cells”. *Journal of Power*

Sources 194.1 (2009). DOI: 10.1016/j.jpowsour.2009.04.052 (cit. on p. 105).

[Guid2014] R. Guidelli, R. G. Compton, J. M. Feliu, E. Gileadi, J. Lipkowski, W. Schmickler, and S. Trasatti. “Defining the transfer coefficient in electrochemistry: An assessment (IUPAC Technical Report)”. *Pure and Applied Chemistry* 86.2 (2014). DOI: 10.1515/pac-2014-5026 (cit. on p. 14).

[Gupt2006] N. Gupta, M. Gattrell, and B. MacDougall. “Calculation for the cathode surface concentrations in the electrochemical reduction of CO_2 in $KHCO_3$ solutions”. *J. Appl. Electrochem.* 36.2 (2006). DOI: 10.1007/s10800-005-9058-y (cit. on p. 48).

[Guth1969] H. Guthrie. “Capital cost estimation for the chemical and process industries”. *Chem. Eng* 32 (1969). (Cit. on p. 120).

[Ha1995] S. Ha, K. Doblhofer, et al. “The electrochemical interface between copper (111) and aqueous electrolytes”. *Journal of Electroanalytical Chemistry* 380.1-2 (1995). DOI: 10.1016/0022-0728(94)03650-R (cit. on p. 45).

[Haas2018] T. Haas, R. Krause, R. Weber, M. Demler, and G. Schmid. “Technical photosynthesis involving CO_2 electrolysis and fermentation”. *Nature Catalysis* 1.1 (2018). DOI: 10.1038/s41929-017-0005-1 (cit. on pp. 19, 23, 110).

[Hash2018] H. Hashiba, L.-C. Weng, Y. Chen, H. K. Sato, S. Yotsuhashi, C. Xiang, and A. Z. Weber. “Effects of Electrolyte Buffer Capacity on Surface Reactant Species and the Reaction Rate of CO_2 in Electrochemical CO_2 Reduction”. *J. Phys. Chem. C* 122.7 (2018). DOI: 10.1021/acs.jpcc.7b11316 (cit. on pp. 66, 76).

[Hats2014] T. Hatsukade, K. P. Kuhl, E. R. Cave, D. N. Abram, and T. F. Jaramillo. “Insights into the electrocatalytic reduction of CO_2 on metallic silver surfaces”. *Phys. Chem. Chem. Phys.* 16.27 (2014). DOI: 10.1039/C4CP00692E (cit. on pp. 38, 42, 44, 45, 62, 65).

[He2009] X. He, J. Arvid Lie, E. Sheridan, and M.-B. Hägg. “CO_2 capture by hollow fibre carbon membranes: Experiments and process simulations”. *Energy Procedia* 1.1 (2009). DOI: 10.1016/j.egypro.2009.01.037 (cit. on p. 153).

[Hend2020] K. Henderson, D. Pinner, M. Rogers, B. Smeets, C. Tryggestad, and D. Vargas. “Climate math: What a 1.5-degree pathway would take”. *McKinsey Quarterly* 2 (2020). (Cit. on p. 1).

[Hern2017] S. Hernández, M. A. Farkhondehfal, F. Sastre, M. Makkee, G. Saracco, and N. Russo. “Syngas production from electrochemical reduction of CO_2: current status and prospective implementation”. *Green Chemistry* 19.10 (2017). DOI: 10.1039/C7GC00398F (cit. on p. 2).

[Hess2022] M. Hesselmann, B. C. Bräsel, R. G. Keller, and M. Wessling. “Simulation-based guidance for improving CO_2 reduction on silver gas diffusion electrodes”. *Electrochemical Science Advances* (2022). DOI: 10.1002/elsa.202100160 (cit. on p. 126).

[Hess2023] M. Hesselmann, H. Minten, T. Geissler, R. G. Keller, A. Bardow, and M. Wessling. “Why Membranes Matter: Ion Exchange Membranes in Holistic Process Optimization of Electrochemical CO_2 Reduction”. *Advanced Sustainable Systems* (2023). DOI: 10.1002/adsu.202300077 (cit. on p. 121).

[Heus2005] J. Heuser, H. Kauth, and C. Kords. *Phosgene having low content of carbon tetrachloride*. US Patent 6,930,202. 2005 (cit. on p. 115).

[Higg2018] D. Higgins, C. Hahn, C. Xiang, T. F. Jaramillo, and A. Z. Weber. “Gas-diffusion electrodes for carbon dioxide reduction: a new paradigm”. *ACS Energy Letters* 4.1 (2018). DOI: 10.1021/acsenergylett.8b02035 (cit. on pp. 4, 16, 17, 58).

[Hori1989] Y. Hori, A. Murata, and R. Takahashi. “Formation of hydrocarbons in the electrochemical reduction of carbon dioxide at a copper electrode in aqueous solution”. *Journal of the Chemical Society, Faraday Transactions 1: Physical Chemistry in Condensed Phases* 85.8 (1989). DOI: 10.1039/F19898502309 (cit. on p. 20).

[Hori2003] Y. Hori, H. Ito, K. Okano, K. Nagasu, and S. Sato. “Silver-coated ion exchange membrane electrode applied to electrochemical reduction of carbon dioxide”. *Electrochimica Acta* 48.18 (2003). DOI: 10.1016/S0013-4686(03)00311-6 (cit. on p. 23).

[Hua2022] Y. Hua, J. Wang, T. Min, and Z. Gao. “Electrochemical CO_2 conversion towards syngas: Recent catalysts and improving strategies for ratio-tunable syngas”. *Journal of Power Sources* 535 (2022). DOI: 10.1016/j.jpowsour.2022.231453 (cit. on p. 129).

[Huan2021] J. E. Huang, F. Li, A. Ozden, A. Sedighian Rasouli, F. P. Garca de Arquer, S. Liu, S. Zhang, M. Luo, X. Wang, Y. Lum, et al. “CO_2 electrolysis to multicarbon products in strong acid”. *Science* 372.6546 (2021). DOI: 10.1126/science.abg6582 (cit. on p. 129).

[IEA] IEA. *IEA, Norway - Energy System Overview*. URL: https://www.iea.org/countries/norway (visited on 05/11/2022) (cit. on p. 130).

[Inst2013] B. M. Institute. *Manufacturing Cost Analysis of 10 kW and 25 kW direct Hydrogen Polymer Electrolyte Membrane (PEM) Fuel Cell for Material Handling Applications*. 2013. URL: https://www.energy.gov/sites/prod/files/2014/06 (visited on 10/20/2020) (cit. on pp. 119, 154, 155).

[Jaya2005] R. S. Jayashree, L. Gancs, E. R. Choban, A. Primak, D. Natarajan, L. J. Markoski, and P. J. A. Kenis. “Air-breathing laminar flow-based microfluidic fuel cell”. *J. Am. Chem. Soc.* 127.48 (2005). DOI: 10.1021/ja054599k (cit. on p. 64).

[Jaya2010] R. S. Jayashree, S. K. Yoon, F. R. Brushett, P. O. Lopez-Montesinos, D. Natarajan, L. J. Markoski, and P. J. Kenis. “On the performance of membraneless laminar flow-based fuel cells”. *Journal of Power Sources* 195.11 (2010). DOI: 10.1149/MA2022-02491942mtgabs (cit. on p. 17).

[Jean2018] P. Jeanty, C. Scherer, E. Magori, K. Wiesner-Fleischer, O. Hinrichsen, and M. Fleischer. “Upscaling and continuous operation of electrochemical CO_2 to CO conversion in aqueous solutions on silver gas diffusion electrodes”. *Journal of CO_2 Utilization* 24 (2018). DOI: 10.1016/j.jcou.2018.01.011 (cit. on pp. 19, 21, 22, 60, 84, 136).

[Jeng2020] E. Jeng and F. Jiao. “Investigation of CO_2 single-pass conversion in a flow electrolyzer”. *Reaction Chemistry & Engineering* 5.9 (2020). DOI: 10.1039/D0RE00261E (cit. on pp. 136, 137).

[Jeon2018] H. S. Jeon, S. Kunze, F. Scholten, and B. Roldan Cuenya. “Prism-shaped Cu nanocatalysts for electrochemical CO_2 reduction to ethylene”. *ACS Catalysis* 8.1 (2018). DOI: 10.1021/acscatal.7b02959 (cit. on p. 23).

[Jeon2021] H. S. Jeon, J. Timoshenko, C. Rettenmaier, A. Herzog, A. Yoon, S. W. Chee, S. Oener, U. Hejral, F. T. Haase, and B. Roldan Cuenya. “Selectivity control of Cu nanocrystals in a gas-fed flow cell through CO_2 pulsed electroreduction”. *Journal of the American Chemical Society* 143.19 (2021). DOI: 10.1021/jacs.1c03443 (cit. on pp. 22, 23).

[Jhon2012] H.-R. M. Jhong, F. R. Brushett, L. Yin, D. M. Stevenson, and P. J. Kenis. “Combining structural and electrochemical analysis of electrodes using micro-computed tomography and a microfluidic fuel cell”. *J. Electrochem. Soc.* 159.3 (2012). DOI: 10.1149/2.033203jes (cit. on p. 151).

[John2023] E. F. Johnson, E. Boutin, and S. Haussener. “Surface Charge Boundary Condition Often Misused in CO_2 Reduction Models”. *The Journal of Physical Chemistry C* (2023). DOI: 10.1021/acs.jpcc.3c05364 (cit. on pp. 45, 52).

[Joun2018] M. Jouny, W. Luc, and F. Jiao. “General techno-economic analysis of CO_2 electrolysis systems”. *Industrial & Engineering Chemistry Research* 57.6 (2018). DOI: 10.1021/acs.iecr.7b03514 (cit. on pp. 33, 112, 123, 124, 131).

[Jung2021] B. Jung, S. Park, C. Lim, W. H. Lee, Y. Lim, J. Na, C.-J. Lee, H.-S. Oh, and U. Lee. “Design methodology for mass transfer-enhanced large-scale electrochemical reactor for CO_2 reduction”. *Chemical Engineering Journal* 424 (2021). DOI: 10.1016/j.cej.2021.130265 (cit. on p. 16).

[Kas2021] R. Kas, A. G. Star, K. Yang, T. Van Cleve, K. C. Neyerlin, and W. A. Smith. “Along the channel gradients impact on the spatioactivity of gas diffusion electrodes at high conversions during CO_2 electroreduction”. *ACS Sustainable Chemistry & Engineering* 9.3 (2021). DOI: 10.1021/acssuschemeng.0c07694 (cit. on pp. 5, 59, 92).

[Kasu1991] F. Kasuya and T. Tsuji. “High purity CO gas separation by pressure swing adsorption”. *Gas separation & purification* 5.4 (1991). DOI: 10.1016/0950-4214(91)80031-Y (cit. on p. 33).

[Keit2018] D. W. Keith, G. Holmes, D. S. Angelo, and K. Heidel. “A process for capturing CO_2 from the atmosphere”. *Joule* 2.8 (2018). DOI: 10.1016/j.joule.2018.05.006 (cit. on pp. 138, 140).

[Kim2013] Y. E. Kim, J. A. Lim, S. K. Jeong, Y. I. Yoon, S. T. Bae, and S. C. Nam. “Comparison of carbon dioxide absorption in aqueous MEA, DEA, TEA, and AMP solutions”. *Bulletin of the Korean Chemical Society* 34.3 (2013). DOI: 10.5012/bkcs.2013.34.3.783 (cit. on p. 30).

[Kim2015] B. Kim, S. Ma, H.-R. M. Jhong, and P. J. Kenis. “Influence of dilute feed and pH on electrochemical reduction of CO_2 to CO on Ag in a continuous flow electrolyzer”. *Electrochim. Acta* 166 (2015). DOI: 10.1016/j.electacta.2015.03.064 (cit. on pp. 21, 84, 126).

[Kim2016] B. Kim, F. Hillman, M. Ariyoshi, S. Fujikawa, and P. J. Kenis. “Effects of composition of the micro porous layer and the substrate on performance in the electrochemical reduction of CO_2 to CO”. *J. Power Sources* 312 (2016). DOI: 10.1016/j.jpowsour.2016.02.043 (cit. on p. 23).

[Kim2020] C. Kim, L.-C. Weng, and A. T. Bell. “Impact of pulsed electrochemical reduction of CO_2 on the formation of C2+ products over Cu”. *ACS Catalysis* 10.21 (2020). DOI: 10.1021/acscatal.0c02915 (cit. on pp. 22, 45).

[Ko2020] B. H. Ko, B. Hasa, H. Shin, E. Jeng, S. Overa, W. Chen, and F. Jiao. “The impact of nitrogen oxides on electrochemical carbon dioxide reduction”. *Nature communications* 11.1 (2020). DOI: 10.1038/s41467-020-19731-8 (cit. on p. 23).

[Koda2022] M. S. Kodaimati, R. Gao, S. E. Root, and G. M. Whitesides. “Magnetic fields enhance mass transport during electrocatalytic reduction of CO_2”. *Chem Catalysis* 2.4 (2022). DOI: 10.1016/j.checat.2022.01.023 (cit. on p. 16).

[Kost1994] R. Kostecki and J. Augustynski. “Electrochemical reduction of CO_2 at an activated silver electrode”. *Berichte der Bunsengesellschaft für physikalische Chemie* 98.12 (1994). (Cit. on p. 42).

[Kutz2017] R. B. Kutz, Q. Chen, H. Yang, S. D. Sajjad, Z. Liu, and I. R. Masel. “Sustainion imidazolium-functionalized polymers for carbon dioxide electrolysis”. *Energy Technology* 5.6 (2017). DOI: 10.1002/ente.201600636 (cit. on pp. 17, 23).

[Lama2022] S. Lamaison and D. Wakerley. “Dont cross the streams”. *Nature Catalysis* 5.4 (2022). DOI: 10.1038/s41929-022-00774-7 (cit. on p. 24).

[Land2018] M. Landstorfer. “On the dissociation degree of ionic solutions considering solvation effects”. *Electrochem. Commun.* 92 (2018). DOI: 10.1016/j.elecom.2018.05.011 (cit. on p. 79).

[Larr2019] G. O. Larrazábal, P. Strøm-Hansen, J. P. Heli, K. Zeiter, K. T. Therkildsen, I. Chorkendorff, and B. Seger. “Analysis of mass flows and membrane cross-over in CO_2 reduction at high current densities in an MEA-type electrolyzer”. *ACS applied materials & interfaces* 11.44 (2019). DOI: 10.1021/acsami.9b13 (cit. on pp. 110, 135, 138).

[Lee2001] J. Lee and Y. Tak. “Electrocatalytic activity of Cu electrode in electroreduction of CO_2”. *Electrochimica acta* 46.19 (2001). DOI: 10.1016/S0013-4686(01)00527-8 (cit. on pp. 22, 23).

[Lehn2014] M. Lehner, R. Tichler, H. Steinmüller, and M. Koppe. *Power-to-gas: technology and business models*. Springer, 2014. DOI: 10.1007/978-3-319-03995-4 (cit. on p. 103).

[Leon2020] M. E. Leonard, L. E. Clarke, A. Forner-Cuenca, S. M. Brown, and F. R. Brushett. “Investigating electrode flooding in a flowing electrolyte, gas-fed carbon dioxide electrolyzer”. *ChemSusChem* 13.2 (2020). DOI: 10.1002/cssc.201902547 (cit. on p. 79).

[Lepa2011] H. Lepaumier, E. F. da Silva, A. Einbu, A. Grimstvedt, J. N. Knudsen, K. Zahlsen, and H. F. Svendsen. “Comparison of MEA degradation in pilot-scale with lab-scale experiments”. *Energy Procedia* 4 (2011). DOI: 10.1016/j.egypro.2011.02.037 (cit. on p. 139).

[Li2016] X. Li, P. Anderson, H.-R. M. Jhong, M. Paster, J. F. Stubbins, and P. J. Kenis. “Greenhouse gas emissions, energy efficiency, and cost of synthetic fuel production using electrochemical CO_2 conversion and the Fischer–Tropsch process”. *Energy & Fuels* 30.7 (2016). DOI: 10.1021/acs.energyfuels.6b00665 (cit. on pp. 112, 131).

[Li2019] T. Li, E. W. Lees, M. Goldman, D. A. Salvatore, D. M. Weekes, and C. P. Berlinguette. “Electrolytic conversion of bicarbonate into CO in a flow cell”. *Joule* 3.6 (2019). DOI: 10.1016/j.joule.2019.05.021 (cit. on p. 24).

[Lin2019] M. Lin, L. Han, M. R. Singh, and C. Xiang. “An experimental- and simulation-based evaluation of the CO_2 utilization efficiency of aqueous-based electrochemical CO_2 reduction reactors with ion-selective membranes”. *ACS Applied Energy Materials* 2.8 (2019). DOI: 10.1021/acsaem.9b00986 (cit. on p. 112).

[Lins2005] P. J. Linstrom. “NIST chemistry webbook”. *http://webbook. nist. gov* (2005). (Cit. on p. 157).

[Liu2016] M. Liu, Y. Pang, B. Zhang, P. De Luna, O. Voznyy, J. Xu, X. Zheng, C. T. Dinh, F. Fan, C. Cao, et al. “Enhanced electrocatalytic CO_2 reduction via field-induced reagent concentration”. *Nature* 537.7620 (2016). DOI: 10.1038/nature19060 (cit. on p. 3).

[Liu2018] Z. Liu, H. Yang, R. Kutz, and R. I. Masel. “CO_2 electrolysis to CO and O_2 at high selectivity, stability and efficiency using Sustainion membranes”. *J. Electrochem. Soc.* 165.15 (2018). DOI: 10.1149/2.0501815jes (cit. on pp. 88, 110, 111, 114, 116, 128, 135, 154, 156).

[Liu2019] Y. Liu, K. Y. Leung, S. E. Michaud, T. L. Soucy, and C. C. McCrory. “Controlled Substrate Transport to Electrocatalyst Active Sites for Enhanced Selectivity in the Carbon Dioxide Reduction Reaction”. *Comments Inorg. Chem.* 39.5 (2019). DOI: 10.1080/02603594.2019.1628025 (cit. on p. 88).

[Lópe2022] A. P. López-Monroy and J. S. Garca-Salinas. “Neural networks and deep learning”. In*Biosignal Processing and Classification Using Computational Learning and Intelligence*. Elsevier, 2022. Pp. 177–196. (Cit. on p. 94).

[Löwe2019] A. Löwe, C. Rieg, T. Hierlemann, N. Salas, D. Kopljar, N. Wagner, and E. Klemm. “Influence of Temperature on the Performance of Gas Diffusion Electrodes in the CO_2 Reduction Reaction”. *ChemElectroChem* 6.17 (2019). DOI: 10.1002/celc.201900872 (cit. on p. 83).

[Lu2007] Y. Lu and T. Lee. “Influence of the feed gas composition on the Fischer-Tropsch synthesis in commercial operations”. *Journal of Natural Gas Chemistry* 16.4 (2007). DOI: 10.1016/S1003-9953(08)60001-8 (cit. on p. 115).

[Lu2014] Q. Lu, J. Rosen, Y. Zhou, G. S. Hutchings, Y. C. Kimmel, J. G. Chen, and F. Jiao. “A selective and efficient electrocatalyst for carbon dioxide reduction”. *Nature communications* 5.1 (2014). DOI: 10.1038/ncomms4242 (cit. on p. 42).

[Lu2020] X. Lu, C. Zhu, Z. Wu, J. Xuan, J. S. Francisco, and H. Wang. “In situ observation of the pH gradient near the gas diffusion electrode of CO_2 reduction in alkaline electrolyte”. *Journal of the American Chemical Society* 142.36 (2020). DOI: 10.1021/jacs.0c06779 (cit. on p. 50).

[Luc2019] W. Luc, B. H. Ko, S. Kattel, S. Li, D. Su, J. G. Chen, and F. Jiao. “SO2-induced selectivity change in CO_2 electroreduction”. *Journal of the American Chemical Society* 141.25 (2019). DOI: 10.1021/jacs.9b03215 (cit. on pp. 23, 24).

[Ludw2020] T. Ludwig, J. A. Gauthier, C. F. Dickens, K. S. Brown, S. Ringe, K. Chan, and J. K. Nørskov. “Atomistic insight into cation effects on binding energies in Cu-catalyzed carbon dioxide reduction”. *The Journal of Physical Chemistry C* 124.45 (2020). DOI: 10.1021/acs.jpcc.0c07004 (cit. on p. 36).

[Ma2017] L. Ma, S. Fan, D. Zhen, X. Wu, S. Liu, J. Lin, S. Huang, W. Chen, and G. He. “Electrochemical reduction of CO_2 in proton exchange membrane reactor: the function of buffer layer”. *Industrial & Engineering Chemistry Research* 56.37 (2017). DOI: 10.1021/acs.iecr.7b00819 (cit. on pp. 110, 112, 128).

[Ma2020a] M. Ma, E. L. Clark, K. T. Therkildsen, S. Dalsgaard, I. Chorkendorff, and B. Seger. “Insights into the carbon balance for CO_2 electroreduction on Ag using gas diffusion electrode reactor designs”. *Energy & Environmental Science* 13.3 (2020). DOI: 10.1039/d0ee00047g (cit. on pp. 110, 112, 138).

[Ma2020b] M. Ma, S. Kim, I. Chorkendorff, and B. Seger. “Role of ion-selective membranes in the carbon balance for CO_2 electroreduction via gas diffusion electrode reactor designs”. *Chemical science* 11.33 (2020). DOI: 10.1039/D0SC03047C (cit. on p. 112).

[Ma2022] Z. Ma, Z. Yang, W. Lai, Q. Wang, Y. Qiao, H. Tao, C. Lian, M. Liu, C. Ma, A. Pan, et al. “CO_2 electroreduction to multicarbon products in strongly acidic electrolyte via synergistically modulating the local microenvironment”. *Nature Communications* 13.1 (2022). DOI: s41467-022-35415-x (cit. on p. 19).

[Magn2019] O. M. Magnussen and A. GroSS. “Toward an atomic-scale understanding of electrochemical interface structure and dynamics”. *Journal of the American Chemical Society* 141.12 (2019). DOI: 10.1021/jacs.8b13188 (cit. on p. 36).

[Mard2021] P. Mardle, S. Cassegrain, F. Habibzadeh, Z. Shi, and S. Holdcroft. “Carbonate Ion Crossover in Zero-Gap, KOH Anolyte CO_2 Electrolysis”. *The Journal of Physical Chemistry C* 125.46 (2021). DOI: 10.1021/acs.jpcc.1c08430 (cit. on p. 18).

[Mart2015] A. J. Martín, G. O. Larrazábal, and J. Pérez-Ramírez. “Towards sustainable fuels and chemicals through the electrochemical reduction of CO_2: Lessons from water electrolysis”. *Green Chemistry* 17.12 (2015). DOI: 10.1039/c5gc01893e (cit. on p. 13).

[Mase2021] R. I. Masel, Z. Liu, H. Yang, J. J. Kaczur, D. Carrillo, S. Ren, D. Salvatore, and C. P. Berlinguette. “An industrial perspective on catalysts for low-temperature CO_2 electrolysis”. *Nature nanotechnology* 16.2 (2021). DOI: 10.1038/s41565-020-00823-x (cit. on p. 17).

[Mate2009] D. Materials. 2009. URL: https://dioxidematerials.com/ (visited on 01/20/2023) (cit. on p. 24).

[Meli2007] T. Melin and R. Rautenbach. *Membranverfahren: Grundlagen der Modul-und Anlagenauslegung*. Springer-Verlag, 2007 (cit. on pp. 25, 27, 28).

[Mist2016] H. Mistry, F. Behafarid, R. Reske, A. S. Varela, P. Strasser, and B. Roldan Cuenya. “Tuning catalytic selectivity at the mesoscale via interparticle interactions”. *Acs catalysis* 6.2 (2016). DOI: 10.1021/acscatal.5b02202 (cit. on p. 20).

[Molb] Molbase. *Iridium(IV) Oxide Preis*. URL: http://www.molbase.com/en/12030-49-8-moldata-1536144.html (visited on 10/12/2020) (cit. on p. 154).

[Mont2021] M. C. Monteiro, M. F. Philips, K. J. P. Schouten, and M. Koper. “Efficiency and selectivity of CO_2 reduction to CO on gold gas diffusion electrodes in acidic media”. *Nature communications* 12.1 (2021). DOI: 10.1038/s41467-021-24936-6 (cit. on p. 129).

[Mura1991] A. Murata and Y. Hori. “Product selectivity affected by cationic species in electrochemical reduction of CO_2 and CO at a Cu electrode”. *Bull. Chem. Soc. Jpn.* 64.1 (1991). DOI: 10.1246/bcsj.64.123 (cit. on pp. 20, 78).

[Mura2010] R. S. Murali, S. Sridhar, T. Sankarshana, and Y. Ravikumar. “Gas permeation behavior of Pebax-1657 nanocomposite membrane incorporated with multiwalled carbon nanotubes”. *Industrial & Engineering Chemistry Research* 49.14 (2010). DOI: 10.1021/ie9016495 (cit. on pp. 118, 153).

[Muro2020] A. P. Muroyama, A. Ptru, and L. Gubler. “CO_2 separation and transport via electrochemical methods”. *Journal of The Electrochemical Society* 167.13 (2020). DOI: 10.1149/1945-7111/abbbb9 (cit. on p. 18).

[Newm1962] J. S. Newman and C. W. Tobias. “Theoretical analysis of current distribution in porous electrodes”. *J. Electrochem. Soc.* 109.12 (1962). DOI: 10.1149/1.2425269 (cit. on p. 65).

[Newm2004] J. S. Newman and K. E. Thomas-Alyea. *Electrochemical systems*. 3. ed. Electrochemical Society series. Hoboken, N.J.: Wiley, 2004 (cit. on pp. 65, 149–152).

[Nigh1959] E. Nightingale Jr. “Phenomenological theory of ion solvation. Effective radii of hydrated ions”. *The Journal of Physical Chemistry* 63.9 (1959). (Cit. on p. 150).

[Niu2018] Z. Niu, Z. Bao, J. Wu, Y. Wang, and K. Jiao. “Two-phase flow in the mixed-wettability gas diffusion layer of proton exchange membrane fuel cells”. *Applied Energy* 232 (2018). DOI: 10.1016/j.apenergy.2018.09.209 (cit. on p. 105).

[Nwab2020] U. O. Nwabara, E. R. Cofell, S. Verma, E. Negro, and P. J. Kenis. “Durable cathodes and electrolyzers for the efficient aqueous electrochemical reduction of CO_2”. *ChemSusChem* 13.5 (2020). DOI: 10.1002/cssc.201902933 (cit. on p. 23).

[Nwab2021] U. O. Nwabara, A. D. Hernandez, D. A. Henckel, X. Chen, E. R. Cofell, M. P. De-Heer, S. Verma, A. A. Gewirth, and P. J. Kenis. “Binder-Focused Approaches to Improve the Stability of Cathodes for CO_2 Electroreduction”. *ACS Applied Energy Materials* 4.5 (2021). DOI: 10.1021/acsaem.1c00715 (cit. on p. 110).

[Ogur2010] K. Ogura, J. R. Ferrell III, A. V. Cugini, E. S. Smotkin, and M. D. Salazar-Villalpando. “CO_2 attraction by specifically adsorbed anions and subsequent accelerated electrochemical reduction”. *Electrochimica acta* 56.1 (2010). DOI: 10.1016/j.electacta.2010.08.065 (cit. on p. 20).

[Ozde2020] A. Ozden, F. Li, F. P. Garcia de Arquer, A. Rosas-Hernández, A. Thevenon, Y. Wang, S.-F. Hung, X. Wang, B. Chen, J. Li, et al. “High-Rate and Efficient Ethylene Electrosynthesis Using a Catalyst/Promoter/Transport Layer”. *ACS Energy Lett.* 5.9 (2020). DOI: 10.1021/acsenergylett.0c01266 (cit. on p. 88).

[Pan2022] B. Pan, J. Fan, J. Zhang, Y. Luo, C. Shen, C. Wang, Y. Wang, and Y. Li. “Close to 90% Single-Pass Conversion Efficiency for CO_2 Electroreduction in an Acid-Fed Membrane Electrode Assembly”. *ACS Energy Letters* 7 (2022). DOI: 10.1021/acsenergylett.2c02292 (cit. on p. 129).

[Pang2022] X. Pang, S. Verma, C. Liu, and D. V. Esposito. “Membrane-free electrochemical CO_2 conversion using serially connected porous flow-through electrodes”. *Joule* 6.12 (2022). DOI: 10.1016/j.joule.2022.11.003 (cit. on p. 24).

[Parr2014] J. Parrondo, C. G. Arges, M. Niedzwiecki, E. B. Anderson, K. E. Ayers, and V. Ramani. “Degradation of anion exchange membranes used for hydrogen production by ultrapure water electrolysis”. *Rsc Advances* 4.19 (2014). DOI: 10.1039/C3RA46630B (cit. on p. 138).

[Pasz2017] A. Paszke, S. Gross, S. Chintala, G. Chanan, E. Yang, Z. DeVito, Z. Lin, A. Desmaison, L. Antiga, and A. Lerer. “Automatic differentiation in PyTorch”. In*NIPS-W*. 2017 (cit. on p. 96).

[Patr2019] A. Patru, T. Binninger, B. Pribyl, and T. J. Schmidt. “Design principles of bipolar electrochemical co-electrolysis cells for efficient reduction of carbon dioxide from gas phase at low temperature”. *Journal of The Electrochemical Society* 166.2 (2019). DOI: 10.1149/2.1221816jes (cit. on pp. 111, 112).

[Paul1979] D. Paul. “Gas sorption and transport in glassy polymers”. *Berichte der Bunsengesellschaft für physikalische Chemie* 83.4 (1979). DOI: 10.1002/bbpc.19790830403 (cit. on p. 27).

[Paul1988] J. Paul and F. Hoffmann. “CO_2 conversion and oxalate stability on alkali promoted metal surfaces: Sodium modified Al (100)”. *Catalysis letters* 1.12 (1988). DOI: 10.1007/BF00766205 (cit. on p. 74).

[Perc2018] K. Percin, A. Rommerskirchen, R. Sengpiel, Y. Gendel, and M. Wessling. “3D-printed conductive static mixers enable all-vanadium redox flow battery using slurry electrodes”. *Journal of power sources* 379 (2018). DOI: 10.1016/j.jpowsour.2018.01.061 (cit. on p. 16).

[Petr2018] J. Petropoulos. “Mechanisms and theories for sorption and diffusion of gases in polymers”. In*Polymeric gas separation membranes*. CRC Press, 2018. Pp. 17–81. (Cit. on p. 27).

[Petr2022] K. V. Petrov, J. Bui, L. M. Baumgartner, L.-C. Weng, S. Dischinger, D. M. Larson, D. Miller, A. Z. Weber, and D. A. Vermaas. “Anion-exchange membranes with internal microchannels for water control in CO_2 electrolysis”. *Sustainable Energy & Fuels* (2022). DOI: 10.1039/d2se00858k (cit. on p. 135).

[Pinn2011] S. Pinnow, N. Chavan, and T. Turek. “Thin-film flooded agglomerate model for silver-based oxygen depolarized cathodes”. *J. Appl. Electrochem.* 41.9 (2011). DOI: 10.1007/s10800-011-0311-2 (cit. on p. 65).

[Ponn2017] S. Ponnurangam, I. V. Chernyshova, and P. Somasundaran. “Nitrogen-containing polymers as a platform for CO_2 electroreduction”. *Adv. Colloid Interface Sci.* 244 (2017). DOI: 10.1016/j.cis.2016.09.002 (cit. on p. 88).

[Prib2021] B. Pribyl-Kranewitter, A. Beard, T. Schuler, N. Dikli, and T. J. Schmidt. “Investigation and optimisation of operating conditions for low-temperature CO_2 reduction to CO in a forward-bias bipolar-membrane electrolyser”. *Journal of The Electrochemical Society* 168.4 (2021). DOI: 10.1149/1945-7111/abf063 (cit. on p. 18).

[Prib2022] B. Pribyl-Kranewitter, A. Beard, C. Gjiu, D. Dinculescu, and T. Schmidt. “Influence of low-temperature electrolyser design on economic and environmental potential of CO and HCOOH production: A techno-economic assessment”. *Renewable and Sustainable Energy Reviews* 154 (2022). DOI: 10.1016/j.rser.2021.111807 (cit. on p. 112).

[R L 2003] R. L. Rowley, W. V. Wilding, J. L. Oscarson, Y. Yang, N. A. Zundel, T. E. Daubert, R. P. Danner. *DIPPR Data Compilation of Pure Compound Properties*. New York, NY, 2003 (cit. on pp. 62, 151).

[Rabi2020] J. A. Rabinowitz and M. W. Kanan. “The future of low-temperature carbon dioxide electrolysis depends on solving one basic problem”. *Nature Communications* 11.1 (2020). DOI: 10.1038/s41467-020-19135-8 (cit. on pp. 18, 110, 112, 137, 138).

[Rasc2019] S. Raschka and V. Virjalili. *Python Machine Learning. Machine Learning and Deep Learning with Python, scikit-learn, and TensorFlow 2*. Packt Publishing, 2019 (cit. on pp. 93, 94).

[Rene2018] RenewCO_2. 2018. URL: https://www.renewco2.com/ (visited on 01/20/2023) (cit. on p. 24).

[Resa2017] J. Resasco, L. D. Chen, E. Clark, C. Tsai, C. Hahn, T. F. Jaramillo, K. Chan, and A. T. Bell. “Promoter effects of alkali metal cations on the electrochemical reduction of carbon dioxide”. *Journal of the*

American Chemical Society 139.32 (2017). DOI: 10.1021/jacs.7b06765 (cit. on pp. 3, 36, 74).

[Resa2018] J. Resasco, Y. Lum, E. Clark, J. Z. Zeledon, and A. T. Bell. "Effects of anion identity and concentration on electrochemical reduction of CO_2". *ChemElectroChem* 5.7 (2018). DOI: 10.1002/celc.201701316 (cit. on p. 20).

[Rieb2011] U. Riebesell, V. J. Fabry, L. Hansson, and J.-P. Gattuso. *Guide to best practices for ocean acidification research and data reporting*. Office for Official Publications of the European Communities, 2011 (cit. on p. 43).

[Ring2019] S. Ringe, E. L. Clark, J. Resasco, A. Walton, B. Seger, A. T. Bell, and K. Chan. "Understanding cation effects in electrochemical CO_2 reduction". *Energy Environ. Sci.* 12.10 (2019). DOI: 10.1039/C9EE01341E (cit. on p. 74).

[Ring2020] S. Ringe, C. G. Morales-Guio, L. D. Chen, M. Fields, T. F. Jaramillo, C. Hahn, and K. Chan. "Double layer charging driven carbon dioxide adsorption limits the rate of electrochemical carbon dioxide reduction on Gold". *Nature communications* 11.1 (2020). DOI: 10.1038/s41467-019-13777-z (cit. on pp. 36, 37).

[Roch2009] G. T. Rochelle. "Amine scrubbing for CO_2 capture". *Science* 325.5948 (2009). DOI: 10.1126/science.1176731 (cit. on pp. 29, 30, 139).

[Roge2017] C. Rogers, W. S. Perkins, G. Veber, T. E. Williams, R. R. Cloke, and F. R. Fischer. "Synergistic enhancement of electrocatalytic CO_2 reduction with gold nanoparticles embedded in functional graphene nanoribbon composite electrodes". *Journal of the American Chemical Society* 139.11 (2017). DOI: 10.1021/jacs.6b12217 (cit. on p. 23).

[Roh2021] K. Roh, L. Brée, P. Schäfer, D. Strohmeier, and A. Mitsos. "Flexible operation of modular electrochemical CO_2 reduction processes". *ChemRxiv. Cambridge: Cambridge Open Engage* (2021). DOI: 10.26434/chemrxiv-2021-49lwd (cit. on p. 113).

[Rous1987] R. W. Rousseau. *Handbook of separation process technology*. John Wiley & Sons, 1987 (cit. on pp. 28, 32).

[Ruma2019] M. Rumayor, A. Dominguez-Ramos, P. Perez, and A. Irabien. “A techno-economic evaluation approach to the electrochemical reduction of CO_2 for formic acid manufacture”. *Journal of CO_2 Utilization* 34 (2019). DOI: 10.1016/j.jcou.2019.07.024 (cit. on p. 112).

[Ruth1984] D. M. Ruthven. *Principles of adsorption and adsorption processes*. John Wiley & Sons, 1984 (cit. on p. 32).

[Salv2017] D. A. Salvatore, D. M. Weekes, J. He, K. E. Dettelbach, Y. C. Li, T. E. Mallouk, and C. P. Berlinguette. “Electrolysis of Gaseous CO_2 to CO in a Flow Cell with a Bipolar Membrane”. *ACS Energy Letters* 3.1 (2017). DOI: 10.1021/acsenergylett.7b01017 (cit. on pp. 111, 112, 114, 116, 128, 154, 156).

[Salv2019] D. Salvatore and C. P. Berlinguette. “Voltage matters when reducing CO_2 in an electrochemical flow cell”. *ACS Energy Letters* 5.1 (2019). DOI: 10.1021/acsenergylett.9b02356 (cit. on p. 112).

[Salv2021] D. A. Salvatore, C. M. Gabardo, A. Reyes, C. P. OBrien, S. Holdcroft, P. Pintauro, B. Bahar, M. Hickner, C. Bae, D. Sinton, et al. “Designing anion exchange membranes for CO_2 electrolysers”. *Nature Energy* 6.4 (2021). DOI: 10.1038/s41560-020-00761-x (cit. on p. 111).

[Schm2003] V. M. Schmidt. *Elektrochemische Verfahrenstechnik: Grundlagen, Reaktionstechnik, Prozeszoptimierung*. Weinheim: WileyVCH Verlag GmbH & Co. KGaA, 2003. DOI: 10.1002/ange.200385119 (cit. on pp. 10–14, 65).

[Schn2011] M. Schneider, M. Romer, M. Tschudin, and H. Bolio. “Sustainable cement productionâpresent and future”. *Cement and concrete research* 41.7 (2011). DOI: 10.1016/j.cemconres.2011.03.019 (cit. on p. 121).

[Scho2013a] M. Scholz, B. Frank, F. Stockmeier, S. Falss, and M. Wessling. “Techno-economic analysis of hybrid processes for biogas upgrading”. *Industrial & Engineering Chemistry Research* 52.47 (2013). DOI: 10.1021/ie402660s (cit. on pp. 117, 121).

[Scho2013b] M. Scholz, T. Melin, and M. Wessling. “Transforming biogas into biomethane using membrane technology”. *Renewable and Sustainable Energy Reviews* 17 (2013). DOI: 10.1016/j.rser.2012.08.009 (cit. on p. 113).

[Scho2015] M. Scholz, M. Alders, T. Lohaus, and M. Wessling. “Structural optimization of membrane-based biogas upgrading processes”. *Journal of membrane science* 474 (2015). DOI: 10.1016/j.memsci.2014.08.032 (cit. on p. 115).

[Schu2006] K. G. Schulz, U. Riebesell, B. Rost, S. Thoms, and R. E. Zeebe. “Determination of the rate constants for the carbon dioxide to bicarbonate inter-conversion in pH-buffered seawater systems”. *Mar. Chem.* 100.1-2 (2006). DOI: 10.1016/j.marchem.2005.11.001 (cit. on pp. 66, 152).

[Scot2020] Scott Jenkins. *2019 Chemical Engineering plant cost index annual average*. 2020. URL: https://www.chemengonline.com/2019-chemical-engineering-plant-cost-index-annual-average/ (visited on 10/28/2020) (cit. on p. 155).

[Shen2017] C. Shen, R. Wycisk, and P. N. Pintauro. “High performance electrospun bipolar membrane with a 3D junction”. *Energy & Environmental Science* 10.6 (2017). DOI: 10.1039/C7EE00345E (cit. on p. 18).

[Shi2020] R. Shi, J. Guo, X. Zhang, G. I. Waterhouse, Z. Han, Y. Zhao, L. Shang, C. Zhou, L. Jiang, and T. Zhang. “Efficient wettability-controlled electroreduction of CO_2 to CO at Au/C interfaces”. *Nat. Commun.* 11.1 (2020). DOI: 10.1038/s41467-020-16847-9 (cit. on p. 58).

[Shin2021] H. Shin, K. U. Hansen, and F. Jiao. “Techno-economic assessment of low-temperature carbon dioxide electrolysis”. *Nature Sustainability* (2021). DOI: 10.1038/s41893-021-00739-x (cit. on pp. 33, 112, 123, 125, 139, 140).

[Shin2022] S.-J. Shin, D. H. Kim, G. Bae, S. Ringe, H. Choi, H.-K. Lim, C. H. Choi, and H. Kim. “On the importance of the electric double layer structure in aqueous electrocatalysis”. *Nature communications* 13.1 (2022). DOI: 10.1038/s41467-021-27909-x (cit. on p. 36).

[Shuk2019] P. R. Shukla, J. Skeg, E. C. Buendia, V. Masson-Delmotte, H.-O. Pörtner, D. Roberts, P. Zhai, R. Slade, S. Connors, S. Van Diemen, et al. “Climate Change and Land: an IPCC special report on climate change, desertification, land degradation, sustainable land management, food security, and greenhouse gas fluxes in terrestrial ecosystems”. (2019). (Cit. on p. 1).

[Sing2015] M. R. Singh, E. L. Clark, and A. T. Bell. “Effects of electrolyte, catalyst, and membrane composition and operating conditions on the performance of solar-driven electrochemical reduction of carbon dioxide”. *Physical Chemistry Chemical Physics* 17.29 (2015). DOI: 10.1039/C5CP03283K (cit. on pp. 149, 150).

[Sing2017] M. R. Singh, J. D. Goodpaster, A. Z. Weber, M. Head-Gordon, and A. T. Bell. “Mechanistic insights into electrochemical reduction of CO_2 over Ag using density functional theory and transport models”. *Proceedings of the National Academy of Sciences* 114.42 (2017). DOI: 10.1073/pnas.1713164114 (cit. on pp. 62, 149, 150).

[Skar1960] C. W. Skarstrom. *Method and apparatus for fractionating gaseous mixtures by adsorption*. US Patent 2,944,627. July 1960 (cit. on p. 32).

[Solc2001] O. Solcová, H. Snajdaufová, and P. Schneider. “Multicomponent counter-current gas diffusion in porous solids: the Graham’s-law diffusion cell”. *Chemical Engineering Science* 56.17 (2001). DOI: 10.1016/S0009-2509(01)00149-X (cit. on p. 64).

[Spör2017] C. Spöri, J. T. H. Kwan, A. Bonakdarpour, D. P. Wilkinson, and P. Strasser. “The Stability Challenges of Oxygen Evolving Catalysts: Towards a Common Fundamental Understanding and Mitigation of Catalyst Degradation”. *Angewandte Chemie (International ed. in English)* 56.22 (2017). DOI: 10.1002/anie.201608601 (cit. on p. 154).

[Spur2018] J. M. Spurgeon and B. Kumar. “A comparative technoeconomic analysis of pathways for commercial electrochemical CO_2 reduction to liquid products”. *Energy & Environmental Science* 11.6 (2018). DOI: 10.1021/acs.iecr.7b03514 (cit. on pp. 33, 112).

[Step2022] I. E. Stephens, K. Chan, A. Bagger, S. W. Boettcher, J. Bonin, E. Boutin, A. K. Buckley, R. Buonsanti, E. R. Cave, X. Chang, et al. “2022 roadmap on low temperature electrochemical CO_2 reduction”. *Journal of Physics: Energy* 4.4 (2022). DOI: 10.1088/2515-7655/ac7823 (cit. on pp. 17, 23).

[Sull2012] B. P. Sullivan. *Electrochemical and Electrocatalytic Reactions of Carbon Dioxide*. Burlington: Elsevier Science, 2012 (cit. on p. 66).

[Suwa2003] R. Suwanwarangkul, E. Croiset, M. W. Fowler, P. L. Douglas, E. Entchev, and M. A. Douglas. “Performance comparison of Fick’s, dusty-gas and Stefan–Maxwell models to predict the concentration overpotential of a SOFC anode”. *J. Power Sources* 122.1 (2003). DOI: 10.1016/S0378-7753(02)00724-3 (cit. on p. 59).

[T Sm2011] J. T. Smolinka M. Günther. *NOW-Studie: Stand und Entwicklungspotenzial der Wasserelektrolyse zur Herstellung von Wasserstoff aus regenerativen Energien, Revision, 1st ed.* Tech. rep. Frauenhofer ISE, 2011 (cit. on p. 122).

[Tafe1905a] J. Tafel. “Über die Polarisation bei kathodischer Wasserstoffentwicklung”. *Zeitschrift für physikalische Chemie* 50.1 (1905). (Cit. on p. 14).

[Tafe1905b] J. Tafel and K. Naumann. “Beziehungen zwischen Kathodenpotential und elektrolytischer Reduktionswirkung”. *Zeitschrift für Physikalische Chemie* 50.1 (1905). (Cit. on p. 14).

[Tan2020] Y. C. Tan, K. B. Lee, H. Song, and J. Oh. “Modulating Local CO_2 Concentration as a General Strategy for Enhancing C- C Coupling in CO_2 Electroreduction”. *Joule* 4.5 (2020). DOI: 10.1016/j.joule.2020.03.013 (cit. on pp. 59, 60).

[Thor2012] M. R. Thorson, K. I. Siil, and P. J. Kenis. “Effect of cations on the electrochemical conversion of CO_2 to CO”. *J. Electrochem. Soc.* 160.1 (2012). DOI: 10.1149/2.052301jes (cit. on p. 74).

[Torl2018] M. Torli, L. Geer, G. M. Kontogeorgis, and P. L. Fosbøl. “Solubility of Syngas Components in Water, Acetic Acid, and Alcohol Using New Standard Fugacity Methodology”. *Ind. Eng. Chem. Res.* 57.49 (2018). DOI: 10.1021/acs.iecr.8b03954 (cit. on p. 67).

[twel2015] twelve. 2015. URL: https://www.twelve.co/ (visited on 01/20/2023) (cit. on p. 24).

[Van 2022] S. Van Daele, L. Hintjens, J. Van den Hoek, S. Neukermans, N. Daems, J. Hereijgers, and T. Breugelmans. “Influence of the target product on the electrochemical reduction of diluted CO_2 in a continuous flow cell”. *Journal of CO_2 Utilization* 65 (2022). DOI: 10.1016/j.jcou.2022.102210 (cit. on p. 21).

[Vass2022] Á. Vass, A. Kormányos, Z. Kószó, B. Endrodi, and C. Janáky. “Anode Catalysts in CO_2 Electrolysis: Challenges and Untapped Opportunities”. *ACS Catalysis* 12 (2022). DOI: 10.1021/acscatal.1c04978 (cit. on p. 129).

[Vata2002] W. M. Vatavuk et al. “Updating the CE plant cost index”. *Chemical Engineering* 109.1 (2002). (Cit. on p. 155).

[Venn2019a] J.-B. Vennekoetter, R. Sengpiel, and M. Wessling. “Beyond the catalyst: How electrode and reactor design determine the product spectrum during electrochemical CO_2 reduction”. *Chemical Engineering Journal* 364 (2019). DOI: 10.1016/j.cej.2019.01.045 (cit. on pp. 19, 58, 59, 85, 111, 112, 114, 116, 128, 154, 156).

[Venn2019b] J.-B. Vennekötter, T. Scheuermann, R. Sengpiel, and M. Wessling. “The electrolyte matters: Stable systems for high rate electrochemical CO_2 reduction”. *J. CO_2 Util.* 32 (2019). DOI: 10.1016/j.jcou.2019.04.007 (cit. on p. 111).

[Verm1998] P. Vermeiren, W. Adriansens, J. Moreels, and R. Leysen. “Evaluation of the Zirfonő separator for use in alkaline water electrolysis and Ni-H2 batteries”. *International Journal of Hydrogen Energy* 23.5 (1998). DOI: 10.1016/S0360-3199(97)00069-4 (cit. on p. 20).

[Verm2016a] S. Verma, B. Kim, H.-R. Jhong, S. Ma, and P. J. Kenis. “A gross-margin model for defining technoeconomic benchmarks in the electroreduction of CO_2”. *ChemSusChem* 9.15 (2016). DOI: 10.1002/cssc.201600394 (cit. on pp. 2, 112, 123, 124, 131).

[Verm2016b] S. Verma, X. Lu, S. Ma, R. I. Masel, and P. J. Kenis. “The effect of electrolyte composition on the electroreduction of CO_2 to CO on Ag based gas diffusion electrodes”. *Phys. Chem. Chem. Phys.* 18.10

(2016). DOI: 10.1039/C5CP05665A (cit. on pp. 18, 20, 52, 60, 70, 73, 74, 87, 151).

[Vija2005] B. Vijayasekaran and C. Ahmed Basha. “Modeling in Electrochemical Engineering – A critical review”. *Transactions of the SAEST* 40.1 (2005). (Cit. on p. 67).

[Webe1970] H. Weber and J. Falbe. “Oxo Synthesis Technology”. *Industrial & Engineering Chemistry* 62.4 (1970). (Cit. on p. 115).

[Weis1996] S. Weisenberger and d. A. Schumpe. “Estimation of gas solubilities in salt solutions at temperatures from 273 K to 363 K”. *AIChE Journal* 42.1 (1996). DOI: 10.1002/aic.690420130 (cit. on pp. 43, 150).

[Weng2018] L.-C. Weng, A. T. Bell, and A. Z. Weber. “Modeling gas-diffusion electrodes for CO_2 reduction”. *Phys. Chem. Chem. Phys.* 20.25 (2018). DOI: 10.1039/C8CP01319E (cit. on pp. 58, 59, 85, 105).

[Weng2019] L.-C. Weng, A. T. Bell, and A. Z. Weber. “Towards membrane-electrode assembly systems for CO_2 reduction: a modeling study”. *Energy & Environmental Science* 12.6 (2019). DOI: 10.1039/C9EE00909D (cit. on p. 59).

[Whee2020] D. G. Wheeler, B. A. Mowbray, A. Reyes, F. Habibzadeh, J. He, and C. P. Berlinguette. “Quantification of water transport in a CO_2 electrolyzer”. *Energy Environ. Sci.* 13.12 (2020). DOI: 10.1039/D0EE02219E (cit. on p. 61).

[Whip2010a] D. T. Whipple, E. C. Finke, and P. J. Kenis. “Microfluidic reactor for the electrochemical reduction of carbon dioxide: the effect of pH”. *Electrochemical and Solid-State Letters* 13.9 (2010). DOI: 10.1149/1.3456590 (cit. on pp. 17, 151).

[Whip2010b] D. T. Whipple, E. C. Finke, and P. J. A. Kenis. “Microfluidic Reactor for the Electrochemical Reduction of Carbon Dioxide: The Effect of pH”. *Electrochem. Solid-State Lett.* 13.9 (2010). (Cit. on p. 73).

[Wijm2006] J. G. Wijmans and R. W. Baker. “The solution-diffusion model: a unified approach to membrane permeation”. *Materials science of membranes for gas and vapor separation* 1 (2006). (Cit. on pp. 25, 27).

[Wils2020] S. M. Wilson, D. A. Kennedy, and F. Tezel. “Adsorbent screening for CO_2/CO separation for applications in syngas production”. *Separation and Purification Technology* 236 (2020). DOI: 10.1016/j.seppur.2019.116268 (cit. on p. 33).

[Wu2014] K. Wu, E. Birgersson, P. J. Kenis, and I. A. Karimi. “Modeling and Simulating Electrochemical Reduction of CO_2 in a Microfluidic Cell”. In*Comput.-Aided Chem. Eng.* Vol. 34. Elsevier, 2014. Pp. 639–644. (Cit. on pp. 58, 59).

[Wu2016] J. Wu, S.-G. Sun, and X.-D. Zhou. “Origin of the performance degradation and implementation of stable tin electrodes for the conversion of CO_2 to fuels”. *Nano Energy* 27 (2016). DOI: 10.1016/j.nanoen.2016.06.028 (cit. on p. 23).

[Wu2022] Y. Wu, L. Charlesworth, I. Maglaya, M. N. Idros, M. Li, T. Burdyny, G. Wang, and T. E. Rufford. “Mitigating Electrolyte Flooding for Electrochemical CO_2 Reduction via Infiltration of Hydrophobic Particles in a Gas Diffusion Layer”. *ACS Energy Letters* 7.9 (2022). DOI: 10.1021/acsenergylett.2c01555 (cit. on p. 19).

[Xia2019] C. Xia, P. Zhu, Q. Jiang, Y. Pan, W. Liang, E. Stavitski, H. N. Alshareef, and H. Wang. “Continuous production of pure liquid fuel solutions via electrocatalytic CO_2 reduction using solid-electrolyte devices”. *Nature Energy* 4.9 (2019). DOI: 10.1038/s41560-019-0451-x (cit. on p. 24).

[Xie2022a] K. Xie, R. K. Miao, A. Ozden, S. Liu, Z. Chen, C.-T. Dinh, J. E. Huang, Q. Xu, C. M. Gabardo, G. Lee, et al. “Bipolar membrane electrolyzers enable high single-pass CO_2 electroreduction to multicarbon products”. *Nature communications* 13.1 (2022). DOI: 10.1038/s41467-022-31295-3 (cit. on p. 112).

[Xie2022b] K. Xie, A. Ozden, R. K. Miao, Y. Li, D. Sinton, and E. H. Sargent. “Eliminating the need for anodic gas separation in CO_2 electroreduction systems via liquid-to-liquid anodic upgrading”. *Nature Communications* 13.1 (2022). (Cit. on p. 140).

[Xie2022c] Y. Xie, P. Ou, X. Wang, Z. Xu, Y. C. Li, Z. Wang, J. E. Huang, J. Wicks, C. McCallum, N. Wang, et al. “High carbon utilization in CO_2 reduction to multi-carbon products in acidic media”. *Nature*

Catalysis (2022). DOI: 10.1038/s41929-022-00788-1 (cit. on pp. 19, 129).

[Xu2013] L. Xu, W. Li, Y. You, S. Zhang, and Y. Zhao. “Polysulfone and zirconia composite separators for alkaline water electrolysis”. *Frontiers of Chemical Science and Engineering* 7 (2013). DOI: 10.1007/s11705-013-1331-8 (cit. on p. 20).

[Xu2020] Y. Xu, J. P. Edwards, J. Zhong, C. P. OBrien, C. M. Gabardo, C. McCallum, J. Li, C.-T. Dinh, E. H. Sargent, and D. Sinton. “Oxygen-tolerant electroproduction of C 2 products from simulated flue gas”. *Energy & Environmental Science* 13.2 (2020). DOI: 10.1039/C9EE03077H (cit. on pp. 23, 24).

[Xu2021] Y. Xu, J. P. Edwards, S. Liu, R. K. Miao, J. E. Huang, C. M. Gabardo, C. P. OBrien, J. Li, E. H. Sargent, and D. Sinton. “Self-cleaning CO_2 reduction systems: unsteady electrochemical forcing enables stability”. *ACS Energy Letters* 6.2 (2021). DOI: 10.1021/acsenergylett.0c02401 (cit. on pp. 18, 23, 78, 82, 135).

[Yamp2006] Y. Yampolskii, I. Pinnau, and B. D. Freeman. *Materials science of membranes for gas and vapor separation*. 2006 (cit. on p. 28).

[Yang2020] K. Yang, R. Kas, W. A. Smith, and T. Burdyny. “Role of the carbon-based gas diffusion layer on flooding in a gas diffusion electrode cell for electrochemical CO_2 reduction”. *ACS Energy Letters* 6.1 (2020). DOI: 10.1021/acsenergylett.0c02184 (cit. on p. 19).

[Yang2021a] K. Yang, M. Li, S. Subramanian, M. A. Blommaert, W. A. Smith, and T. Burdyny. “Cation-driven increases of CO_2 utilization in a bipolar membrane electrode assembly for CO_2 electrolysis”. *ACS energy letters* 6.12 (2021). DOI: 10.1021/acsenergylett.1c02058 (cit. on p. 18).

[Yang2021b] Y. Yang, Y. Feng, K. Li, S. Ajmal, H. Cheng, K. Gong, and L. Zhang. “Ultrasound-boosted selectivity of CO in CO_2 electrochemical reduction”. *Ultrasonics sonochemistry* 76 (2021). DOI: 10.1016/j.ultsonch.2021.105623 (cit. on p. 16).

[Yin2019] Z. Yin, H. Peng, X. Wei, H. Zhou, J. Gong, M. Huai, L. Xiao, G. Wang, J. Lu, and L. Zhuang. “An alkaline polymer electrolyte CO_2 electrolyzer operated with pure water”. *Energy & Environmental Science* 12.8 (2019). DOI: 10.1039/C9EE01204D (cit. on p. 135).

[Yu2023] T. Yu, H. Tao, J. Li, C. Lian, and H. Liu. “Regulation of electrical double layers promotes electrochemical reduction of carbon dioxide”. *Chemical Engineering Science* (2023). DOI: 10.1016/j.ces.2023.118759 (cit. on p. 37).

[Yuan2014] J. Yuan and B. Sundén. “On mechanisms and models of multicomponent gas diffusion in porous structures of fuel cell electrodes”. *Int. J. Heat Mass Transfer* 69 (2014). DOI: 10.1016/j.ijheatmasstransfer.2013.10.032 (cit. on pp. 62, 63).

[Yuba2008] C. Yubao, N. Ping, X. Youchang, C. Yunhua, S. Hao, and L. Zhiyun. “Pilot-scale experiment for purification of CO from industrial tail gases by pressure swing adsorption”. *Chinese Journal of Chemical Engineering* 16.5 (2008). DOI: 10.1016/S1004-9541(08)60145-7 (cit. on p. 33).

[Zaer2012] F. Zaera. “Probing liquid/solid interfaces at the molecular level”. *Chemical reviews* 112.5 (2012). DOI: 10.1021/cr2002068 (cit. on p. 36).

[Zeny2016] I. V. Zenyuk, P. K. Das, and A. Z. Weber. “Understanding Impacts of Catalyst-Layer Thickness on Fuel-Cell Performance via Mathematical Modeling”. *J. Electrochem. Soc.* 163.7 (2016). DOI: 10.1149/2.1161607jes (cit. on p. 151).

[Zhai2009] Y. Zhai, L. Chiachiarelli, and N. Sridhar. “Effect of gaseous impurities on the electrochemical reduction of CO_2 on copper electrodes”. *ECS Transactions* 19.14 (2009). DOI: 10.1149/1.3220175 (cit. on p. 23).

[Zhan2011] Y. Zhang, H. Que, and C.-C. Chen. “Thermodynamic modeling for CO_2 absorption in aqueous MEA solution with electrolyte NRTL model”. *Fluid Phase Equilibria* 311 (2011). DOI: 10.1016/j.fluid.2011.08.025 (cit. on p. 30).

[Zhan2020] Z. Zhang, L. Melo, R. P. Jansonius, F. Habibzadeh, E. R. Grant, and C. P. Berlinguette. “pH matters when reducing CO_2 in an electrochemical flow cell”. *ACS Energy Letters* 5.10 (2020). DOI: /10.1021/acsenergylett.0c016 (cit. on pp. 47, 49, 50).

[Zhao2009] L. Zhao, R. Menzer, E. Riensche, L. Blum, and D. Stolten. “Concepts and investment cost analyses of multi-stage membrane systems used in post-combustion processes”. *Energy Procedia* 1.1 (2009). DOI: 10.1016/j.egypro.2009.01.038 (cit. on pp. 121, 122, 153).

[Zhen2019] T. Zheng, K. Jiang, N. Ta, Y. Hu, J. Zeng, J. Liu, and H. Wang. “Large-scale and highly selective CO_2 electrocatalytic reduction on nickel single-atom catalyst”. *Joule* 3.1 (2019). DOI: 10.1016/j.joule.2018.10.015 (cit. on p. 110).

[Zhon2017] H. Zhong, K. Fujii, and Y. Nakano. “Effect of KHCO3 concentration on electrochemical reduction of CO_2 on copper electrode”. *Journal of The Electrochemical Society* 164.9 (2017). DOI: 10.1149/2.0601709jes (cit. on p. 52).

[Zhou1989] S. Zhou and S. Stern. “The effect of plasticization on the transport of gases in and through glassy polymers”. *Journal of Polymer Science Part B: Polymer Physics* 27.2 (1989). DOI: 10.1002/polb.1989.090270201 (cit. on p. 27).

[Zhu2021] X. Zhu, J. Huang, and M. Eikerling. “Electrochemical CO_2 Reduction at Silver from a Local Perspective”. *ACS Catalysis* 11.23 (2021). DOI: 10.1021/acscatal.1c04791 (cit. on pp. 37, 52).

[Zimm2017] A. Zimmermann, M. Kant, T. Strunge, E. Tzimas, W. Leitner, W. Arlt, P. Styring, K. Arning, M. Ziefle, R. Meys, A. Kätelhön, A. Bardow, A. Castillo Castillo, N. Flanders, S. Marini, and S.-P. Mechnig. *CO_2 utilisation today : report 2017*. 2017. DOI: 10.14279/depositonce-5806 (cit. on p. 155).